

## INFORMATION TO USERS

This manuscript has been reproduced from the microfilm master. UMI films the text directly from the original or copy submitted. Thus, some thesis and dissertation copies are in typewriter face, while others may be from any type of computer printer.

**The quality of this reproduction is dependent upon the quality of the copy submitted.** Broken or indistinct print, colored or poor quality illustrations and photographs, print bleedthrough, substandard margins, and improper alignment can adversely affect reproduction.

In the unlikely event that the author did not send UMI a complete manuscript and there are missing pages, these will be noted. Also, if unauthorized copyright material had to be removed, a note will indicate the deletion.

Oversize materials (e.g., maps, drawings, charts) are reproduced by sectioning the original, beginning at the upper left-hand corner and continuing from left to right in equal sections with small overlaps. Each original is also photographed in one exposure and is included in reduced form at the back of the book.

Photographs included in the original manuscript have been reproduced xerographically in this copy. Higher quality 6" x 9" black and white photographic prints are available for any photographs or illustrations appearing in this copy for an additional charge. Contact UMI directly to order.

# UMI

A Bell & Howell Information Company  
300 North Zeeb Road, Ann Arbor MI 48106-1346 USA  
313/761-4700 800/521-0600



STUDIES OF COMPOSITIONAL VARIATIONS IN THE THERMOSPHERE AND  
IONOSPHERE USING FAR-ULTRAVIOLET IMAGES FROM DE 1.

A  
THESIS

Presented to the Faculty  
of the University of Alaska Fairbanks  
in Partial Fulfillment of the Requirements  
for the Degree of

DOCTOR OF PHILOSOPHY

By  
Thomas Jerome Immel, B.A.

Fairbanks, Alaska

May 1998

**UMI Number: 9838835**

---

**UMI Microform 9838835**  
**Copyright 1998, by UMI Company. All rights reserved.**

**This microform edition is protected against unauthorized  
copying under Title 17, United States Code.**

---

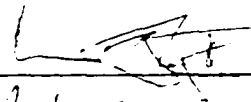
**UMI**  
**300 North Zeeb Road**  
**Ann Arbor, MI 48103**

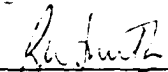
STUDIES OF COMPOSITIONAL VARIATIONS IN THE THERMOSPHERE AND  
IONOSPHERE USING FAR-ULTRAVIOLET IMAGES FROM DE 1

By

Thomas J. Immel

RECOMMENDED:

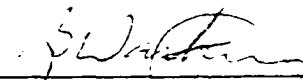
  
\_\_\_\_\_

  
\_\_\_\_\_

  
\_\_\_\_\_

  
\_\_\_\_\_

Advisory Committee Chair

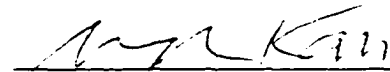
  
\_\_\_\_\_

Department Head

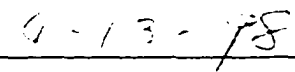
APPROVED:

  
\_\_\_\_\_

Dean, College of Science, Engineering and Mathematics

  
\_\_\_\_\_

Dean of the Graduate School

  
\_\_\_\_\_

Date

### Abstract

The Dynamics Explorer mission returned a wealth of information from its two orbiting platforms. Of interest here are the three scanning photometers aboard the high-altitude platform DE-1, which obtained hundreds of thousands of global images of Earth, beginning in September of 1981, while using broad- and narrow-band filters to isolate particular terrestrial emissions. The far-ultraviolet (FUV) emissions include the line emissions of OI (130.4 and 135.6 nm) and the band emissions of N<sub>2</sub> LBH, the brightness of each yielding information on the composition of the upper atmosphere. The OI emissions are related to the column density of atomic oxygen in the upper-atmosphere as well as the abundance of thermospheric N<sub>2</sub>, both of which are affected by geomagnetic processes.

This thesis presents a model of the DE-1 response to the OI emissions during periods of low geomagnetic activity and uses this model for studies of thermospheric response to geomagnetic storms and substorms. Variations in brightness observed after geomagnetic events are most often seen as decreases corresponding to reduced thermospheric O column densities. The relation between compositional variations in the morning sector at middle latitudes and the orientation of the magnetic field embedded in the solar wind is investigated. The orientation, which strongly affects the circulation of the thermosphere at high latitudes where these variations originate, is shown to be a significant parameter. Variations in brightness within the southern polar cap are investigated in the first study of its kind, demonstrating 20–30% decreases in brightness with the onset of magnetic activity and revealing structure in composition over distances on the order of ~300 km. Compositional disturbances are observed immediately after heating takes place, demonstrating for the first time that an FUV instrument can detect changes in thermospheric composition on time scales under one hour. During these events, mid-latitude composition often remains relatively unperturbed. The first survey of FUV images to include ground-based measurements of ionospheric properties demonstrates that decreases in OI brightness correspond to decreases in peak F2 electron densities, known to be related to the ratio of the densities of O and N<sub>2</sub>.

## Table of Contents

Signature Page .....	i
Title Page .....	ii
Abstract .....	iii
Table of Contents .....	iv
List of Figures.....	vi
List of Tables.....	ix
Acknowledgments .....	x
<b>Chapter 1 - Introduction.....</b>	<b>1</b>
1.1 Earth's Atmosphere.....	3
1.2 The Thermosphere.....	6
1.2.1 Chemistry and Heating.....	6
1.2.2 Ionization and Reactive Chemistry .....	9
1.2.3 Physics and Composition .....	13
1.2.4 Thermospheric Dynamics.....	14
1.3 The FUV Dayglow .....	19
1.4 Thermospheric Models.....	26
1.5 Exploring the Thermosphere.....	29
1.5.1 Direct Measurements of Thermospheric Properties.....	29
1.5.2 Global FUV Measurements of Thermospheric Properties .....	35
<b>Chapter 2 - Instrumentation .....</b>	<b>38</b>
2.1 The Dynamics Explorer Mission.....	38
2.2 Earth's Dayglow Observed by DE 1 .....	45
<b>Chapter 3 - The DE-1 Auroral Imager's Response to the FUV Dayglow for Thermospheric Studies .....</b>	<b>48</b>
3.1 Introduction .....	48
3.2 Image Selection and Initial Processing .....	50
3.3 Modeling Method .....	56
3.3.1 Dependence on Azimuth Angle .....	60
3.3.2 Dependence on Phase Angle.....	64
3.3.3 Dependence on Solar 10.7-cm Radio Emission.....	70
3.3.4 Iterative Technique for Separating Dependences.....	73
3.3.5 Dependence on Solar and Satellite Zenith Angle.....	74
3.4 Series of Images, Quiet .....	81
3.5 Summary .....	92
<b>Chapter 4 - The Influence of IMF By on Large Scale Decreases in O Column Density at Middle Latitudes .....</b>	<b>94</b>
4.1 Introduction .....	94

4.2 Comparison of Two Images .....	96
4.3 Four Consecutive Orbits.....	102
4.4 Statistical Analysis .....	107
4.5 Summary .....	118
<b>Chapter 5 - Decreases in FUV Dayglow Brightness within the Polar Caps.....</b>	<b>122</b>
5.1 Introduction .....	122
5.2 Dynamics Explorer 1 Observations.....	123
5.3 Variations in Polar Cap Dayglow.....	128
5.3.1 Temporal Variability .....	128
5.3.2 Spatial Variations .....	132
5.4 Summary .....	137
<b>Chapter 6 - Comparison of Images, Magnetic Indices, and Ground-Based Measurements.....</b>	<b>139</b>
6.1 Introduction .....	139
6.2 Data Selection and Processing .....	142
6.3 Discussion of Images in Survey .....	143
6.3.1 Days 267 and 269, 1981 .....	143
6.3.2 Quiet Period of day 291, 1981.....	147
6.3.3 Storm Period of days 293 through 296. 1981.....	148
6.3.4 Days 307 and 311, 1981 .....	150
6.3.5 Days 312–325, 1981 .....	152
6.4 Summary .....	153
<b>Chapter 7 - Synthesis .....</b>	<b>175</b>
7.1 Review of Significant Results .....	175
7.2 Future Work with DE 1 .....	178
7.3 Present and Future Missions .....	179
<b>Bibliography .....</b>	<b>183</b>
<b>Appendix A - Coefficients from Reference Model .....</b>	<b>193</b>
<b>Appendix B - Statistical Correlation .....</b>	<b>195</b>

## List of Figures

1-1 Atmospheric regions and identifying parameters.....	4
1-2 Altitude of unit optical depth .....	7
1-3 Comparison of $R(N_m)$ and $R(O/N_2)$ for negative ionospheric storms.....	12
1-4 General circulation of neutral thermospheric constituents at 1200 UT .....	15
1-5 Convection of magnetospheric/ionospheric plasma.....	17
1-6 The solar spectrum.....	22
1-7 Solar irradiance from X-ray to NUV wavelengths.....	23
1-8 Earth's ultraviolet dayglow .....	24
1-9 Earth's FUV dayglow.....	25
1-10 Earth's UV albedo.....	27
1-11 Effects of geomagnetic activity on thermospheric composition.....	31
1-12 Development of composition disturbance zone .....	32
1-13 Results from UCL-TGCM showing global-scale composition variations.....	34
2-1 Representation of DE-1 spin-scan auroral imager (SAI) optics.....	39
2-2 Cross-section of DE 1 .....	42
2-3 Sensitivity profiles of several filters used in FUV SAI experiment.....	43
2-4 Latitude and local time of apogee for DE 1 .....	44
2-5 FUV image of Earth.....	46

3-1 Original DE-1 image of Earth at 1725 UT on October, 18 1981 (day 291) at wavelengths 123–165 nm.....	52
3-2 Graphical illustration of the geometry for DE-1 measurements of dayglow brightness.....	54
3-3 Angular variables for image of Figure 1 .....	55
3-4 Average counting rate in two bins of azimuth .....	61
3-5 Dependence of photometer response on azimuth angle.....	62
3-6 Emission altitudes inferred from azimuth analysis .....	65
3-7 Dependence of photometer response on P .....	66
3-8 Plot of MSIS-86 number densities for fixed altitude and geographic position, and low geomagnetic activity for a range of local times.....	68
3-9 Dependence of $\langle r \rangle$ on F.....	72
3-10 Summary of dependence of $\langle r \rangle$ on F, P, and A.....	75
3-11 Average response $\langle r \rangle$ of the DE-1 FUV photometer for the quiet-time data set for filter #2(123–165 nm) for zenith angles $S=0^\circ-105^\circ$ and $D=0^\circ-65^\circ$ .....	77
3-12 Calculated reference values $\langle r \rangle'$ for the DE-1 FUV photometer response normalized to $A=90^\circ$ , $P=90^\circ$ , and $F=200$ Jy, using filter #2.....	79
3-13 Percent deviations of the average response $\langle r \rangle$ (Figure 3-11) from the reference values $\langle r \rangle'$ (Figure 3-12) for all S and four values of D.....	80
3-14 Reference image $I_r$ constructed from the original image of 1725 UT on October 18, 1981, shown in Figure 1 .....	82
3-15 Comparison of dayglow image to model .....	83

3-16. Series of 14 images taken by DE 1 on October 18, 1981 between 1536 and 1838 UT.....	85
3-17 Statistical distribution of PD values in images from day 291.....	87
3-18 Histogram of percent deviation from reference values of pixels in a synthetic image, $I_s$ .....	89
4-1 AE indices and selected PD (percent difference) images from days 267 and 279, 1981, respectively, in Figures 4-1a and 4-1b.....	97
4-2 IMF magnitude and the $B_y$ and $B_z$ components for days 267 and 279, 1981, respectively, in Figures 4-2a and 4-2b.....	100
4-3 AE indices, IMF magnitude, and the $B_z$ and $B_y$ components for days 280 and 281, 1981.....	103
4-4 Four selected PD images derived from FUV observations in four consecutive DE-1 orbits.....	105
4-5 AE index and five percent difference (PD) representations of images taken during one hour on Day 015, 1983.....	111
4-6 Variation in F and dayglow brightness at fixed S in the study period.....	112
4-7 Average Percent difference values in sectors 1 and 2 vs. six hour average values of AE.....	114
4-8 Difference between PD values of sectors 1 and 2 as a function of $B_y$ .....	116
4-9 Difference between sectors 1 and 2 as a function of $\langle AE \rangle$ .....	117
4-10 $\langle AE \rangle$ indices for images of the 1983 study period as a function of $\langle B_y \rangle$ .....	119
5-1 Percent Difference (PD) representations of images from successive orbits on days 2 (1b and 1c) and 3 (1e and 1f), 1983.....	125
5-2 PD representations of images from successive orbits on days 5 (2b and 2c) and 15 (2e and 2f), 1983.....	127

5-3 Average polar cap percent difference values at orbit times indicated in AE plots .....	131
5-4 $\langle PD \rangle$ values calculated from images in second orbit of each sequence.....	133
5-5 Average $\langle PD \rangle$ values within the polar cap for second orbit of each sequence.....	135
6-1 DST index for study period.....	156
6-2 Ionosonde $f_oF2$ values for selected stations in North America.....	157
6-3 Ionosonde $f_oF2$ values for selected stations in Europe.....	160
6-4 Ionosonde $f_oF2$ values for selected stations in the Far East.....	163
6-5 Mapped $\langle PD \rangle$ images and AE indices for study period.....	166
6-6 Comparison of $\langle PD \rangle$ and $PD(N_m)$ values for days 267 and 269.....	174

### List of Tables

4-1 Listing of Images Used in Statistical By Study.....	109
5-1 Images Used in Polar Cap Study and IMF y- and z- components during 6 Hours Previous to Imaging.....	130
6-1 Ionosonde Stations in Figures 6-2–6-4 .....	141
6-2 List of Days for Figure 6-5 .....	144
A-1 Slopes of Azimuth Dependence of $\langle r \rangle$ .....	194

### **Acknowledgements**

This thesis was written with the support of NASA grants NAGS-1915, NAGW-3436 and NAGW-3441. The UAF Graduate School also provided financial support through the Thesis Completion Scholarship and Eagle Tuition Scholarship programs, which allowed me to concentrate on my particular interests.

Many other people contributed to this effort. My advisor John Craven influenced my research and writing more than any other person, with good results. My committee members Roger Smith, Channon Price and Davis Sentman provided impetus and direction to my work. Celia Rohwer was largely responsible for maintaining the research computers used to perform the analyses described herein, and my computer technician David Lev built the machine on which I composed this thesis. I must thank all former and current Graduate Students of the Geophysical Institute who gave me their support and friendship. You know who you are!

This thesis is dedicated to Burney Dunn, who showed me the way to Alaska.

## Chapter 1

### Introduction

The lowest part of the atmosphere, which humans inhabit, is characterized by daily, seasonal, and epochal variations in temperature, water content and bulk atmospheric motion (wind). The state of these variables at any one time and place on Earth is a description of the local weather. The upper atmosphere (at altitudes of ~100–1000 km) is also subject to daily and seasonal variations but at these high altitudes the ranges of temperature and density are larger and wind velocities are greater overall. The state of these variables may also be called weather. The mechanisms controlling these weather effects are different, however, and little can be inferred about one region by making observations in the other.

One driver that is common to each system is the sun. The seasonal variations observed at all altitudes and latitudes are due, directly or indirectly, to changes in the average incident solar energy flux with geographic latitude. Variations in total solar radiant energy output with the sunspot cycle are on the order of  $\pm 0.1\%$  over the associated 11-year period and as large as several tenths of a percent during periods of strong flare variability [Lean, 1989]. It has been suggested that the lower atmosphere is affected both by prolonged periods of depressed solar activity on the order of 100 years (*e.g.*, the Little Ice Age of ~1400–1850 AD [Burroughs, 1992]) and on shorter time scales as well [National Academy of Sciences, 1982]. The true magnitude of the effect of variations in the total solar energy output on weather and climate in the lower atmosphere is frequently debated. On the other hand, temperatures and densities in the upper atmosphere respond strongly to solar variations in the 11-year cycle. This reflects the fact that the largest variations in the solar spectrum in the course of a solar cycle are in the far- and extreme-ultraviolet emissions (FUV and EUV wavelengths, respectively) that interact strongly with constituents of the upper atmosphere. Temperatures at positions in the upper atmosphere can increase by as much as 100 K with an increase in solar flare activity and differ by as much as 500 K between the minimum and maximum of the solar cycle. Examples of such large-scale variations can be seen in MSIS-86 model results [Hedin,

1987]. Epochal variations in the upper atmosphere can only be supposed, as no long-term observations are available. However, prolonged periods of depressed solar activity and decreased UV emissions at the shorter wavelengths would likely be matched by a period of decreased temperatures in the upper atmosphere.

A source of energy that is dissipated primarily in the upper atmosphere (vs. the lower atmosphere of Earth) is the energy extracted from the solar wind by Earth's magnetosphere. This highly variable energy source affects temperatures, densities and winds in the polar upper atmosphere via energetic particle precipitation along magnetic field lines and currents driven through Earth's ionosphere by magnetospheric electric fields. The aurora is the optical manifestation of this energy input. During periods of auroral substorms [Akasofu, 1964], the impulsive energy input can affect the atmosphere well outside of the polar region [Burns *et al.*, 1991; Burns and Killeen, 1992]. During the most energetic geomagnetic storms, where magnetospheric currents can be enhanced for many days, upper-atmospheric temperatures and winds are strongly affected on a global scale. Composition may also be sufficiently disturbed such that the ratio of the abundance of heavy to light species can vary by a factor of 100 at auroral latitudes, where these effects are most immediate. Auroral energy inputs are difficult to predict compared to the dominant solar input, just as lower-atmospheric equivalents such as hurricanes, blizzards and heat waves are difficult to predict during the regularly occurring seasons.

Human activity in space is increasing. Placement of numerous communication satellites in low-altitude orbits (300–1000 km) and a planned continuous human presence necessitates a continuous knowledge of weather in the upper atmosphere, where many of these activities actually take place. Now, more than ever, it is imperative that humans be able to immediately describe and even predict the state of the upper atmosphere, or the weather, at a given point or along a satellite's orbital track. Real-time global observations of density and temperature are highly desirable.

Various ground- and space-based methods are now used to quantify in real time variations in upper-atmospheric properties. From the ground, radar experiments have been performed from which the density of certain upper-atmospheric constituents can be

inferred [Bauer *et al.*, 1970]. The DMSP (Defense Meteorological Satellite Program) and TIROS/NOAA satellites are polar orbiting platforms that pass through the two auroral ovals with each orbit to provide routine measurements of auroral energy fluxes. Global parameters describing the global energy influx are subsequently inferred from these spatially limited measurements [Evans, 1987]. Analysis of the signals received at the ground from the constellation of satellites of the Global Positioning System (GPS) has recently been used by Ho *et al.* [1996] to infer the total electron content (TEC) of the ionosphere over large areas of Earth. The TEC, in turn, is related to the density of other atmospheric constituents, both neutral and ionized [Prölss, 1993; Rishbeth and Garriot, 1969].

This thesis concentrates on a method that uses the measurement of solar FUV emissions scattered by the upper atmosphere to indirectly infer some properties of upper-atmospheric weather. These analyses provide simultaneous observations of the properties of the upper atmosphere over a broad range of geographic locations and, when combined with observations from other space-based platforms, indicate factors which strongly influence the development of upper-atmospheric storms.

### 1.1 Earth's Atmosphere

For the sake of classification, regions of Earth's atmosphere are defined by the physical processes or attributes characteristic of a particular altitude range. As examples, different regions can be identified by changes in the vertical temperature gradient, by ion concentration, or whether the species are evenly mixed or vary in density relative to one another with altitude. Profiles of atmospheric neutral temperature and ion and neutral number densities are shown in Figure 1-1a through 1-1c [Rees, 1989] and will be referred to often in this introduction. The atmospheric regions designated by the sign of the vertical temperature gradient are indicated in the first panel while electron densities shown in the center panel identify the two peaks in density that correspond to the E and F regions of the ionosphere. Neutral number density is shown in the last panel. Separation between the homosphere, where the relative proportion of major neutral components

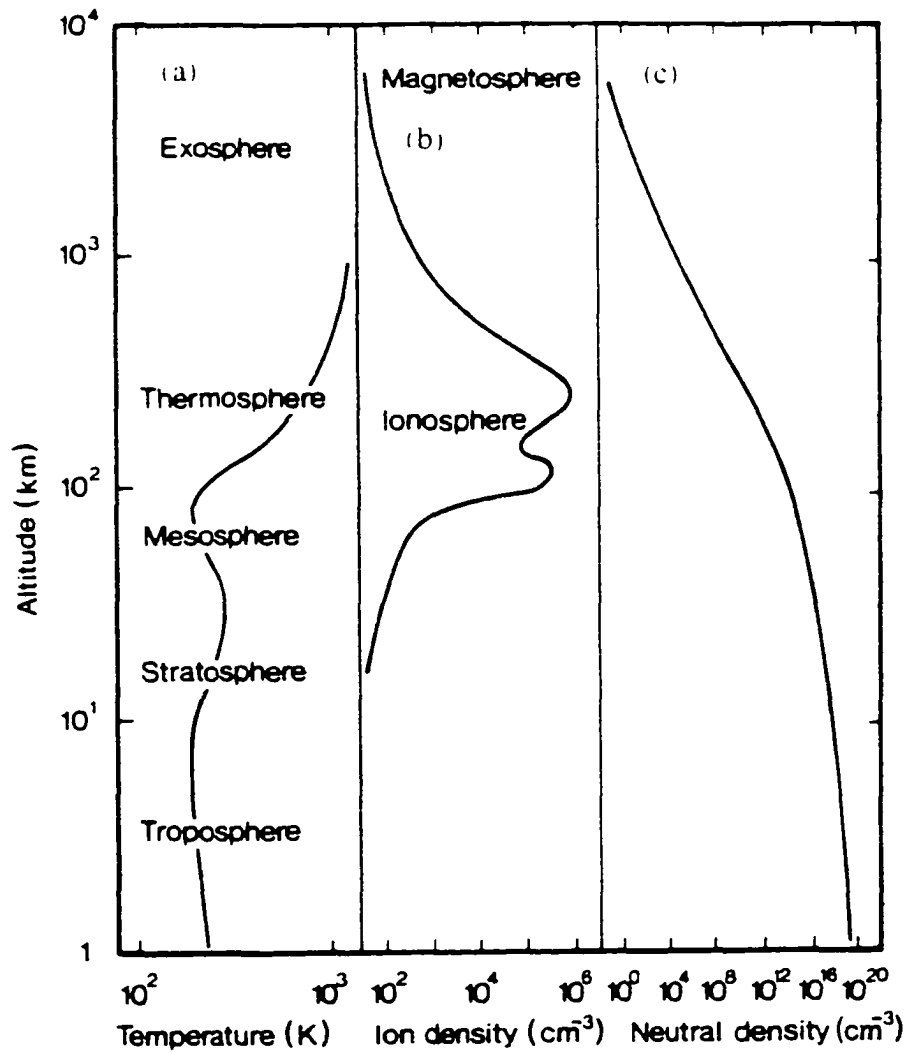


Figure 1-1. Atmospheric regions and identifying parameters. The regions of the atmosphere are identified by (a) the sign of the vertical temperature gradient (b) the ion density altitude profile (with density maxima at E and F region altitudes) and (c) the neutral density gradient. [Figure from Rees, 1989].

changes little with altitude due to vertical mixing, and the heterosphere, where diffusive separation of heavy and light neutrals occurs, depends on the density of atmospheric constituents. While the upper atmosphere is not a strictly defined region, the significant ionization of atmospheric constituents and the diffusive separation of constituents by mass are effects measured only at altitudes well above the inhabitable lower atmosphere. By these criteria, the lower boundary of the upper atmosphere is between 80 and 90 kilometers, within the mesosphere (an atmospheric region to be described presently).

The troposphere is the atmospheric region closest to Earth, where the temperature decreases with altitude. The solid lower boundary of Earth's surface efficiently absorbs infrared solar radiation, providing heat through direct contact with the atmosphere. The temperature gradient in the troposphere is approximately given by

$$\left(\frac{dT}{dz}\right)_{ad} = -\frac{g(z)}{c_p} \quad (1.1)$$

where  $c_p$  is the specific heat of dry air and  $g(z)$  is the acceleration due to gravity. This temperature gradient is often referred to as the adiabatic lapse rate and is  $\sim 9.8$  K/km for dry air [Chamberlain and Hunten, 1987]. At an altitude which is considered the upper boundary of the troposphere (the tropopause), the gradient reverses and temperature increases with altitude throughout the stratosphere. The tropopause altitude, on average, ranges from 15 to 8 km at tropical to polar latitudes, respectively. The increase in stratospheric temperature with altitude is caused by heating due to absorption of middle- and near-ultraviolet solar radiation (MUV and NUV wavelengths, respectively) by  $O_3$  and  $H_2O$ , which subsequently transfer vibrational energy to major atmospheric constituents through collisional deactivation.

Whereas  $O_3$  provides a source of heat,  $CO_2$  is effective in radiatively cooling this and other atmospheric regions. Collisions between  $CO_2$  and major constituents excite vibrational states in the  $CO_2$  molecule that re-radiate the energy in the infrared, an emission to which the upper atmosphere is largely transparent. Temperature once again begins to decrease with altitude around 25–35 km (from high to low latitudes.

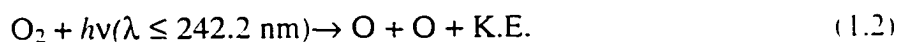
respectively) as the value of  $[\text{CO}_2]/[\text{O}_3]$  continues to increase with altitude [Rees, 1987]. The position of this temperature gradient reversal is termed the stratopause, above which is the mesosphere, for which a temperature gradient of approximately  $-5 \text{ K/km}$  is maintained up to the mesopause (at  $\sim 85 \pm 5 \text{ km}$  altitude), the coldest region in the atmosphere. The mesopause altitude varies daily and seasonally and is often not a standout feature, rather a temperature plateau. [Webb, 1966]

The region of the atmosphere studied in this thesis is the thermosphere, so called for the increase in neutral temperature with altitude above the mesopause, up to a limiting value in the exosphere, the collisionless region where the majority of neutral atmospheric constituents have ballistic trajectories. At lower altitudes the boundary between the mesosphere and the thermosphere is determined by the balance of different heating processes in the thermosphere with the still-present radiative loss due to  $\text{CO}_2$  at lower altitudes.

## 1.2 The Thermosphere

### 1.2.1 Chemistry and Heating

The conversion of solar radiative energy into thermal energy in the thermosphere requires the action of the dominant atmospheric constituents. Thermospheric temperatures are affected mainly by the photo-dissociation and exothermic recombination of  $\text{O}_2$ , written, respectively, as



and



'K.E.' indicates a variable kinetic energy imparted to the products of the reaction, depending on the energy of the photon reactant, and M indicates any local neutral constituent of the thermosphere. The UV wavelength indicated in Equation 1.2 identifies the minimum energy (5.12 eV) required to dissociate  $\text{O}_2$ . However, the absorption cross section of  $\text{O}_2$  is extremely small at this wavelength. The  $1/e$  attenuation altitude of UV radiation shown in Figure 1-2 [Meier, 1991] illustrates that the attenuation of radiation at

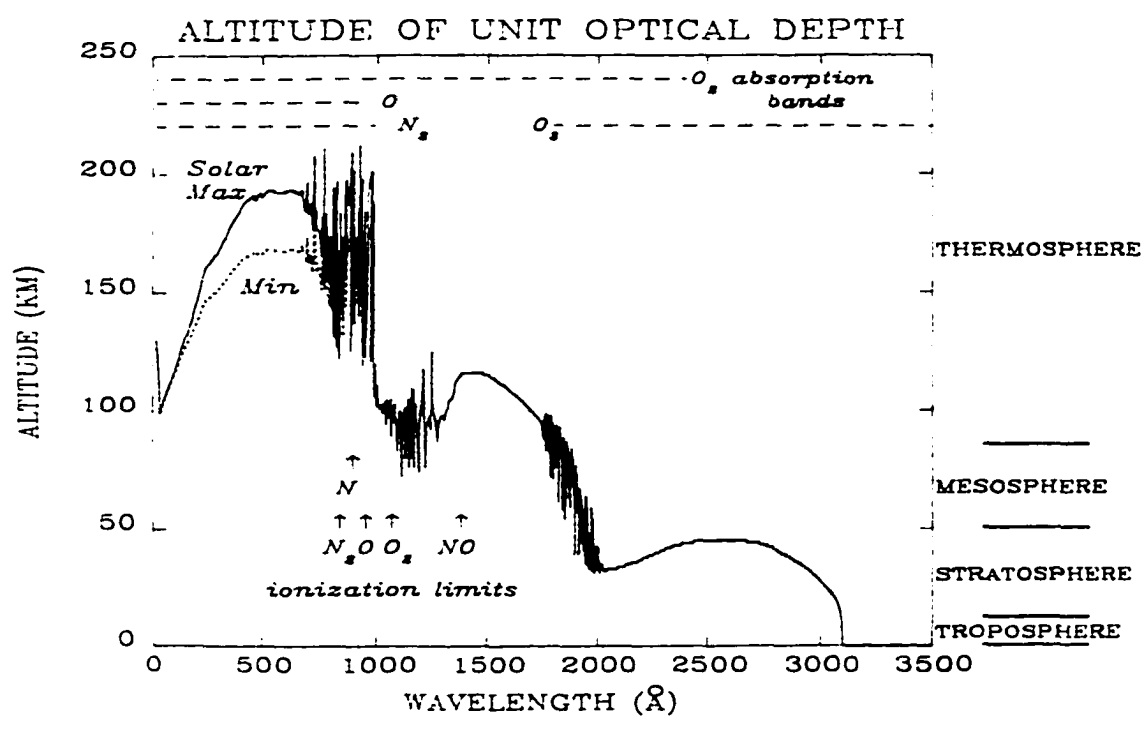
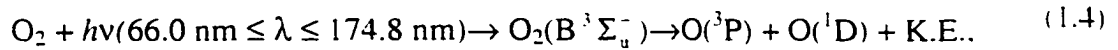


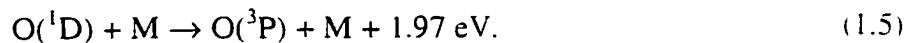
Figure 1-2. Altitude of unit optical depth. The altitude at which solar emissions are reduced by a factor of  $e^{-1}$  is indicated for a range of wavelengths from 10 Å (EUV) to 3500 Å (NUV) and for two MSIS atmospheres. The wavelength ranges of discrete and continuous absorption by O, O<sub>2</sub>, O<sub>3</sub>, and N<sub>2</sub> are also indicated. The two MSIS atmospheres represent low and high levels of solar activity resulting in changes in unit optical depth at  $\lambda < 1000 \text{Å}$ . [Figure from Meier, 1991].

$\lambda > 175$  nm takes place primarily in the mesosphere and stratosphere and is due to absorption by  $O_3$ . Coincidentally, this 175 nm wavelength limit corresponds to the minimum energy necessary to excite the unstable  $O_2(B^3\Sigma_u^-)$  state. The photo-dissociative reaction most common for thermospheric  $O_2$  is, therefore,

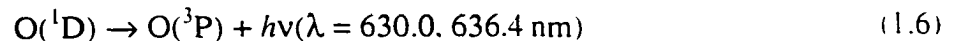


yielding O in ground and metastable excited states, where one of a variety of possible product states is given here. The reaction in Equation 1.4 describes the fate of most molecular oxygen in the thermosphere that interacts with solar FUV radiation, though there are other less probable outcomes.

The extra kinetic energy imparted to the reaction products in Equation 1.4 leads to higher average kinetic energies per particle in the thermosphere (i.e., higher temperatures). The excited  $O(^1D)$  state may relax to the  $O(^3P)$  ground state through either collisional deexcitation (quenching) that transfers additional energy to a thermospheric constituent or a spin-forbidden electron transition that releases a photon at either 630.0 or 636.4 nm. An example of such a quenching reaction is



The most likely deactivator is  $N_2$ . Note that, as opposed to the recombination reaction of Equation 1.2, this quenching requires only a two-body interaction. The excited state may relax radiatively in the upper thermosphere via the reaction



before being quenched. The half-life of this state is  $\sim 110$  seconds [Rees, 1989] and it yields prominent auroral and airglow emissions. The transition energy diagrams for atomic and molecular oxygen are given by Meier [1991].

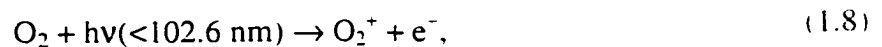
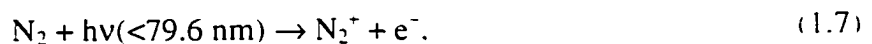
The recombination of atomic oxygen (Equation 1.3) requires a third body to catalyze the reaction and as such this reaction occurs mostly in the lower thermosphere, where collisions are most frequent. The 5.12 eV of exothermic energy (corresponding to  $\lambda \sim 242.2$  nm) is exactly the energy required to disassociate the  $O_2$  molecule into two ground state oxygen atoms. The  $O_2$  and M products share this energy, which is quickly

thermalized in the lower thermosphere, adding energy to the neutral gas and increasing its temperature. This cycle of dissociation and recombination is ultimately governed by the intensity of solar FUV and EUV emissions, and an increased reaction rate brought about by greater solar UV flux leads directly to higher thermospheric (and exospheric) temperatures.

Solar radiation at wavelengths less than 102.6 nm can produce ionization in the form of  $O_2^+$  and an electron, and at wavelengths shorter than 66.2 nm the molecular ion product is unstable, immediately dissociating to O,  $O^+$ , and  $e^-$ . This, and the photoionization of O by solar EUV emissions at wavelengths shorter than 91.1 nm, are the major sources of electrons in the ionosphere (to be addressed in the next section).

### 1.2.2 Ionization and Reactive Chemistry

Electron and ion densities, though well below neutral densities, are of great importance in this region of the atmosphere. The electron density as a function of altitude is shown in Figure 1b. The electrons and ions are equal in density and tend to vertically diffuse upward together above the F-region peak through the process of ambipolar diffusion. The E-region electron density peak (occurring between ~100 and 120 km) is only present during the times where solar photoionization can create ions (*i.e.*, daytime) through the processes



and



whereas the F-region electron density peak (usually between 280 and 400 km) is a consistent feature at all local times, due to the much lower recombination rates at higher altitudes [Ratcliffe, 1960]. Note that the above reactions are a small subset of the possible results of the interaction of solar radiation with neutral atmospheric constituents.

These reactions are the primary source terms for ions and free electrons in the upper atmosphere. Ion density varies with neutral density in the upper thermosphere, with a departure from this trend at the F2 peak, below which ion density tends to decrease while neutral densities continue to increase. In this region, the loss of ionization through chemical reactions is larger than the EUV driven source described above. The loss of ionization through radiative recombination of the dissociated constituents (*i.e.*, the reversal of reactions 1.11, 1.12, and 1.13) occurs at a relatively slow rate, due to the low concentrations of  $N_2^+$  and  $O_2^+$  above ~200 km and the fact that  $O^+ + e^-$  yields a highly excited state of O which usually undergoes immediate autoionization [Rees, 1989]. A more rapid means of removal of ionization involves the intermediate reactions



and



The reaction of 1.10 (*vs.* that of 1.11) is the more likely source of molecular ions, since  $N_2$  is more abundant than  $O_2$  throughout the upper atmosphere. Ionospheric electrons dissociatively recombine with the new charged species via



and



shunting the energy of ion-electron recombination into the dissociation of the molecular species. The products of these two reactions can be in excited electronic states, but usually radiate that energy as light and remain neutral. The combination of the reactions listed in 1.7 through 1.13 effectively describe the role of neutrals in determining F2-region ionization and height density profile, with 1.7–1.9 indicating source terms and 1.10–1.13 indicating loss terms. In this manner, the composition of the thermosphere and ionosphere are closely related. Changes in the abundance of O or  $N_2$  at F-region altitudes have a significant effect on the magnitude of electron densities in the upper atmosphere as

O is an important source of electrons and  $N_2$  acts to create molecular ions from  $O^+$ , which then may more readily recombine with electrons.

The important relation between O,  $N_2$ , and ionospheric electron densities can be seen in a comparison of F2 layer maximum electron densities ( $N_mF2$ ) and neutral composition measurements for a geomagnetic storm occurring in February, 1973 [Prölss and von Zahn, 1974; Prölss, 1980]. Given the opposing effects of O and  $N_2$  on electron densities, the ratio of their densities is a useful parameter to measure for comparison to electron densities. A comparison of  $O/N_2$  values at 280–320 km above six ground stations, as measured by the mass spectrometer aboard the satellite ESRO 4, and corresponding values of  $N_mF2$  is shown in Figure 1-3a. Observed values of  $O/N_2$  are compared to mean values, as are the values of  $N_mF2$ , by calculating the ratio between the observed and mean values, resulting in  $R(N_m)$  and  $R(O/N_2)$ . Thus, unity indicates no deviation from mean values. The covariance of these two parameters over the eight-day period is striking. Note that these are stations in the Southern Hemisphere, their geographic locations denoted to the right of their international (geophysical) abbreviation. Each of these stations was equipped with an ionosonde to determine  $N_mF2$  values, an instrument further described in Chapter 6. A decrease in ionospheric electron densities from monthly mean values during a geomagnetic event is termed a 'negative' ionospheric storm effect, while increases are described as 'positive' storm effects.

The overall relation of  $R(N_m)$  to  $R(O/N_2)$  is shown in Figure 1-3b, where the data from another comparison of 'negative' ionospheric storm effects over the Northern Hemisphere are included in the data set. Each point represents the  $R(N_m)$  and  $R(O/N_2)$  values over a station on a particular day. The linear relationship between these parameters is highlighted by a line with slope of unity. This linear relationship only holds during negative storm effects. Strong increases in ionospheric electron densities associated with positive storms are not well correlated with increases in  $R(O/N_2)$  [Prölss *et al.* 1975; Prölss, 1980].

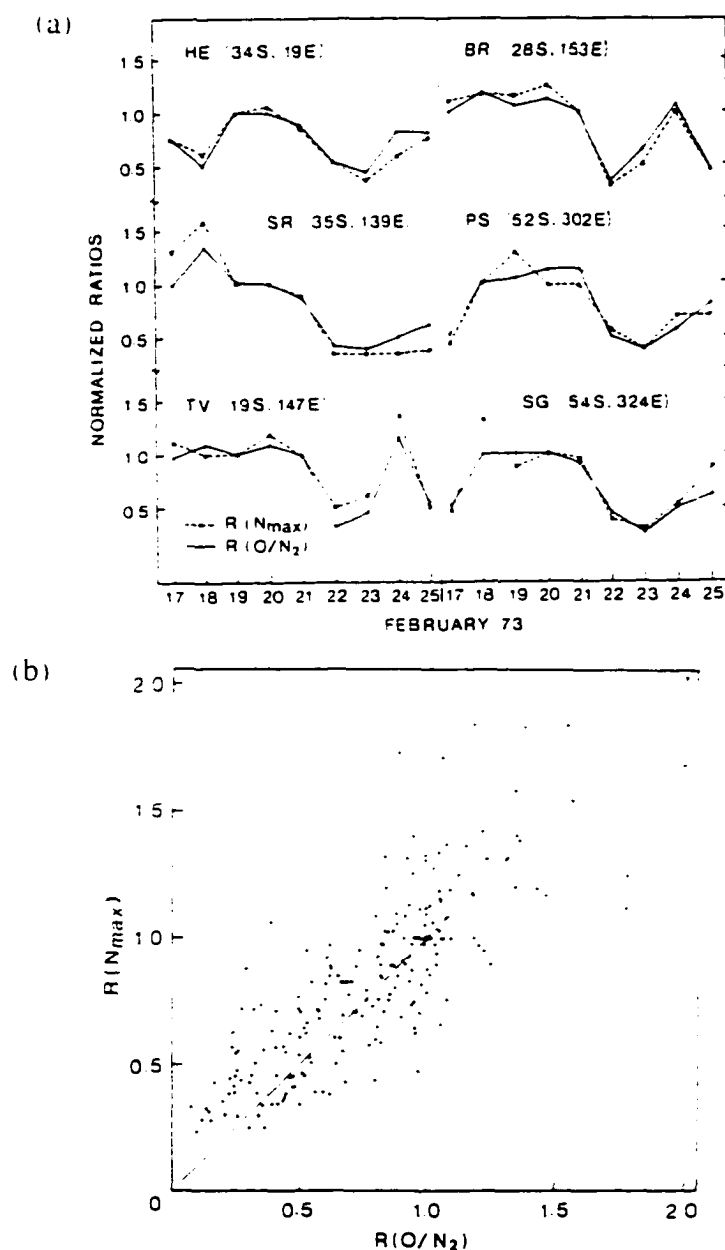


Figure 1-3. Comparison of  $R(N_m)$  and  $R(O/N_2)$  for negative ionospheric storms. (a) ESRO-4 neutral composition measurements are compared to electron densities over six southern ionosonde stations during a storm in February, 1983. The geographic positions of the ionosonde stations are shown to the right of their international symbols. (b) A scatter plot of  $R(N_m)$  vs.  $R(O/N_2)$  including the 54 daily comparisons shown in Figure 1-3a is shown, including 36 more comparisons from northern latitude measurements of a negative ionospheric storm in October, 1973. A line of slope=1 is overlain for comparison. [Figure from Prölss, 1980].

### 1.2.3 Physics and Composition

The thermosphere can be described as an atmospheric region in nearly hydrostatic equilibrium. The O and O<sub>2</sub> source and loss reactions described above have little direct impact on total neutral density at any thermospheric altitude [Rees, 1989]. However, the temperature at the base of the thermosphere directly affects the diffusive equilibrium of the various neutral constituents, so the intensity of solar EUV radiation governs the neutral densities of the thermosphere. Mass mixing ratios are largely governed by processes of atomic and molecular diffusion and may change by orders of magnitude with temperature variations at the thermobase. Total mass density as a function of altitude is also affected by such variations, but to a much lesser degree.

For the case of hydrostatic equilibrium the balance of gravity and atmospheric pressure may be represented in a restatement of the conservation of momentum equation by

$$\partial p / \partial z = -\rho g \quad (1.14)$$

where  $p$  is pressure,  $\rho$  is the total neutral mass density and  $z$  is altitude. The atmosphere is assumed to be an ideal gas where pressure is defined as:

$$p = nkT \quad (1.15)$$

Given a mean neutral mass,  $\bar{m} = \rho/n$ , the momentum equation can now be written as:

$$\frac{1}{p} \frac{\partial p}{\partial z} = -(\bar{m}g)/kT \quad (1.16)$$

which indicates an exponential decrease in pressure with altitude. The inverse of the right hand term is often referred to as the scale height. This equation, of course, cannot give an exact representation of the pressure at all altitudes for  $T$  varies strongly with  $z$ . The above equation represents an atmosphere in hydrostatic equilibrium which generally describes the region below ~100 km. If some forcing takes place, large-scale vertical motion of mass can occur. This also occurs above 80 km and is discussed in the following section on thermospheric dynamics.

At higher altitudes, the atomic and molecular constituents of the atmosphere can move separately from the mass averaged motion; i.e., the constituents can diffuse through the atmospheric medium and  $\bar{m}$  is now  $\bar{m}(z)$ . This can occur in atmospheric regions where mixing between altitudes takes place at a slower rate than diffusive processes. Following the development for hydrostatic equilibrium, but allowing for variations in relative abundance of the constituents (of differing mass), one may derive for a particular constituent its density as a function of altitude  $z$ ,

$$n_j(z) = n_j(z_0) \left[ \frac{T(z_0)}{T(z)} \right]^{(1-\alpha_j)} \exp \left[ - \int_{z_0}^z \frac{m_j(z')g(z')}{kT(z')} dz' \right], \quad (1.17)$$

given a base altitude, density and temperature ( $z_0$ ,  $n_0$ , and  $T_0$ , respectively). The coefficient of thermal diffusion,  $\alpha_j$ , for certain interactions (such as  $N_2$ - $N_2$ ) is also necessary [Rees, 1989]. The integral containing the inverse of the scale height appears in this expression as in Equation 1.9, but is specified for the  $j$ -th constituent. The densities of heavier constituents such as O and  $N_2$  will decrease more rapidly with altitude than those of light constituents, such as H and He. It is for this reason that H and He have greater concentrations than O in the upper thermosphere and exosphere.

#### 1.2.4 Thermospheric Dynamics

A large temperature gradient exists in the thermosphere between the day and night hemispheres due to uneven heating by solar UV radiation. The resulting difference in number density at given altitudes sets up significant horizontal pressure gradients, with highest pressure in the mid-afternoon sector. The force resulting from this pressure gradient, coupled with the coriolis forces of the rotating frame of reference, generates a large-scale flow of neutrals, the neutral wind, that is directed from the dayside toward the nightside over much of Earth. This can be seen in Figure 1-4, which shows global neutral wind vectors at 300-km altitude and 1200 UT calculated using a thermospheric general circulation model (TGCM) with  $15^\circ$  resolution in geographic latitude and longitude [Dickinson *et al.*, 1984]. The plot is centered at the Greenwich meridian.

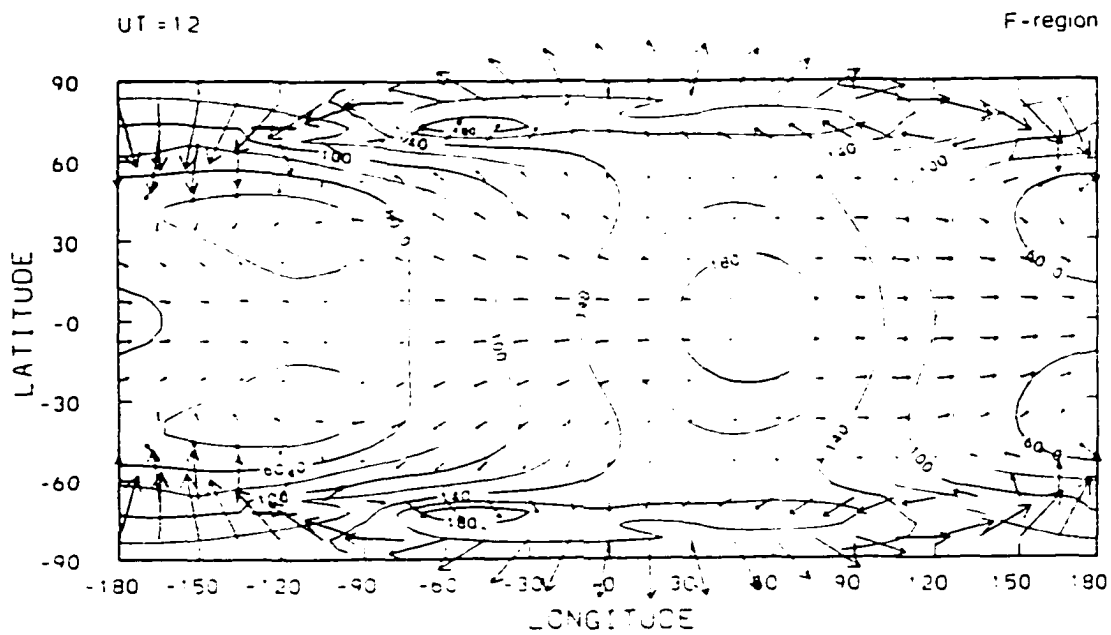


Figure 1-4. General circulation of neutral thermospheric constituents at 1200 UT. Global neutral wind vectors at 300 km altitude are shown at 15° intervals of geographic latitude and longitude. The longest vector indicates a horizontal speed of 336 m·sec<sup>-1</sup>. [Figure from Dickinson, 1984].

Diverging from an area at the equator near 1400 hours local solar time (LST), the solar-forced winds advect heated portions of the atmosphere most strongly across the mid-latitude evening terminator and into the nightside. The winds can be seen to converge at ~0600 LST. Zonal winds dominate near the equator due in part to the effect of coriolis forces present in the rotating system; parcels of air moving north or south from the equator will gain an eastward velocity component. Furthermore, the offset of the divergence zone towards the afternoon sector and the even stronger offset of the convergence zone to the morning terminator are partially the result of the eastward corotation of the atmosphere with Earth. The large wind velocities at the poles are only partially caused by solar forcing. Ion-drag forces due to collisional interaction of convecting ions with neutral constituents act in the same direction. The resulting neutral winds in the polar regions are the most rapid on the planet.

The direction of the ion flow is determined primarily by magnetospheric electric fields imposed on the ionosphere. The motion thus induced in the ionized portion of the atmosphere plays an important role in the dynamics of the neutral atmosphere. In the approximation that magnetic field lines are equipotentials, electric fields of magnetospheric origin map down to the polar regions of Earth, forcing a circulation of the ionospheric plasma. Magnetospheric plasma is driven sunward in the distant magnetotail through a northward magnetic field comprising the superposition of Earth's dipole field and the field associated with currents generated by the dawn-to-dusk electric field as shown in an equatorial cross-section of the magnetosphere in Figure 1-5a. The return flow of plasma in the flanks near the magnetopause also moves through this field. The result of the bulk motion of plasma is the generation of electric fields in the  $-\vec{v} \times \vec{B}$  sense in the Earth/magnetosphere rest frame. This 'dynamo' electric field maps to the ionosphere along magnetic field lines, which can be considered equipotentials due to the high conductivity in the direction of the field.

The electric potential pattern due to one possible electric field configuration (actual output from AMIE modeling technique discussed in section 1.4) is shown in the inset of Figure 1-5. The electric field is directed perpendicular to these potential lines and

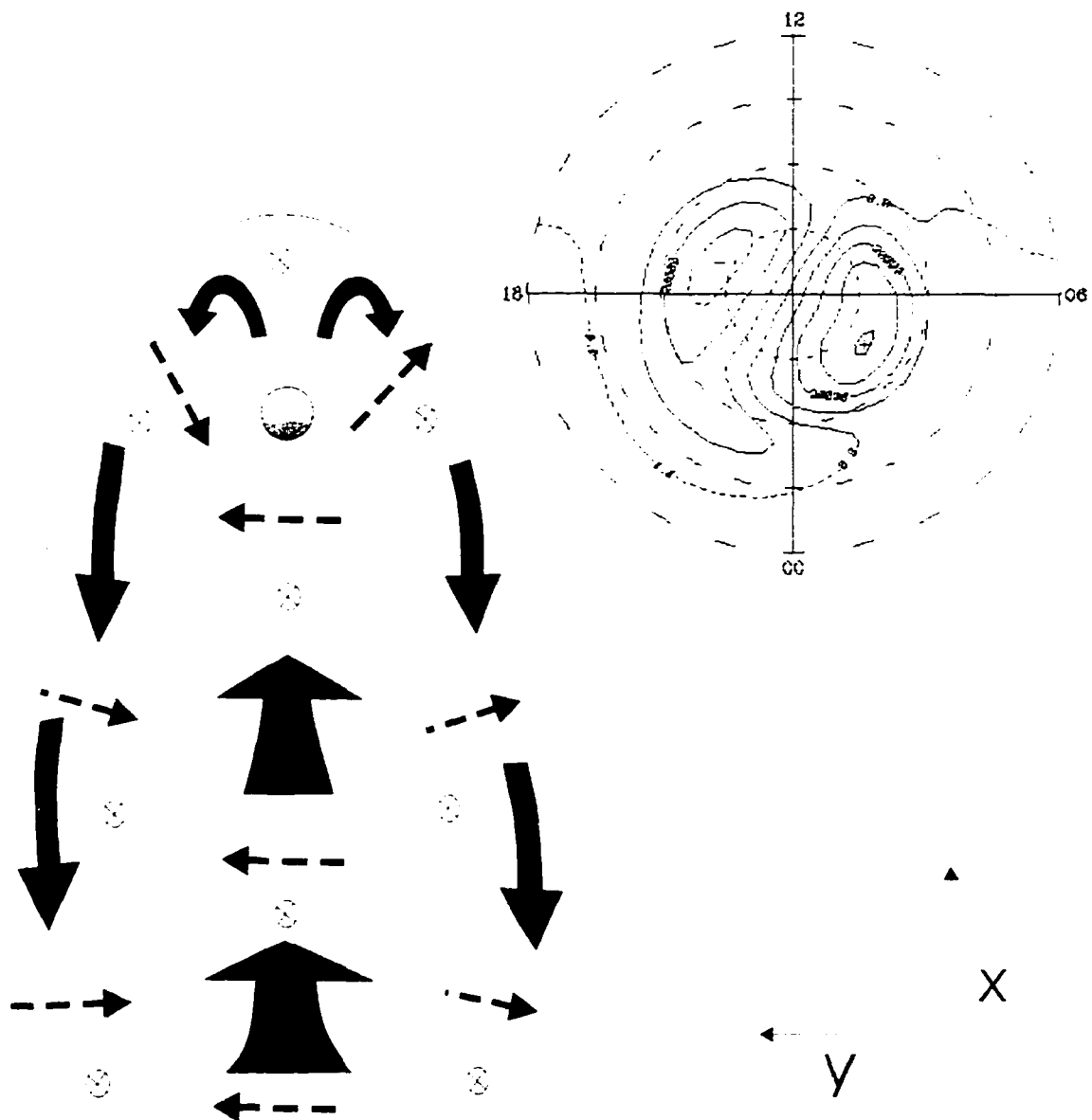


Figure 1-5. Convection of magnetospheric/ionospheric plasma. (a) An idealized cross-section of Earth's magnetosphere in the Geocentric-Solar-Magnetospheric x-y plane is shown from a viewpoint at  $z > 0$ . Bulk motion of magnetospheric plasma driven by magnetic reconnection is shown with large grey arrows. Dipole magnetic field vectors oriented in the  $+z$  direction are indicated with crossed open circles. The "dynamo" electric field in the  $-\bar{v} \times \bar{B}$  sense is indicated with dashed arrows. (inset) A representative electric potential pattern from AMIE for the northern hemisphere where dipole magnetic field vectors are now everywhere oriented downward. The resultant  $\bar{E} \times \bar{B}$  drift of ionospheric plasma (at F-region altitudes) is (counter-)clockwise in the (morning) evening vortex. [AMIE model results from Gang Lu, private communications, 1997].

generally in the dawn-to-dusk sense (right-to-left) at polar cap latitudes. The low and high electric potential values of the pattern are indicated and the dotted lines indicate constant geomagnetic latitudes with the outer contour at 50°N. The resultant (nearly horizontal)  $\bar{\mathbf{E}} \times \bar{\mathbf{B}}$  drift of ionospheric constituents describes a two-celled system with (anti-) clockwise rotation in the (dawn) dusk sector. The diagrams in Figure 1-5 are for the Northern Hemisphere, where the sun is toward the top of the page in this geomagnetic coordinate system.

This plasma convection in the polar regions can strongly affect the general flow of thermospheric neutrals. The global neutral wind vectors of Figure 1-4, for example, are calculated with an assumed cross-polar cap potential of 60 kV. This large potential generated by magnetospheric convection is indicative of strong geomagnetic activity, for which the longest vector represents a horizontal wind velocity of 336 m/sec. Note that the high latitude winds exhibit (1) a very strong anti-sunward flow from the noon sector to midnight sector (where pressure-gradient and ion-drag forces are similarly directed) and (2) a less intense sunward flow equatorward of the strongest anti-sunward winds (where pressure-gradient and drag forces are in opposition). The ion-drag force is a result of ion-neutral collisions in the ion circulation vortices described above.

In the absence of collisions, charged particles will gyrate about magnetic field lines with a cyclotron angular frequency  $\omega_c = qB/m$  and, as noted above, charged particles subjected to non-parallel electric and magnetic fields will drift in the  $\bar{\mathbf{E}} \times \bar{\mathbf{B}}$  direction. At F-region altitudes, the collision frequency of both ions ( $\nu_{in}$ ) and electrons ( $\nu_{en}$ ) with neutrals is much lower than the cyclotron period of either species and the  $\bar{\mathbf{E}} \times \bar{\mathbf{B}}$  drift is unimpeded. Collisions between drifting ions and neutrals are frequent enough, however, to impart the same general large-scale direction of motion to the neutrals at these high altitudes. Observations made by satellites passing through this region have observed the strong correspondence between neutral wind velocities and plasma drifts [Killeen *et al.*, 1982; Hays *et al.*, 1984].

At E-region altitudes, the collision frequency of ions with neutrals is greater than their gyrofrequency, so the gyromotion-dependent  $\bar{\mathbf{E}} \times \bar{\mathbf{B}}$  drift of ions is impeded. Ions will tend not to drift but move in the direction of the electric field. Electrons, with a two-thousand-fold larger gyrofrequency, will continue to gyrate about field lines, and consequently drift. This differential motion of the two charge species results in a net current that is measured by ground-based magnetometers. An array of magnetometers located in the polar regions can provide an indicator of the amount of energy transferred from the plasma to the neutral atmosphere [Spiro *et al.*, 1982]. A portion of this energy goes towards heating the atmosphere; this is referred to as Joule heating.

Joule heating of the lower thermosphere is a continuous process, as a dynamo electric field of some magnitude is nearly always present in the magnetosphere. Even during periods of low magnetic activity, thermospheric constituents in the auroral region are heated and forced upward. The mixing ratio,  $n_i/n_{total}$ , of thermospheric constituents is affected, increasing the density of heavier constituents. Strong forcing can cause disturbances in mixing ratios and total densities which extend to middle and low latitudes. In what manner disturbed portions of the atmosphere advect out of the polar cap to eventually appear at mid-latitudes on the dayside is one question this thesis addresses. The influence of magnetospheric convection is at once obvious and complicated. The two-celled circulation pattern that drives neutrals anti-sunward across the polar cap clearly reaches to mid-latitudes during storm events, but the exact configuration of the pattern varies strongly with orientation of the interplanetary magnetic field (IMF) [Smith *et al.*, 1988; Thayer *et al.*, 1987; McCormac *et al.*, 1985]. Furthermore, strong Joule heating can generate composition disturbances, the phase of which can propagate from one polar region to the other [Prölss, 1980] and eventually around Earth.

### 1.3 The FUV Dayglow

All constituents of the atmosphere interact with solar radiation, and an understanding of the interactions enables the observer to interpret atmospheric optical observations.

Light may be scattered by atmospheric constituents via several different processes and it may also be produced by the same constituents via quantum excitation and relaxation processes as described previously. The radiation originating in Earth's atmosphere is termed the dayglow and consists of both scattered solar radiation and in-situ emissions.

Resonance scattering occurs when an atom interacts with a photon whose energy is very close to that of an accessible electron transition. Often, the photons that resonantly interact with an atom have been previously emitted by the same element. This is the case for solar emissions by species such as H, He, O and N, which have corresponding components in Earth's atmosphere. Atomic species resonantly scatter incident photons much more efficiently than molecular species, as a cascading path through rotational and vibrational states is available to the excited molecular electron, resulting in a wide range of emissions possible for a given incident photon energy. Often, a photon can be resonantly scattered many times by a particular atomic constituent before exiting the atmosphere or being attenuated by a different constituent. If a slight amount of energy is lost or gained by the photon during the scattering process, the photon will be shifted slightly away from line-center and into the Doppler-broadened 'wings' of the line. In this case, the photon is much less likely to resonate with the related atmospheric constituent. Observations of resonant emissions in the thermosphere at high resolution often reveal a decrease in line center brightness.

The principal local source of light is due to photoelectrons stripped from O in the thermosphere by solar EUV emissions ( $<91.1$  nm). These electrons are energetic enough to stimulate the emission of FUV photons by thermospheric O and N<sub>2</sub> through collisional interactions. This is the main source of many dayglow emissions and can contribute to resonantly scattered emissions. Dayglow emissions at FUV wavelengths are stimulated primarily by photoelectrons, including the N<sub>2</sub> Lyman-Birge-Hopfield (LBH) bands between 126.0 nm and 152.0 nm and the OI forbidden transition at 135.6 nm. Dayglow emissions which have both a resonant and photoelectron stimulated component include NI lines between 113.4 nm and 124.3 nm and the bright OI 130.4 nm emission.

The solar spectrum is, to first order, that of a blackbody with a temperature of ~6000 K. However, there are many higher energy emissions in the solar spectrum, up to and including x-rays, which cannot be represented by a corresponding blackbody emission curve. The solar spectrum from FUV to Near-IR wavelengths is shown in Figure 1-6 using a logarithmic intensity versus wavelength format, with the overlain curves indicating pure blackbody spectra for several temperatures. The solar spectrum deviates significantly from a fixed temperature blackbody at short wavelengths. This is clearly demonstrated in Figure 1-7 [Meier, 1991] which shows logarithmic solar flux vs. wavelengths 0–4000 Å (0–400.0 nm). The monotonic decrease of blackbody radiation with wavelength is only evident at  $\lambda > 1300 \text{ \AA}$  (130.0 nm), modified by certain emission and absorption lines. Atomic emission lines dominate at shorter wavelengths, with intensities thousands of times greater than the respective blackbody. Note that in comparing these figures,  $1 \text{ nm} = 10 \text{ \AA}$ .

When viewed from space, the dayside of Earth also radiates in the same high-energy portion of the spectrum as the sun. The spectrum of these dayglow emissions is shown in Figure 1-8 for the near-ultraviolet (NUV) to extreme-ultraviolet (EUV) wavelengths. These data are a compilation of measurements from three space-borne satellites, each of which observed the dayglow in different wavelength regimes. The dayglow is clearly most intense in the NUV range, where the solar UV component is also most intense. This dayglow component originates in Rayleigh scattering processes occurring below the thermosphere. In the MUV range, absorption by  $\text{O}_3$  in the Huggins bands becomes significant and results in a strong decrease in the albedo. The brightness decreases again in the FUV range with absorption by  $\text{O}_2$ , first in the Schumann-Runge bands, and in the similarly named continuum at shorter wavelengths. The trend of decreasing dayglow brightness with wavelength is interrupted in the short wavelength end of the FUV range, where there are several prominent emissions. These are of both thermospheric and exospheric origin and are of most interest here.

The FUV dayglow in the 1200–1400 Å (120–140 nm) range is dominated by O,  $\text{N}_2$ , and H emissions. This particular range is shown with better resolution in Figure 1-9. The

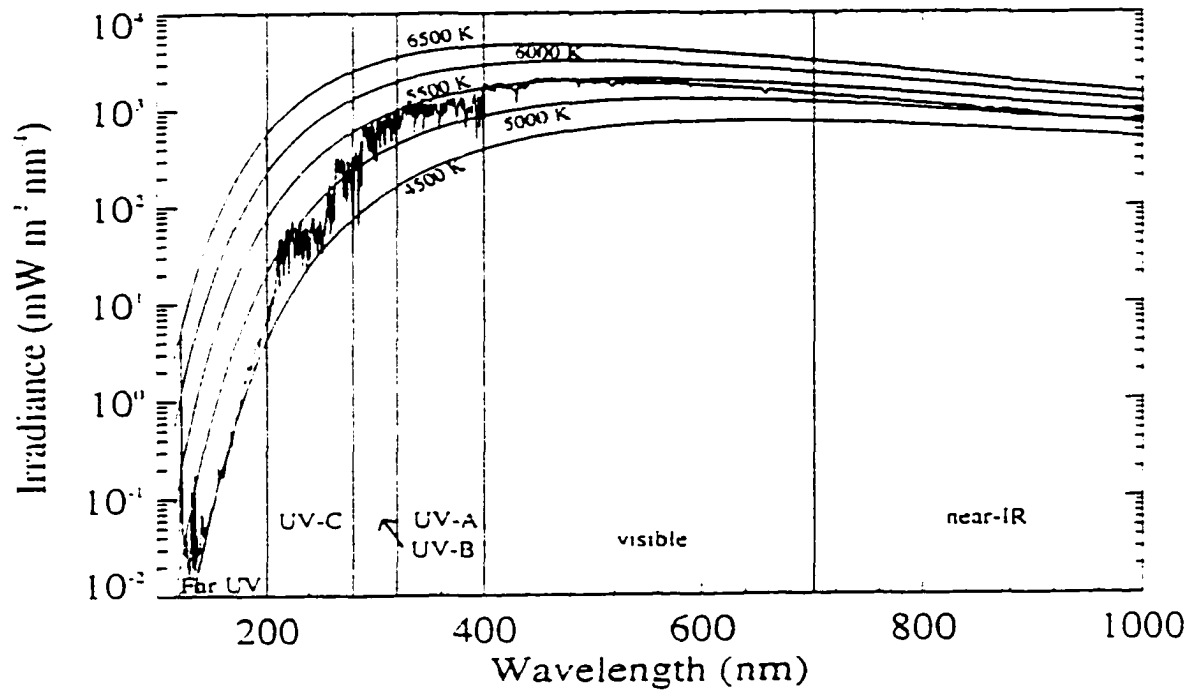


Figure 1-6. The solar spectrum. Solar irradiance as a function of wavelength is shown on a logarithmic scale. Five sample blackbody irradiance curves are overlain for comparison. [Stamnes and Thomas, 1998].

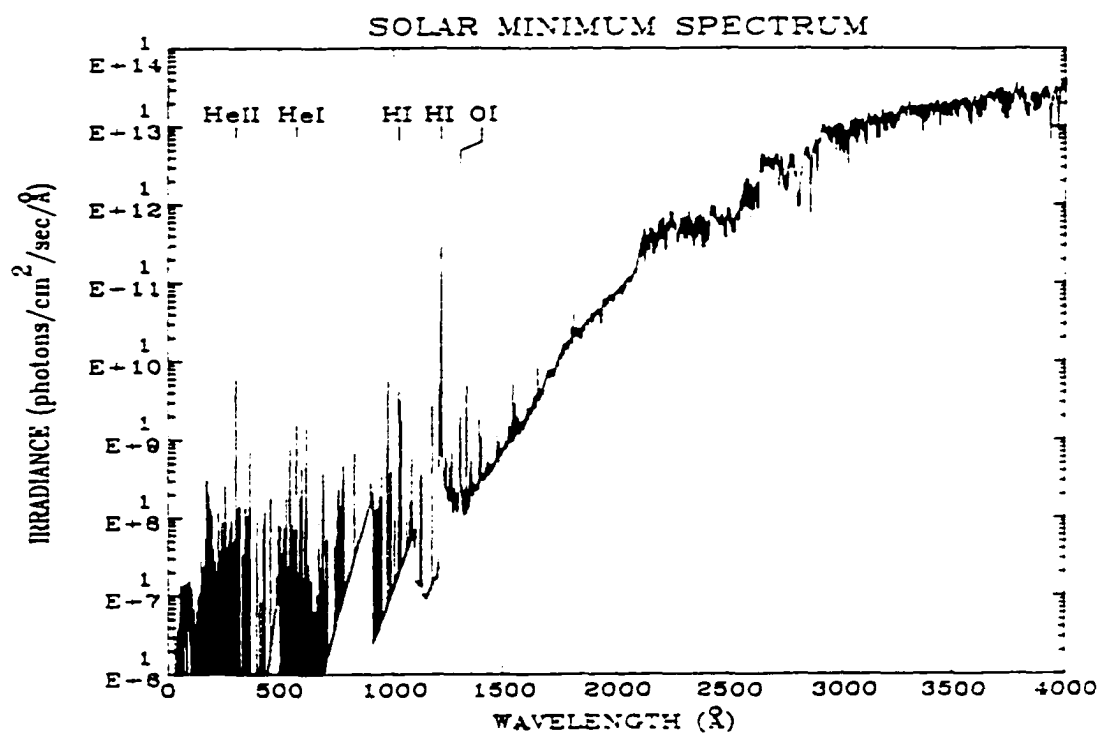


Figure 1-7. Solar irradiance from X-ray to NUV wavelengths. Strong line emissions at wavelengths shorter than  $\sim 1300 \text{ \AA}$  ( $130.0 \text{ nm}$ ) are indicated, including those due to OI and HI at  $1304 \text{ \AA}$  ( $130.4 \text{ nm}$ ) and  $1214 \text{ \AA}$  ( $121.4 \text{ nm}$ ), respectively. The plot is for solar minimum conditions. [Figure from Meier, 1991].

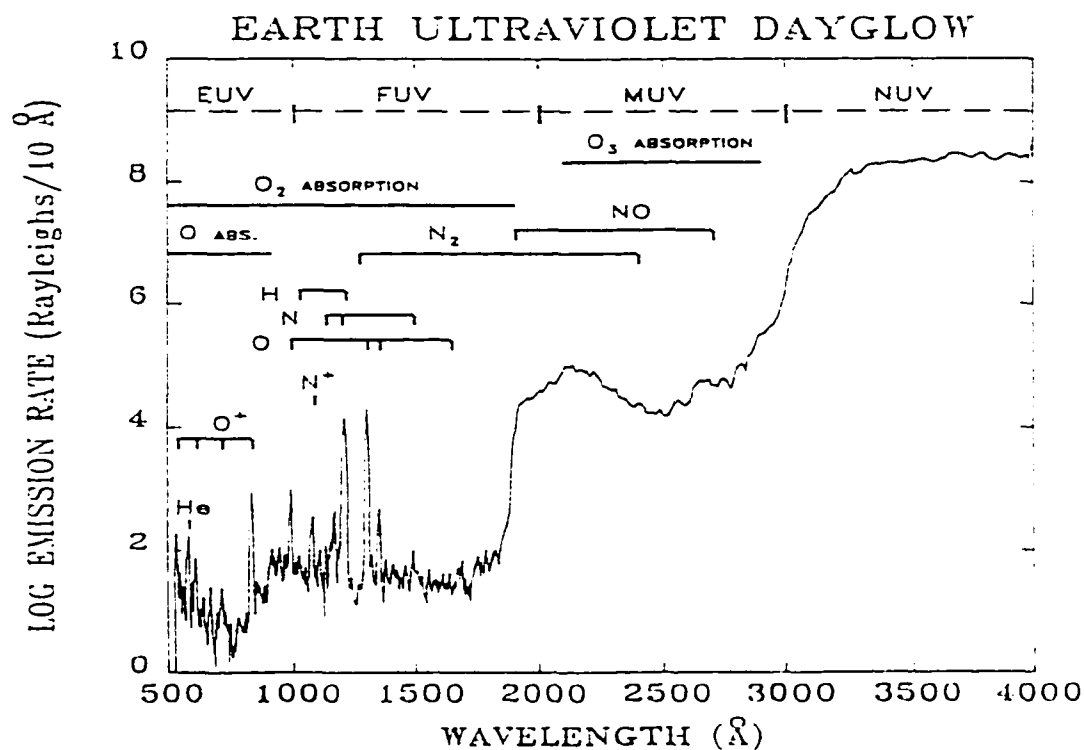


Figure 1-8. Earth's ultraviolet dayglow. A representative spectrum of Earth's UV dayglow is characterized by log emission rate in the 500–4200 Å (50.0–420.0 nm) wavelength range. This plot summarizes three data sets from nadir viewing measurements by Barth [1965] in the MUV, Huffman *et al.* [1980] in the FUV, and Gentieu *et al.* [1979] in the EUV. Ranges in which absorption by O, O<sub>2</sub>, and O<sub>3</sub> occur are indicated as well as prominent emission bands and lines of thermospheric constituents. [Figure from Meier, 1991].

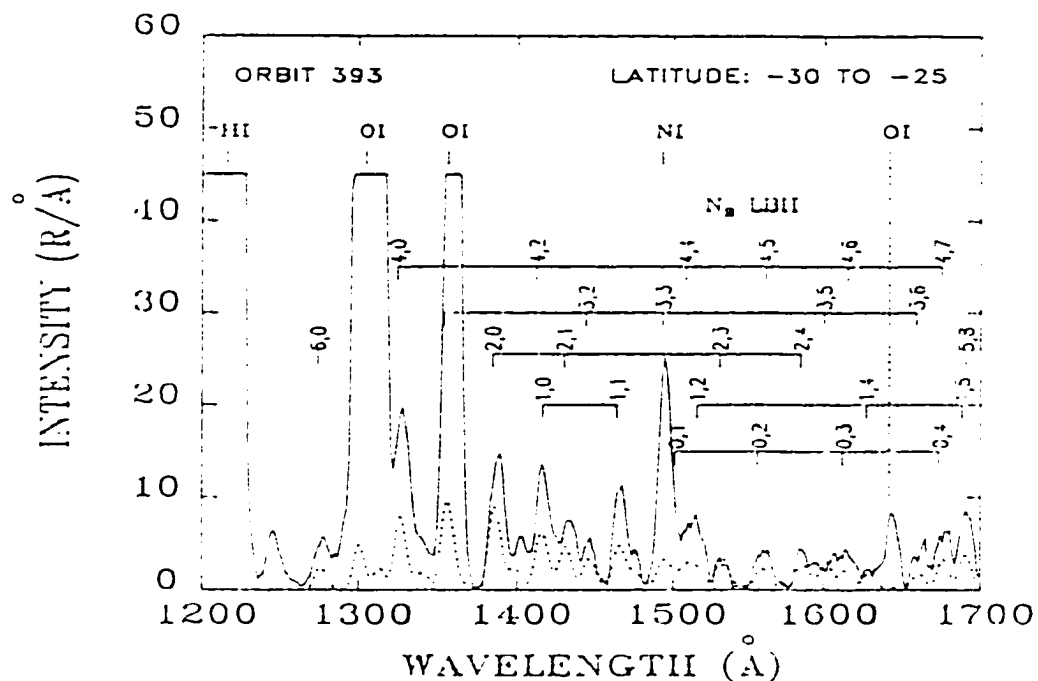


Figure 1-9. Earth's FUV dayglow. Earth's dayglow measured from a nadir pointing platform at 205 km with a spectral resolution of  $7 \text{ \AA}$  ( $0.7 \text{ nm}$ ). Prominent neutral oxygen (OI) emission lines at  $1304 \text{ \AA}$  ( $130.4 \text{ nm}$ ),  $1356 \text{ \AA}$  ( $135.6 \text{ nm}$ ) and  $1641 \text{ \AA}$  ( $164.1 \text{ nm}$ ) are identified. The prominent line at  $1214 \text{ \AA}$  ( $121.4 \text{ nm}$ ) is identified as an emission by neutral hydrogen (HI). The Lyman-Birge-Hopfield (LBH) vibrational band of  $\text{N}_2$  is identified as are many discrete lines within the band. [Figure from Meier, 1991].

H $\alpha$  emission at 1214 Å (121.4 nm) is due to resonant scattering of the solar line by thermospheric and exospheric neutral hydrogen, with a less significant photoelectron stimulated component also present. As mentioned earlier, the emission at 1304 Å (130.4 nm) has both a resonantly scattered (spin-allowed) and a photoelectron induced component while the 1356 Å (135.6 nm) line is a spin-forbidden transition in O that is not resonantly scattered; it is due entirely to photoelectron excitation. The 130.4 nm OI emission is actually a triplet, with fine-structure emissions lines at 130.2 nm, 130.4 nm and 130.6 nm. The 135.6 nm emission also exhibits fine structure as a doublet with lines at 135.8 nm and 135.5 nm [Meier, 1991].

The ratio of the intensity of Earth's UV emission spectrum to that of the solar input at Earth is termed the albedo and is plotted in Figure 1-10 for the same wavelength range as in Figure 1-8. From this one should note that at several discrete wavelengths in the FUV range the terrestrial FUV output exceeds the solar input. This indicates emissions that are due not only to scattering of solar radiation but have a particularly strong photoelectron component which is produced locally, in the thermosphere.

#### 1.4 Thermospheric Models

The necessity of describing thermospheric conditions without real-time global-scale observations has driven intensive modeling efforts. This complicated problem has been approached in many ways. A short overview of these various methods is included here.

Satellite and rocket experiments performed since the 1950s have measured density, temperature, degree of ionization, and relative abundance of thermospheric constituents. The large amount of data collected has been fitted as a function of several solar and geophysical parameters to yield the Mass-Spectrometer-Incoherent Scatter (MSIS) neutral atmosphere model [Hedin, 1983, 1987]. Also included in the fitted database are temperature and density measurements obtained by ground-based incoherent scatter radars. Given a time, position on Earth, Ap index (or 3 hour indices), and solar 10.7-cm radio emission values, this empirical model returns average densities and relative abundances of the neutral atmospheric constituents O, O<sub>2</sub>, N<sub>2</sub>, N, Ar, H and He, as well as

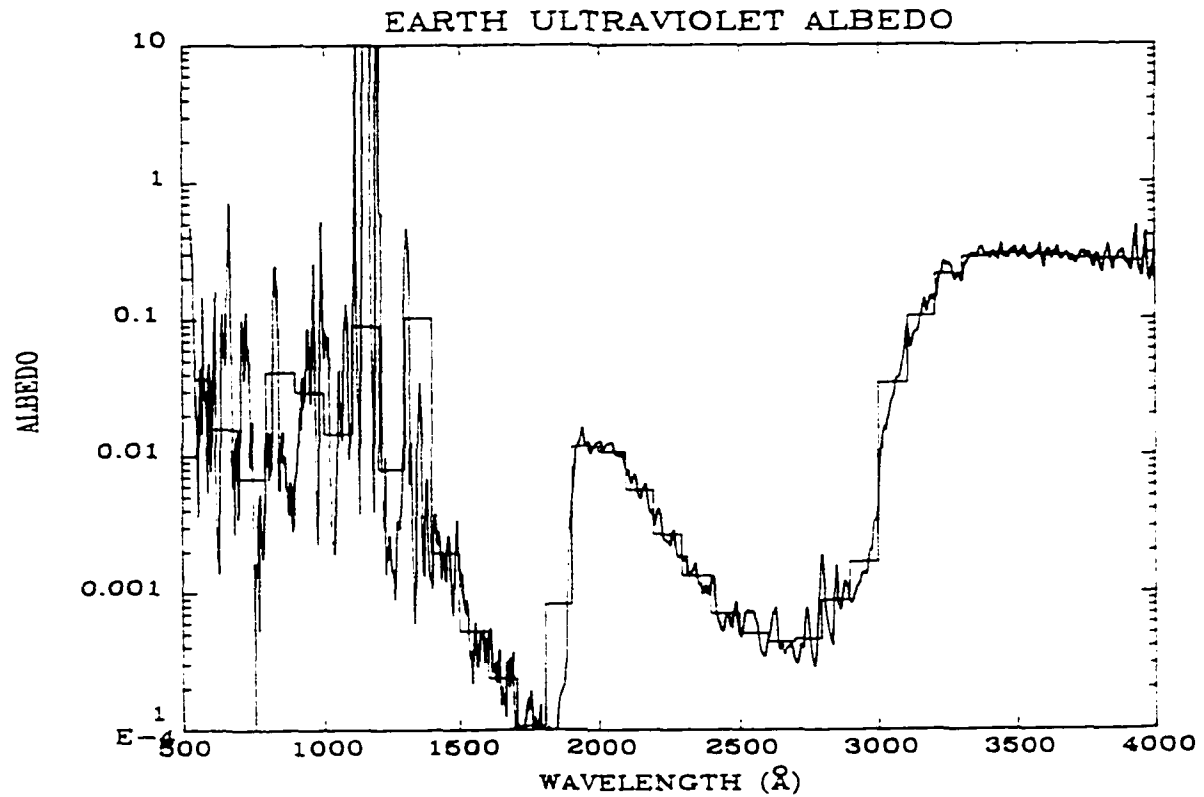


Figure 1-10. Earth's UV albedo. The ratio of the intensity of radiation emitted by Earth vs. solar radiation received by Earth is shown on a log scale. The two large minima at  $\sim 1700 \text{ \AA}$  (170.0 nm) and  $\sim 2700 \text{ \AA}$  (270.0 nm) are the result of strong absorption by  $\text{O}_2$  and  $\text{O}_3$ , respectively. Large excursions above unity in the FUV range suggest local production of emissions at the corresponding wavelengths. [Figure from Meier, 1991].

the neutral temperature, at altitudes from ~100 to 1000 km. The parameter  $A_p$  provides a measure of geomagnetic activity and the solar radio flux at 10.7 cm ( $F_{10.7}$ ) correlates fairly well with the solar EUV and FUV flux [Barth *et al.*, 1990; Hedin, 1984]. This interesting correlation between short- and long-wavelength solar radiation is discussed by Lean [1987] and references described therein.

MSIS is useful in representing atmospheric parameters during periods of low geomagnetic activity or sustained increased levels of activity. Since the model results are based on the weighted average of observations, impulsive storm onsets and associated rapid changes in thermospheric parameters cannot be modeled with accuracy. Also, for given  $F_{10.7}$ ,  $A_p$ , day of year and position on Earth, thermospheric parameters can vary widely depending on the current dynamical state and electric field configuration of the upper atmosphere. Even so, the MSIS model provides excellent reference values for thermospheric composition and temperatures to which experimental values and the results of dynamical models are often compared.

The basic limitation of MSIS is that it is not a time dependent model, but presents only average values of thermospheric constituents for given geophysical parameters. It is not capable of simulating the development of a thermospheric disturbance due to an impulsive heating event. A time dependent model which self-consistently includes winds, polar cap electric fields, and variable heating rates should produce a more realistic 'picture' of thermospheric quantities during particular storm events, as opposed to an empirical model such as MSIS which is better suited to representing long term trends and quiet-time thermospheric composition.

The development of time-dependent models of the upper-atmosphere was begun in the 1960s with the first scientific computers and largely came of age in the 1980s. The work by Dickinson *et al.* [1981] describes a finite-differencing numerical scheme treating the dynamics of the thermosphere. In this effort the focus is to simulate thermospheric dynamics. Composition and temperature of the neutral atmosphere are provided by MSIS while ion and electron densities are provided by another empirical model [Chiu, 1975]. Other necessary numerical inputs include solar flux values, high-latitude heat sources and

collisional cross-sections to describe ion-drag effects on the neutral atmosphere. This model has been refined greatly and is referred to as NCAR-TGCM (National Center for Atmospheric Research - Thermosphere General Circulation Model). It has been greatly improved [Roble *et al.*, 1988] to calculate densities for major and minor ion species as well as major neutral species throughout the thermosphere. The inclusion of ion chemistry codes and effects of auroral particle precipitation [Roble and Ridley, 1987] complete a Thermosphere/Ionosphere General Circulation Model (NCAR-TIGCM). Another successful model is that developed at the University College in London [Fuller-Rowell and D. Rees, 1980; Fuller-Rowell *et al.*, 1987]. Today, sophisticated models self-consistently calculate thermospheric and ionospheric properties while accounting for the polarization electric fields which can be generated in the upper-atmosphere, generating additional ion and electron drift motion. This electrodynamic NCAR model is entitled TIEGCM.

For simulation of actual geomagnetic events or storm time periods, the electrodynamic state of the upper atmosphere is included via sophisticated algorithms which invert ground magnetometer and incoherent-scatter radar data to resolve current systems that drive large-scale motions in the atmosphere. The complex technique is described by Richmond and Kamide [1988] and its utilization is described by Richmond *et al.* [1988]. This technique is commonly referred to as the AMIE (Assimilative Mapping of Ionospheric Electrodynamics) technique. The results can be incorporated into the TIGCM, replacing modeled convection electric field inputs with real-time data. Data from geomagnetic events have been compared to simulations of those events in several papers that make use of this method [Buonsanto *et al.*, 1997, Crowley *et al.*, 1989, Roble *et al.*, 1988].

## 1.5 Exploring the Thermosphere

### 1.5.1 Direct Measurements of Thermospheric Properties

Satellite mass-spectrometer measurements of thermospheric constituents have proved valuable in describing magnetic storm induced effects on thermospheric weather. Satellite

data has also helped identify seasonal, IMF and UT-dependent effects. The effect of Joule heating on the thermosphere during geomagnetic storms can be summarized in a plot of density measurements from a single pass of the ESRO-4 satellite. In this pass, the satellite passed over the North American morning sector at approximately 1700 UT during the strong magnetic storm of October 29, 1973 [Prölss, 1980]. The planetary K index for that day is shown in Figure 1-11a. The changes in densities of Ar, N<sub>2</sub>, O and He are shown in Figure 1-11b, as well as the ratio of N<sub>2</sub> to O and the change in the total mass density. Changes are determined by making comparisons to observations in a quiet-time reference orbit. The range of satellite altitudes corresponding to the magnetic latitudes at which measurements were made is indicated above the plotted parameters. These altitudes change very little from one orbit to the next. Note that the densities of Ar and N<sub>2</sub> (heavier constituents) are strongly enhanced at high geomagnetic latitudes, while He densities are depressed. O densities show variability and generally are slightly decreased. The change in O/N<sub>2</sub> ratio is a good indicator of the degree of thermospheric disturbance (as well as negative ionospheric disturbances) and is also used by modelers to trace disturbances generated in their simulations.

The development of a thermospheric disturbance can be observed through successive orbits of the same satellite. The relative change in the ratio of O/N<sub>2</sub> from a reference orbit is again shown in Figure 1-12 but now in the Southern Hemisphere and for successive orbits numbered 1-7 and 9. The top frame of Figure 1-12 shows hourly average values of the AE index, where values of ~1 μT indicate very strong auroral currents and associated Joule heating. Neither the local time (~1100 LT) nor the geographic latitude of observations changes, however the invariant magnetic latitude at with fixed geographic latitudes does change with local time (as Earth's dipole is offset from the rotation axis). The 40° and 60°S magnetic latitude increments for each orbit are indicated using vertical bars. The geographic latitude scale is fixed and ranges from 75°S to 0°S. ESRO 4 is passing closer to the southern polar cap with each orbit.

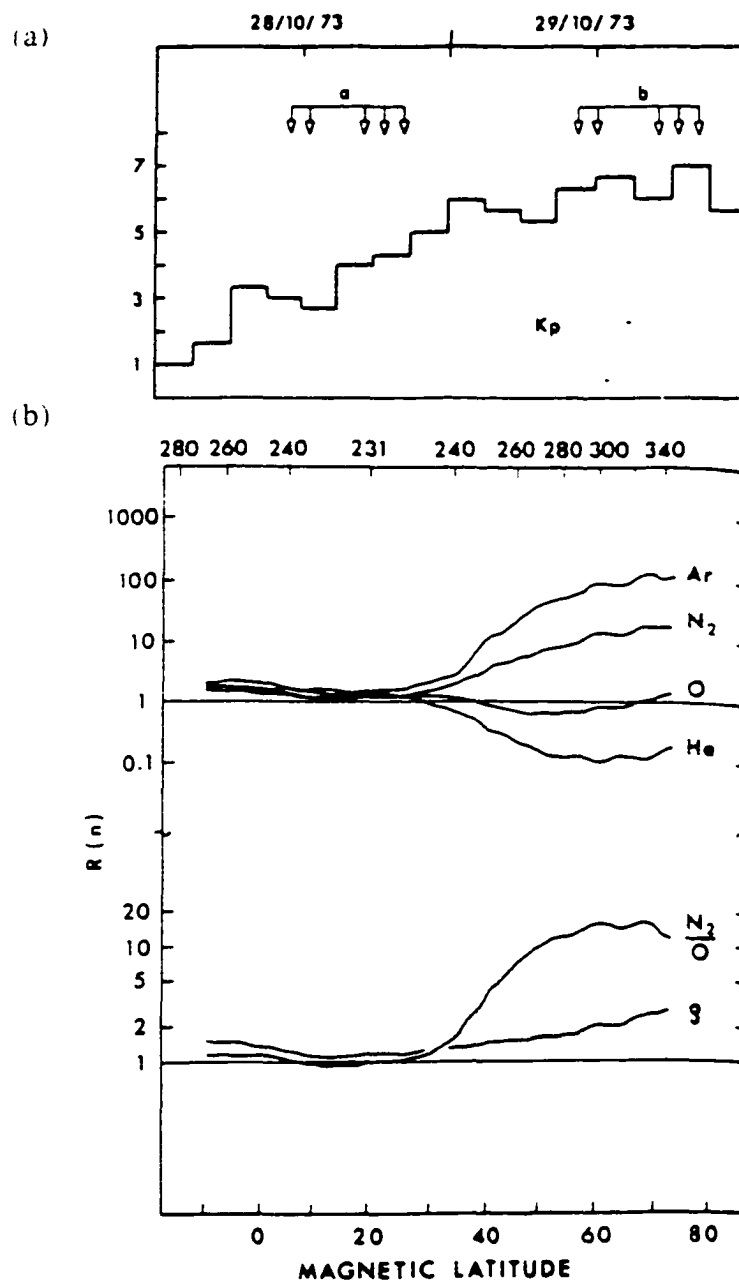


Figure 1-11. Effects of geomagnetic activity on thermospheric composition. (a) Time history of geomagnetic activity for October 28–29, 1973 as indicated by Kp. (b) Composition perturbations measured during a single orbit of ESRO 4 at ~1700 UT on October 29, 1973. In the upper plot, the relative change in mass density of four upper atmospheric neutral constituents is shown as a function of magnetic latitude. This ratio is calculated by comparing measurements from this disturbed period to those from quiet times. In the lower plot, the relative change in the  $N_2/O$  ratio is shown as well as the change in the total mass density,  $\rho$ . The altitude at which these measurements were made is shown on the upper ordinate and the magnetic latitude is shown on the lower ordinate. [Figures from Prolss, 1980].

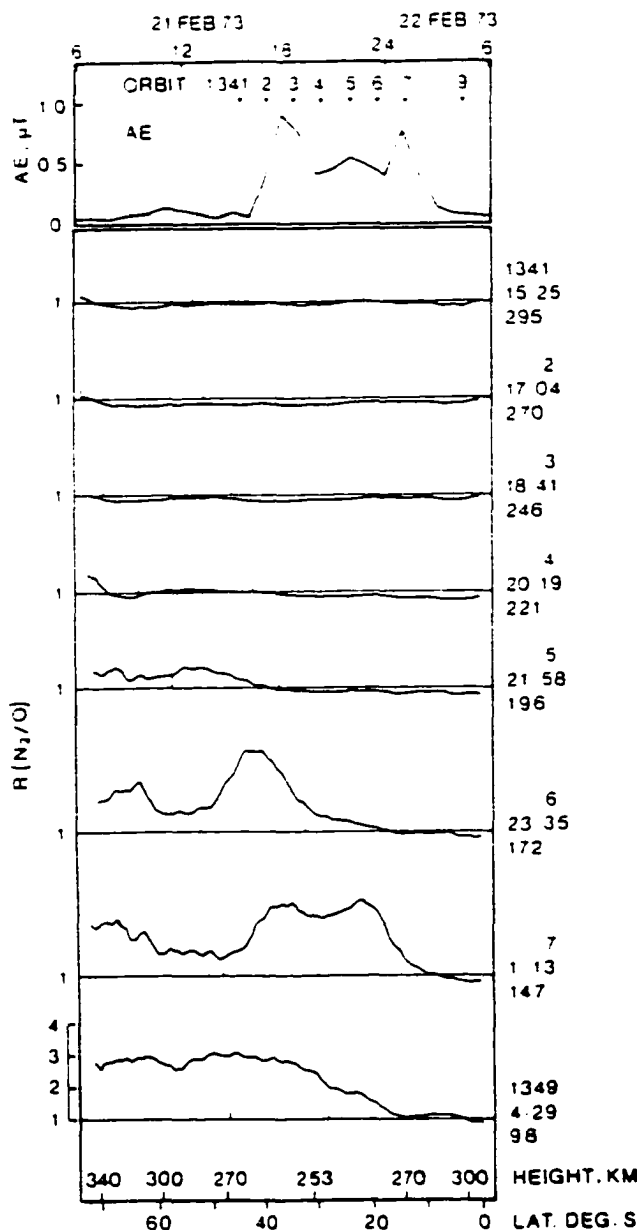


Figure 1-12. Development of composition disturbance zone. The development of a composition disturbance is observed in data from eight orbits of ESRO 4. Where the first orbit shown is labeled 1, subsequent orbits 2-7 and 9 are plotted here. The upper panel indicates the hourly AE indices for this period and the equator-crossing times for each orbit during which the composition data were obtained. Eight subsequent panels indicate changes in the  $N_2/O$  ratio relative a sample quiet time orbit for orbits 1-7 and 9 obtained at times and geographic longitudes indicated to the right. [Figure from Prolss, 1980].

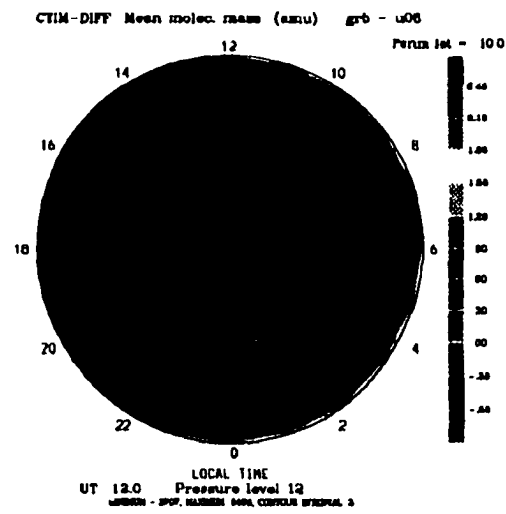
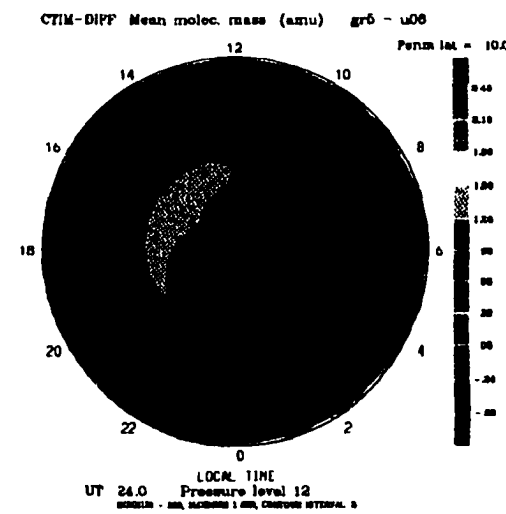
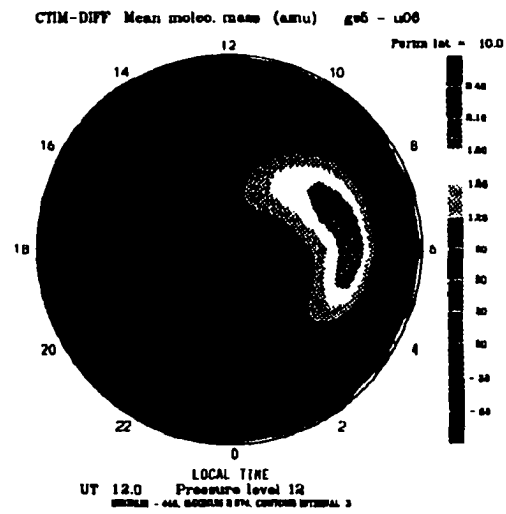
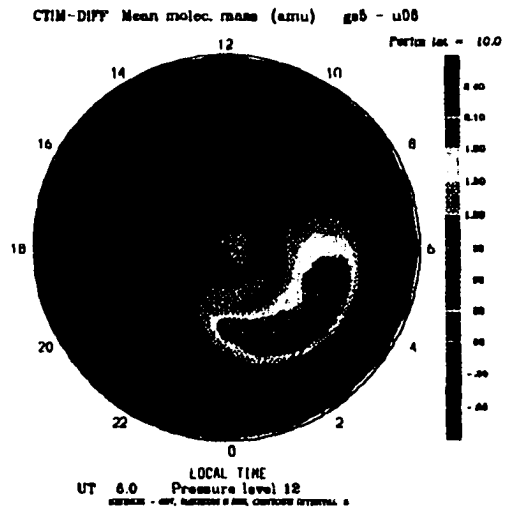
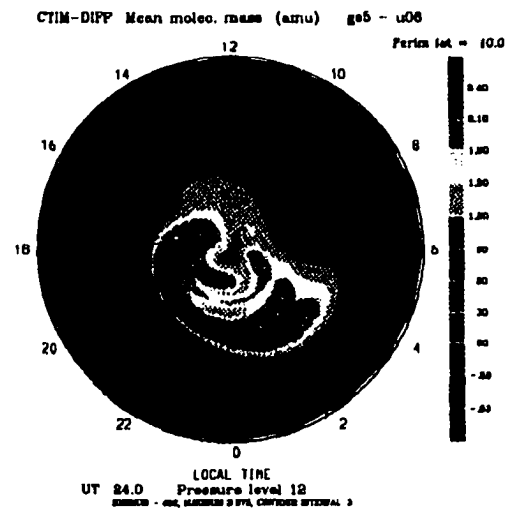
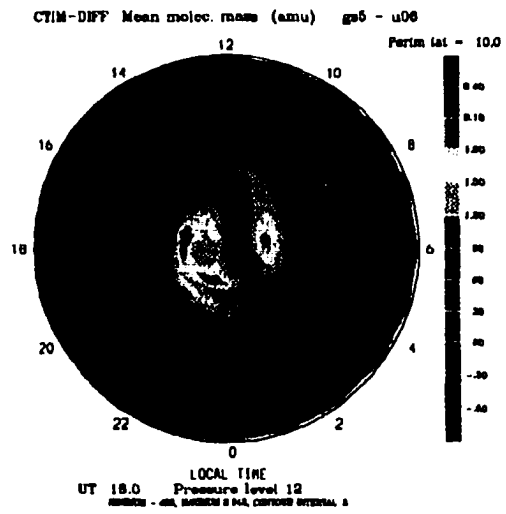
Intense geomagnetic activity begins around 1600 UT. The first observation of the effect of this activity on the thermosphere is observed around 2000 UT at the highest latitude. With the next three orbits the disturbance in the  $O/N_2$  ratio from quiet-time levels apparently propagates from high to low latitudes with the greatest changes appearing in the seventh orbit. By the ninth orbit the level of magnetic activity has decreased considerably, but the disturbance is still large in magnitude at high and middle latitudes and extends equatorward of  $20^\circ\text{S}$ .

These data are limited in that the mechanism by which the disturbance propagates from the polar region to mid-latitudes is not obvious, nor is that which impedes or cancels the disturbance at equatorial latitudes. Simple interpretation of the satellite data as the propagation of a pressure disturbance from the heating region (auroral oval) to low-latitudes ignores global neutral winds and possible co-rotational effects. Furthermore, even as this disturbance seems large in magnitude and extent,  $O/N_2$  ratios at equatorial latitudes are nearly unaffected. This is somewhat misleading as the densities of nearly all constituents of the low-latitude thermosphere rise during geomagnetic storms [Mayr and Volland, 1973], and here in such a manner as to not change the  $O/N_2$  ratio.

These types of satellite data have been very useful in determining the global morphology of thermospheric disturbances as well as seasonal and daily trends [Prölss 1980, 1981; Prölss *et al.*, 1988]. Density and composition measurements taken by orbiting platforms provided data upon which the basic theory and understanding of the thermosphere were developed. Global observations are now necessary to fully separate the spatial and temporal variations in thermospheric composition during storm-times.

The development of a composition disturbance zone, its extension to mid-latitudes, and subsequent dissipation can be seen in results from the UCL-TGCM shown in Figure 1-13a through 1-13f (from Fuller-Rowell *et al.*, 1994) for  $50^\circ$ – $90^\circ\text{N}$  latitude. The six panels show the development of changes in the mean molecular mass at a given pressure level (which is in effect a normalization which allows for meaningful global comparisons). Each panel represent a step in a time series of atmospheric conditions 6.

Figure 1-13. Results from UCL-TGCM showing global-scale composition variations. The mean molecular mass at a fixed pressure level is shown at six time intervals after the onset of modeled geomagnetic activity. Panels a–f indicate conditions north of 50°N latitude at 6, 12, 18, 24, 36, and 48 hours after onset. Mean molecular mass is given in atomic mass units and is indicated by a range of colors, with an appropriate color bar next to each panel. [Figure from Fuller-Rowell *et al.*, 1994].



12, 18, 24, 36 and 48 hours after the onset of 12 hours of sustained activity beginning at 1200 UT. The noon sector is at the top of each panel.

Within six hours of onset, large perturbations in the mean molecular mass are found at high latitudes. Twelve hours after the onset, strong perturbations are seen throughout the nightside. Strong activity ceases at this time and the remaining four panels describe the recovery of the thermosphere. The disturbance zone is found mainly at mid-latitudes and at later morning sectors at 18 and 24 hours, whereas the polar region has begun to equilibrate. This changes by 36 hours from the beginning of activity, as the global neutral winds advect the weakened disturbance through the polar region again. Finally, 48 hours after the onset of activity, the disturbance zone is again in the morning sector.

It is just these types of temporal and spatial variations from sophisticated modeling efforts that call for validation by global measurements. In-situ observations of neutral winds [Roble *et al.*, 1988] and composition [Burns *et al.* 1992] have been compared to TGCM runs to validate model results. However, global observations of storm effects would provide a much broader test of thermospheric models.

### 1.5.2 Global FUV Measurements of Thermospheric Properties

Performing simultaneous global in-situ thermospheric observations at even a low spatial resolution would require continuous reinsertion of detectors into orbits which are subject to rapid decay, especially during periods of high solar activity and thermospheric heating. Optical observations from a single high-altitude platform may reveal global variations in thermospheric constituents, and observations of the FUV emissions of O and N<sub>2</sub> should be particularly useful in determining the total oxygen content and the ratio of O to N<sub>2</sub> at emission altitudes.

Variations in the intensity of particular dayglow emissions have been linked to auroral activity since early observations were made from low-altitude sensors. Meier [1970] noted that passes of the polar orbiting OGO-4 satellite over the poles revealed decreased OI 130.4 nm and H $\alpha$  121.4 nm emissions in the polar cap (bounded by the auroral oval). Later, Strickland and Thomas [1976] examined data from OGO 6 and determined that the

strongest decreases in OI emissions occurred at high latitudes during periods of strong geomagnetic activity. These nadir pointing satellites were the first instruments to make FUV measurements from space. Later missions (*e.g.* S3-4 [Huffman *et al.*, 1980; Conway *et al.*, 1988] and STP 78-1 [Bowyer *et al.*, 1981; Parish *et al.*, 1994]) have yielded further understanding of the relationship between the FUV dayglow and local atmospheric composition. These missions have provided critical scientific data, the analysis of which has provided a foundation for interpretation of global FUV observations [*e.g.* Meier and Lee, 1982; Meier and Anderson, 1983; Conway *et al.*, 1988; Meier, 1994]. Sub-orbital rocket missions have also made important observations of Earth's FUV dayglow [*e.g.* Fastie *et al.*, 1964; Rottman *et al.*, 1973; Strickland *et al.*, 1996]. Aside from these references, rocket missions will not be discussed further in this work.

Early results from DE 1, using the 123–165 nm bandpass filter, revealed decreases in OI 130.4 nm dayglow brightness after strong geomagnetic activity similar to those observed in earlier missions, but on a global scale [Craven and Frank, 1984; Frank and Craven, 1988]. A quantitative comparison of the disturbed dayglow to that observed during quiet times was first performed by Craven *et al.* [1994] with a wide range of images examined by Nicholas *et al.* [1997]. These comparisons required the development of a model representing the DE-1 FUV imager's response to the quiet-time dayglow for a wide range of observational and solar zenith angles. A similar effort, using different modeling methods, is described by Meier *et al.* [1995]. The geometric model devised by Craven *et al.* has undergone a series of improvements which are described herein. These improvements allow for investigation of thermospheric composition in many images of the sunlit earth, taken in the effective lifetime of this FUV filter (September, 1981 to ~1986). With this model as the primary tool, a series of investigations into the wide range of effects of geomagnetic activity on the thermosphere have been undertaken. Those studies are described herein.

In 1981, Dynamics Explorers 1 and 2 (DE 1 and 2) were launched with the mission of making simultaneous low- and high-altitude measurements in Earth's magnetosphere-ionosphere-thermosphere system. DE 1 was placed in a highly eccentric elliptical polar

orbit to obtain magnetospheric measurements and provide a high apogee-altitude platform for global FUV images [Hoffman *et al.*, 1981; Frank *et al.* 1981]. DE 2 was placed in a nearly circular polar orbit with both apogee and perigee within the thermosphere. Its mission included measurements of density, composition, electric fields, and neutral winds. The satellites orbits were co-planar, such that DE 2 repeatedly passed directly below DE 1. Thus, the satellites were often positioned to make direct comparisons between remote FUV and *in-situ* composition measurements.

Weather satellites now monitor all parts of the world to infer conditions at the ground and their possible impact upon human activities. The measurement and analysis techniques described here have the capability of providing users a real-time measure of upper-atmospheric conditions. Furthermore, the studies we undertake may provide a better basis for predicting the state of the upper atmosphere many hours in advance. Such information can make human operations in space more reliable.

## Chapter 2

### Instrumentation

#### 2.1 The Dynamics Explorer Mission

The Dynamics Explorer 1 satellite was equipped with three spin-scan imaging photometers, two of which were configured to sample light in the visible range (imagers A and B), while the third (imager C) made measurements at far ultraviolet (FUV) wavelengths. Data presented in this thesis were obtained primarily from the FUV instrument. Narrowband and broadband filters ( $\Delta\lambda \sim 2$  and 20 nm for visible and ultraviolet filters, respectively) were used to isolate particular atomic emission lines and molecular bands from the full auroral and dayglow spectra.

The Dynamics Explorer flight mission began with launch on August 3, 1981, from Vandenberg Air Force Base, California, on a Delta 3913 launch vehicle into a 90° inclination (polar) orbit. The hardware mission consisted of two satellites, DE 1 and 2, for remote and in-situ observations of the upper atmosphere and magnetosphere. Once separated, DE 2 remained in a low altitude orbit (nominal apogee and perigee of 1300 and 305 km, respectively), while DE 1 was placed in a highly elliptical polar orbit using a solid rocket upper stage. An apogee altitude of  $\sim 3.65 R_E$  and a perigee altitude of  $\sim 570$  km were achieved, with an orbital period of 6.85 hours.

The main components of each imaging photometer are shown in the simplified view of Figure 2-1 [Frank *et. al.*, 1981]. A collimator with a series of knife-edge low-reflectivity baffles limits and minimizes internal reflection of extraneous light. A stepping mirror is the optical component that allows the imager to scan a range of angles out of the spin plane of the satellite (described later in Figure 2-2). Its 0.125° incremental movement shifts the photometer field of view by 0.25°. The next optical element is a parabolic mirror ( $f=19.9$  cm), focusing incoming light onto a small pinhole ( $d=1.13$  mm), behind which is situated a small lens that directs the light into a parallel beam through a filter and onto the photocathode of a photomultiplier tube. Brightness of the

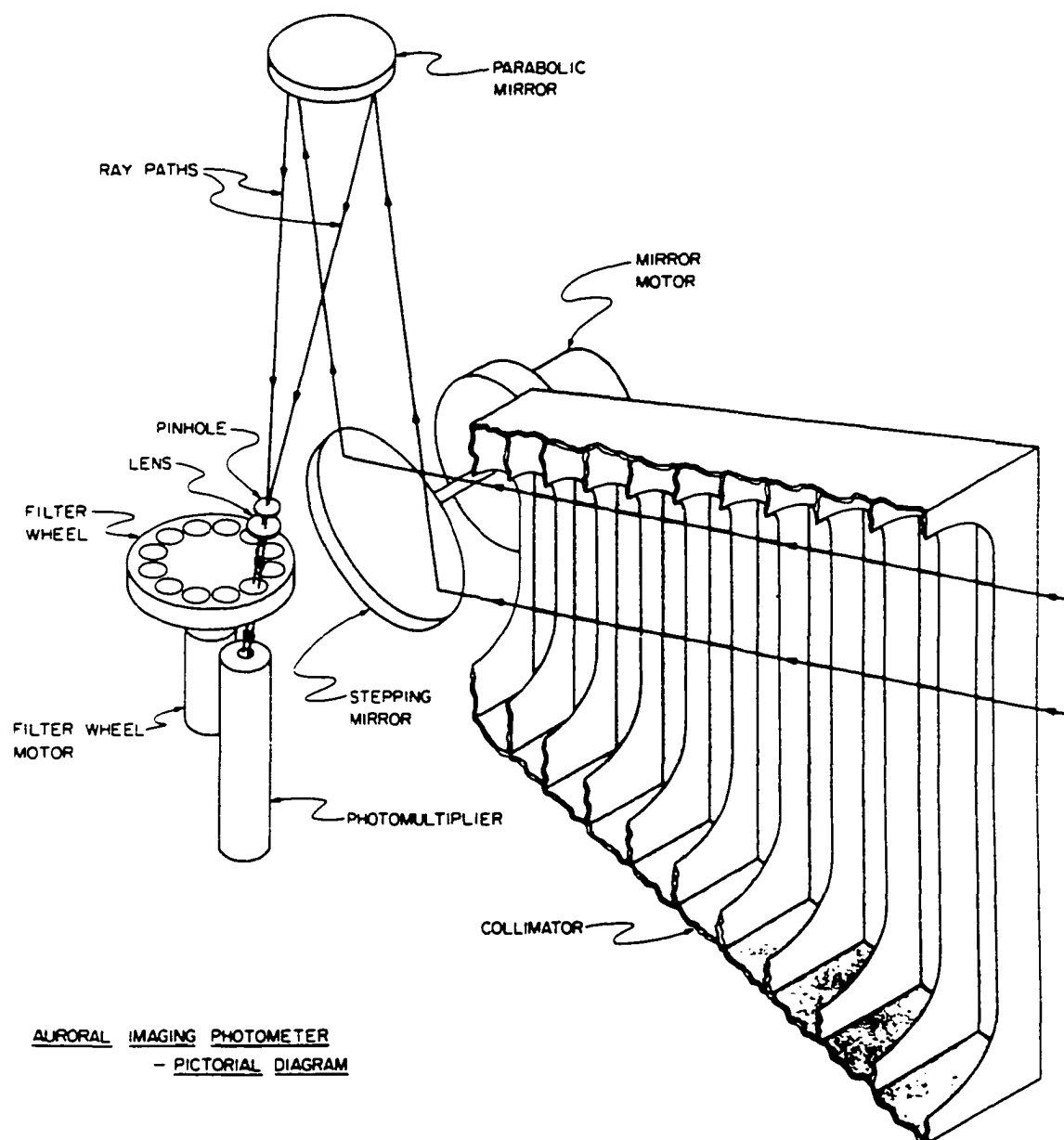


Figure 2-1. Representation of DE-1 spin-scan auroral imager (SAI) optics. Components such as the collimator, stepping and parabolic mirrors, lens, filter wheel and photometer are indicated. [Figure from Frank *et al.*, 1981].

object field is proportional to detector response, measured in counts per unit time, where a count is the result of a single event cascade within the multiplier.

The three imaging photometers were calibrated before launch in the laboratory such that the brightness of a subject could be measured in Rayleighs ( $10^6$  photons /  $\text{cm}^2\text{-sec-ster}$ ) for each of the 12 filters that were mounted in each filter wheel. For example, the pre-launch calibration of the FUV instrument using filter #2 showed the peak sensitivity of the photometer ( $S_p$ ) to be 3.08 (counts/kR·pixel) at 130 nm, where pixel implies an integration time of 3.4 msec. It has been shown that the FUV instrument [Rairden, 1986] suffered some degradation after laboratory calibration, resulting in an overall reduction in instrument sensitivity from pre-launch values. In particular,  $S_p$  of the FUV instrument with filter #2 in place was found to be ~30% lower soon after operations began in orbit than when measured in the lab. Nevertheless, as this value of  $S_p$  changed throughout the mission (*e.g.*, reduced another 50% by January, 1983), and for the sake of continuity, the pre-launch value of 3.08 counts/(kR·pixel) will be used to report dayglow brightness.

The DE-1 satellite was a spin-stabilized platform rotating at 10 revolutions per minute with the axis of rotation normal to the orbit plane. The three imagers were directed in the plane perpendicular to the rotation axis. This allowed the field of view of each imager to pass over Earth's disk once each six seconds. During the rotation of the satellite, the response of each photometer is registered in 3.9-ms intervals, where 3.4 ms of the interval is integration period,  $t_i$ , and the remaining 0.5 ms is off time,  $t_o$ . In the integration time, the imager's  $0.32^\circ$  instantaneous field of view moves by  $0.20^\circ$  (and by  $0.23^\circ$  in  $t_i+t_o$ ). The imaged area that is within the moving field of view for  $\geq 0.5 t_i$  constitutes a roughly circular area of  $0.29^\circ$ . Considering the difference between the motion of the field of view with satellite rotation and its perpendicular incremental motion between adjacent scan lines, an image aspect ratio of  $23/25=0.92$  is obtained. All images shown in this work are resized to account for this factor and to present a circular Earth.

The three imagers were mounted aboard DE 1 approximately  $\sim 120^\circ$  with their exact placement shown in the spin-plane cross-section of the spacecraft in Figure 2-2. The stepping mirrors allowed the photometers to sample  $\pm 15$  degrees out of the plane. This range of angles could be covered in 120 steps of the stepping mirror, or 120 6-second satellite rotation periods. The resulting time to obtain a full image is 12 minutes.

Twelve filters were mounted on the rotating filter wheel in each imager, as shown in Figure 2-1. The sensitivity vs. wavelength profiles for several filters in the FUV imager are shown in Figure 2-3. Prominent dayglow emission lines such as the HI 121.4 nm (Lyman  $\alpha$ ) and OI 130.4 and 135.6 nm emissions are indicated as well as the Lyman-Birge-Hopfield (LBH) emission band for  $N_2$ . Data obtained using filter #2, with a short wavelength half-intensity cutoff at 123 nm and peak sensitivity at  $\sim 130$  nm (as mentioned earlier), are used extensively in this thesis. This filter is most sensitive to the oxygen emissions of the dayglow, with OI emissions constituting  $\sim 90\%$  of the instrument response for Earth observations away from the limb. At Earth's limb, the contribution by  $N_2$  LBH emissions increases considerably, as the thermosphere is optically thin to these emissions.

Approximately 20 12-minute images of the full disk of Earth could be obtained by each imager during a single orbit, though the instruments obtained images throughout the entire orbit. The latitude of apogee changed throughout the mission (as shown in Figure 2-4) due to apsidal motion of the satellite orbit. The rate of motion was approximately  $\sim 0.3^\circ$  per day in the direction opposite to the motion of the satellite. This added provided for imaging at high northern latitude in fall 1981, at midlatitudes and equatorial regions by summer 1982, and at high southern latitudes by Spring of 1983.

The imaging instruments were not designed to withstand direct solar illumination. Thus twice per year, when the sun crossed the orbit plane of the satellite, the imagers were not operated. Exceptions to this procedure were made during special eclipse periods later in the mission, when Earth blocked the solar emissions.

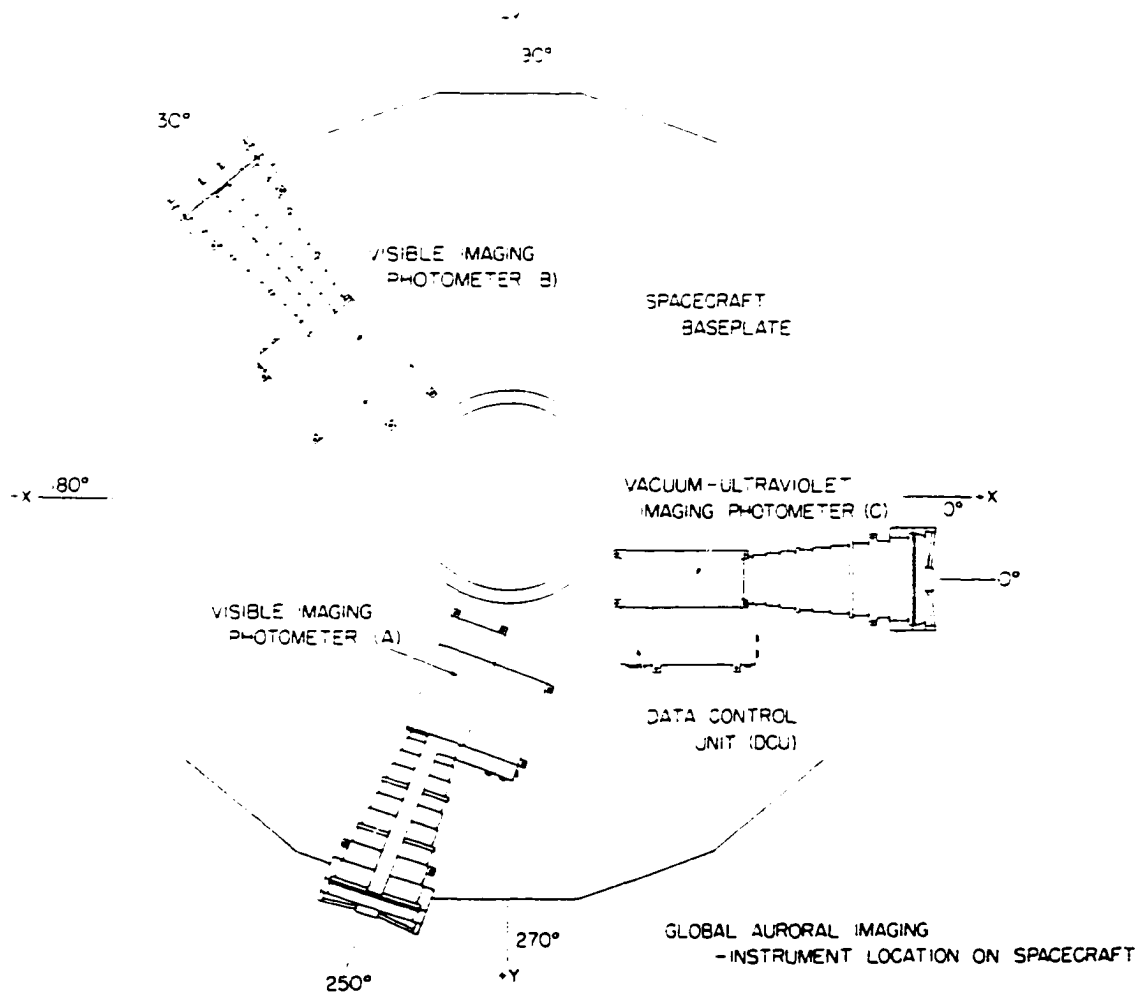


Figure 2-2. Cross-section of DE 1. Placement of visible and FUV wavelength imagers is shown to scale in a spin-plane cross-section of the DE-1 satellite. [Figure from Frank *et al.*, 1981].

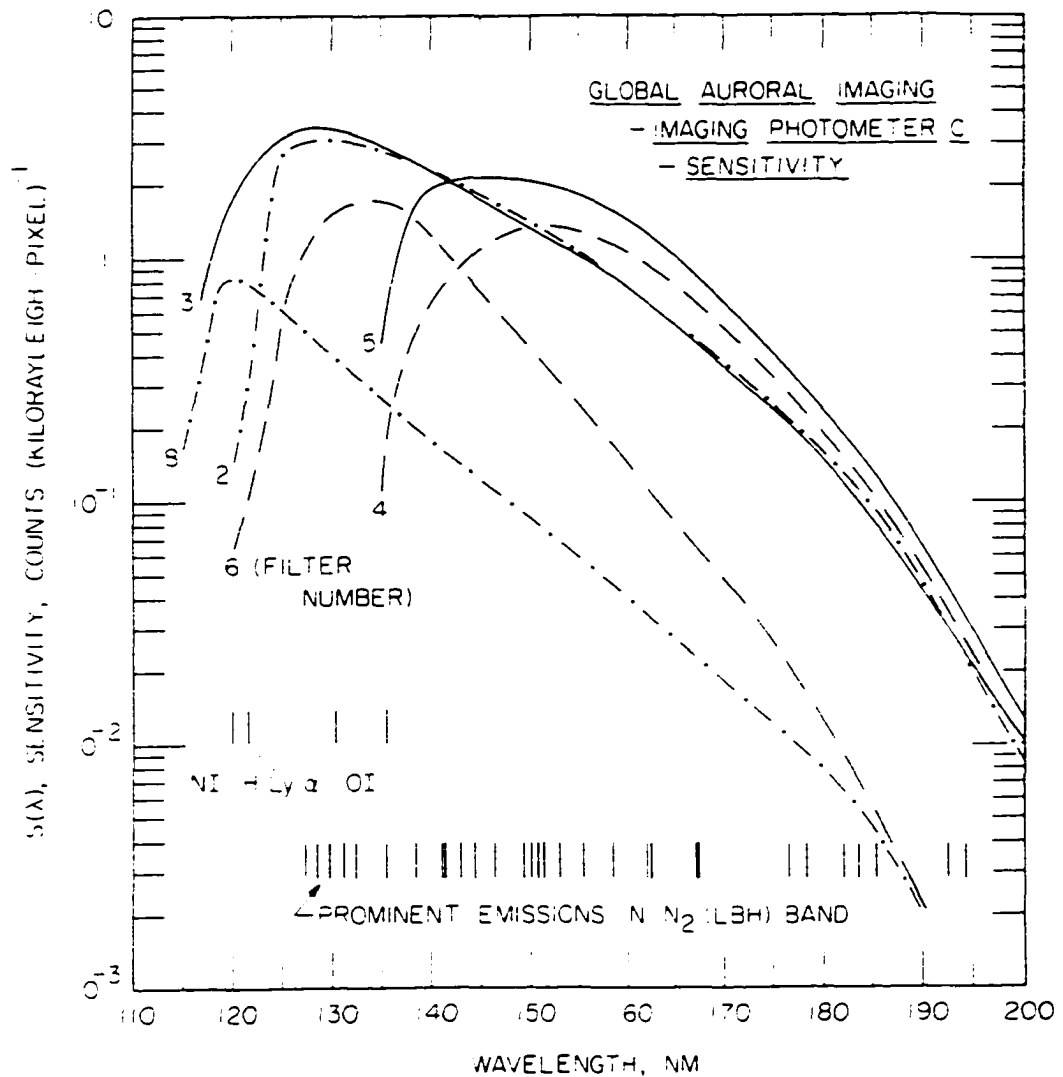


Figure 2-3. Sensitivity profiles of several filters used in FUV SAI experiment. Sensitivity is shown in units of counts  $\cdot$  (kR $\cdot$ pixel)<sup>-1</sup> as a function of wavelength. Filter #2, which allows measurement of the OI 130.4 and 135.6 nm emissions and, to a lesser degree, N<sub>2</sub> LBH emissions, is used extensively in this thesis. [Figure from Frank *et al.*, 1981].

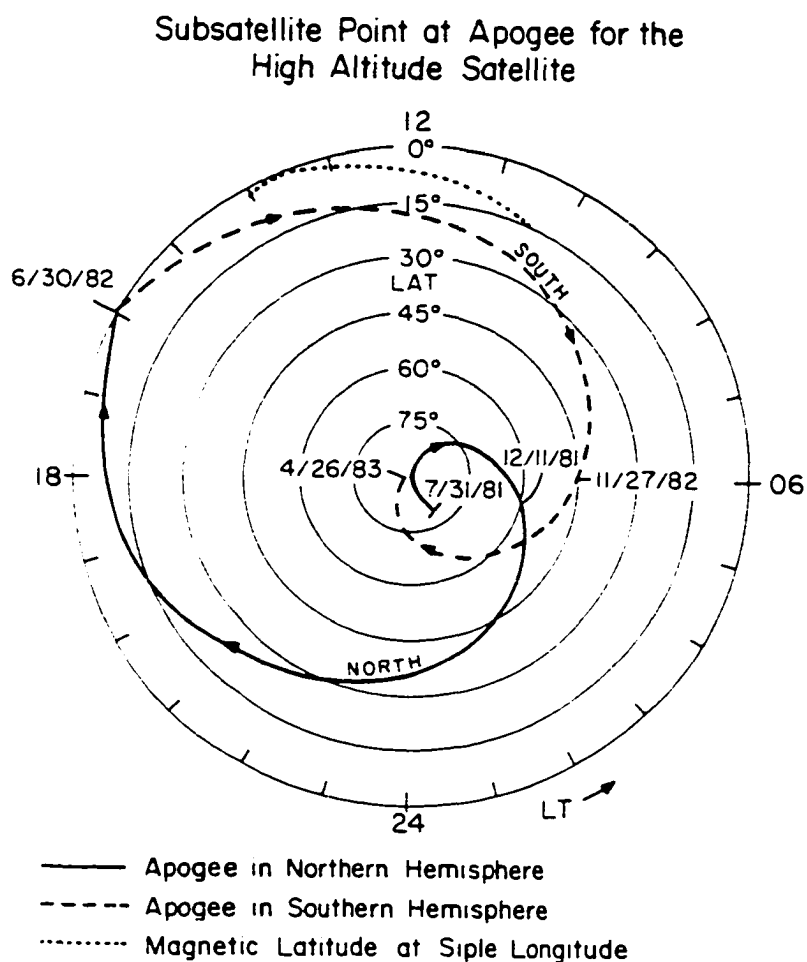


Figure 2-4. Latitude and local time of apogee for DE 1. The latitude of apogee of the DE 1 satellite is shown for northern latitudes with a solid line and a dashed line at Southern Latitudes. Just after placement in orbit, apogee was at high northern latitudes, advancing to southern latitudes by July, 1982. The regression in local time of apogee occurs at the rate of 24 hours per year for this  $0^\circ$  inclination orbit. [Figure from Hoffman *et al.*, 1981].

## 2.2 Earth's Dayglow Observed by DE 1.

A DE-1 FUV image obtained at 1725 Universal Time (UT) on October 18, 1981 is shown in Figure 2-5. This image was obtained using the #2 filter, which is sensitive mainly to OI emissions. Earth's disk and bright limb are plainly visible in this image as approximately half of the observable Earth is directly illuminated by solar radiation. The satellite was approaching apogee over the North Pole, thus the late morning sector on Earth is at the top of the image, with local times increasing to afternoon and evening hours counterclockwise around the image. The DE-1 orbit plane bisects the image. Photometer counting rates are coded by colors which are indicated using the color bar below. The pre-launch sensitivity factor of 3.08 kRayleighs/pixel-count is used to convert from photometer response to dayglow brightness.

Earth's limb is the brightest feature of this image, is due to the effect of limb brightening. As the photometer takes measurements approaching the physical edge of Earth, emissions to which the atmosphere is optically thin (*e.g.*, N<sub>2</sub> LBH) contribute to an increased integrated response due to the greater atmospheric column length in the photometer's line of sight. At the limb, N<sub>2</sub> LBH emissions are dominant, whereas in the central disk region, OI 130.4 nm emissions dominate. Auroral emissions of OI and N<sub>2</sub> are also visible in this image. The auroral oval is a consistent FUV feature and can be observed in any image of the polar regions taken with this instrument.

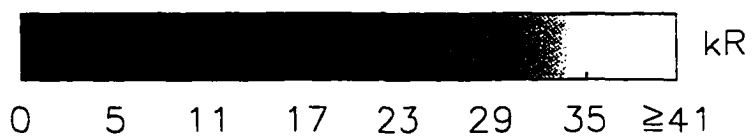
The variations from pixel to pixel are statistical variations in the detector (photomultiplier) counting rates. The sampling distribution for the observed brightness follows normal Poisson statistics. Typical sensor count rates for dayside measurements away from the limb are <100 counts per pixel. The standard deviation for this counting rate is  $\pm 10$  counts per pixel, or  $\pm 10\%$ , which is discernible by the eye in these images. This percentage is greater at lower counting rates. Analysis of images is unhindered by these variations as smoothing techniques can be used that reduce statistical variations to  $\sim 3\%$  and make clear larger-scale physically-significant variations in the dayglow. Photometer response can be averaged over successive images as another means of reducing

Figure 2-5. FUV image of Earth. This FUV image was obtained in a 12 minute period beginning at ~1748 UT on Day 269 of 1981 from an altitude of 3.22 Re using filter #2. The bright dayglow is evident with strongest photometer response at the limb, where optically 'thin' N<sub>2</sub> LBH emissions dominate. This image was taken during a period of intense geomagnetic activity as evidenced by the bright auroral oval at high northern latitudes.

Sep. 26, 1981 (Day 269), 1748:20 UT



Brightness



statistical variations, while losing no spatial resolution. The instrument can collect data with an excellent signal-to-noise ratio, reported to be in the range  $5 \times 10^2$  to  $5 \times 10^4$  for the observation of a 1-kR auroral emission with the outer baffle illuminated by sunlight [Frank et al., 1981].

The imaging mission advanced understanding in the fields of magnetospheric, thermospheric, stratospheric and auroral physics. Highlights of the imaging mission are described by Frank and Craven [1988]. Notable studies include the comparison of DE 2 thermospheric neutral wind measurements to simultaneous observations of auroral morphology by DE 1 [Killeen *et al.*, 1988], global measurements of total ozone concentration derived from comparisons of on- and off-band ozone absorption [Keating *et al.*, 1985], and derivation of auroral electron characteristic energies and total energy flux from visible wavelength images [Rees *et al.*, 1988]. This thesis explores another application of the FUV imager: the study of upper atmospheric properties through investigation of Earth's FUV dayglow.

### Chapter 3

## The DE-1 Auroral Imager's Response to the FUV Dayglow for Thermospheric Studies

### 3.1 Introduction

Response of the DE-1 far-ultraviolet (FUV) photometer to the quiet-time FUV dayglow at wavelengths 123–165 nm is investigated in support of studies of variations in the FUV dayglow and the sunlit aurora. The emphasis here is the development of a means by which the average quiet-time response of the photometer may be reproduced. The results are used to examine the difference between the averaged response and the response in individual images from the quiet-time data set over a range of satellite altitudes. It is demonstrated that the reference response values accurately represent the photometer's response to the quiet-time dayglow. This method is extremely useful for quantitative analyses of variations in thermospheric atomic oxygen (O) density, as the dominant contribution from the disk-region dayglow to the photometer's response is due to OI emissions at 130.4 and 135.6 nm. The reference values provided by this method also provide background levels for investigations of the sunlit FUV aurora.

High-altitude observations of the terrestrial dayglow with broadband FUV-wavelength filters reveal the expected large-scale variations in brightness, including a monotonic increase with decreasing solar zenith angle across the central portion of the sunlit disk and brightening near the limb at all solar zenith angles. Notable exceptions are observed after the onset of intense auroral activity, when large (as least as great as ~50%) decreases in the brightness of OI emissions at 130.4 and 135.6 nm are observed in the morning sector of local time at auroral and subauroral latitudes [*e.g.*, Craven *et al.*, 1994; Meier *et al.*, 1995; Nicholas *et al.*, 1997].

From a preliminary analysis of the photometer's response over its broad 123–165 nm pass band (using filter #2), Craven *et al.* assigned minimum relative contributions to its response for emissions well away from the limb and terminator: ~76% (130.4 nm); ~9% (135.6 nm); ~2% (N<sub>2</sub> LBH band). The remainder was assigned, as a generous upper

limit, to Ly $\alpha$  radiation. A more detailed quantitative analysis by Meier *et al.* [1995] has firmly established the relative contributions to the photometer's response: 85–90% (130.4 nm); 5–8% (135.6 nm); 5–8% (LBH). The work of Meier *et al.* further established the interpretation that the decreases in the photometer's response across the pass band are associated with changes in thermospheric composition, depending mainly on the column density of O. It is clear that broadband observations at these wavelengths are directly useful only because of the dominant contribution by the OI emissions. Observations with relatively low-altitude satellites at one or more wavelengths and narrower pass bands [*e.g.*, Strickland and Thomas, 1976; Conway *et al.*, 1988; Parish *et al.*, 1994] have not been hampered by the DE-1 pass band limitation, and have more clearly demonstrated that the OI emissions decrease during periods of enhanced magnetic activity.

*In situ* observations of variations in thermospheric composition have been extensively reported by Prölss [1980,1981,1984] and Prölss and Roemer [1987] using the low-altitude ESRO-4 satellite, and have shown that the thermospheric composition is altered in the morning sector at auroral and subauroral latitudes following the onset of intense auroral activity. For example, the densities of Ar and N<sub>2</sub> can increase at the 280-km altitude by factors as great as ~100 and ~10, respectively, while He decreases by ~10. Both increases and decreases in O density are observed, but are generally on the order of only a factor of ~2. The O/N<sub>2</sub> ratio at the 280-km altitude can decrease by more than a factor of 10, and the variations in composition can extend to geomagnetic latitudes below 30° during periods of intense magnetic activity. In general, the spatial extent and magnitude of the variations increase with increasing magnetic activity.

Low-altitude satellite observations such as these are limited by the absence of sampling out of the orbital plane, with the result that measurements of composition or FUV brightness are narrowly confined in geographic longitude during each satellite revolution in a high inclination orbit, and that the sampling rate at one local time (*e.g.*, the morning sector) is limited by the orbital period of the satellite. Hence, while the

latitudinal extent has been well sampled both through *in situ* observations and indirectly at FUV and visible wavelengths, the large-scale spatial extent in longitude has been inferred, not measured, and the temporal variations have been measured on the time scale of single auroral substorms. The utility of DE-1 observations is that the full spatial extent within the sunlit hemisphere is revealed in a single image, and multiple images are gained over many hours at 12-minute resolution [Craven *et al.*, 1994].

Analysis of the DE-1 observations can be carried out in the manner of Meier *et al.* [1995] or Gladstone [1994] by making use of highly evolved numerical models and computer facilities. Such work is absolutely necessary to establish quantitatively the details of the instrument's response to the dayglow. It is now seen that a relatively simple method is available for routine image analysis in order to obtain important details on the spatial and temporal variations of the dominant emissions, which in this case are the 130.4 and 135.6-nm multiple line emissions of OI. The technique used by Nicholas [1993], Craven *et al.* [1994], Immel *et al.* [1997], and Nicholas *et al.* [1997] is to create reference values for the photometer's response during intervals of magnetic quiescence and to then compare the observations during active periods against the quiet-time values.

It is important that the reference values be well established, and it is the purpose here to report an improved algorithm for representing the observed response of the DE-1 auroral imaging photometer to the quiet-time FUV dayglow. The result is constructed specifically for the DE-1 broadband 123–165 nm filter #2, but the method used is readily applicable for observations with filters of similar or narrower pass bands. The algorithm created here is used to systematically detect even small deviations in dayglow brightness from quiet-time values in selected images obtained throughout the DE-1 mission.

### 3.2 Image Selection and Initial Processing

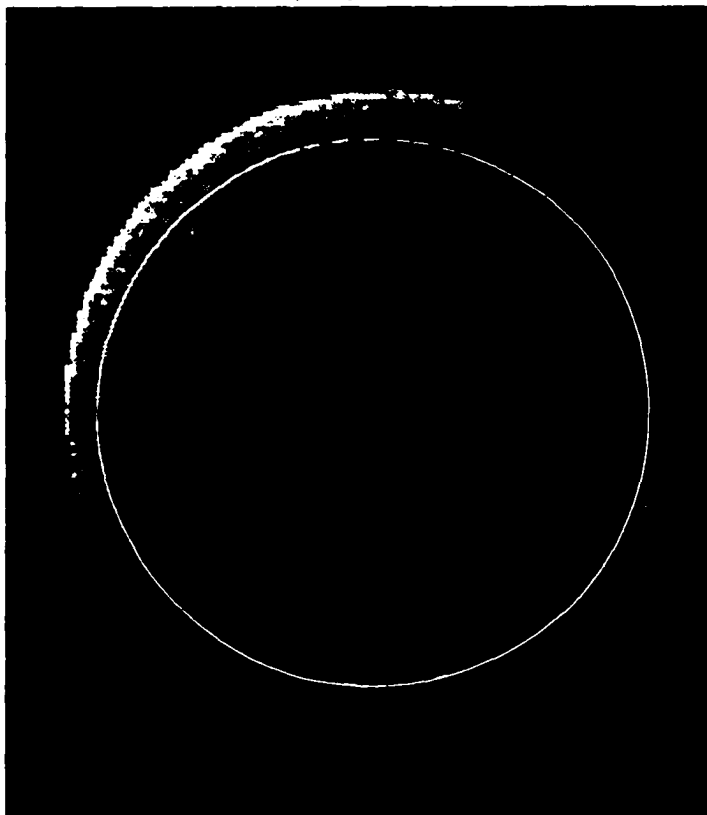
As discussed in the Introduction, the principal objective here is the creation of refined reference values for the photometer's response to the FUV emissions in the sunlit hemisphere during periods of auroral and magnetic quiescence. Image selection was

carried out as originally specified by Nicholas [1993], with the requirements that values of the AE index must remain below 100 nT for a minimum of six hours, that solar flare activity not be high during the six hours prior to imaging, and that there must be a favorable imaging geometry. Observations were limited to the period September 23, 1981 (first day of imaging operations) through February 19, 1982 (last day of operations before the first Sun crossing of the imaging field-of-view). An extension to later time intervals will require consideration of systematic decreases in the photometer's sensitivity across the pass band due to degradation of FUV materials (*e.g.*, lens and mirror coatings) in the intense corpuscular radiation fields of the inner and outer Van Allen radiation belts [see Rairden *et al.*, 1986]. A total of 185 images from 16 days meet the selection criteria, and are used here as in the initial development by Nicholas [1993]. As is discussed later, however, several of these images are strikingly unrepresentative of the remainder of the quiet-time set, with significant deviations of measured brightness from average values. These 29 images have been removed from the quiet-time set, so the final number of images used in the quiet-time model is 156. These unrepresentative images will be discussed in the last section of this report.

Brightness of the dayglow observed with DE 1 increases significantly near the limb, as the thermosphere is optically thin to N<sub>2</sub> LBH band emissions. Because of this, observations near the limb are not used here, avoiding increased complication for no significant gain in the overall objective. Brightness of auroral emissions at the higher magnetic latitudes is comparable with that of the local dayglow and represents a "contamination" of the dayglow. Each image has thus been divided into limb, disk and auroral regions, as illustrated in Figure 3-1, and only samples (images pixels) from the disk region are given further consideration in constructing the algorithm. The altitude-dependent angular separation between the limb and the disk boundary, the outer white contour in the figure, has been empirically determined by Nicholas [1993]. The auroral region (bounded by the inner contour of smaller dimension) is defined as all geomagnetic latitudes > 65°.

Figure 3-1. Original DE-1 image of Earth at 1725 UT on October, 18 1981 (day 291), at wavelengths 123–165 nm. The Sun is toward the upper left in this full image obtained from an altitude of 3.44 Re. Brightness in kiloRayleighs, kR, is coded below the image. Regions dominated by limb brightening effects and the aurora are identified by the outer and inner (white) contours, respectively, which bound the central disk region of interest in this work.

Oct. 18, 1981 (Day 291), 1725:46 UT



Brightness



0 5 11 17 23 28 34  $\geq 40$

Observations in this investigation are organized using four angles (See Figure 3-2), where the first two ( $S$  and  $D$ ) are measured relative to the local zenith direction,  $\mathbf{Z}$ , at the geographic position of an individual pixel, a third ( $A$ ) is determined by the projections of the solar and satellite directions,  $\mathbf{L}$  and  $\mathbf{R}$ , respectively, onto the local horizontal plane at the pixel, and a fourth ( $P$ ) is phase angle of the pixel about the sub-solar point. In this discussion, a right-hand geocentric coordinate system is used with the x-axis defined by  $\mathbf{L}$ , the z-axis perpendicular to  $\mathbf{L}$  in the plane defined by  $\mathbf{L}$  and Earth's rotation axis, and  $\hat{\mathbf{y}} = \hat{\mathbf{z}} \times \hat{\mathbf{x}}$ . The effective emission altitude for the pixel location is assumed at the outset to be 500 km. Selection of this altitude is important, as will be discussed as part of the analysis. Following the geometry in Figure 3-2, the solar zenith angle,  $S$ , is defined as the angle between  $\mathbf{Z}$  and the sun-earth line,  $\mathbf{L}=\mathbf{L}'$ . The DE-1 satellite zenith angle,  $D$ , is the angle between  $\mathbf{Z}$  and the satellite position,  $\mathbf{R}$ , which is directed from the pixel to DE 1. Solar insolation is constant along a contour of constant  $S$ , which is symmetric about  $\mathbf{L}$ , and, for a homogeneous thermosphere, the FUV brightness would be independent of position along this contour. That position is specified by the solar phase angle,  $P$ , which is measured from the y-axis in the z-x plane. The angle  $P=0^\circ$  therefore identifies the afternoon sector. The azimuth angle,  $A$  is defined as the angle between the projections of  $\mathbf{L}'$  and  $\mathbf{R}$  on a plane whose surface normal is  $\mathbf{Z}$ . This plane is illustrated at the surface of the sphere in Figure 3-2, with the projections of  $\mathbf{L}'$  and  $\mathbf{R}$  and the resultant angle  $A$  shown in the inset. The reference angle  $A=0^\circ$  is defined for  $\mathbf{R}$  in the  $\mathbf{L}'$ - $\mathbf{Z}$  plane and sunward of  $\mathbf{Z}$ , for which this pixel is anti-sunward of the geocentric radius vector to the satellite,  $\mathbf{T}$ , which is not shown. For the illustrations of Figure 3-2,  $A \approx 150^\circ$ .

As an example of how the four angles vary for the ensemble of pixels in a single image, the values of the angles  $S$ ,  $D$ ,  $P$  and  $A$  are shown in Figure 3-3 for the disk region of the image shown in Figure 3-1. The general variation in each angle is coded at the bottom of the figure. The dependence on  $S$  is straightforward (Figure 3-3a), with the zenith angle systematically decreasing from  $180^\circ$  toward  $0^\circ$  for pixels approaching  $\mathbf{L}$  at

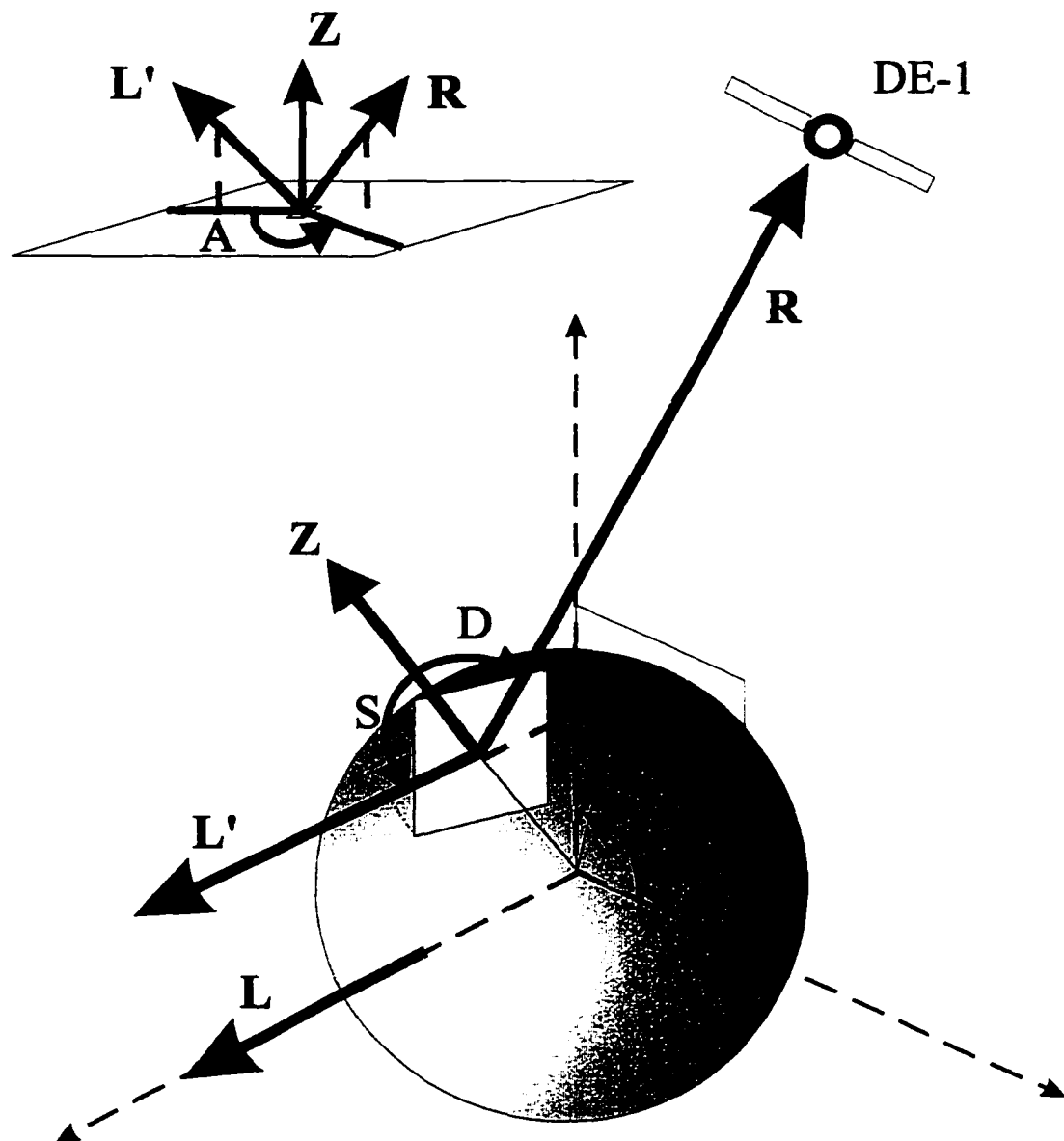


Figure 3-2. Graphical illustration of the geometry for DE-1 measurements of dayglow brightness. The satellite ( $R$ ), solar ( $L'$ ), and local zenith ( $Z$ ) vectors extend outward from an arbitrary pixel at an assumed effective emission altitude. The solar and satellite zenith angles,  $S$  and  $D$  respectively, are indicated. The orthogonal coordinate axes are defined geocentrically by  $L$  (parallel to  $L'$ ),  $\hat{z}$  perpendicular to  $L$  in the plane containing that vector and the earth's rotation axis, and  $\hat{y} = \hat{z} \times \hat{x}$ . The phase angle  $P$  is defined as the angle between the  $y$ -axis and the projection of  $Z$  into the  $y$ - $z$  plane. The azimuth angle  $A$  is shown in the inset for this pixel, where the satellite, solar, and zenith vectors ( $R$ ,  $L$ , and  $Z$ ) and solar and satellite zenith angles ( $S$  and  $D$ ) are shown. The angle  $A$  is drawn between the projections of  $S$  and  $D$  onto the local horizontal.

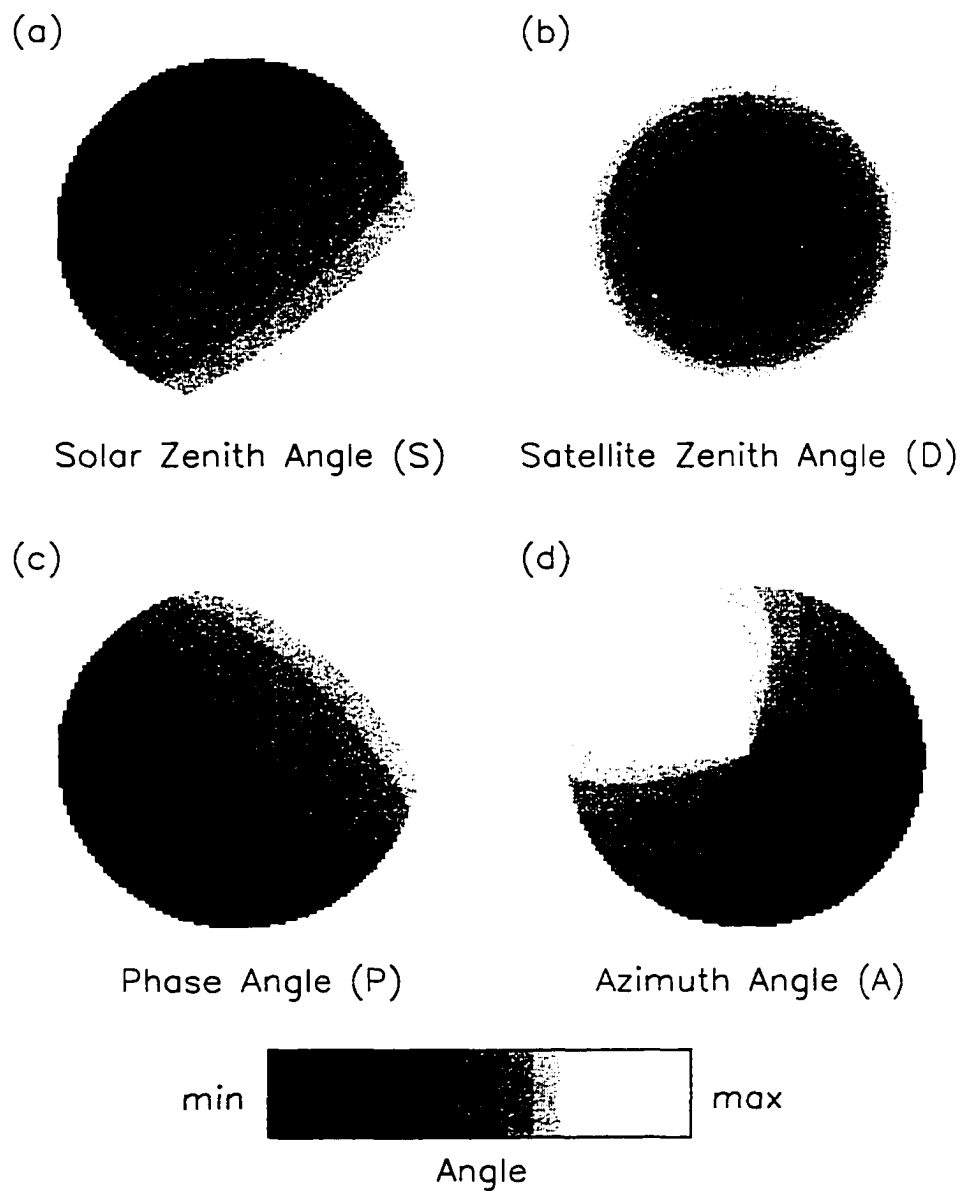


Figure 3-3. Angular variables for image of Figure 1. Variation of (a) solar zenith angle  $S$ , (b) satellite zenith angle  $D$ , (c) phase angle  $P$ , and (d) satellite azimuth angle  $A$  are shown for the image pixels of Figure 1. The variation in magnitude of each angle is coded below. The four angles are defined in the text and actual values are given.

the upper left in the figure. The range of  $D$  is seen in Figure 3-3b to vary between  $0^\circ$  at  $-\mathbf{T}$  (directed from the satellite to the subsatellite point and then to the center of the projected earth) and  $\sim 65^\circ$  near the limb-disk separation. The angle  $P$  varies from a low of  $61^\circ$  in the lower left corner of Figure 3-3c up to  $155^\circ$  in the upper right corner. Variations in  $A$  are more complex, but for a fixed  $D$  (all pixels in a circle about the subsatellite point) the values of  $A$  shown in Figure 3-3d increase progressively from  $0^\circ$  for pixels towards the lower right (anti-sunward from  $-\mathbf{T}$ ) to  $180^\circ$  in the sunward direction.

### 3.3 Modeling Method

The initial analysis by Nicholas [1993] and Nicholas *et al.* [1997] evaluated the dependence of the photometer's response on  $S$  and  $D$  only, while assuming no dependence on  $A$  or  $P$ . The variation with  $S$  dominates, as the response increases by  $\sim 300\%$  between  $S=80^\circ$  and  $20^\circ$ , for example, while the maximum variation for  $D=10^\circ$  to  $60^\circ$  is on the order of  $\sim 10\%$ . In this new analysis, the response as a function of  $A$  and  $P$  is also determined for given ranges of  $S$  and  $D$ . Although the dependence of the response on these parameters may be slight (in comparison to the strong dependence on  $S$  and weak dependence on  $D$ ), some physical properties of the thermosphere may be revealed in this analysis. Furthermore, the inclusion of these two angles in the quiet-time analysis serves to uniquely specify any point on a surface above Earth in the sun-satellite coordinate system described in the previous section.

A photon of the solar 130.4-nm OI emission incident on Earth's atmosphere is readily scattered by thermospheric O through resonance. The thermosphere is optically thick to this emission and relatively thin to the 135.6-nm line emission as the latter is associated with a spin-forbidden transition and is  $\sim 1000$  times less likely to resonate with incident radiation. There is a particular altitude below which the optical depth,  $\tau$ , is large enough to prevent a measurement (by DE-1) of the origin of the thermospheric

130.4-nm emission. Photons that are not attenuated by  $O_2$  in the lower thermosphere scatter multiple times and appear to originate from this altitude where  $\tau \approx 1$ . For a particular set of inputs to MSIS-86 [Hedin, 1987] and at  $S=30^\circ$ , for example, Meier [1991] determined that at line center the  $\tau=1$  surface is at an altitude between 500 and 700 km. This altitude depends on the density altitude profile of O which varies with the overall level of solar activity and the corresponding EUV flux. Using this work by Meier [1991], we calculate the  $\tau=1$  O density for line center OI 130.4-nm emission to be  $\sim 5.5 \times 10^6 / \text{cm}^3$ . A large part of the 130.4-nm emission measured by the photometer will appear to originate from a surface at the  $\tau=1$  altitude, including the entire photoelectron excited component and a large part of the resonance scattered component. A smaller part of OI emissions will originate from higher altitudes through single-scattering of solar OI in the upper thermosphere.

Variation in the photometer's response with A at fixed S and D is inherent to this analysis of DE-1 images, where all angles are calculated at a fixed altitude. For instance, if the altitude used for the calculation is higher than the actual  $\tau=1$  altitude, then the response at  $A=0^\circ$  (and fixed S and D) will appear to be smaller than the response at  $A=180^\circ$ . This reflects the fact that the photometer is actually sampling regions of lower S and greater emission rate at the true  $\tau=1$  surface. The converse is true for observations at  $A=0^\circ$ . For example, sampling at fixed S,  $D=45^\circ$ , and the entire range of A, where the angles are calculated at a surface 200 km above the true  $\tau=1$  surface, for example, will yield count rates from portions of the dayglow which are actually  $> 400$  km apart, or several pixel widths at DE-1 apogee. There should be no A dependence if the  $\tau=1$  altitude is chosen correctly, however this altitude varies with position on the dayside and with the degree of heating related to temporally varying solar EUV and FUV inputs. Characterization of the photometer's response with A is performed in the following section.

The column emission rate of 130.4- and 135.6-nm OI emissions varies with solar EUV and FUV input. Long-term (>30 days) variations in the EUV flux affect the temperature of the thermosphere and the scale heights of constituents such as  $N_2$  and O. Short-term variations in EUV flux will have a smaller effect on thermospheric composition. However, these and related variations in the FUV flux may rapidly affect the column emission rate and thus the observed brightness of the FUV dayglow. A known correlation [Hedin 1984; Barth *et al.*, 1990] between solar UV intensities and the 10.7-cm solar radio flux (F) is used to characterize these brightness variations. In the relatively short period of five months, from which quiet time images are used for modeling, the monthly average values of F,  $F_m$ , range from a maximum of 222.8 Janskys (Jy) in October, 1981, to a minimum of 173.4 Jy in January, 1982 [NOAA, 1984]. The corresponding decrease in the  $\tau=1$  altitude for this range, calculated using MSIS-86 [Hedin, 1987], is ~80 km, where the required input for 24-hour averaged F is set to the monthly value. This is calculated at 1000 LT, day 80,  $A_p=6$ , and at the geographic location  $32^\circ N$ ,  $254^\circ E$ , following the example by Meier [1991]. For this modeling effort, it is assumed that overall variations in thermospheric temperatures are small and that variations in the solar UV spectrum only affect dayglow brightness and not the  $\tau=1$  altitude. It is thus recognized that extreme daily values of F may have a significant effect, as is investigated in a later section.

Variations in thermospheric composition, specifically variations in the O column density with local time and latitude, may affect the brightness of the OI dayglow. It is therefore important to examine the dependence of the response on P, which, together with S, effectively represent local time and latitude. Variations in the  $\tau=1$  altitude with P are not investigated here, but can be as great as ~150 km between  $P=0^\circ$  and  $180^\circ$  (as determined at  $S=66^\circ$  using MSIS-86 with  $F=F_m=173.4$  Jy, at 1725 UT of day 291). However, this wide range of P for large S is never observed in individual images, where data are taken mainly in the morning sector. Therefore the  $\tau=1$  altitude is determined

only as a function of  $S$  and  $D$ . Variations of brightness with  $P$ , rather than  $\tau$  with  $P$ , will have a more direct effect on the photometer's response,  $r$ . Such variations can be seen at high, fixed values of  $S$  in model images generated by Meier *et al.* [1995], using the MSIS model for thermospheric constituents. These images clearly show that contours of constant OI brightness do not follow contours of equal  $S$ , an effect especially apparent at large  $S$ .

Variations in brightness with stepping mirror angle are not included in this analysis. Rairden's [1985] analysis of photometer response vs. stepping mirror angle found an asymmetry in the reflectivity of the optics (to HI  $L\alpha$  emissions) on the order of a factor of two between minimum and maximum excursions of the stepping mirror. However, our analysis shows nearly uniform reflectivity across most of the mirror, with a gradual reduction in sensitivity after scan line 80 (of 120) near maximum mirror excursion (maximum angle between photometer line-of-sight and DE-1 spin vector). Since the outer section of all images (limb region) is excluded from this analysis, brightness measurements near maximum excursion are rarely included in the quiet-time data set. Furthermore, in this imaging period (late 1981/early 1982) the sunlit portion of Earth is found in scans closer to minimum mirror excursion. Variations in mirror reflectivity are therefore assumed to have a negligible effect on the photometer's response in this study.

For an initial demonstration of the relative importance of these parameters, the data are binned in  $S$ ,  $D$  and the third parameter of interest, either  $F$ ,  $P$  or  $A$ , resulting in values for the average response  $\langle r \rangle$  as a function of the selected variables. This results in a representation of the photometer's response with greater statistical significance than if the data were binned at once in all five parameters. The last step is to separate the dependence on  $F$ ,  $P$  and  $A$  through an iterative technique which is described in a later section. There are two goals: (1) To identify and separate the dependence of  $\langle r \rangle$  on  $F$ ,  $P$  and  $A$ , and (2) To develop the means for normalizing  $\langle r \rangle$  in images to fixed values

of these parameters for development of an S and D dependent reference response model. The source of variations in  $\langle r \rangle$  with each variable will also be investigated.

### 3.3.1 Dependence on Azimuth Angle

To demonstrate the azimuth dependence, the response for each pixel within the disk region of every image (as previously defined) is binned in increments  $\Delta S=3^\circ$ ,  $\Delta D=5^\circ$  and  $\Delta A=30^\circ$ , where the increments are made as small as possible while maintaining a reasonable sample in most sample bins. Throughout this discussion, bins may be denoted by the full range of angle values represented, or more simply by lowest integer value of the range (*e.g.*,  $\Delta S=3^\circ$ ,  $S=66^\circ$  indicates the bin for which  $66^\circ \leq S < 69^\circ$ ).

The mean photometer response  $\langle r \rangle_i$ , in counts/pixel, and the standard error of the mean,  $\sigma_{mi}$ , are computed for the contents of the *i*-th azimuth bin. As an example,  $\langle r \rangle_2$  for  $30^\circ \leq A < 60^\circ$  is shown in the three-dimensional projection of Figure 3-4a with S and D in the horizontal plane (x and y axes, respectively) and the mean photometer response in the vertical (z) direction. No smoothing has been applied. The number of pixel samples accumulated in each S-D bin is given in Figure 3-4b, as coded below the panel. Values for  $\langle r \rangle_5$  ( $120^\circ \leq A < 150^\circ$ ) are presented in Figures 3-4c and 3-4d using the same format. The number of samples is significantly larger for the larger values of A, and there is no obvious strong dependence of  $\langle r \rangle$  on A. Limitations in sampling for  $S < 20^\circ - 60^\circ$  are seen in the figures, where the range of S is largely determined by the latitude and local time of apogee.

An analysis of the dependence on A is provided by investigating variations in  $\langle r \rangle_i$  as a function of azimuth (*i*) for each  $3^\circ$  bin of S and  $5^\circ$  bin of D. This is shown in Figure 3-5a for three ranges of S at a fixed range of D. The data points give the values of  $\langle r \rangle_i$  for the *i*-th  $30^\circ$  bin in A, and are plotted at the mean value of A determined from the samples in each bin. The coverage in S is insufficient to observe the dayglow in the first

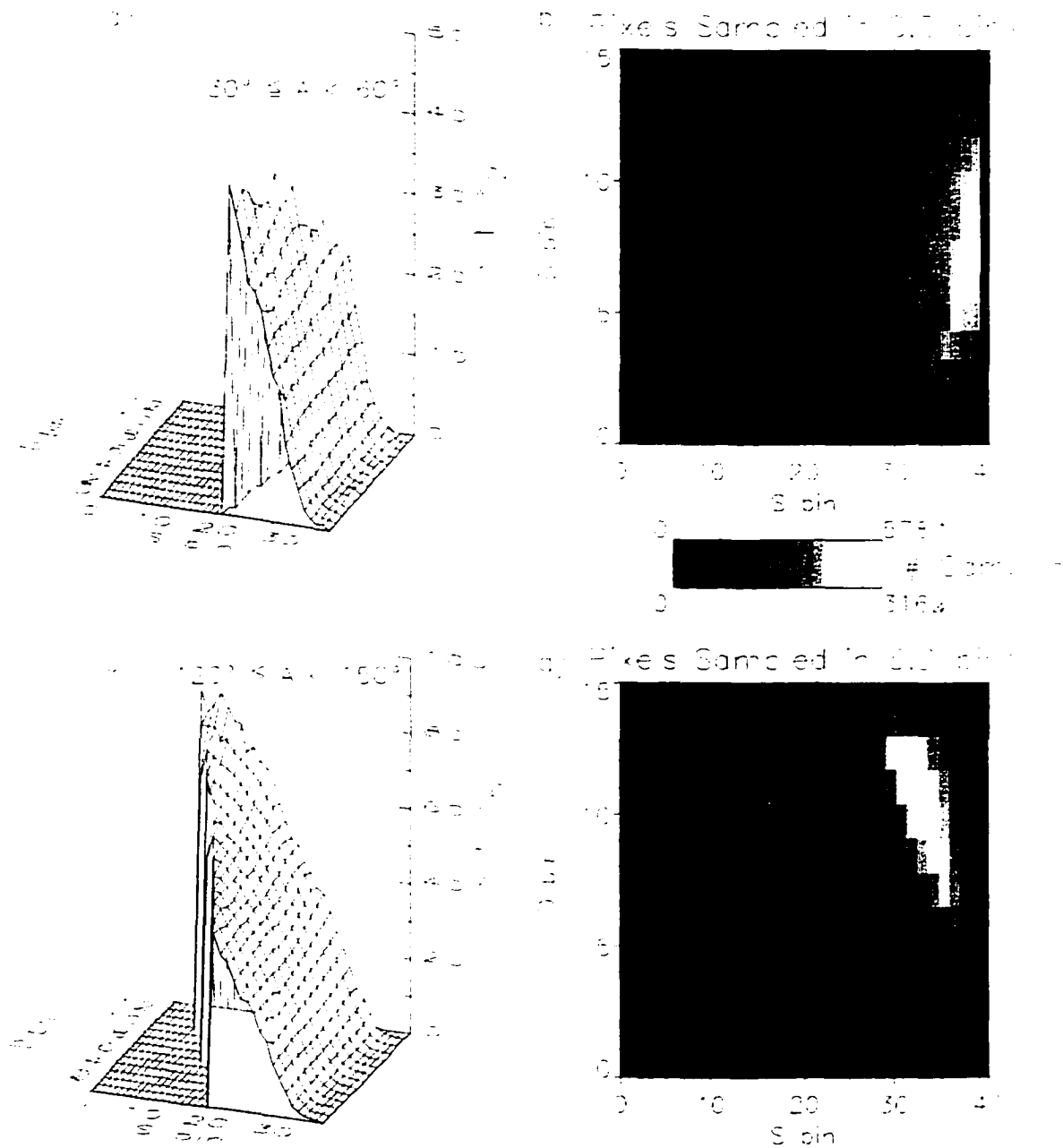
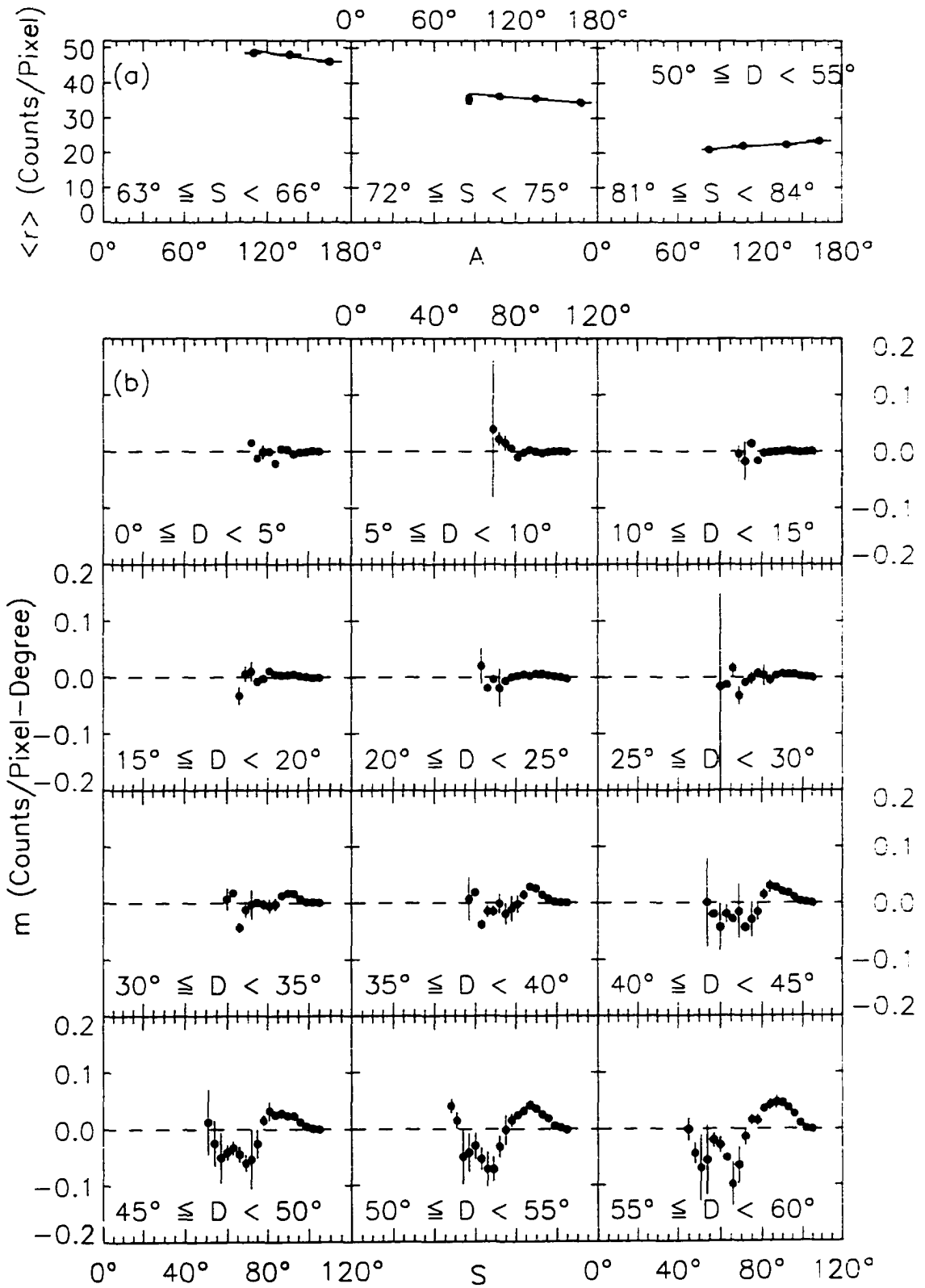


Figure 3-4. Average counting rate in two bins of azimuth. (a) Mean photometer response  $\langle r \rangle$  in counts/pixel, as functions of S and D for the azimuth angles  $30^\circ \leq A < 60^\circ$ . (b) Number of pixel samples used to determine  $\langle r \rangle$ . (c, d) Repeat of 4a and 4b for  $120^\circ \leq A < 150^\circ$ . The number of samples in each S-D bin is coded in according to the accompanying color bar

Figure 3-5. Dependence of photometer response on azimuth angle. (a) Mean photometer response  $\langle r \rangle$  at  $50^\circ \leq D < 55^\circ$  is shown as a function of azimuth angle for three ranges of  $S$ . See the text for definitions of the angles. Uncertainty in  $A$  is given by the standard deviation for all samples in the bin. Uncertainty in  $\langle r \rangle$  is the standard error of the mean for all samples in the bin. The least-squares fitted slope,  $m$ , is negative at  $63^\circ \leq S < 66^\circ$  and  $72^\circ \leq S < 75^\circ$ , but positive at  $81^\circ \leq S < 84^\circ$ . These three slopes are included in the lower center panel in Figure 5b. (b) Values of  $m$  are shown as a function of  $S$  for twelve  $5^\circ$  bins of  $D$ . The stronger dependence of  $\langle r \rangle$  on  $A$  at higher values of  $D$  is evident. Slopes for  $60^\circ \leq D < 70^\circ$  are not shown.



two or three  $30^\circ$  bins of  $A$  ( $i=1,2,3$ ), depending on the range of  $D$ . Each horizontal bar specifies the standard deviation for the values of  $A$  in the bin, and the vertical bars indicate  $\sigma_{mi}$  for  $\langle r \rangle_i$ . A linear fit is determined for this and all other  $S$ - $D$  bins (least-squares, weighted by  $1/\sigma_{mi}^2$ ) if three or more values of  $\langle r \rangle_i$  are available to calculate a slope and intercept. The sole parameter later used from this fit is the slope,  $m$ ; the values of which are given in Figure 3-5b for all  $S$  and for  $D$  up to  $60^\circ$ . The uncertainties in  $m$  due to the uncertainties in the fit to  $\langle r \rangle_i$  are denoted by vertical bars.

Within the error of the individual fits the slope correctly remains at zero for all values of  $S$  at  $D < 30^\circ$ , with the exception of some small number of points. The slope deviates from zero at greater values of  $D$ , with negative values at  $S < 81^\circ$  and positive values at  $S \geq 81^\circ$ . Negative (positive) slopes indicate a decrease (increase) in brightness with increasing azimuth. The overall result is that the dependence of  $\langle r \rangle$  on  $A$  is significant, at least implying the necessity of applying corrections to the low counting rates measured at solar zenith angles  $> 81^\circ$ . The slopes reported here may be used to calculate the corrections necessary to normalize any observed photometer count rate to a fixed value of  $A$ .

The variations in  $\langle r \rangle$  at  $S < 81^\circ$  are less than 10% of the average count rate, suggesting that variations with  $A$  can be ignored in the initial phases of investigations or for those in which variations on the order of 10% are of secondary importance. Values of  $m$  in (counts/degree of  $A$ ) for  $D > 20^\circ$  and  $S > 81^\circ$  are reported in Table 1 of Appendix A, as corrections here are of greater significance compared to the values of  $\langle r \rangle$ . When necessary, corrections of the response to  $A=90^\circ$  are carried out using the values of  $m$  for all values of  $S$  and  $D$  which could be calculated from the 156 images in the quiet time set. These corrections are for  $S$ ,  $D$  and  $A$  calculated at an assumed emission altitude of 500 km. The non-zero slopes indicate that this choice of emission altitude is too low at low solar zenith angles. Conversely, 500 km is too high at values of  $S$  on either side of

the solar terminator ( $S=90^\circ$ ). It is believed these results are due to changes in thermospheric composition and solar illumination with  $S$ . In particular, the effects of atmospheric absorption and shadowing by Earth are apparent at  $S>90^\circ$ , where the slope decreases with increasing  $S$ , indicating that the effective emission altitude is increasing with  $S$ . Local time and latitudinal dependences are ignored for this first analysis, as are variations in  $\langle r \rangle$  with  $F$ .

It is possible to estimate an effective emission altitude by repeating the procedure described here at several altitudes and then determining (at each  $S$  and  $D$ ) the  $m=0$  altitude by means of a linear interpolation of the  $m$  values. In practice, the 156 images provide only enough coverage in azimuth to establish, with reasonable certainty, the  $\tau=1$  altitude at  $S>60^\circ$  (note large error bars for slopes at low  $S$  in Figure 3-5b). Also, it is not possible to determine this altitude for small  $D$ , where, by geometric construction, the azimuth dependence must be zero. Plots of the  $m=0$  effective altitude vs.  $S$  are shown in Figure 3-6a through 3-6c for  $D=25^\circ$ ,  $40^\circ$  and  $55^\circ$ , respectively, based on a fit to values of  $m$  calculated at altitudes 200, 400, 500, 600, and 800 km. Note that there is a minimum in the  $\tau=1$  altitude at or near  $S=90^\circ$  for each value of  $D$ .

### 3.3.2 Dependence on Phase Angle

An initial analysis of the response of the dayglow as a function of  $S$ ,  $D$  and phase angle,  $P$ , is performed by organizing the data from the 156 quiet-time images in bins of  $\Delta S=3^\circ$  and  $\Delta P=15^\circ$ . It is determined, but not shown here, that the variation in the phase dependence with  $D$  is negligible. The mean photometer response,  $\langle r \rangle_i$ , is calculated at all  $S$  and  $P$ , where the index now indicates a  $15^\circ$  bin in  $P$ , and is shown in Figure 3-7a as a function of  $P$  at  $S=66^\circ$ . The standard error of the mean is shown with a vertical errorbar, and a linear least squares fit is superposed. This plot clearly shows a trend of increasing response with decreasing  $P$ , and greatest values in the low-latitude afternoon sector. A positive inflection is expected at  $P\sim 180^\circ$  as greater values of  $P$  indicate points

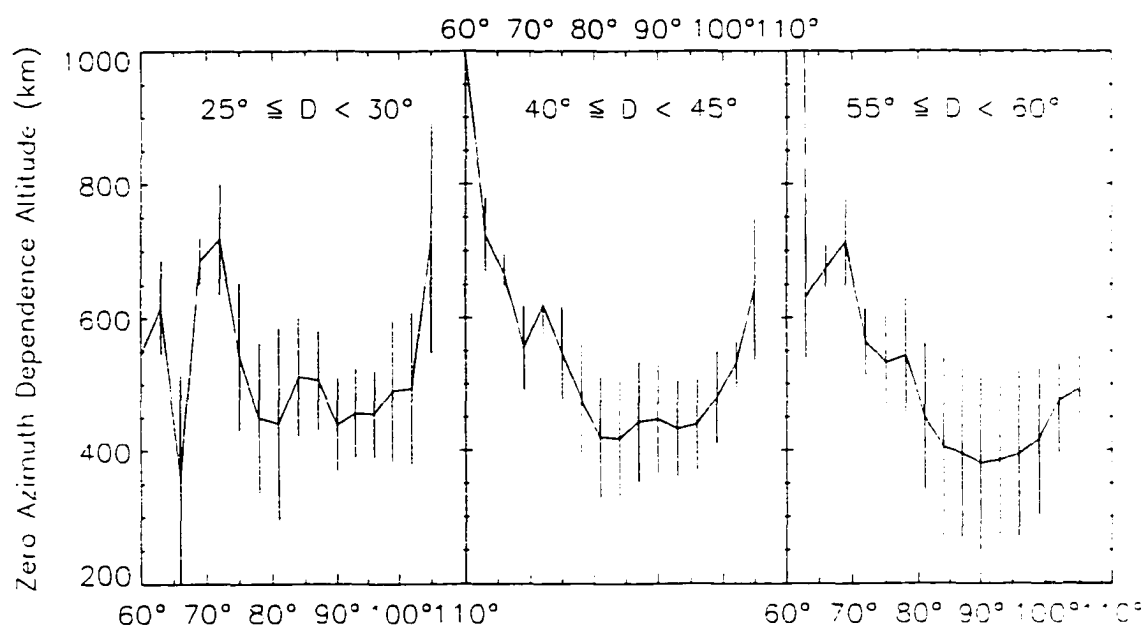


Figure 3-6. Emission altitudes inferred from azimuth analysis. Effective emission altitude ( $\tau=1$ ) calculated for  $60^\circ \leq S < 105^\circ$  in bins of  $D$  ( $\Delta D=5^\circ$ ) at  $D=25^\circ$ ,  $40^\circ$ , and  $55^\circ$ . Vertical bars at each point indicate uncertainties.

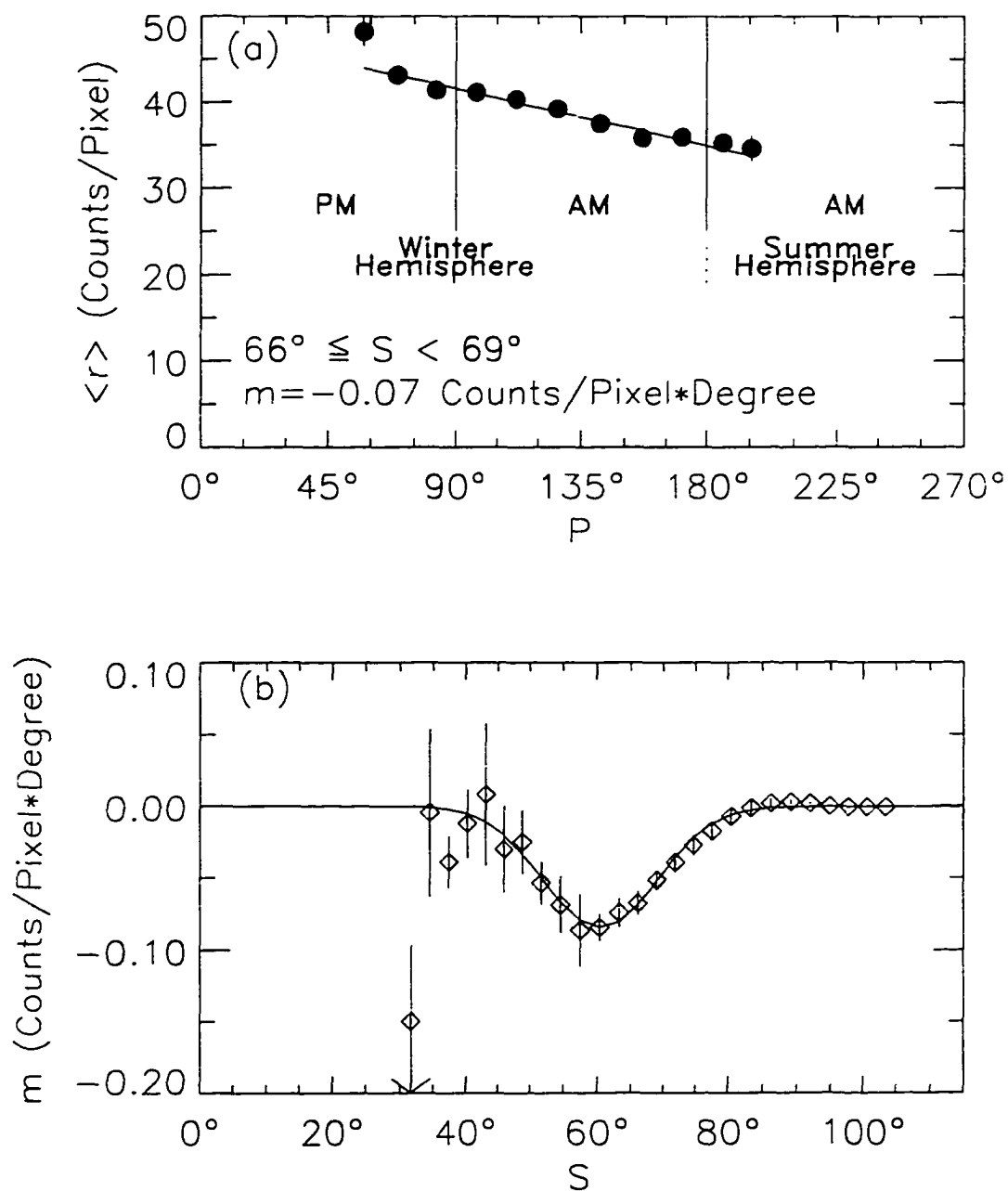


Figure 3-7. Dependence of photometer response on  $P$ . (a) Plot of  $\langle r \rangle$  vs.  $P$  for  $66^\circ \leq S < 69^\circ$ . Values of  $\langle r \rangle$  are indicated with filled circles and standard deviation from the mean counting rate in the  $15^\circ$  bins in  $P$  are indicated with vertical bars. The differing local times and season corresponding to ranges of  $P$  are indicated. Linear least-squares fit is overlain, the slope of which,  $m$ , is indicated in the figure. (b) The values of  $m$  for all  $S$ , where  $m$  is indicated with open diamonds. The uncertainty in the value of  $m$  is indicated with vertical bars. A gaussian curve, least-squares fitted to the data, is overlain.

on Earth approaching the brighter afternoon sector (as observed here at  $P < 180^\circ$ ). The slope of the fit for each range of  $S$  is shown in Figure 3-7b. The standard deviation of  $S$  is not shown in either plot of Figure 3-7, as it is  $\sim 1^\circ$  for each bin.

Corrections with which to convert  $\langle r(S,P) \rangle$  to  $\langle r(S,P=90^\circ) \rangle$  are calculated from these observed slopes,  $m$ , smoothed over bins of  $S$  with a  $9^\circ$ -wide boxcar window. A least-squares fitted gaussian function, weighted by the inverse of the variance in each value of  $m$ , is obtained for the data to provide an overall estimate of  $m$  where no data are available ( $S < 29^\circ$ ) or where large uncertainties are present. This combination of actual and fitted values eliminates the large variations between bins of  $P$  at low  $S$  but preserves the observed variations in  $m$  at high  $S$ , where the gaussian function cannot exactly fit both the positive and negative values of  $m$ . An artificially weighted data point of  $m=0$  at  $S=0^\circ$  is provided to control the gaussian fit. This is the correct value since at  $S=0^\circ$  all values of  $P$  indicate the same point on Earth, the sub-solar point.

These data imply that the photometer's response at a given value of  $S$  is a function of the position of the observed location about the sun-earth line. Earlier assumptions of equal irradiance along a contour of constant  $S$  being true, the assumption of equal FUV dayglow brightness is not. An understanding of this variation comes from efforts in modeling the pertinent thermospheric constituents ( $O$  and  $N_2$ ).  $O_2$  is not modeled as it was shown by Nicholas [1993] that during quiet times, at most approximately 2% of the OI dayglow at 130.4 and 135.6 nm is absorbed by this constituent.

A simple graph of constituent densities, calculated using MSIS-86 [Hedin, 1987] with the following set of parameters:  $F=297$  Jy,  $F_m=218$  Jy and  $A_p=6$ , is shown in Figure 3-8, where the image in Figure 3-1 is used in selecting  $S$ ,  $P$  and geographic coordinates. The densities shown in Figure 3-8 are for 500 km altitude,  $S=66^\circ$ , and at geographic coordinates corresponding to the observable range of  $P$ . This demonstrates the large-scale changes in thermospheric densities with increasing phase angles that may well affect the observed FUV brightness during periods of low magnetic activity. The oxygen

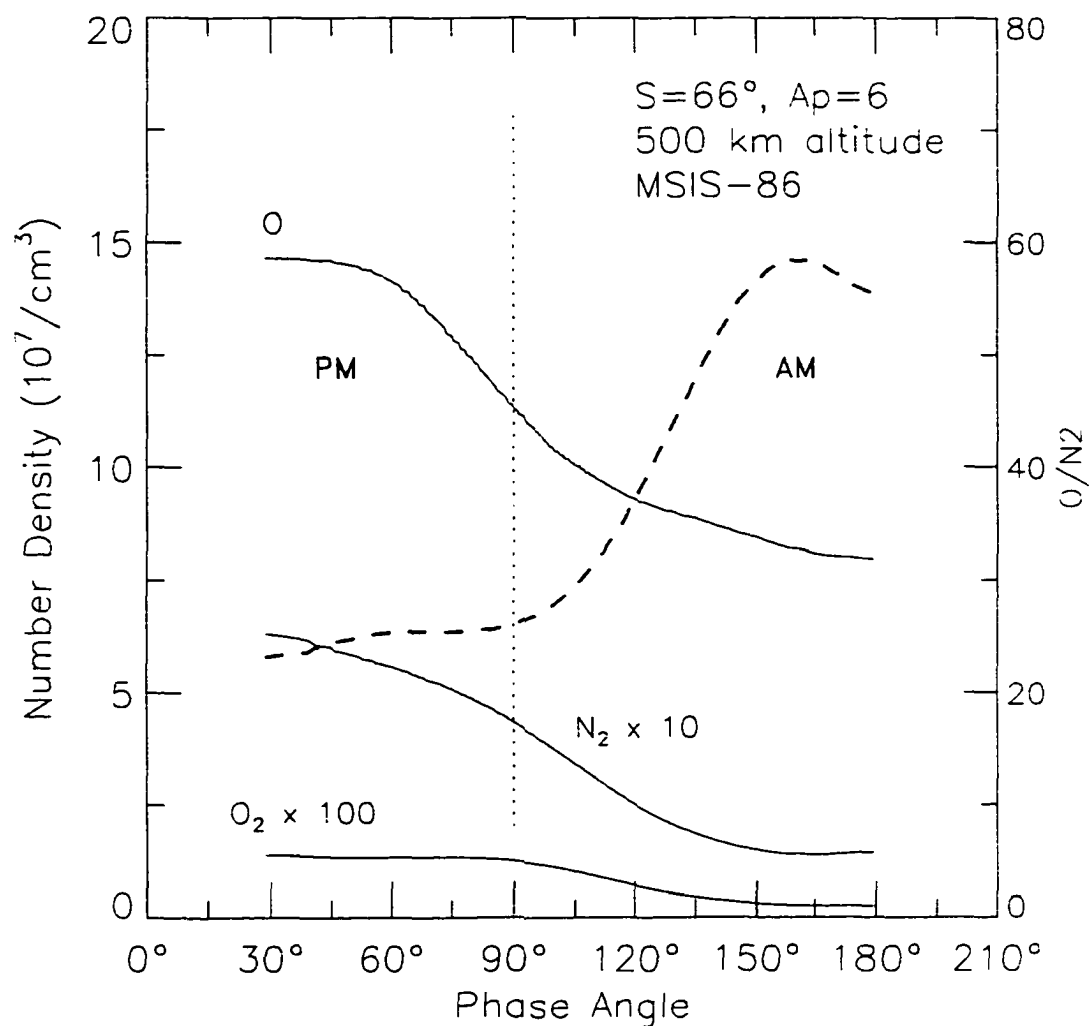


Figure 3-8. Plot of MSIS-86 number densities for fixed altitude and geographic position, and low geomagnetic activity for a range of local times. This simulates the diurnal variations at altitude in O, N<sub>2</sub>, and O<sub>2</sub> that may be viewed as a phase dependence in  $\langle r \rangle$ .

density at 500 km is markedly greater in the afternoon sector at this altitude, while the ratio of O to N<sub>2</sub>, represented with a dashed line, decreases. The importance of O/N<sub>2</sub> at this altitude to the FUV brightness problem is probably very small. However, the trend in the O densities seems similar to variations in  $\langle r \rangle$  with P.

To further investigate the relation between thermospheric composition and dayglow brightness, an analysis which compares average neutral densities (calculated with MSIS) to average photometer response is performed. The densities of O and N<sub>2</sub> are calculated at altitudes 200 and 500 km using the correct MSIS inputs for locations given by all pixels in the 156 images used in the quiet-time response model. These altitudes are selected to (1) investigate the high altitude composition where the OI dayglow is unaffected by N<sub>2</sub> (500 km) and (2) investigate densities at altitudes where N<sub>2</sub> may have an effect on the FUV OI dayglow and where O presents a good proxy for column densities (200 km). The average neutral densities  $\langle O \rangle$  and  $\langle N_2 \rangle$  are calculated at each of these fixed altitudes as a function of S and P, by replacing the observed count rates in the 156 images with corresponding number densities. This allows for direct comparison of composition variations to the  $\langle r \rangle$  vs. P dependence shown for all S in Figure 3-7b. The correlation between composition and photometer response as a function of P is determined for each 3° bin of S at these two altitudes. Results indicate that during quiet times, the observed brightness varies most closely with the O density at 500 km altitude, with a correlation factor of .98 (see Appendix B) between the two data sets at S=66°, for example. The average correlations of  $\langle r \rangle$  to  $\langle O \rangle$  and  $\langle O/N_2 \rangle$  over all values of S=0–105° at this altitude are 0.47 and –0.37 respectively, indicating a fair overall correlation of photometer response with O density. Furthermore, a weak anti-correlation between the response and  $\langle O/N_2 \rangle$  is revealed.

MSIS results for 200 km, where N<sub>2</sub> number densities are much closer to those of O, indicate a different relationship. At this altitude, where density variations more closely reflect the variation in total column density, the correlation of  $\langle r \rangle$  with O at S=66° is

only .37. whereas the correlation of  $\langle r \rangle$  with the  $\langle O/N_2 \rangle$  ratio is .47. The average correlations over all S between the average count rate,  $\langle r \rangle$ , and values of  $\langle O \rangle$  and  $\langle O/N_2 \rangle$  are -0.10 and 0.26, respectively, indicating a closer relation between  $\langle r \rangle$  and  $\langle O/N_2 \rangle$  at this altitude than at 500 km. This correlation is clearly quite low

In all cases, the percent variations in  $\langle r \rangle$  with P at fixed S are less than the variations in O. For example,  $\langle r(S=66^\circ) \rangle$  has high and low values of 48.1 and 34.6 counts/pixel at  $P=45^\circ$  and  $P=195^\circ$ , respectively, corresponding to a decrease of 28%. Again utilizing MSIS to provide quiet time values, decreases in  $\langle O \rangle$  densities of 31% and 55% are observed at 500 and 200 km, respectively. The high and low values of  $\langle O \rangle$  concentration at 500km are at  $P=60^\circ$  and  $195^\circ$ , respectively, which is reflected in the high correlation of  $\langle O \rangle$  and  $\langle r \rangle$  described above. The lower correlation of  $\langle O \rangle$  with  $\langle r \rangle$  at 200 km is reflected in the much closer proximity of high and low values of  $\langle O \rangle$  at  $P=135^\circ$  and  $195^\circ$ , respectively.

These calculations suggest that the photometer's response is representative of O density at the higher altitudes. However the  $O/N_2$  ratio at altitudes where photo-electron excitation dominates show a weak correlation with the observed variations in average photometer response. That no strong correlation with either parameter was revealed in this analysis indicates that the counting rate is controlled by no single parameter. Rather, it is influenced by both high altitude O density and by lower-thermospheric  $O/N_2$  ratio. Variations in total column density are well represented by variations in O densities at lower altitudes, and by this analysis, are not shown to correlate strongly with variations in the OI quiet time dayglow brightness.

### 3.3.3 Dependence on Solar 10.7-cm Radio Emission

Brightness of the FUV oxygen dayglow is directly related to the intensities of the solar EUV and FUV fluxes. An increase in the solar FUV component results in an increase of the resonantly scattered OI 130.4-nm dayglow emission. Furthermore, an

increase in related solar EUV emissions [Hinteregger, 1981; Lean, 1987] increases the secondary electron flux in the thermosphere, which in turn increases the intensity of the collisionally excited portion of the OI 130.4-nm dayglow. It is expected therefore that the photometer's response, for a given observational geometry, will also be closely related to the values of the solar EUV and FUV fluxes. Measurements of the full solar UV spectrum were not made throughout the time of the quiet-time observations, so as a proxy for measurements of ultraviolet solar emissions we utilize the 10.7-cm solar radio flux. A long-term correlation between the intensity of the solar FUV and EUV emissions and the intensity of the 10.7-cm solar radio flux has been established [Hedin, 1984; Barth *et al.*, 1990].

The quiet-time images are averaged in  $3^\circ$  bins of S and are ordered by the discrete value of the 10.7-cm solar flux (hereafter denoted simply by F) obtained at local noon in Ottawa on that day (1700 UT). It has been determined, but not shown here, that the variation in  $\langle r \rangle$  with F is similar at all D. The values of F in the quiet-time set range from 127.5 Jy on January 13, 1982, to 296.5 Jy on October 18, 1981, and are different on each day of the quiet-time observations. The average brightness in the  $S=66^\circ-69^\circ$  bin is shown as a function of F in Figure 3-9a where the ten points correspond to ten days from the quiet-time set. A linear least squares fit, weighted by the inverse of the variance of  $\langle r(S,F) \rangle$ , is shown as a solid line. Note that the positive slope indicates an increase in photometer response with increasing F, which is the expected relationship.

Expanding this result to include all S, a linear fit is obtained whenever three or more values of F are included in a given bin of S. The value of the slope from each of these fits is shown as a single point in Figure 3-9b, with the range of uncertainty in these values shown above and below these points using thin solid lines. This range lies almost entirely above zero. The effect of variations in solar flux is now evident at all solar zenith angles. A fit of the form  $((1-\tanh(S/a-b))/c)^d$  is provided, where the coefficients a, b, c, and d are determined iteratively to be 21.46, 3.030, 6.519 and 1.361, respectively.

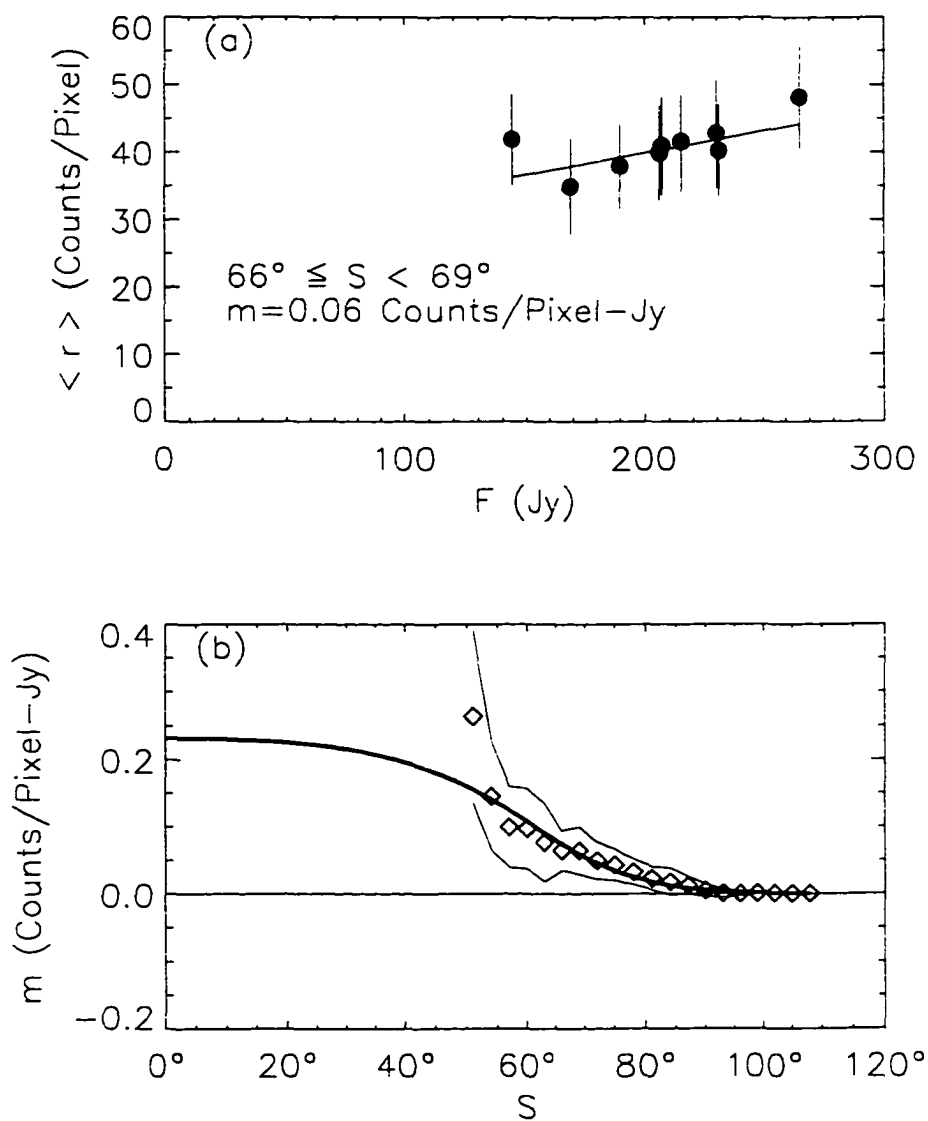


Figure 3-9. Dependence of  $\langle r \rangle$  on  $F$ . (a) Plot of  $\langle r \rangle$  vs.  $F$  at  $66^\circ \leq S < 69^\circ$  for ten quiet-time days with separate values of  $F$ . Average counts in are indicated with open circles. A least-squares fitted linear function is fit is overlain and the value of the slope,  $m$ , is shown in the figure. (b) The values of  $m$  for all  $S$ , where  $m$  is indicated with open diamonds. The uncertainty in the value of  $m$  is indicated with solid lines above and below the values of  $m$ . An iterative fit using a function of the form  $((1 - \tanh(S/a - b))/c)^d$  is performed. The resulting smoothly varying curve is plotted over the values of  $m$ .

The resultant curve is shown in Figure 3-9b as a heavy solid line. This fit provides a statistically valid, smoothly varying approximation to the slopes for all  $S$  observed in the quiet-time set. Furthermore, it provides an estimate of the slopes at smaller values of  $S$  not observed in this quiet-time set, but which may be observed later in other DE-1 images and the fit then tested. Images are corrected to  $F=200$  Jy using the values resulting from the fit at all  $S$ . It should be stated that the coefficients for the fitted function, described above, are preliminary and that definitive values are given in the next section.

#### 3.3.4 Iterative Technique for Separating Dependences

The parameters  $A$ ,  $P$  and  $F$  have been shown to influence the photometer's response to dayglow brightness at fixed values of  $S$  and  $D$ . It is necessary to make corrections so that variations in brightness over the entire observed disk region may be reduced to variations in  $S$  and  $D$  only. Modeling of Earth's FUV dayglow as a function of these two angles can then be performed. The results of preliminary analyses shown in Figures 3-5, 3-7, and 3-9 may be used to correct images to fixed values of each parameter. However, since the parameters  $A$ ,  $P$  and  $F$  were initially examined separately, the analysis of one parameter may be compromised by effects of the other two parameters. In an attempt to separate these dependences, an iterative technique is developed under the assumption that the effects of these parameters are independent, and therefore separable. It is clear that this is not entirely true with regard to the probable small change in the azimuth angle dependence with phase angle, for example, but the data from 156 images provides insufficient coverage to fully characterize all the dependences of dayglow brightness simultaneously. Furthermore, the effects of variations in the angle parameters are on the order of only 10% of the brightness for most solar zenith angles. A variation in the response that depends on the product  $A \cdot P$ , for example, would presumably have even less of an effect over the sunlit disk.

The dependences on the three parameters  $F$ ,  $P$ , and  $A$  are calculated in the following manner. First, the initial dependence of  $\langle r \rangle$  on  $F$  is taken to be that described previously and all quiet-time images are corrected to  $F=200$  Jy. Second, the initial dependence of  $\langle r(F=200 \text{ Jy}) \rangle$  on  $P$  is found and all quiet-time images are normalized to  $P=90^\circ$ ,  $F=200$  Jy. Third, the dependence of  $\langle r(F=200 \text{ Jy}, P=90^\circ) \rangle$  on  $A$  is found and all images are corrected to  $A=90^\circ$ . Images are normalized to  $P=90^\circ$  before azimuth corrections are determined since symmetry in the  $\tau=1$  surface ( $A$  dependence) across the Sun-Earth-DE plane is assumed.

In the second iteration, the corrections for  $A$  and  $P$  alone are applied to quiet-time images in order to determine an  $A$ - and  $P$ -corrected  $F$  dependence that is superior to that obtained in the first iteration. This is repeated until each dependence changes insignificantly between iterations; i.e., values of  $i$ -th iteration are all within the range of uncertainty of values from the previous iteration. The analysis shows that the  $A$  and  $P$  dependences determined in the third iteration do not differ significantly from the results of the second iteration anywhere in the observed range of  $S$ . The  $F$  dependence determined in the fourth iteration is similar to that found in the third. The values of  $m$  determined in each iteration for  $F$ ,  $P$ , and  $A$  are shown in Figures 3-10a, 3-10b and 3-10c, respectively, and no error bars are included. The solid line in each plot corresponds to the values used to normalize images to fixed values of  $F$ ,  $P$  and  $A$  at all  $S$ . Corrections for  $A$  are only shown for  $50^\circ \leq D < 55^\circ$ . The final coefficients of the fits to the  $F$  and  $P$  slopes are reported in Appendix A, as well as the final values for the  $A$  slopes, described earlier.

### 3.3.5 Dependence on Solar and Satellite Zenith Angles

The mean photometer response  $\langle r \rangle$  is determined as a function of  $S$  and  $D$  only after scaling the value of each disk-region pixel to  $A=90^\circ$ ,  $P=90^\circ$  and  $F=200$  Jy. The corrected images are binned in increments  $\Delta S=1^\circ$  and  $\Delta D=6^\circ$ . The smaller bin size for  $S$

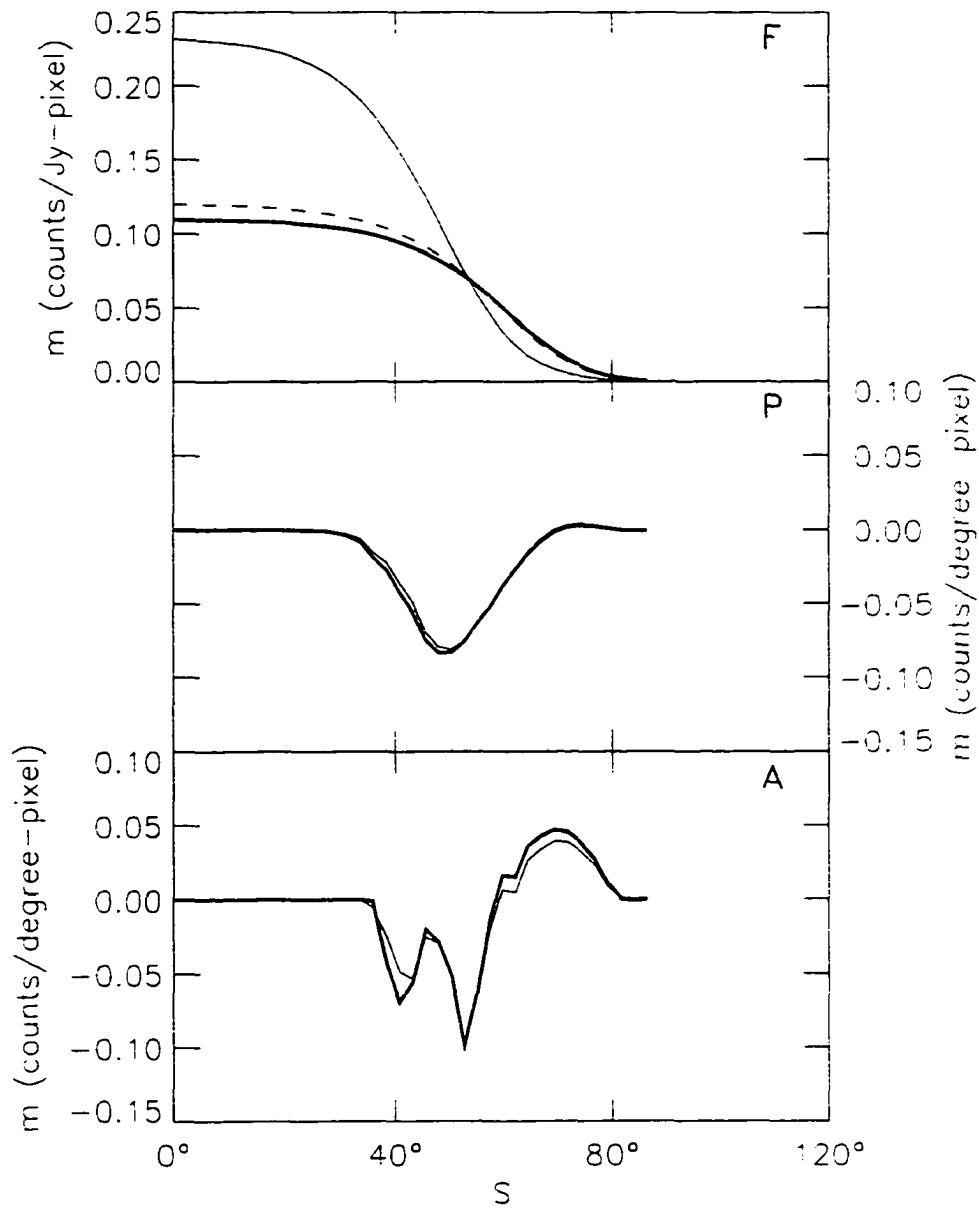


Figure 3-10. Summary of dependence of  $\langle r \rangle$  on F, P, and A. Iteratively determined fits to slopes of F and P dependences of  $\langle r \rangle$  and iteratively determined slopes of A dependence at all S. In all cases the heavy line indicates final values. (a) Fit to slope of  $\langle r \rangle$  vs. F. (b) Fit to slope of  $\langle r \rangle$  vs. P. (c) Slope of  $\langle r \rangle$  vs. A at  $50^\circ \leq D < 55^\circ$ .

is needed to characterize the more rapid variations in brightness with  $S$ , as compared to the weak linear dependence on  $D$ . The mean photometer response  $\langle r \rangle$  is then computed for the contents of each bin. Values of  $\langle r \rangle$  thus obtained are summarized in the 3-D projection of Figure 3-11 as functions of  $S$  and  $D$ . The ranges of  $S$  and  $D$  for available measurements were summarized in Figure 3-4 for two examples at fixed  $A$  and are typical of the other angles.

It is useful to select a well-behaved function to represent the values of  $\langle r \rangle$  so that it can provide a reliable extrapolation of the photometer's response at values of  $S$  and  $D$  not available in the original quiet-time data set, but which do exist in other images obtained in the mission. For example, a least-squares fit to the data with a polynomial function of  $S$  and  $D$  results in values that closely match the data for a large range of  $S$  and  $D$  sampled [Nicholas, 1997]. Such a function does not fit the data over the entire observed range of  $S$  and  $D$ , however, and rapidly departs from a realistic representation of the photometer response at  $S$  and  $D$  outside the domain of the quiet-time observations. The use of a trigonometric function of the form  $\langle r \rangle = B \cdot \cos^n(S)$  results in a better fit to the data at fixed  $D$  and is well-behaved at low values of  $S$ . A linear least-squares fit of  $\ln \langle r \rangle$  as a function of  $\ln \cos(S)$  then yields the coefficients  $\ln(B)$  and  $n$ . Through several trials it has been found that this function provides a good fit to the data for  $S < 80^\circ$ . A separate treatment is required for greater  $S$ , as an attempt to fit the trigonometric function for greater zenith angles results in increasingly large deviations of the fit from the data at  $S > 60^\circ$ .

The trigonometric fit to  $\langle r \rangle$  is carried out for  $S \leq 80^\circ$  in each  $6^\circ$  bin of  $D$  shown in Figure 3-11, resulting in coefficients  $\ln B$  and  $n$  for each bin of  $D$ . A linear function is then separately fit (least-squares, no weighting) to all the values of  $\ln B$  and  $n$  so that values of these coefficients that vary smoothly over the range of  $D$  are found. The smoothly varying coefficients for each bin of  $D$  are given here:

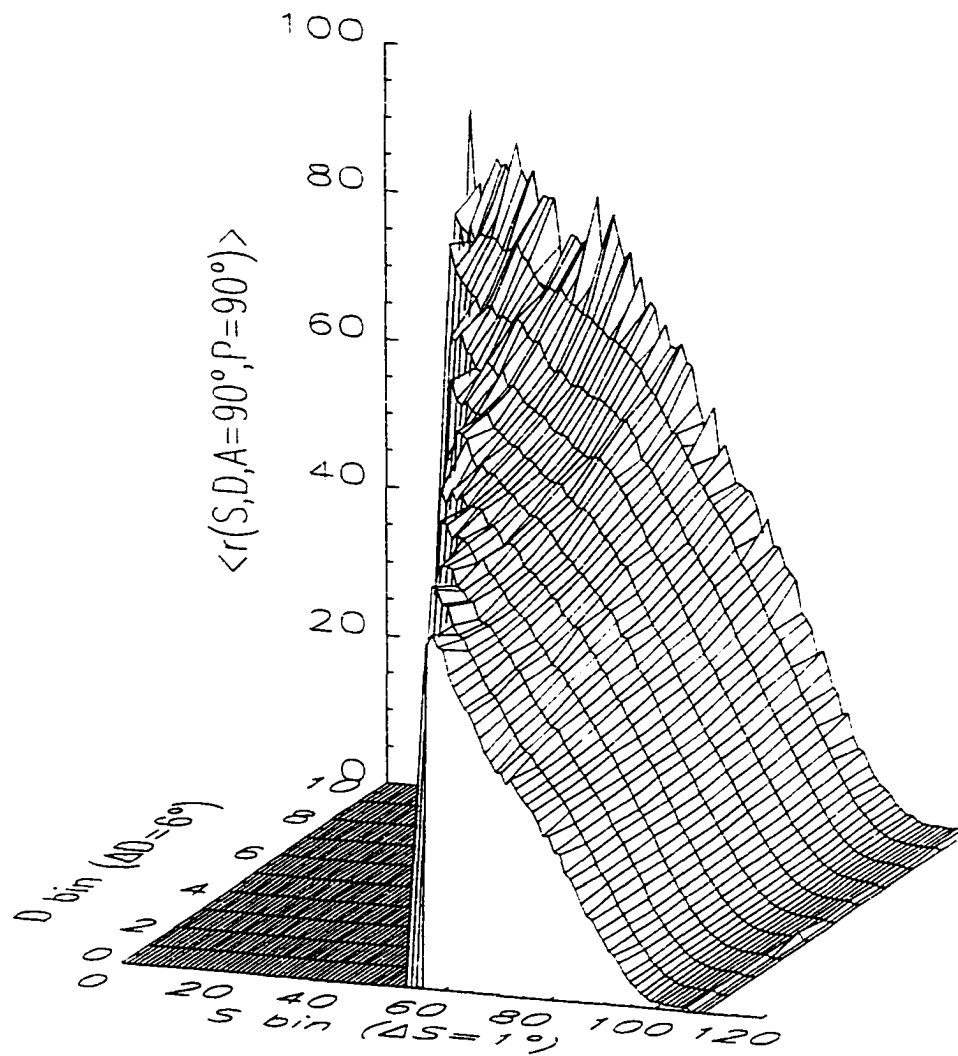


Figure 3-11. Average response  $\langle r \rangle$  of the DE-1 FUV photometer for the quiet-time data set for filter #2 (123–165 nm) for zenith angles  $S=0^\circ$ – $105^\circ$  and  $D=0^\circ$ – $65^\circ$ . The response in individual images is normalized to  $A=90^\circ$ ,  $P=90^\circ$  and  $F=200$  Jy.

$$\ln B = (4.32 \pm 0.04) + (0.002 \pm 0.001) \cdot D \quad (3.1)$$

$$n = (0.75 \pm 0.04) - (0.003 \pm 0.001) \cdot D \quad (3.2)$$

This provides for the calculation of  $\ln B$  and  $n$  at any  $D$ . The variation of each term with  $D$  is small but significant. This fit represents improvements to the model since the original fit used by Nicholas et al [1997] and shown in Figure 3 of that work.

No fit is performed for  $80^\circ < S \leq 105^\circ$ , as an appropriate function was not determined. Instead a table is constructed of values of  $\langle r \rangle$  in increments  $\Delta S = 1^\circ$ ,  $\Delta D = 1^\circ$ . A  $3^\circ \times 3^\circ$  boxcar averaging technique is applied to smooth the data, after empty bins are replaced with interpolated values. The edges of the average data array ( $D = 0^\circ$ ,  $65^\circ$  and  $S = 105^\circ$ ) are smoothed by simply averaging over all neighboring bins. Using these data instead of a fitted function reduces the large percent deviations that occur when a function such as a quadratic is fit to data that ranges from 10 counts ( $S = 80^\circ$ ) to fractional counts ( $S = 105^\circ$ ). Such a function tends to show large percent deviations from the fitted data at low counts.

A 3-D projection of the reference values  $\langle r \rangle'$  calculated from these two methods is shown in Figure 3-12 for  $S = 0^\circ - 105^\circ$  and  $D = 0^\circ - 65^\circ$ . The trigonometric fit and smoothed tabular data meet at  $S = 80^\circ$ . A final  $5^\circ \times 5^\circ$  boxcar averaging is performed in the overlap region  $S = 75^\circ - 85^\circ$  for all  $D$  with smoothing at the array edge performed as described previously. This smoothes slight discontinuities between the trigonometric function and smoothed values of the data.

A quantitative comparison of the original quiet-time observations (in  $1^\circ \times 1^\circ$  bins) and the reference values of Figure 3-12 is obtained by computing the percent deviations of the data from the reference values:

$$PD = 100 \cdot (\text{data} - \text{reference value}) / \text{reference value}.$$

Four examples are presented in Figure 3-13 for  $D = 10^\circ$ ,  $25^\circ$ ,  $40^\circ$  and  $55^\circ$  over the range of  $S$  in which measurements were obtained. It is clear that the reference values  $\langle r \rangle'$  provide an accurate representation of the measured response of the photometer to within

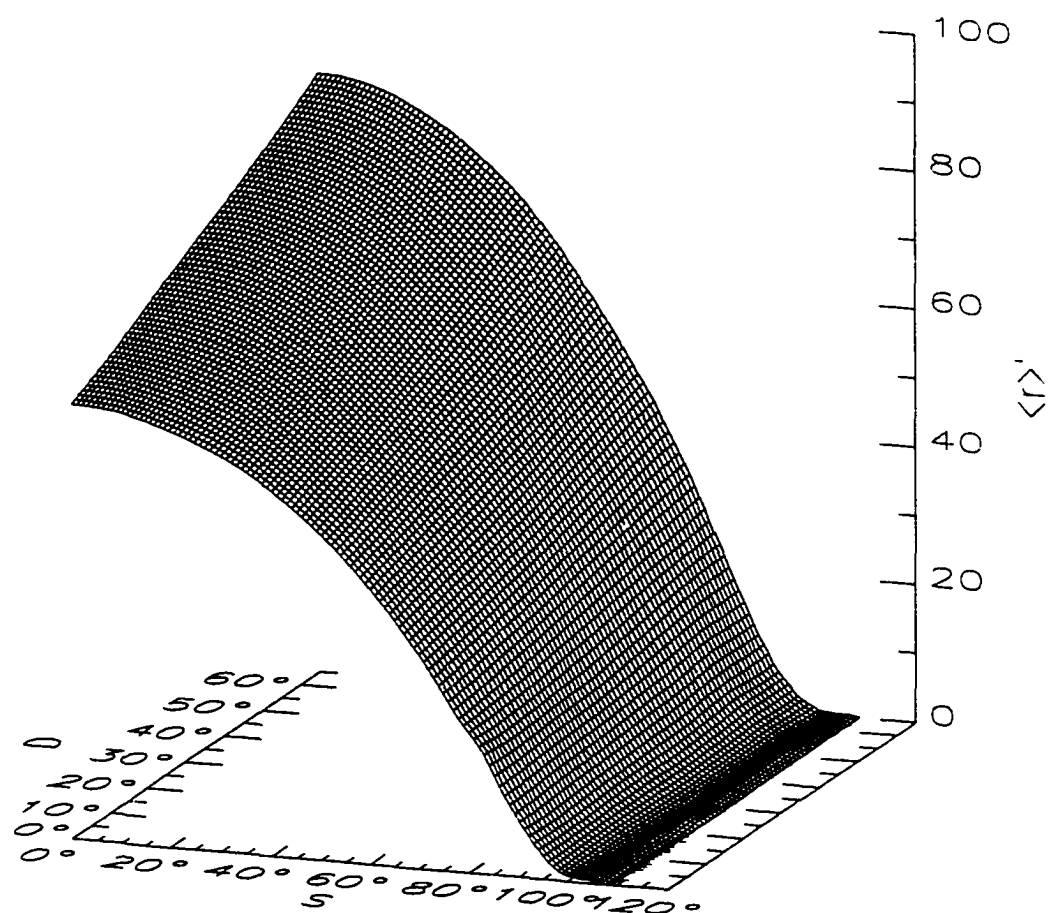


Figure 3-12. Calculated reference values  $\langle r \rangle'$  for the DE-1 FUV photometer response normalized to  $A=90^\circ$ ,  $P=90^\circ$ , and  $F=200$  Jy, using filter #2. The solar and satellite zenith angles are  $S=0^\circ-105^\circ$  and  $D=0^\circ-65^\circ$  respectively.

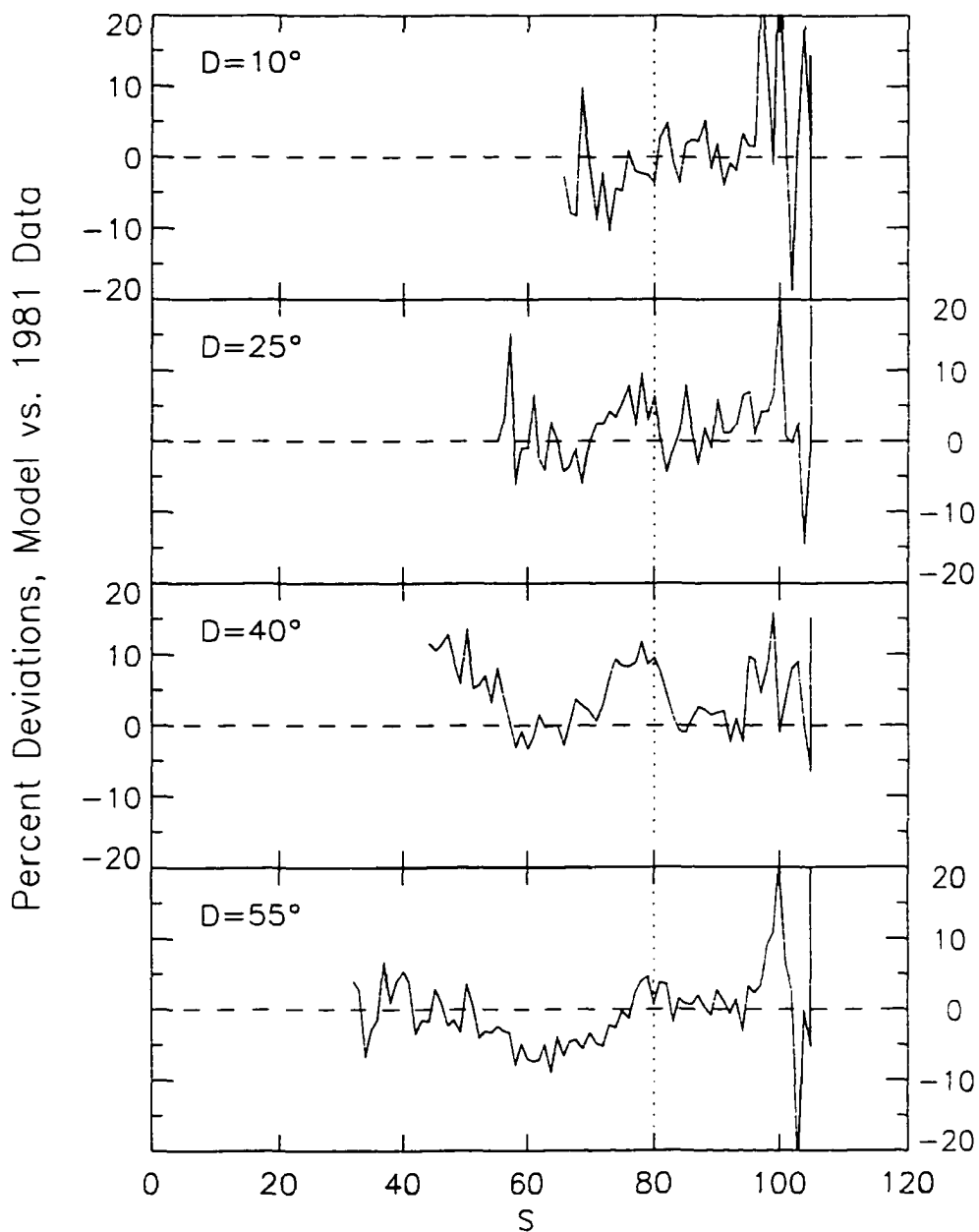


Figure 3-13. Percent deviations of the average response  $\langle r \rangle$  (Figure 3-11) from the reference values  $\langle r \rangle'$  (Figure 3-12) for all  $S$  and four values of  $D$ : (a)  $D=10^\circ$ , (b)  $D=25^\circ$ , (c)  $D=40^\circ$  and (d)  $D=55^\circ$ .

~10% for all D at  $S < 95-100^\circ$ , as no larger percent deviations are apparent at these or other values of D.

A first application of the resulting reference response values is provided by creating a model image of the disk and auroral regions in the format of a standard image, such as that presented in Figure 3-1. The limb region is deleted and the observed values for the photometer's response in the disk and auroral regions are replaced by the computed reference values. This is done pixel by pixel for each pixel's individual values of S, D and A. The resulting "image",  $I_r$ , is presented in Figure 3-14, where the response has been converted to brightness as coded by the color bar to the right using the conversion 3.08 counts/kR-pixel, and can be compared directly with the inner regions (disk) of Figure 3-1. In preparation for use as an analysis tool, the DE-1 image of Figure 3-1 is smoothed using a 5x5 pixel boxcar average to reduce statistical variations. We refer to this image as  $I_o$  and present it in Figure 3-15a where the brightness is color coded by the bar in the center of the figure using numerical values to the left of the bar. Weak auroral emissions at the lower right in the image are difficult to detect in the figure. To demonstrate how the reference image in Figure 3-14 compares quantitatively with  $I_o$ , the percentage deviation of  $I_o$  from  $I_r$  is constructed in Figure 3-15b, and coded using a color table representing PD values listed to the right of the color bar. In this format, the auroral emissions are very prominent, as the auroral "contamination" represents a ~60% increase in brightness from the quiet-time dayglow. At lower latitudes the disk region displays local variations on the order of ~10%.

### 3.4 Series of Images, Quiet

As part of DE-1 imaging operations on October 18, 1981 (day 291), a series of images were obtained with the FUV imager using the 123-165 nm passband filter (#2), 14 of which are presented here. This took place during a period of low geomagnetic activity, and the images obtained were included in the original 185 quiet-time images, but not as part of the data set used here to derive the model. The reasons for excluding

Figure 3-14. Reference image  $I_r$  constructed from the original image of 1725 UT on October 18, 1981, shown in Figure 1. This image is constructed by replacing, pixel by pixel, the original photometer response by that derived from the reference values for the corresponding S,D, and A, which are applicable only to the disk region of the original image. The color bar to the right of the image gives reference brightness values in kiloRayleighs.

Model Dayglow for Day 291 Image

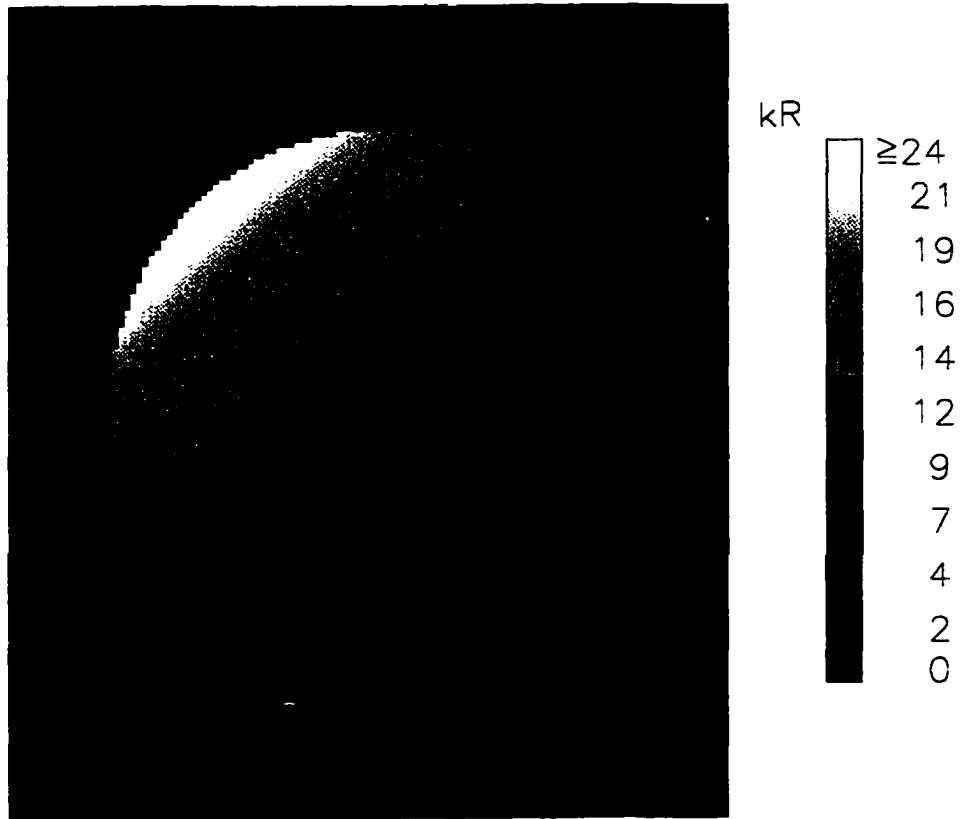
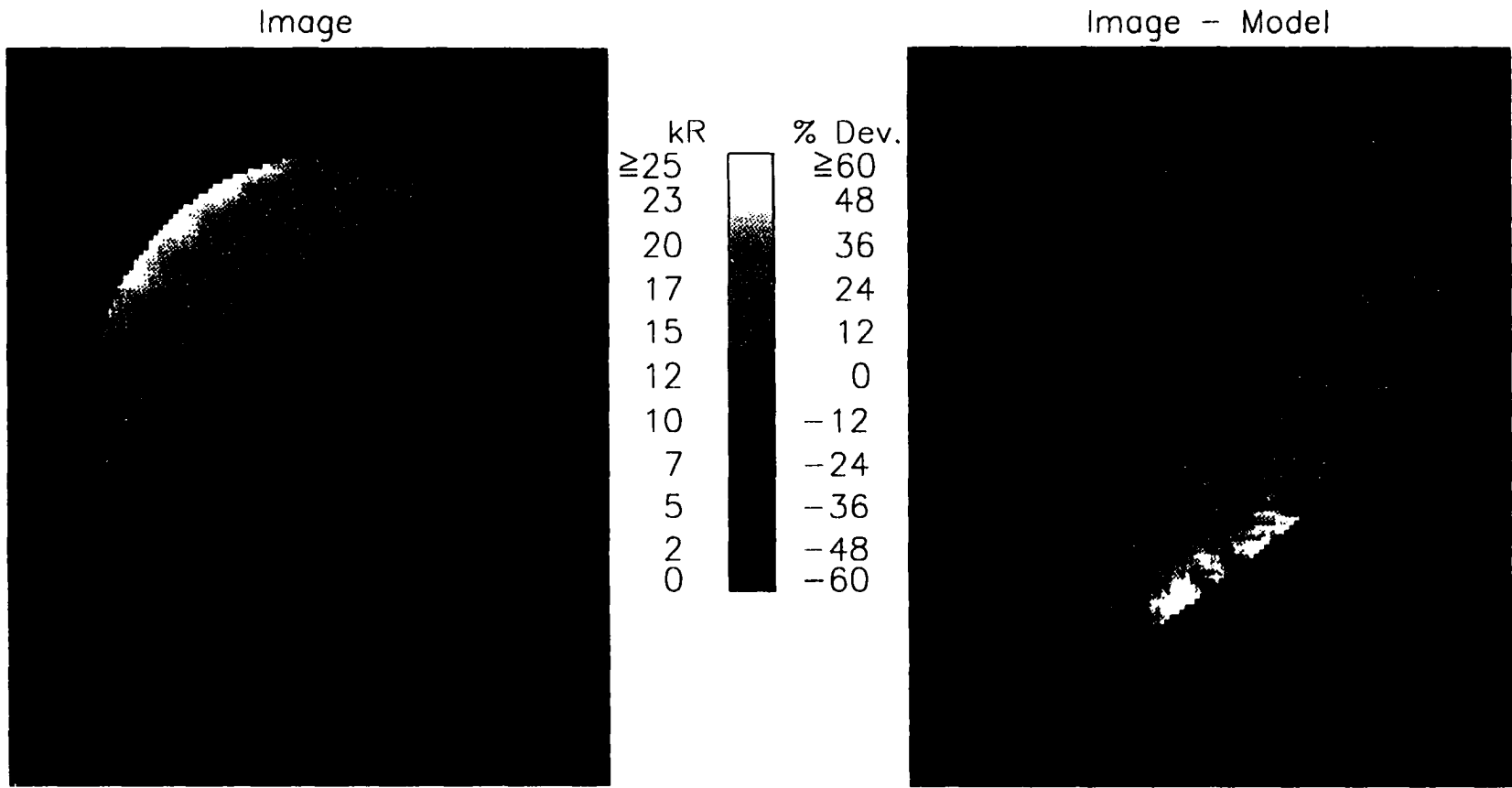


Figure 3-15. Comparison of dayglow image to model. (a) Image obtained on October 18, 1981 at 1725 UT, but with the limb region removed and smoothed using a 5x5 pixel boxcar technique. The color bar is coded on its left side with the measured brightness in kR. (b) Percent difference image, PD, showing deviations of the measured brightness in the original image  $I_0$  from the reference image  $I_r$ . A contour describing regions of brightness 20% below reference values indicates only small areas near the terminator. The color bar is coded on its right side with the percent deviation range of  $\pm 60\%$  .

Oct. 18, 1981 (Day 291), 1725:46 UT

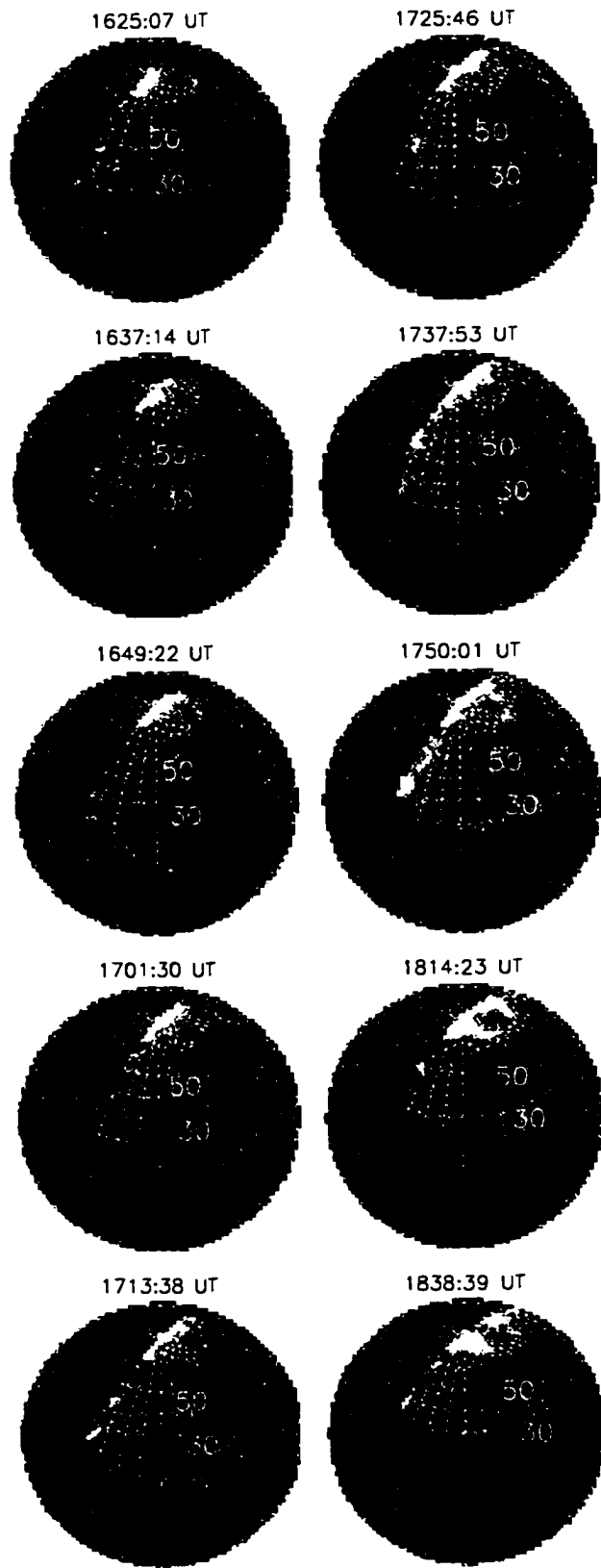
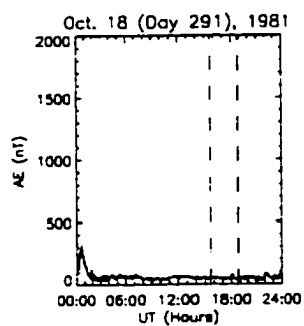


these images in the final set will be described later in this section. The images presented in this section were taken from altitudes ranging from  $\sim 1.3 R_e$  just after perigee to  $3.65 R_e$  at apogee, an altitude which is reached at  $\sim 1815$  UT during the twelfth image. The time to obtain these 14 images was  $\sim 3.0$  hours. During this sequence, the angles S, D and P and A change dramatically at each geographical location: D varies from  $0^\circ$  to  $65^\circ$  for some pixels and S changes by up to  $45^\circ$  (largest variation at equatorward pixels). The solar flux at 1700 UT is 296.5 Jy, the highest of all quiet-time image days.

To examine a series of images with changing viewing geometries, it is useful to project them onto a grid of geographic coordinates that clearly shows the morning sector, auroral zone and terminator. The 14 PD images are shown in Figure 3-16, each mapped to an orthographic grid with the time of the first scan listed above each mapping. A one-to-one mapping of pixels from a PD image to their geographic position on the projection is performed for all pixels in the disk region. Knowing the coordinates at the center of each pixel, the dimension of each pixel is determined using a nearest-neighbors scheme. The orientation of Earth in each projection is such that the center of the coordinate grid corresponds to a fixed local solar time (1000 LST), effectively fixing the position of the terminator for this series.

The AE indices for October 18, 1981, are shown in the upper-left-hand panel of Figure 3-16. AE is  $< 100$  nT for nearly the entire day, indicating that the level of geomagnetic activity is quite low. The first image, taken at 1536 UT from an altitude of  $1.3 R_e$ , is shown below the AE indices. In the 12 minutes required to obtain this image, the photometer's field of view progressed toward the morning terminator (right to left in mapped image) as the imager scanned from low to high latitudes and the satellite altitude increased to  $1.7 R_e$ . The center of this image is at geographic coordinates of  $40^\circ\text{N}$ ,  $243^\circ\text{E}$ . For each subsequent image the longitude of the center of the mapping decreases by  $3^\circ$ , corresponding to the rotation of Earth between consecutive 12 minute images. In this way, the local solar time of an observer is held constant and variations of

Figure 3-16. Series of 14 images taken by DE 1 on October 18, 1981 between 1536 and 1838 UT. Images are shown using an orthographic projection of geographic coordinates, with the center of the first projection at 40°N and 243°E. Constant local solar time is maintained through the sequence by decreasing the longitude in the center of the projection by 15° per hour of time elapsed from the beginning of the imaging series (3° per successive 12 minute image).



the dayglow are more easily discriminated from changes in viewing geometry. The satellite's motion to higher latitudes is evident in the changing image field of view, of which only the disk region pixels are shown. By the time of the third image (1600 UT), the disk region includes part of the terminator. Note also that the image field of view covers a significantly larger portion of the sunlit Earth in the images that follow as the satellite moves to higher altitudes. Near the time of the last image, taken at 1838 UT, the imager provides less observational coverage of dayglow emissions at subauroral latitudes (than images taken earlier) as the satellite begins to descend in altitude over the nightside. Note the signature of the aurora in the polar region.

An analysis of this series of images is used to demonstrate that the photometer's response is independent of observing altitude. To do this the percent differences are calculated between the number of counts for each disk-region pixel in the original images and the corresponding reference values at the same S, D, and A. The number of pixels is then counted for each 1% increment of PD values from -100% to +100%. Pixels at auroral latitudes (geomagnetic latitude  $> 65^\circ$ ) are excluded. The results are plotted as histograms where, for example, the result for the first image taken at 1536 UT is shown in Figure 3-17a. The number of samples in each bin is plotted as a function of the percent difference. Each data point is represented by an open diamond and the result of a gaussian least-squares fit by a smooth line. Parameters of the fit include a peak in the distribution of PD values ( $PD_{MAX}$ ) at -8.9%, with a full-width-at-half-maximum (FWHM) of 29.0% (FWHM =  $2.35 \cdot \sigma$ ). The peak in the percent difference histogram will be referred to as  $PD_{MAX}$ .

Similar gaussian fits are calculated for the other 13 images in the series and values of  $PD_{MAX}$  are presented in Figure 3-17b for all 14 images (open diamonds) along with the results of a linear least-squares fit. This fit shows a small increase in the average overall response of the photometer with respect to modeled values. The value of  $PD_{MAX}$  ranges from -8.9% to -2.5% over the series of images while the FWHM of the distributions ranges from 29.4% to 38.2%. The larger width values are calculated for later images and

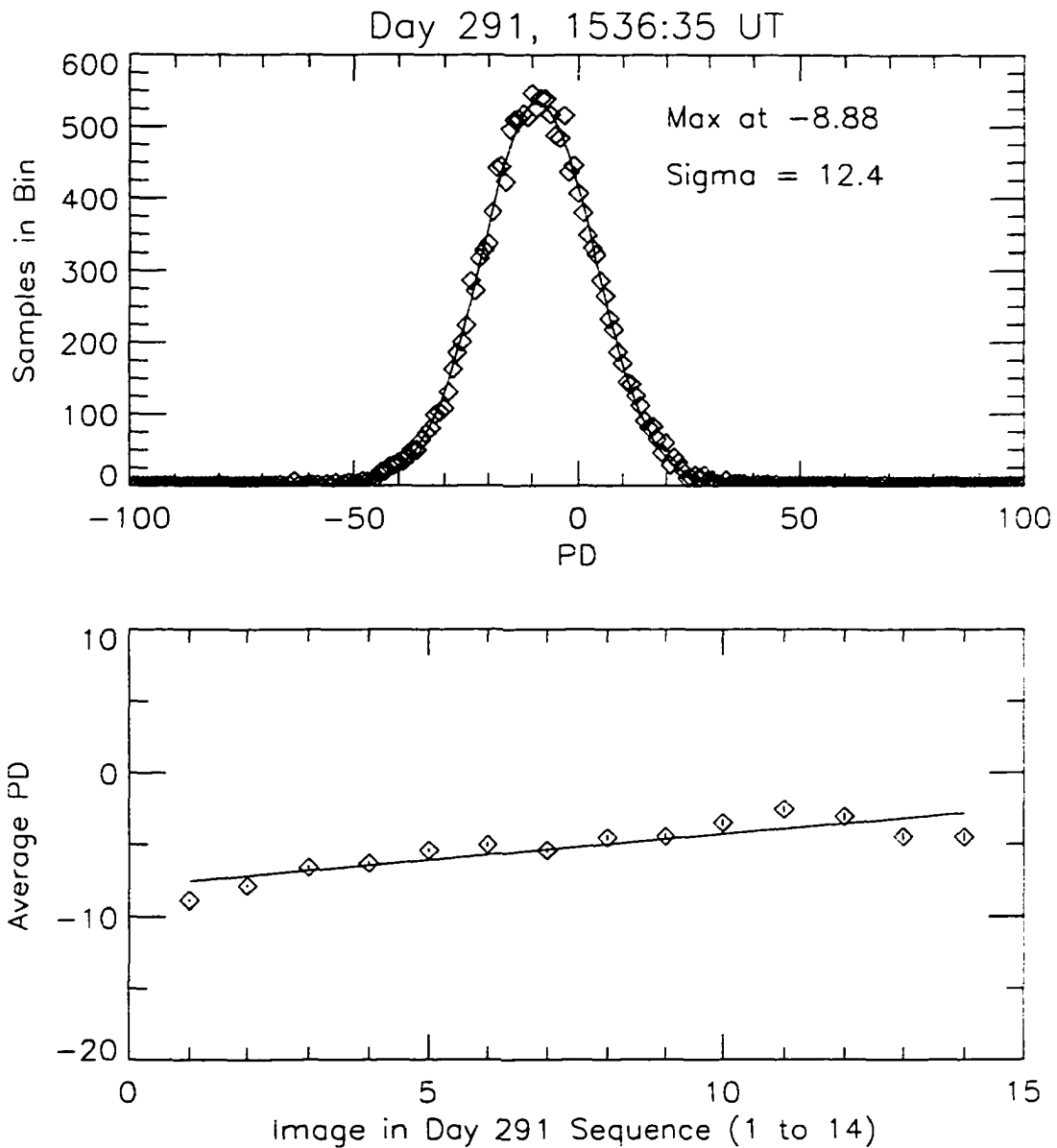


Figure 3-17. Statistical distribution of PD values in images from day 291. (a) Frequency of percent differences of photometer response from reference values for all disk-region pixels in the image of 1536 UT on October 18, 1981. The most frequently observed percent difference value is found by fitting a gaussian function (solid line) which peaks at the most probable value of the PD image. (b) Most probable value of percent deviation distribution for the 14 images in the series of Figure 14.

are possibly due to larger percent deviations observed at or near the terminator, an area which is not imaged extensively until ~1625 UT.

The approximately gaussian distribution of the percent differences can be simulated by imposing counting statistics on the calculated reference image  $I_r$  to create a noisy image. The counting statistics are assumed to reflect a normal distribution, with Poisson statistics applied for rates less than 10 counts/pixel and a gaussian distribution used to approximate Poisson statistics at greater rates. This is done by constructing a large integer array for each count rate, where elements are assigned values at or distributed about the reference response. The frequency with which a value appears (say 8 counts/pixel for an initial rate of 10 counts/pixel) is determined using statistics of a normal distribution. A single element is then randomly selected as the noisy count rate for the pixel. A histogram of the percent deviations of the noisy synthetic response from the noiseless reference values, similar to that in Figure 3-17a for an actual image, is shown in Figure 3-18. The gaussian fit to this distribution is centered approximately at 0% with a FWHM of 26.6%. The corresponding width of the histogram for the real image was shown previously to be 29.0%.

The histograms for all of the 14 synthetic images indicate FWHM values ranging from 26.6% to 35.8% over the 14 image sequence, which is nearly identical to the values from the histograms derived from original images. Thus the variations in measured dayglow brightness for the quiet-time set may be attributed primarily to counting statistics inherent to the measuring instrument and viewing geometry. This demonstrates that the reference values for instrument response generated from quiet-time images provide a statistically valid and accurate measure of dayglow brightness.

There are several possible causes for the small variation in the value of  $PD_{MAX}$  over the orbit sequence. (1) The dayglow is actually brightening over the three hour imaging time; (2) An increase in the response due to increasing length of the optically thin  $H\ L\alpha$  column emission at 121.6 nm; and (3) The correction to  $\langle r \rangle$  to  $A=90^\circ$  or  $P=90^\circ$  at all disk-region pixels is insufficient, due to atmospheric conditions strongly affected by the

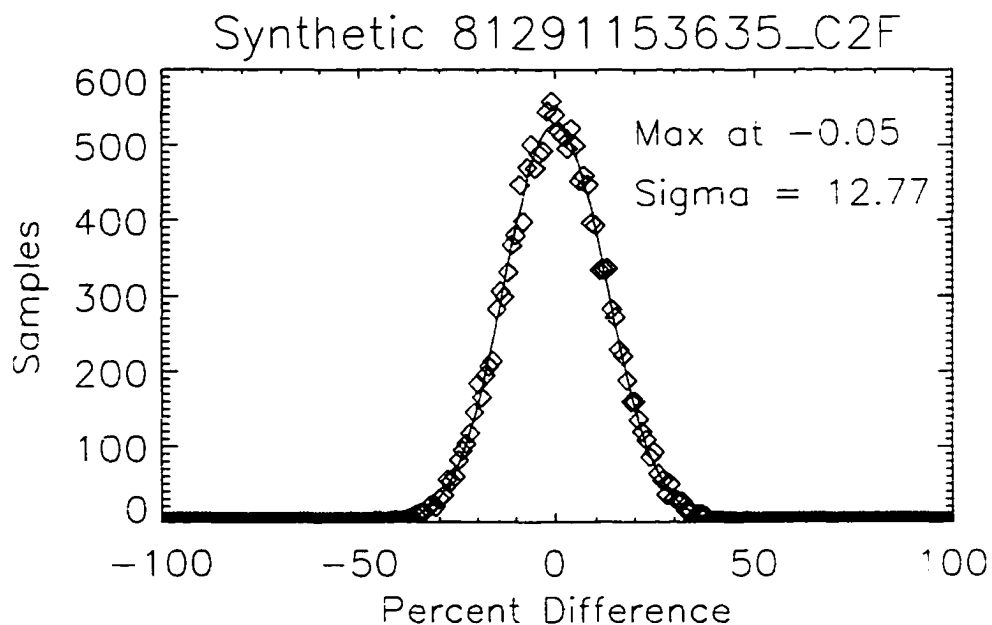


Figure 3-18. Histogram of percent deviation from reference values of pixels in a synthetic image,  $I_S$ . This is developed by determining a new response according to normal counting statistics for every pixel in the disk region of the reference image  $I_R$  shown in Figure 14. The resulting percent deviations from the original reference value of all pixels are binned in 1% increments. The frequency distribution is depicted here by open diamonds, and a gaussian fit is superposed (solid line).

high solar flux. Regarding the first point, only solar flare activity (or strong geomagnetic activity which is not the cause here) could influence the dayglow brightness on these short timescales. The ground-based H $\alpha$  solar flare observations [NOAA Solar-Geophysical Data, 1984], indicate a flare of importance 1N at 1546 UT. The importance is based a scale of 1 to 4 indicating size and qualifiers F.N.B indicating brightness. It is unlikely that the this minor solar flare activity can account for the  $\sim 8\%$  variation in the dayglow brightness.

The second possible explanation for the increase in  $PD_{MAX}$  with time in the imaging series is the increasing column of H which resonantly scatters solar H L $\alpha$  radiation. Confirmation of this effect is difficult in that the post-launch sensitivity of the 123 filter (#2) to this emission is known to decrease with time. An upper limit of  $\sim 13\%$  ( $S=60^\circ$ ,  $D=20^\circ$ ) for the contribution of H L $\alpha$  to the total count rate of is established by Craven *et al.* [1994], while Meier *et al.* [1995] argue that the contribution of L $\alpha$  is much smaller than this upper limit, as the instrument response for observations well off the limb is virtually zero. Rairden *et al.* [1986] presented DE-1 measurements of geocoronal H L $\alpha$  emissions, but their work concentrated on data obtained using the 117A and 120W filters, which more readily pass the short wavelength emissions. The portions of their work that are useful here are the measured and modeled brightness of the H L $\alpha$  emission in the nadir and the variation in the zenith brightness with altitude. Variations in H L $\alpha$  nadir brightness with altitude using the 120W filter were not measured, but may be estimated and compared with the variations observed here.

Rairden *et al.* give the spin-plane emission profile for H L $\alpha$  brightness, including values in the zenith and nadir directions. The observations in the nadir, however, most certainly include significant contributions from O and N $_2$  emissions, whereas zenith observations with the photometer pointed away from the Earth do not. At 1025 UT on September 28, 1981 (day 271), DE 1 is located at  $53^\circ N$ ,  $358^\circ E$  at an altitude of 2.67 Re. The solar zenith angle in the nadir direction is  $\sim 55^\circ$ , where the observed brightness of

the combined H, O, and N<sub>2</sub> is ~44 kR. Using an iterative radiative transfer code, Rairden *et al.* calculate that 10 kR is due to H L $\alpha$ : i.e., a fourth of the total on-disk response is due to H L $\alpha$ . Farther along in the orbit as the DE-1 altitude increases from 1.3 Re to 3.6 Re, the zenith brightness decreases by ~1 kR. Assuming that the emission is isotropic at these altitudes, one may infer that the apparent variation in H L $\alpha$  nadir brightness for fixed S and increase in altitude from 1.3 Re to 3.6 Re (similar to the increase on day 291) is ~+10%, the largest variation occurring at lower altitudes. If 13% of the 123W filtered photometer response were due to H L $\alpha$  emissions, the variation in PD<sub>MAX</sub> during the day 291 imaging series would be on the order of 1–2%, which is substantially lower than the observed change in PD<sub>MAX</sub>. It appears that the possible increase in H L $\alpha$  emissions with altitude does not explain the variation over the eleven image series.

To investigate the third possible explanation, the variation in  $\langle r \rangle$  with A over the day 291 imaging time may be examined, as was done in a previous section for the entire quiet-time set. In the absence of other influencing factors, this will provide an indicator of the correctness of the assumed  $\tau=1$  altitude, here 500 km. The azimuth dependence of  $\langle r \rangle$ , not shown here, is such that at *all* observed S (20° to 105°),  $\langle r \rangle$  decreases with increasing A. This result indicates that all S and D angles have been calculated at an assumed emission altitude which is too low, an interpretation that is not unreasonable in light of the high solar flux value of this and previous days. On October 13–17, the values of F increase from 256.2 Jy to 302.9 Jy, the maximum value for the 1980–1981 period. The extreme solar flux may have had a significant effect on thermospheric temperatures and scale heights. The model developed here does not account for variations in the dependence on A due to global changes in the  $\tau=1$  altitude with F.

In any event, these quiet-time images are not included in the quiet-time set as there is a systematic variation in the PD values with latitude. The decreases in brightness in the morning sector at mid-latitudes are of the order 10%. For similar reasons, images from days 266 and 267 also are excluded because large scale decreases as large as –30% are

observed in the afternoon sector. The earliest images to be included in the model are from day 304. That these images passed the quiet-time selection criteria but still exhibited significant dayglow decreases is of interest. In each case, some enhancement in magnetic activity was observed ~24 hours previous to imaging. These enhancements occurred during periods where the interplanetary field (IMF) had a strong and consistently negative y component ( $B_y$ ). It has been shown that positive  $B_y$  can speed the appearance of disturbed portions of the thermosphere on the dayside in the Northern Hemisphere [Immel *et al.*, 1997]. It is possible that negative  $B_y$  may delay the transport of heated air to the dayside, owing to the large difference in neutral circulation patterns in the auroral zone [McCormac *et al.*, 1985; Hernandez *et al.*, 1991]. However, the question of how the thermospheric disturbance is maintained for 24 hours without additional Joule heating input remains. The importance of these 'quiet but disturbed' images will be addressed in a later chapter of this thesis.

### 3.5 Summary

A method of calculating reference values for the response of the DE-1 imager to the quiet-time FUV dayglow in the 123–165 nm bandwidth (filter #2) has been developed. The response with this filter is due primarily to the 130.4- and 135.6-nm OI dayglow emissions. A total of 156 FUV images obtained during periods of geomagnetic quiescence ( $AE < 100$  nT for the preceding six hours) are selected and binned in solar and satellite zenith angles, S and D respectively, observational azimuth angle A and phase angle P, and sorted with respect to the solar 10.7-cm radio flux F. The average photometer response  $\langle r \rangle$  is determined as a function of A, P, and F, and all quiet-time images are corrected to  $A=90^\circ$ ,  $P=90^\circ$ ,  $F=200$  Jy. The photometer responses in the now normalized quiet-time data are binned in increments of  $\Delta S=1^\circ$  and  $\Delta D=6^\circ$  and reference values are created, as a function of S and D only, using a cosine functional form at  $S \leq 80^\circ$  and smoothed values of the response at  $S > 80^\circ$ . Images in the large FUV database (for filter #2) may be compared to these reference values once small corrections are

made for the A, P and F dependences. The comparison with quiet-time images verifies our assertion that the fitted values of the photometer response  $\langle r \rangle'$  are an accurate representation of the FUV brightness during periods of low activity.

The quiet-time reference values provide a baseline FUV brightness for investigation of large scale variations in dayglow brightness that are observed during periods of strong geomagnetic activity [Frank and Craven, 1988; Craven *et al.*, 1994; Immel *et al.*, 1997; Nicholas *et al.*, 1997]. With the refinements to the method detailed here (azimuth corrections, analysis of effective altitudes, phase and  $F_{107}$  corrections), it is anticipated that oxygen density variations associated with traveling ionospheric disturbances (TIDs) and planetary tides may eventually be identified in FUV images.

This method will prove useful in future analyses of the dayglow and may be applied to any large set of spectrally separated FUV data for which S, D, A, and P are known for each measurement. A broad range of instruments now constantly monitor the solar UV spectrum and the solar wind speed, density, and imbedded magnetic field. All of these factors have a direct or indirect effect on auroral intensity and thermospheric perturbations. Dayglow perturbations may be monitored globally with 50-100 km spatial and 1 minute temporal resolution for as many hours as spacecraft like POLAR are well away from perigee (~12 hour periods). Current investigations are well suited to the task of generating a large database amenable the type of analysis shown here for DE-1 images and of extracting new information about the transfer of energy from the Sun to Earth.

## Chapter 4

### Influence of IMF $B_y$ on Large-Scale Decreases of O Column Density at Middle Latitudes

#### 4.1 Introduction

Compositional variations in Earth's thermosphere indicated by changes in its FUV dayglow signature are most often the result of Joule heating in the auroral regions. In these regions, the motion of the neutral atmosphere is strongly influenced by magnetospheric convection, especially during geomagnetic disturbances. The magnetosphere is, in turn, strongly affected by the strength and orientation of the interplanetary magnetic field (IMF). The question of whether or not the orientation of the IMF has an influence on the development of thermospheric disturbances related to enhancements in geomagnetic activity is addressed in this chapter.

For periods of negative IMF  $B_z$ , the configuration of the high-latitude, two-cell convection pattern is affected by the sign and magnitude of  $B_y$ , while the cross-polar-cap potential is affected by the magnitude of  $B_z$ . This  $B_y$  effect on ion convection was first described by Heppner [1972], later by Heelis [1984], and more recently by Rhohonemi and Greenwald [1995]. From these and other works, we know that the Northern Hemisphere dusk (dawn) convection cell increases in size relative to its counterpart with increasingly positive (negative)  $B_y$ , and that the electric field strength is greater in the dusk (dawn) cell for  $B_y$  positive (negative) relative to the field in the cell's counterpart. The total cross-cap potential increases with increasing magnitude of negative  $B_z$ , as described by Reiff *et al.* [1981] and Doyle and Burke [1983]. The magnitude and configuration of the electric field have been empirically modeled as a function of IMF orientation by Heelis [1984] and Heppner and Maynard [1987], and more recently by Weimer [1994], Rich and Hairston [1994] and Rhohonemi and Greenwald [1996]. These studies have clearly demonstrated the strong influence of the IMF  $y$  and  $z$  components on electric fields and ion convection in the high-latitude regions.

These IMF components similarly influence the circulation of neutrals at high latitudes through collisional interactions between the convecting ions and local neutrals. McCormac *et al.* [1985], Thayer *et al.* [1987] and McCormac *et al.* [1991] have investigated the  $B_y$  dependence of the neutral circulation patterns using the neutral wind measurements taken during thousands of orbits of the low-altitude Dynamics Explorer 2 (DE-2) satellite. More recently, the IMF influence on polar cap neutral winds in the Northern Hemisphere has been described by Killeen *et al.* [1995] through studies involving ground-based Fabry-Perot interferometry. These studies have clearly demonstrated the enhancement observed in the size of the northern dusk (dawn) circulation cell and its increased neutral wind speeds with positive (negative)  $B_y$ , very similar to the  $B_y$  effect in the ion convection patterns. An earlier study by Hernandez *et al.* [1991] indicated a similar effect in the Southern Hemisphere, except that the dawn (dusk) cell is enhanced with positive (negative)  $B_y$ .

The  $B_y$  dependence has also been investigated with thermospheric models such as UCL's 3D-TD model [Rees *et al.*, 1986] and NCAR's TGCM [Roble *et al.*, 1988]. In each of these studies, the models were run for IMF conditions observed in late 1981 and early 1982 when thermospheric neutral winds and other properties were simultaneously measured by instruments aboard DE 2. The simulation by Roble *et al.* is for a period in which IMF  $B_y$  was positive. The model results are characterized by high velocity anti-sunward flow in the post-midnight sector of the northern polar cap that is associated with an enhanced clockwise dusk circulation vortex. These observations compare well to the DE-2 data available for that period. In addition, the UCL results of Rees *et al.* show, for periods of IMF  $B_y$  positive, that the anti-sunward winds drive neutrals into a region of the post-midnight sector where strong equatorward-directed winds (out of the polar cap) dominate. Hence, this  $B_y$ -dependent mechanism can transport neutrals from the northern polar cap to middle latitudes at preferred local times. Compositional disturbances in the polar thermosphere due to Joule heating in the surrounding auroral oval are presumably also driven into preferred local time sectors. There are other mechanisms by which

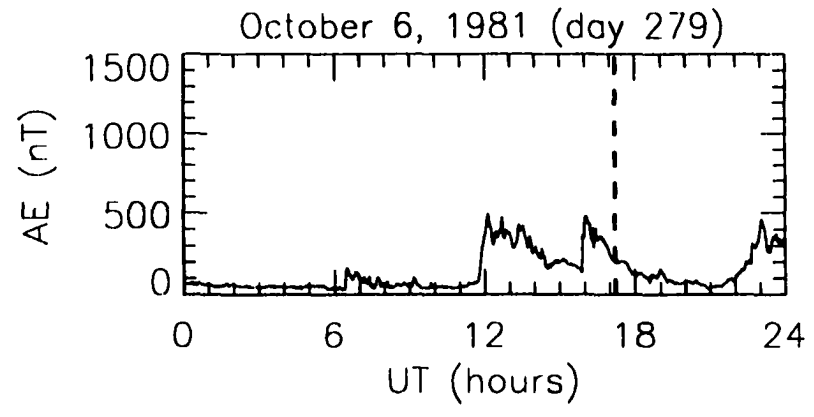
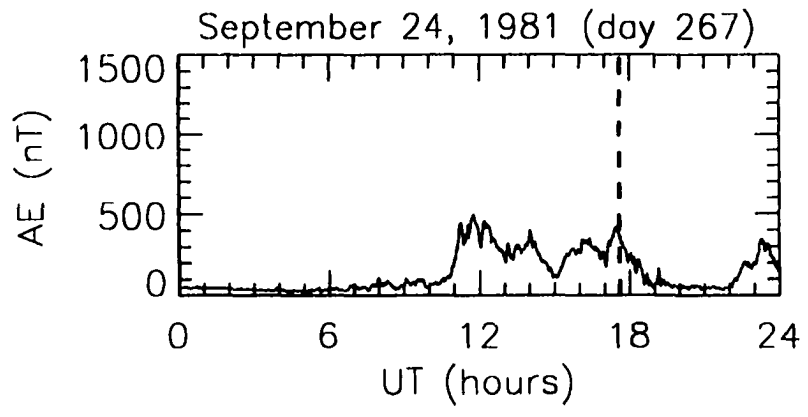
composition disturbances propagate or are transported from the polar cap to the middle latitudes, such as those described by Burns *et al.* [1989] and Fuller-Rowell *et al.* [1994]. It is the magnitude and sign of  $B_y$  that are apparently effective in determining the extent and magnitude of compositional disturbances occurring at middle latitudes in the post-midnight/morning sectors of the thermosphere, where their occurrence is observed in the sunlit hemisphere with DE 1.

#### 4.2 Comparison of Two Images

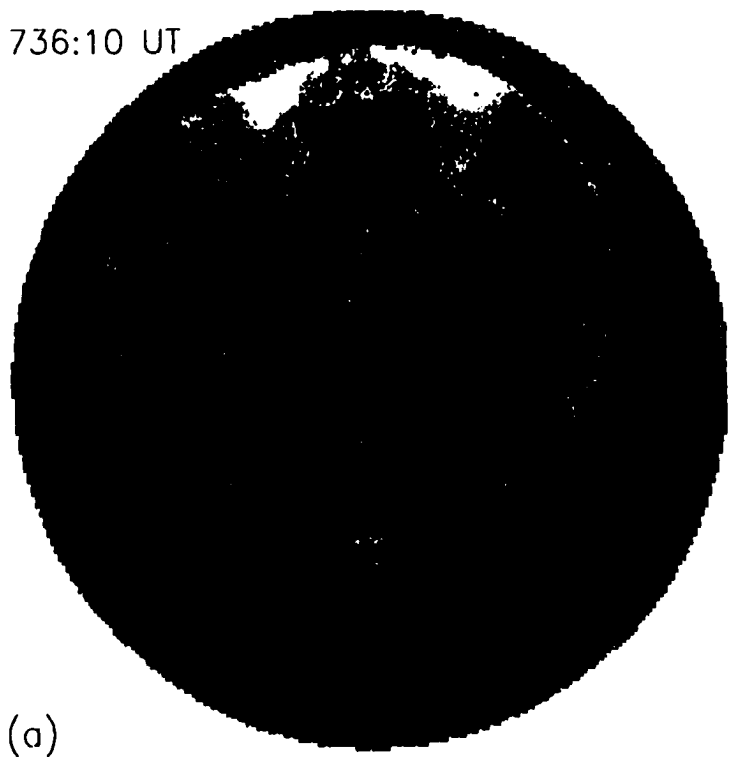
Presented here is a comparison of two images for which the time histories of magnetic activity are strikingly similar, yet the dayglow brightness in the morning sector is markedly different. The PD images presented in Figure 4-1 are constructed from selected original FUV images obtained in 1981 on September 24 (day 267) at 1736 UT and on October 6 (day 279) at 1713 UT. The altitude of DE 1 was  $\sim 3.2 R_E$  for each observation. These percent deviations of the measured dayglow brightness from quiet-time values are mapped to an orthographic projection in geographic coordinates, where the center of each image is at  $40^\circ\text{N}$  and 1100 hours local solar time (LST), thereby roughly centering the mapped PD images in the projection. Percent differences in the images are coded with the same color scale shown in Figure 3-15, and contours at  $\pm 20\%$  are overlain in white. Auroral emissions represent a "contamination" of the dayglow, increasing the measured response and leading to large positive percent differences at auroral latitudes. The PD representation used here is similar to that first presented by Craven *et al.* [1994]. The effect of the aurora on these PD images is not strong in the local noon sector. Also shown above the images in Figure 4-1 are the one-minute AE indices for the days in which the images were obtained, with vertical dashed lines indicating the two imaging times.

The time histories of AE for the two days are remarkably similar, with each characterized by low values during the first  $\sim 6$  hours in the day, slightly elevated values for the next 4–5 hours, and then sharp increases to  $\sim 400$ – $500$  nT at 1100–1200 UT. The

Figure 4-1. AE indices and selected PD (percent difference) images from days 267 and 279, 1981, respectively, in Figures 4-1a and 4-1b. The original images of Earth's FUV dayglow were obtained at 1736 and 1713 UT on days 267 and 279, respectively. The images are mapped to an orthographic projection in geographic coordinates, where the center of the projection is 40°N and 1100 LST. White contours indicate a percentage decrease of -20% from the quiet-time values. A large area of decreased dayglow brightness at middle latitudes on day 267 extends from the morning terminator to local noon. Values for the color-coded percent deviation are given by the color bar in Figure 3-15.

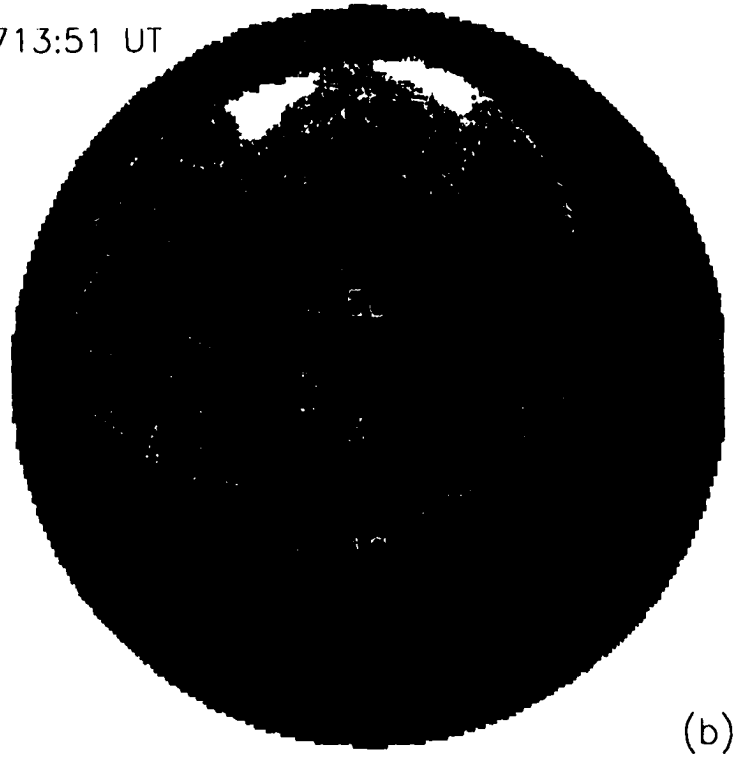


1736:10 UT



(a)

1713:51 UT



(b)

values vary between  $\sim 200$  and  $\sim 500$  nT over the next five hours. Given this remarkable similarity and the correlation between AE and the Joule-heating rates [Baumjohann, 1984] (i.e., the suggestion of nearly equal heating), the difference between the images is striking. The PD representation for the day-267 image (bottom left) shows a region of more than a 20% decrease in dayglow brightness extending from the morning terminator well into the sunlit hemisphere. This area extends equatorward to  $38^\circ\text{N}$  with a minimum value of  $-42\%$  therein. A similar decrease in brightness is evident in the polar cap, as is typical for these levels of geomagnetic activity [Immel *et al.*, 1994; Chapter 5 of this thesis], where the minimum value is  $-45\%$ . Decreases of at least  $\sim 10\%$  are observed at nearly all local times at the middle latitudes. In marked contrast is the PD representation for the day-279 image (bottom right), where no significant decreases are evident at middle latitudes. The dayglow brightness is again diminished in the polar cap, with a minimum value of  $-38\%$ . However, at nearly all sub-auroral latitudes the dayglow brightness is more typical of that observed during quiet times [Immel *et al.*, 1996], with deviations from quiet-time reference brightness generally no greater than about  $\pm 7\%$ . Together, the observations made on these two days raise the question of how such a difference can exist for such similar time histories in geomagnetic activity and, presumably, heating.

An investigation of the  $K_p$  and  $D_{st}$  indices (not shown) does not reveal any increase in activity that was not indicated in AE, particularly during day 267 where higher activity might be expected given the greater compositional disturbance. Furthermore, no signature of intense activity is apparent in any of these three indices for the days preceding the two days of interest here. Thus, the levels of magnetic activity observed before and during these two periods, as indicated by AE,  $K_p$  and  $D_{st}$ , are similar and low. These low levels are not normally associated with great disturbances of the thermosphere. For example, an earlier survey of such images by Nicholas [1993] found that a dayglow signature similar to that shown from day 279 is typical for the observed

level of magnetic activity, while the dayglow signature observed on day 267 is more of an exception.

A significant difference in the size of the oval or signatures of the auroral substorm activity observed on the two days could contribute to an explanation of the great difference in dayglow signatures. Images from the previous orbits on both days, taken between ~1200 and ~1500 UT, show that the oval has a maximum equatorward extent of ~61°N magnetic latitude in the post-midnight sector during each substorm period. No outstanding differences are noted in the progression of the substorms from expansion to recovery phase, except that the day-267 substorm sequence begins about one hour earlier than that of day 279. These observations suggest that the substorm periods are similar in magnitude and spatial extent.

The known influence of the IMF y-z component on ion convection and neutral circulation (as previously summarized) requires that we also consider the possibility of a large difference in the IMF orientation and magnitude on these two days. The magnitude and GSM (geocentric-solar-magnetospheric)  $B_y$  and  $B_z$  components for both days, as measured by ISEE 3 and averaged over five-minute intervals, are presented in Figure 4-2. The IMF observations are corrected for the transit time of the solar wind to Earth, and no interpolations are performed over data gaps. Average solar wind speeds for days 267 and 279, calculated from hourly averages [NSSDC, 1986], are  $324 \pm 11$  and  $354 \pm 13$  km/sec respectively, where standard deviations are given to indicate the degree of variability of the solar wind speed. The average speeds are used to calculate offset times of 81 minutes and 72 minutes, respectively, between observations at the L1 position and Earth. All ISEE-3 times are given with the offset times added.

The dayglow decrease observed on day 267 is preceded by a nine-hour period (0800–1700 UT) in which the  $B_y$  component is positive and generally  $>10$  nT. The  $B_z$  component is strongly negative from about 0900 to 1700 UT. In sharp contrast,  $B_x > 0$  (not shown) is the dominant component of the IMF on day 279, except for a brief period after ~1100–1200 UT in which increased variations are apparent in the three

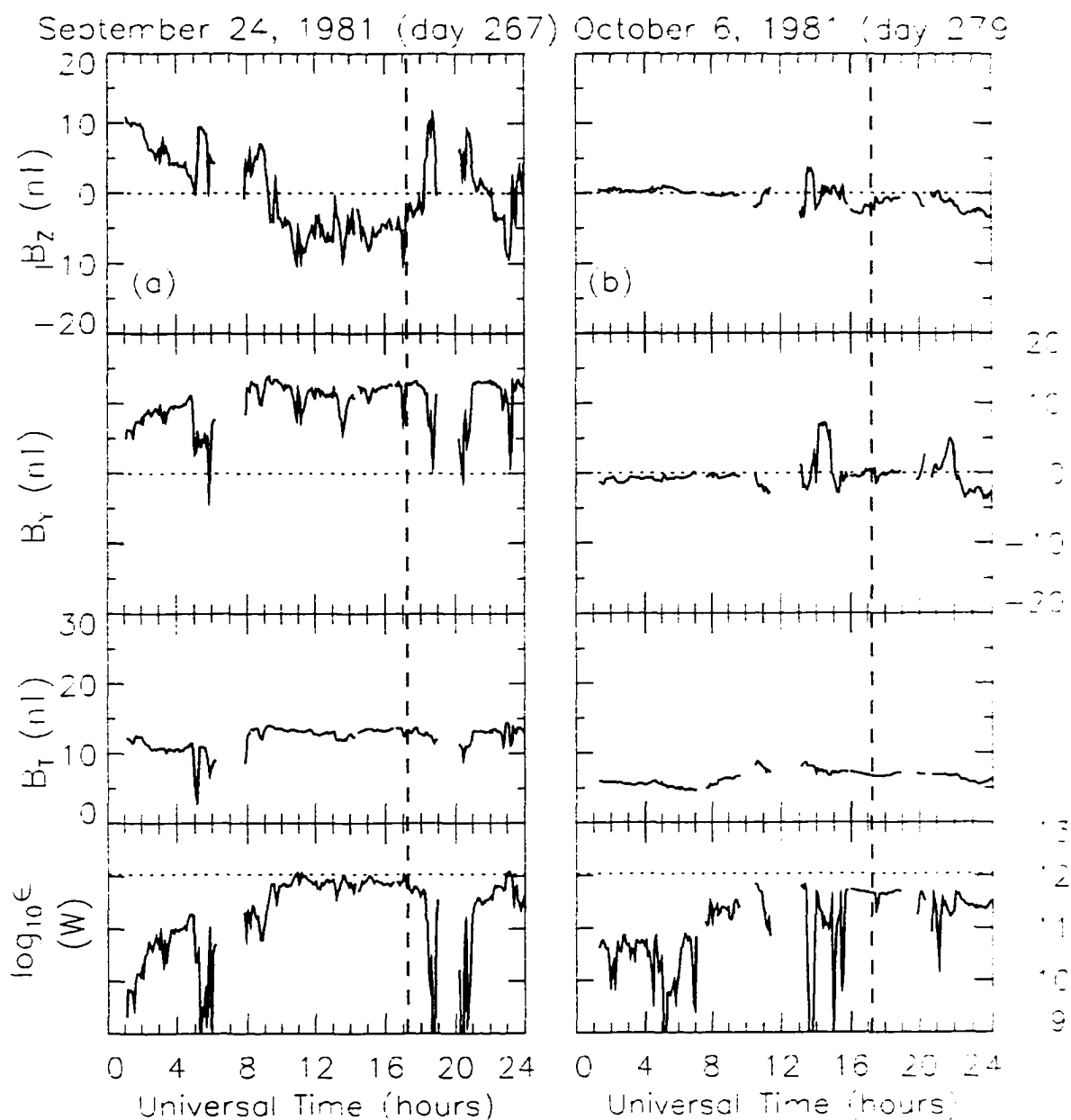


Figure 4-2. IMF magnitude and the  $B_y$  and  $B_z$  components for days 267 and 279, 1981, respectively, in Figures 4-2a and 4-2b. Dashed vertical lines indicate the times at which the images in Figure 1 were obtained. IMF data are advanced 81 and 72 minutes on days 267 and 279, respectively, to account for the transit time of the solar wind and imbedded IMF from ISEE 3 to Earth. The epsilon parameter,  $\epsilon$ , is shown in the bottom panel. To simplify the comparison of  $\epsilon$  in the two days, the  $\epsilon=10^{12}$  watt level is highlighted by a horizontal dotted line.

components. Increased auroral (AE) activity begins at ~1200 UT. The intermittent absence of ISEE-3 data has been partially solved by the equally intermittent presence of IMP-8 observations (not shown), which confirm the presence of fluctuations in the IMF and indicate that the  $B_y$  and  $B_z$  components are weakly negative (~ 0 to -5 nT) at ~1215–1400 UT. Hence, the two sharp increases in AE at ~1200 and ~1600 UT are associated with negative values of  $B_z$ . Simultaneous ISEE-3 and IMP-8 observations within the periods ~0400–0900 UT and ~1700–2400 UT are in good agreement.

The direction of the IMF in the GSM  $y$ - $z$  plane is also associated with the rate of transfer of energy to the magnetosphere from the solar wind. One index of magnetospheric-solar wind coupling is the epsilon parameter described by Akasofu [1981]:  $\epsilon = V_{sw} B^2 l_0^2 \sin^4(\theta/2)$  watts, where  $\tan(\theta) = (|B_y|/|B_z|)$  and  $l_0 = 7 R_e$  is the effective radius of the magnetosphere in the  $y$ - $z$  plane. This parameter is provided below the IMF data for each day in Figure 4-2. The values of  $\epsilon$  are determined using the five-minute average IMF values shown in the figure, and the hourly solar wind speeds interpolated at five-minute intervals. This provides a smoothly varying speed for the calculation of  $\epsilon$ .

Note that  $\epsilon$  is usually greater by a factor of two during the period of interest on day 267 than it ever is on day 279, suggesting greater magnetospheric energy input. This is due in large part to the strongly negative values of  $B_z$  measured on day 267. In contrast, the ground-based geomagnetic data shown here indicate that the energy inputs via electrojet currents are relatively similar. A possible explanation is that the IMF has changed orientation on day 267 in the approximately one-hour propagation time from the L1 point to Earth so that  $B_z$  is less negative and geomagnetic activity less intense. An examination of ISEE-1 IMF observations (not shown), taken from points much closer to Earth, reveals that this is not the case, and that the  $B_z$  component is as strongly negative at Earth as at ISEE 3. ISEE-1 and -3 magnetometer data are similarly well correlated on day 279. However, all of this assumes that  $\epsilon$  is a fair measure of energy input associated

with auroral activity, even though it is derived from parameters measured outside the magnetosphere. AE, as an index, is more directly related to the physical processes active within the auroral region, and thus subject to fewer perturbations by other physical processes that can interfere with a correlation between  $\epsilon$  and Joule heating. A more detailed discussion of this topic is beyond the scope of this chapter.

The difference in the two dayglow signatures can be due to differences in energy input, in neutral circulation associated with IMF orientation, or a combination of these factors. The ground-based magnetic data support the notion that energy input is roughly equal in the two periods, and this interpretation is favored here. Differences in dayglow signatures can then be ascribed to different high latitude neutral circulation patterns and the subsequent alteration of neutral composition at lower latitudes, later observed in the sunlit morning sector. However, as  $B_z$  is strongly negative on day 267 and more nearly zero on day 279, a possible large difference in magnetospheric energy input and cross-polar-cap potential is suggested, so these observations by themselves cannot unambiguously identify whether  $B_y$  or  $B_z$  is the most important parameter. We believe this is resolved in the next section.

#### 4.3 Four Consecutive Orbits

The two imaging sequences discussed in the previous section were chosen for the apparently similar time histories of geomagnetic activity and a similar imaging geometry at the same UT. This fortuitous occurrence is not repeated in the late-1981 to early-1982 DE-1 dataset. To further investigate the effect of IMF orientation on middle-latitude compositional disturbances, we have chosen for analysis images obtained in four consecutive orbits, with  $B_y$  changing from predominately negative to positive after the first two orbits with several cyclic variations in  $B_z$ . The AE indices for days 280 and 281, 1981, are shown in Figure 4-3, along with the IMF's magnitude and y and z components as measured at ISEE 3. The  $\epsilon$  parameter is calculated and shown in the bottom panel of the figure. The IMF data are corrected in time for the 69 and 58 minute

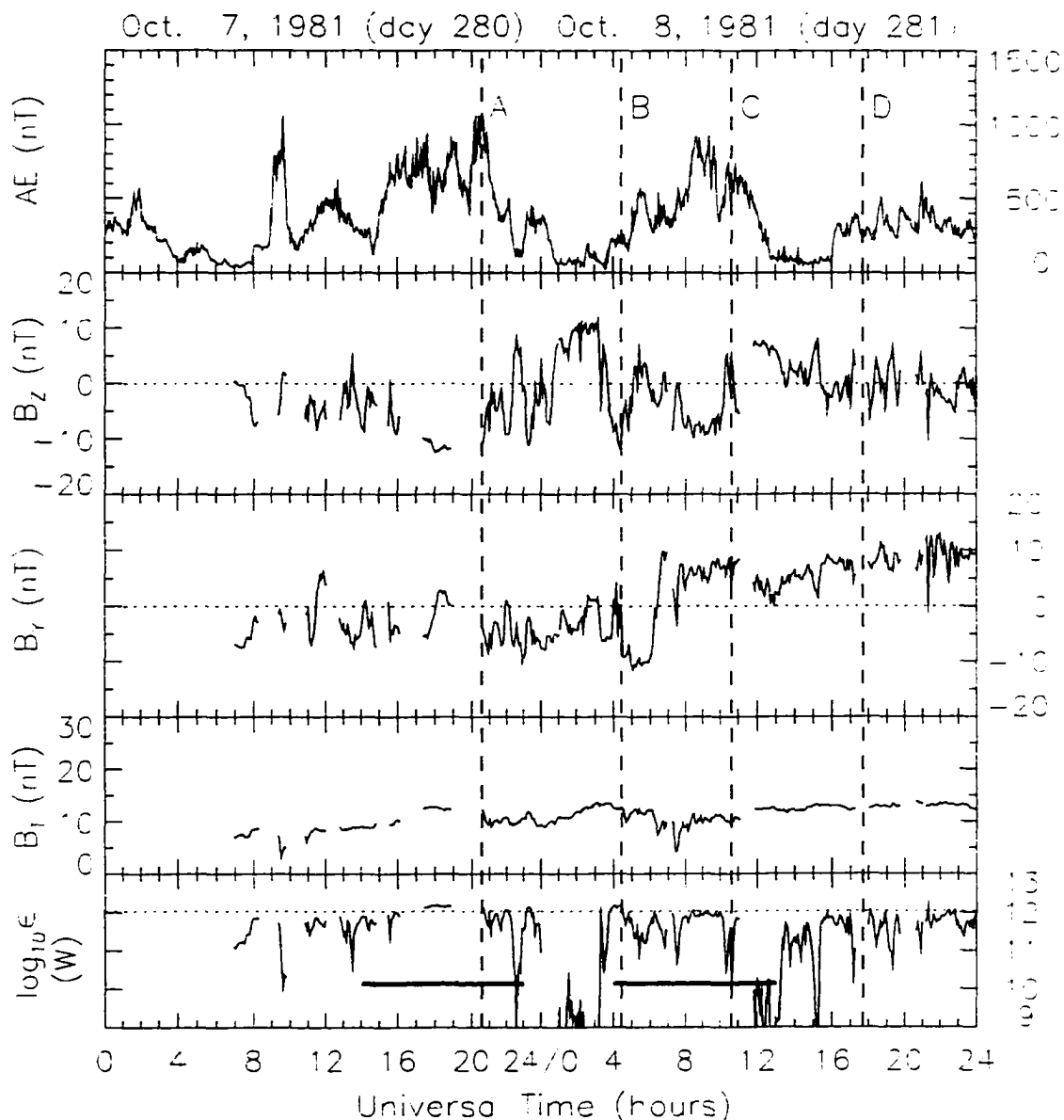


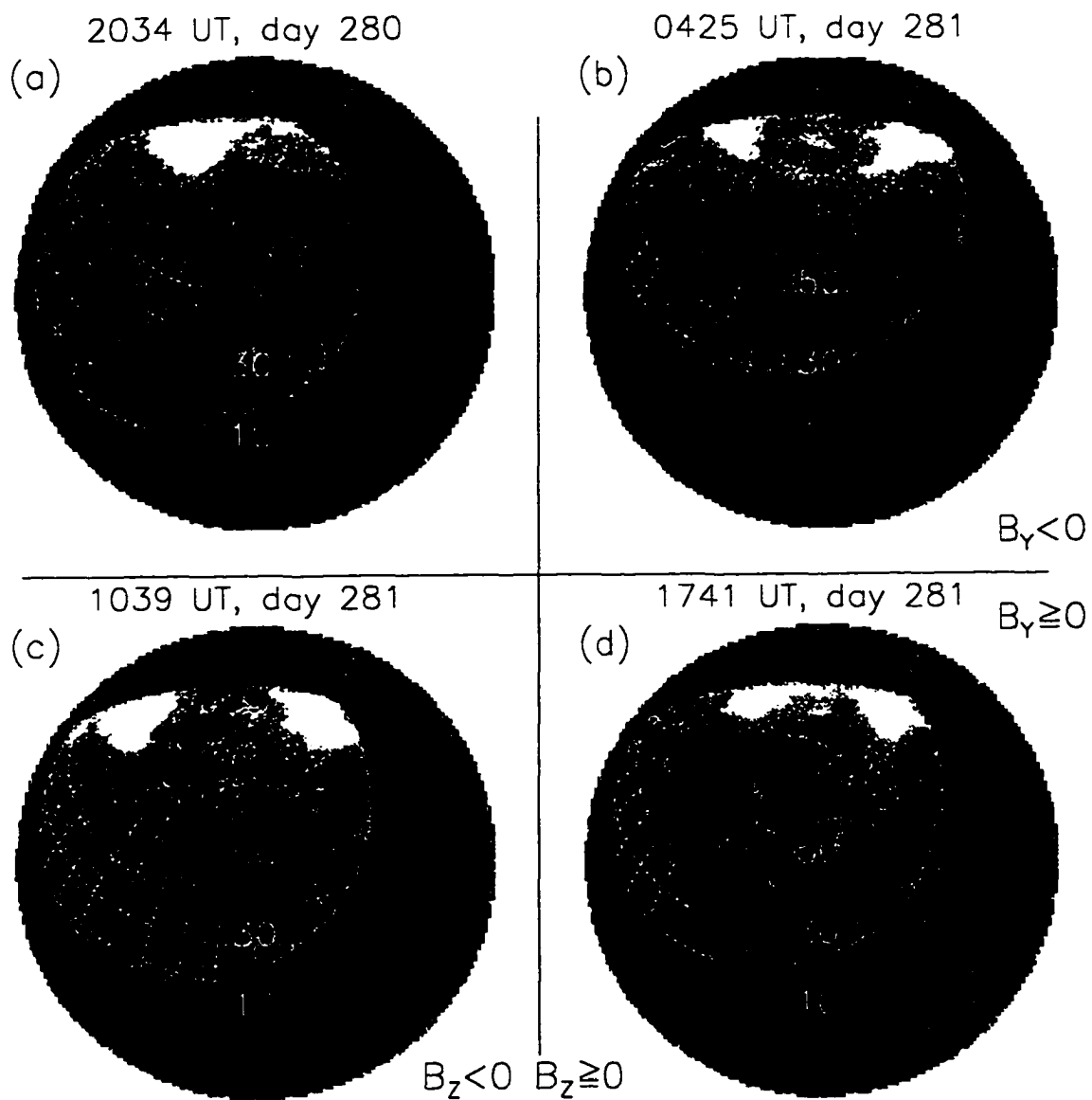
Figure 4-3. AE indices, IMF magnitude, and the  $B_z$  and  $B_y$  components for days 280 and 281, 1981. Dashed vertical lines accompanied by capital letters indicate the times at which images A, B, C and D of Figure 4 were obtained. IMF data are advanced 69 and 58 minutes on days 280 and 281, respectively, to account for transit time of the solar wind and imbedded IMF from ISEE 3 to Earth. The epsilon parameter,  $\epsilon$ , is shown in the bottom panel. The time periods 1400–2300 UT and 0400–1300 hours UT (the times used in calculations of  $\langle \epsilon \rangle$ ) are indicated in the bottom panel by horizontal solid lines. To simplify the comparison of  $\epsilon$  between the two days, the  $\epsilon=10^{12}$  watt level is highlighted by a horizontal dotted line.

transit times to Earth at average solar wind speeds of  $369 \pm 9$  and  $437 \pm 39$  km/sec [NSSDC, 1986] on days 280 and 281, respectively. The  $\epsilon$  values are calculated using these five-minute averaged IMF data and hourly average speeds that have again been interpolated to estimate the average speeds in five-minute increments.

Images selected to summarize the state of the FUV dayglow in the morning sector were obtained at the times indicated by the four vertical dashed lines in Figure 4-3. These will be referred to as images A, B, C, and D. Note that images A and C were obtained at or following peaks in intense magnetic activity, as indicated in the AE data, and that images B and D were obtained after periods of much decreased levels of activity. As expected from an examination of the AE and IMF data, the sign of  $B_z$  is primarily negative (positive) during the periods prior to times A and C (B and D). Note also that  $B_y$  is negative prior to the first two imaging times, A and B, that it becomes positive just after image B acquisition, and then remains so for the remainder of day 281. This includes the imaging times for C and D. In simplest terms, we observe the dayglow signatures following two strong  $B_z$  negative substorm periods, the first occurring with  $B_y$  negative (images A and B) and the second with  $B_y$  positive (images C and D).

PD representations of the four original FUV images A through D are shown in Figure 4-4, with image A as Figure 4-4a, *etc.* They are mapped to an orthographic grid in geographic coordinates identical to that used for the images in Figure 4-1, except that the center of each grid is  $40^\circ\text{N}$  and 1200 LST. Considering image A first, one notes immediately the decreased dayglow brightness in the polar cap and the afternoon sector near the end of an extended period of substorm activity. Decreases of more than 20% are seen to extend  $\sim 10^\circ$  equatorward of the auroral oval in the morning sector. The only effect of the storm seen in the dayglow eight hours later (image B) is a small area of decreased brightness evident between 0700 and 0800 LST. The polar cap appears unperturbed, as is expected from numerous DE-1 observations in the hours after AE returns to low values [Immel *et al.*, 1994]. The ISEE-3 observations of Figure 4-3 show that  $B_y$  is predominately negative throughout the 6–8 hours prior to each of these

Figure 4-4. Four selected PD images derived from FUV observations in four consecutive DE-1 orbits. Images taken at 2034 UT on day 280 and 0425, 1039, and 1741 UT on day 281, all in 1981, are shown in Figures 4a, 4b, 4c, and 4d, respectively. The images are mapped to an orthographic projection of geographic coordinates, similar to that used in Figure 4-1, except that the center of each mapping is at 1200 LST. The images are arranged such that those obtained for IMF  $B_y$  negative are shown in the top row (images A and B), and for IMF positive in the bottom row (images C and D).



imaging times, with only short periods of weak ( $< 2$  nT)  $B_y$  positive. It is most important to note that the morning-sector dayglow disturbance for  $B_y < 0$  and  $B_z < 0$  observed here is much weaker than the disturbance seen on day 267 (with  $B_y > 0$  and  $B_z < 0$ ), even though the geomagnetic activity (AE) and  $\epsilon$  are greater here by a factor of  $\sim 2$ .

$B_y$  then turned positive and remained so for the period in which images C and D were obtained. The first of these images (image C), obtained during a period of moderate magnetic activity, shows that the dayglow brightness is 10–25% below quiet-time levels in an area that extends down to  $50^\circ\text{N}$  in the morning and very early afternoon hours. The next image (image D) was obtained seven hours later, following the decrease in AE from  $\sim 600$  to  $\sim 100$  nT and the later increase to  $\sim 300$  nT. The dayglow signature shows evidence of a strong compositional disturbance, with decreases in brightness to  $< -20\%$  observed from the morning terminator to beyond local noon and in a portion of the polar cap. The area of 10% decreases is observed to extend equatorward of  $30^\circ\text{N}$ . This dayglow signature is similar to that seen on day 267.

The gaps in the five-minute-average IMF data for day 280 hinder comparison of the energy transferred to the magnetosphere during the two series of substorms that are present here. However, nearly continuous IMF data for both days are provided by the (time-delay-corrected) one-hour averages of IMF and  $V_{\text{sw}}$  [NSSDC, 1986]. The average magnetospheric energy input,  $\langle \epsilon \rangle$ , is calculated from hourly values of  $\epsilon$  during each of the two nine-hour periods indicated by bold horizontal lines in the lowest panel of Figure 4-3. The nine-hour periods, from 1400 to 2300 UT and 0400 to 1300 UT on days 280 and 281, respectively, are chosen so that they roughly bound the two prolonged substorm periods and also reflect the energy input for the six hours prior to images A and C. The results of this calculation are  $\langle \epsilon \rangle_1 = 7.1 \times 10^{11}$  and  $\langle \epsilon \rangle_2 = 4.9 \times 10^{11}$  Watts, respectively, for the two substorm periods. That is, the total solar wind-magnetospheric coupling during the first substorm period ( $B_y < 0$ ) is approximately half again as great as that during the second substorm period ( $B_y > 0$ ). This is not an outstanding difference.

However, the effect on the morning-side thermospheric composition is significantly different, with the presence of large-scale perturbations for positive  $B_y$ .

Summarizing, the effects of magnetic substorm activity on the dayside neutral composition during periods of  $B_y$  negative (images A and B) and  $B_y$  positive (Images C and D) are seen to be quite different. The intense  $B_y$  negative substorm period, with AE reaching maximum values at the time of image A, has apparently had only a minor effect on the dayside composition, as can be seen in image B. The somewhat less intense  $B_y$  positive substorm period (as measured by AE or  $\langle \epsilon \rangle$ ) occurring prior to and at the time of image C has a much more pronounced effect on the dayside thermospheric composition, which is clear from image D. We attribute the great difference between images B and D to the different IMF  $B_y$  orientations during the two substorm periods. These observations are seen to be consistent with an interpretation that the significant difference between the two images of Figure 4-1 is due not to the magnitude of  $B_z$  but to the sign of the IMF  $y$  component.

#### 4.4 Statistical Analysis

These examples are open to other possible interpretations. Single cases, or even four orbits of data are not enough to unambiguously determine the influence of IMF orientation on dayglow decreases. Further analysis, using many images obtained over more than one month's time, is performed here with the goal of statistically determining the effect of IMF orientation on dayglow perturbations during periods of magnetic activity.

By December 1983, the apogee of DE 1 had advanced to the Southern Hemisphere. During this time of the year, the southern polar cap is often fully illuminated by solar radiation; particularly so between ~0300 and 1100 UT as the magnetic pole is far sunward of the solar terminator. Images obtained at these times afford the opportunity to monitor the region where heated portions of the thermosphere are first observed at sub-auroral latitudes. It may be seen in thermospheric models [*e.g.*, Figure 1-11] or inferred

from images of large-scale storms that the greatest decreases are often observed in the high latitude morning sector. With the relatively short time at imaging altitudes (~3–4 hours), compared to the development time of thermospheric storms (5–10 hours), it is difficult to track the development of dayglow variations. However, since dayglow emissions can be observed about the entire auroral oval, instantaneous comparisons of percent variations in dayglow brightness at different locales may be made. The spatial extent of dayglow decreases generated by Joule heating can then be compared to IMF orientation.

The images chosen for this analysis were selected from a time interval beginning at ~0600 UT on day 350, 1982, and ending on day 33, 1983, before the sun crossed the orbital plane. Images are selected from times where the 123-nm filter was in use and the entire auroral oval was sunlit. The year, day and UT hour during which images chosen for this statistical analysis were obtained are listed in the first column of Table 4-1. No exclusions are made based on geomagnetic activity and the average AE index for the 6 hours previous to the beginning of the image period is given (to the closest 0.5 nT) in column 2. IMF values as reported by NSSDC [1986] are given for the UT hour shown with no correction for transit time to Earth. The absence of data at the exact time of imaging is indicated by NA. Average values of  $B_y$  from data available during the 6 hours previous to imaging are shown in column 4. In all, 127 images obtained on 16 days were used for this analysis. From the comparison of 23 quiet time images from day 002 and 011 to the earlier quiet-time model (Chapter 3), a decrease in instrument sensitivity by a factor of 0.52 is determined. This is due to degradation of optical surfaces and filter sensitivity, with greater loss of sensitivity at the shorter wavelength range of the 123-nm filter. No additional correction is made for the large percent decrease in  $F$  between quiet time sets, aside from the corrections determined from the 1981 data and described in Chapter 3.

Each image was examined to determine the latitudinal extent of the auroral oval as a function of magnetic local time in order to exclude auroral emissions from the analysis.

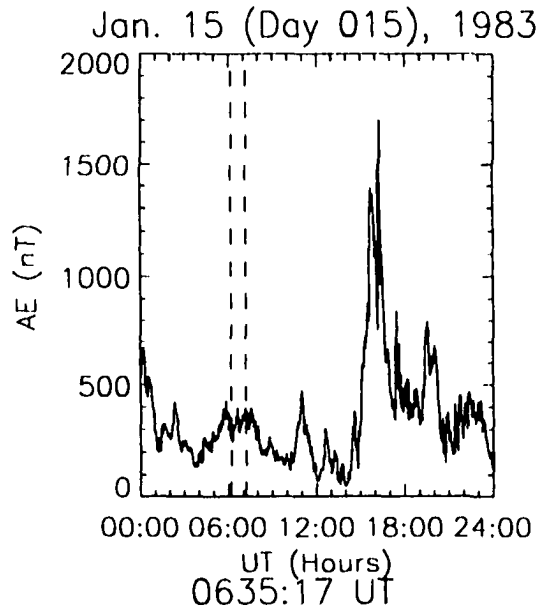
**Table 4-1: Listing of Imaging Periods for Statistical By Study**

Year, Day, UT	<AE> (nT)	By (nT)	<By> (nT)	F (Jy) adj.
82, 350, 0600	30	+18	~+12	213.2
82, 359, 1100	150	+9	~+5	170.6
83, 001, 0600	200	-8	--5	131.4
83, 008, 0300	55	-6	--3	155.9
83, 010, 0300	500	NA	--8	144.2
83, 013, 0600	170	+1	~0	135.1
83, 014, 0900	150	NA	~+3	137.2
83, 015, 0600	270	NA	~+12	141.0
83, 016, 0300	275	+7	~+8	140.2
83, 018, 0300	360	+3	~+4	134.8
83, 020, 0300	220	+7	~+5	120.5
83, 021, 0500	100	0	--1	116.1
83, 022, 0300	75	+2	~+1	113.5
83, 023, 0500	125	NA	--3	115.4
83, 024, 0400	360	-8	--7	114.1
83, 025, 0600	225	+1	--3	122.7
83, 027, 0500	150	-3	--3	133.6
83, 028, 0300	50	-1	~0	140.6
83, 033, 0900	60	-3	~+1	156.5

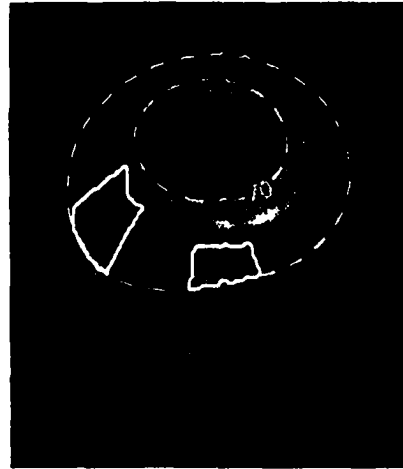
Two sectors of magnetic local time, 0200-0400 and 0600-0800 MLT, were chosen to characterize dayglow emissions in early and middle morning locations and are denoted as sectors 1 and 2, respectively. It is in these areas that one might expect to first observe the effects of Joule heating outside of the auroral oval. The latitudinal extent of each sector was determined by an upper boundary at the equatorward edge of the auroral oval and a lower boundary at 50°S magnetic latitude. These areas can be seen in a series of five PD images from day 015, 1983 in Figure 4-5. In this case the images are not mapped to geographic coordinates, but are presented in spacecraft coordinates with the limb region removed. The noon sector is to the upper left and sectors 1 and 2 are outlined in white. Note that the morning sector in these Southern Hemisphere images is to the left of the noon meridian, where it was to the right in Northern Hemisphere images from 1981. The 1981 quiet-time model is used to calculate reference pixel values as well as corrections for A and F. The reference values are then reduced by a factor of 0.53 to account for estimated reduced sensitivity of the instrument. No correction for variations in  $\langle r \rangle$  with P were made as the variation in P between the MLT sectors was not enough to significantly affect modeled counting rates.

The values of F on the respective imaging days are shown in Figure 4-6 (also in Table 4-1), as well as  $\langle PD \rangle$  values calculated for each image day from all pixels at  $S=66^\circ$  ( $\Delta S=1^\circ$ ), using open diamonds and filled circles, respectively. This survey of all images from this period reveals that the PD values closely follow variations in F, with an overall correlation of 0.87 between F and  $\langle PD(S=66^\circ) \rangle$ . The ~28-day periodicity in F values due to reappearance of FUV-bright regions with the solar rotation is evident from peaks in F on day 007 and 032. In the interim, F decreases from 165 Jy on day 007 to 113 Jy on day 023; a 32.5% decrease. The average dayglow brightness in images varies similarly. For example, between day 008 and 023 the average photometer response at  $S=66^\circ$  decreases from 19.4 to 16.4 counts/pixel, a decrease of 15.5%. Corrections to model values for the variation in F, as determined from the 1981 quiet-time data (Chapter 3), indicate only an additional ~6% correction to quiet time counting rates. This

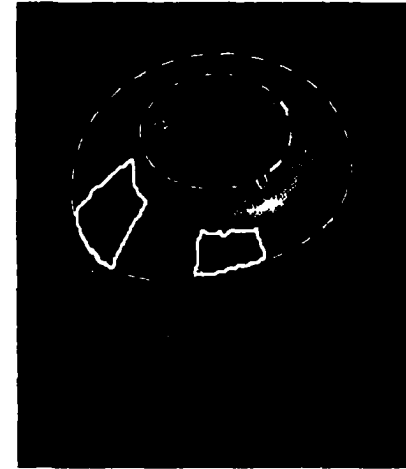
Figure 4-5. AE index and five percent difference (PD) representations of images taken during one hour on Day 015, 1983. The sections of the dayglow studied here are those at 0200–0400 (sector 1) and 0600–0800 (sector 2) MLT, highlighted with solid white contours. The magnetic latitude range for each section extends from  $-50^{\circ}$  to the outer boundary of the auroral oval. Magnetic midnight is located at the lower right of each image, with the sun to the upper left.



0611:08 UT



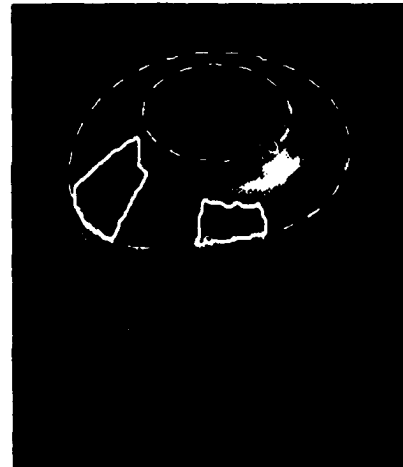
0623:09 UT



0635:17 UT



0647:24 UT



0659:32 UT



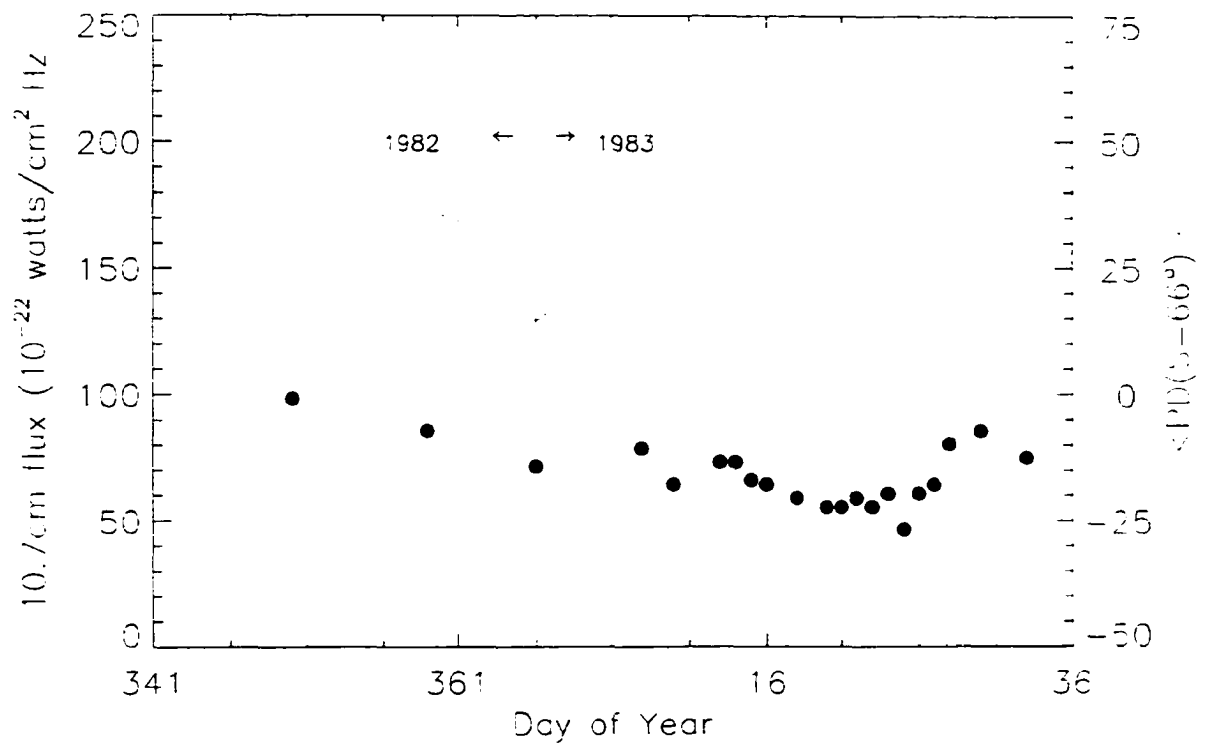


Figure 4-6. Variation in  $F$  and dayglow brightness at fixed  $S$  in the study period. Values of  $F$  and  $\langle PD(S=66^\circ) \rangle$  are shown versus day of year in which images were obtained. Open diamonds denote  $F$  values and the filled circles indicate  $\langle PD \rangle$  values for pixels within  $66^\circ \leq S < 67^\circ$  in the selected images.

is insufficient to correct for the observed variation in average photometer response, as is evident in the trend of PD values at  $S=66^\circ$ , which vary from  $-5\%$  on day 350, 1982 to  $-34\%$  on day 25, 1983. Ideally, PD values would not vary with F and the correlation between F and  $\langle PD(S=66^\circ) \rangle$  would be small. No further corrections are necessary for this analysis, however, as images are independently analyzed from one day to the next. This is, however, an indication that the dependence of  $\langle r \rangle$  on F determined in Chapter 3 is insufficient for these large percent fluctuations in F, and related solar FUV and EUV emissions.

The difficulty of comparing images within the set, due to the large variations in FUV brightness, is addressed by establishing a measure of the morphology of each dayglow signature independent of overall brightness and comparing images by this characterization. One such comparison can be made by determining the degree to which dayglow decreases in the early-morning sector extend to the middle-morning sector. PD values are calculated for all pixels in images obtained in the 1–2 hour imaging periods for each day listed in Table 4-1. The average percent difference values,  $\langle PD \rangle$ , are then calculated for the 0200–0400 and 0600–0800 MLT sectors for each imaging period. For example, the average percent differences observed in sectors 1 and 2 ( $\langle PD \rangle_1$  and  $\langle PD \rangle_2$ , respectively) from five images on day 015 are  $-28\%$  and  $-14\%$ , respectively. The difference of  $14\%$  between the sectors is a measure of the degree to which decreases in dayglow brightness extend from early to middle morning sectors. The difference is calculated for comparison of all sets of images from days of the imaging period.

Values of  $\langle PD \rangle_1$  and  $\langle PD \rangle_2$  for the individual imaging periods are shown in Figure 4-7a and 4-7b as a function of AE. The data are further separated into  $By < 0$  and  $By \geq 0$  bins, which are indicated by filled circles and open diamonds, respectively. The general trend toward greater decreases in brightness (in both sectors) with increased AE indicates again that magnetic activity results in decreased dayglow brightness. Dayglow brightness is lower in sector 1 than sector 2 in almost all cases. All  $\langle PD \rangle$  values indicate

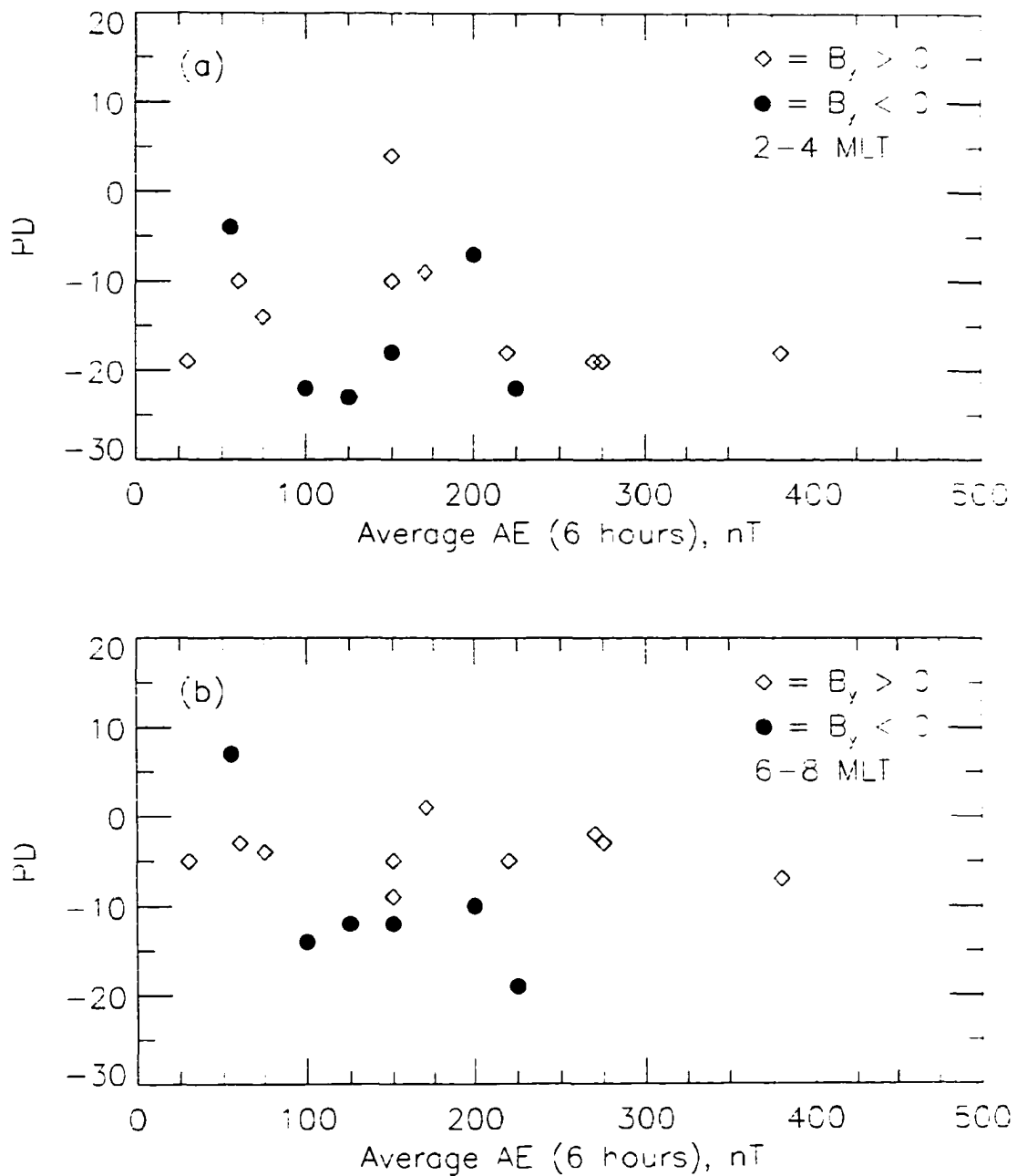


Figure 4-7. Average percent difference (PD) values in sectors 1 and 2 versus the preceding six hour average values of AE. (a) Distribution of average PD in section 1 ( $\langle PD \rangle_1$ ) as a function of AE for  $B_y$  negative (solid circles) and  $B_y$  positive (open diamonds) for all images. (b) Average PD value for section 2 ( $\langle PD \rangle_2$ ). Note trend of decreasing brightness with AE in both sectors and difference in relative distribution of  $B_y$  positive and negative points between sector 1 and 2.

brightness lower than the sensitivity-corrected 1981 reference dayglow values. This is a clearly a consequence of the very low F values during this period.

The values of  $\langle PD \rangle_1$  and  $\langle PD \rangle_2$  are shown again in Figure 4-8a, but now as a function of  $\langle By \rangle$  for all days where  $AE > 100$ . There is a different value for  $\langle By \rangle$  for each day except days for 023, 025 and 027 during which  $\langle By \rangle = -3$  nT: values of  $\langle PD \rangle$  are shown at  $\langle By \rangle = -3.4, -3.0, \text{ and } -2.6$ . The requirement of  $AE > 100$  nT selects days where some degree of Joule heating, and subsequent decrease of high-latitude dayglow brightness, is expected. The vertical line connecting two  $\langle PD \rangle$  values represents the magnitude of the difference between the sectors. The values of  $\langle PD \rangle_2 - \langle PD \rangle_1 = \Delta PD$  are plotted as a function of  $By$  in Figure 4-8b and a linear least-squares fit is overlain for the range of observed  $By$ . The values for  $a$  and  $b$  in the linear function  $\Delta PD = a \cdot \langle By \rangle + b$  are  $a = 0.67 \pm 0.17 \text{ nT}^{-1}$  and  $b = 5.97 \pm 0.95$ . The slope of the line, within the uncertainty of the determined coefficients, is always positive. The correlation coefficient,  $r$ , between  $\Delta PD$  and  $By$  is 0.48. With the number of samples equal to 12, this indicates an approximately 25% probability that these parameters are unrelated.

The possibility that the level of magnetic activity may influence the relation between early morning decreases in brightness to those observed at later MLT is now investigated. From several studies of the FUV dayglow, it would not be surprising to find that dayglow decreases extend farther toward the noon sector with greater activity. Using  $\langle AE \rangle$  as an indicator of the level of Joule heating, the values of  $\Delta PD$  are plotted in Figure 4-9 as a function of  $\langle AE \rangle$ . A least-squares fit of the form  $\Delta PD = a \cdot \langle AE \rangle + b$  is determined, for which the coefficients are  $a = 0.04 \pm 0.02 \text{ nT}^{-1}$  and  $b = -1.2 \pm 6.1$ . The correlation coefficient for these two parameters is 0.41, slightly less than the correlation between  $\Delta PD$  and  $By$ . Within the error of the fit the slope of the fitted function is always positive and indicates an increase in the difference in dayglow brightness between the two sectors of MLT with greater  $AE$ , opposite the expected trend. Thus, there is statistical evidence of a correlation between  $\Delta PD$  and  $\langle AE \rangle$ . Surprisingly, late morning

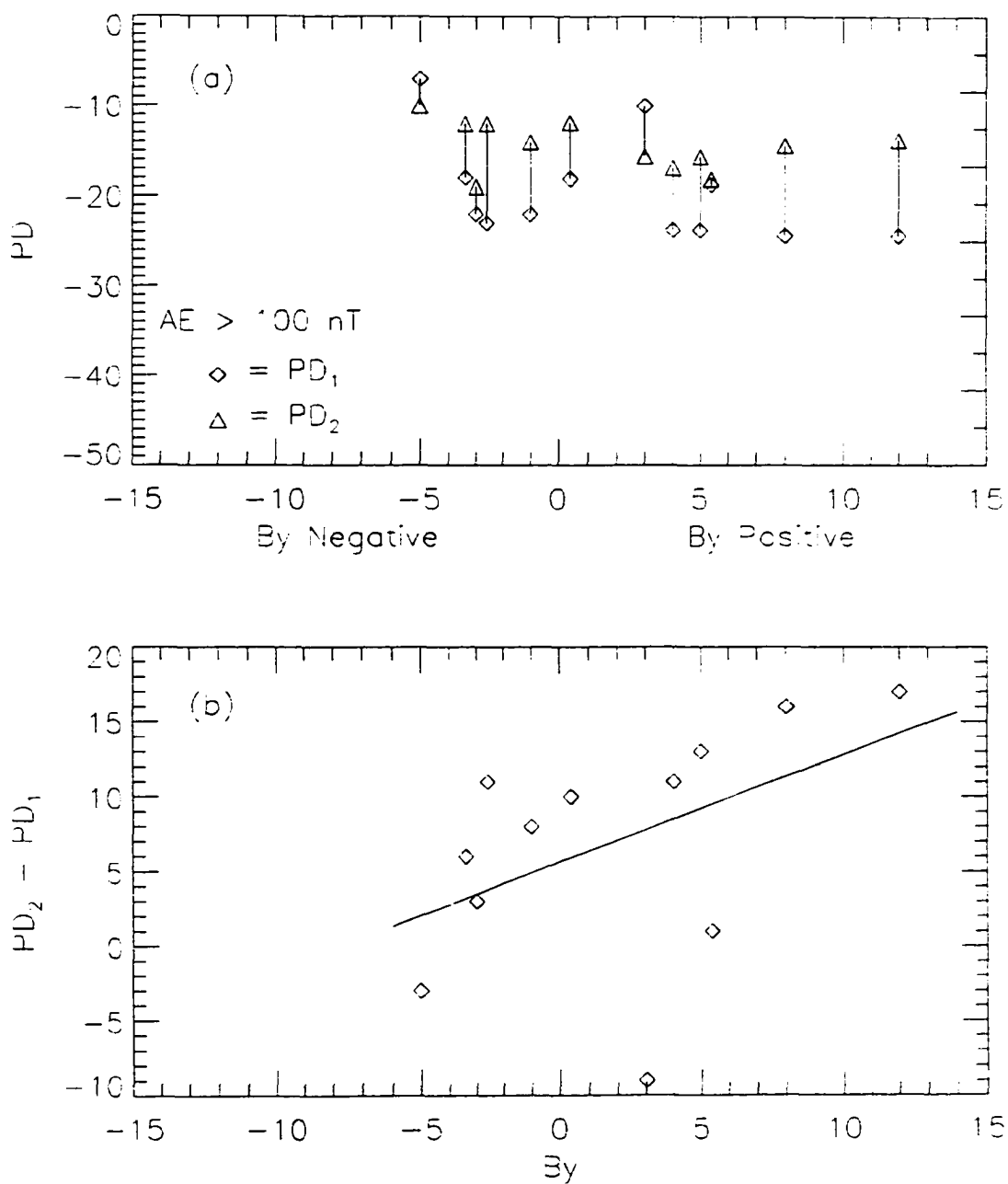


Figure 4-8. Difference between PD values of sectors 1 and 2 as a function of  $B_y$ . (a)  $PD_1$  and  $PD_2$  values for individual study days as a function of 6-hour average  $B_y$ . Observations range from  $-5$  to  $+12$  nT.  $PD_1$  is represented with diamonds,  $PD_2$  with triangles. Lines connecting the points indicate the relative difference in the dayglow decrease observed between the sections. (b) Magnitude of relative difference between  $PD_1$  and  $PD_2$  as a function of  $B_y$ . A linear least-squares fit is performed and overlain. Note the trend towards large differences in PD values for increasingly positive  $B_y$ .

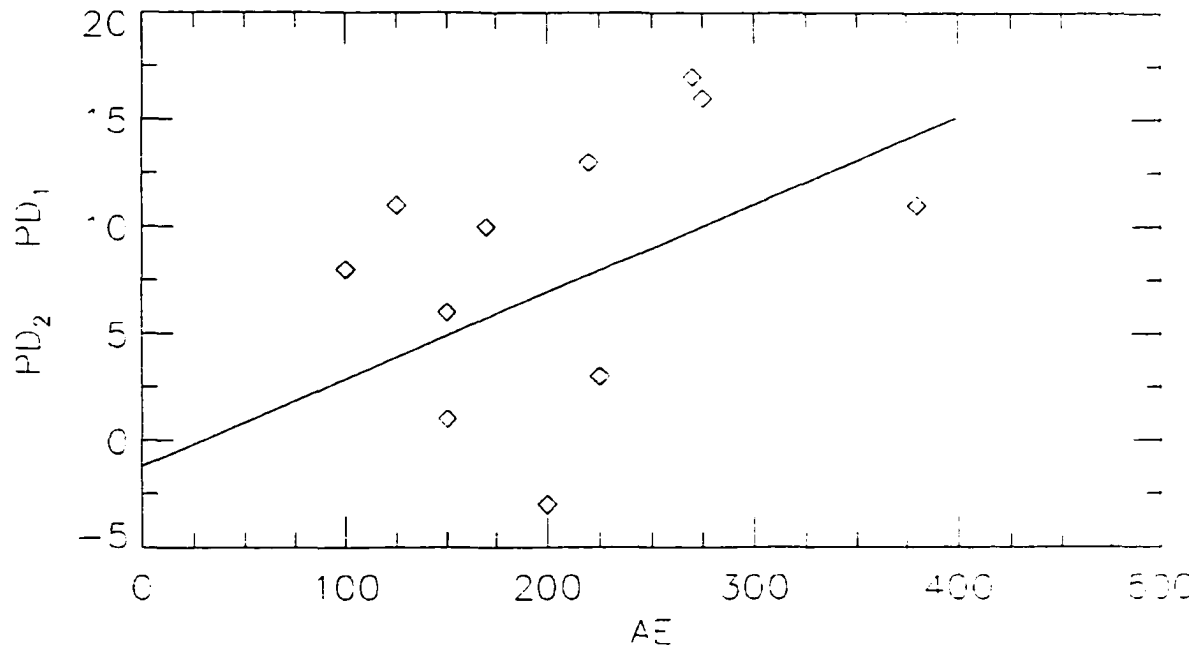


Figure 4-9. Difference between sectors 1 and 2 as a function of  $\langle AE \rangle$ .  $PD_1$  and  $PD_2$  values for individual study days are shown as a function of 6-hour average AE index. A linear least-squares fit is performed and overlain.

$\langle PD \rangle$  values ( $\langle PD \rangle_2$ ) change very little with AE; the variation in  $\Delta PD$  values is due mainly on the variations in  $\langle PD \rangle_1$ .

To determine if the observed dependence of  $\Delta PD$  on  $B_y$  is separate from the dependence on AE, the relation between  $B_y$  and AE is investigated.. For each day of observations, the average  $B_y$  and AE values are compared and plotted in Figure 4-10. A linear least squares fit of the form  $\langle AE \rangle = a \cdot \langle B_y \rangle + b$  is overlain, where  $a = 7.36 \pm 4.17$  and  $b = 187 \pm 22$  nT. The correlation coefficient is 0.41, the least correlation between the three parameters. This confirms that the dependence of  $\Delta PD$  on  $B_y$  described in Figure 4-8b is at least partially influenced by the dependence of  $\Delta PD$  on AE. Had there been no correlation, or positive slope, in the fit of Figure 4-10, one could deduce that two separate effects had been observed. Unfortunately, this is not the case, and this statistical analysis does not provide indisputable evidence of IMF influence on the development of FUV dayglow decreases.

Although the largest differences in PD values between the two sectors are observed when  $B_y$  is positive, the correlation of  $\Delta PD$  values with AE is nearly as significant. Since  $B_y$  and AE also are correlated (to a slightly lesser degree) for this particular dataset, the variation in  $\Delta PD$  cannot be attributed solely to  $B_y$ . One may interpret these results as a demonstration that both AE and  $B_y$  have a significant effect on the appearance of dayglow decreases in the 2–4 MLT sector. An alternative explanation is that either AE or  $B_y$  is responsible, with these variables simply correlated due to the relation of large  $B_y$ , hence large values of  $B_t$ , to large (possibly negative) values of  $B_z$  which could result in an increase in the AE indices.

#### 4.5 Summary

Observations have been made of deviations in the FUV dayglow from baseline brightness values after the onset of moderate ( $AE < \sim 500$  nT) and more intense ( $AE > \sim 900$  nT) geomagnetic activity. These variations in brightness are interpreted as being due to changes in atomic oxygen column densities induced by heating of the

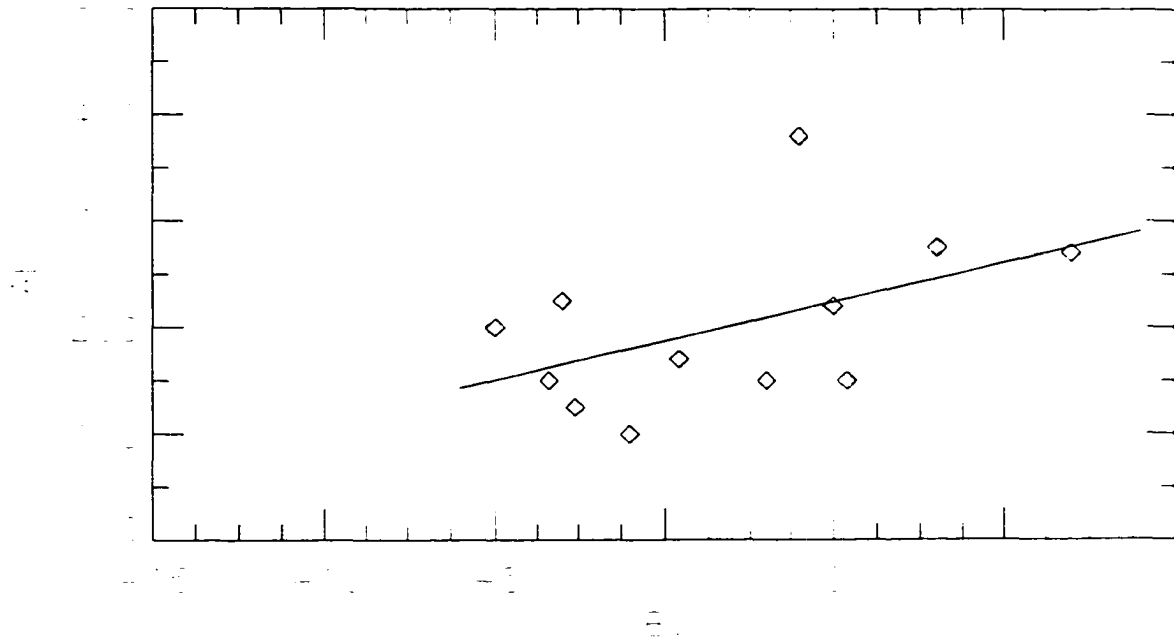


Figure 4-10.  $\langle AE \rangle$  indices for images of the 1983 study period as a function of  $\langle B_y \rangle$ . All values of  $\langle AE \rangle$  over 100 nT are included and a linear least squares fit is performed and overlain to demonstrate the trend in the data.

thermosphere. Large differences in the dayglow signatures between images from day 267 and 279, 1981, are apparently not due to differences in geomagnetic activity preceding the imaging times, as the auroral activity as measured by AE is remarkably similar. The main differences in conditions at the imaging times are the orientation and magnitude of the IMF. We conclude from the full set of observations that the duration and magnitude of positive  $B_y$  in this case has a significant effect on the mid-latitude thermospheric composition, as seen on day 267. Observations on day 279, during which geomagnetic activity is remarkably similar to that of day 267, show little variations in dayglow brightness at mid-latitudes from quiet-time levels.

Imaging sequences obtained in four consecutive DE-1 orbits during a geomagnetically active 21-hour period on days 280 and 281, 1981, have been used to clearly establish the influence of IMF  $B_y$  on the development of decreases in O densities in the dayside thermosphere. Two substorm periods are present within the four-orbit imaging series, the first somewhat more intense than the second. Large-scale decreases in O density associated with the magnetic activity are not observed at middle latitudes in the morning sector after the first series of substorms, during which the sign of the  $B_y$  component is predominately negative. Such large-scale decreases are observed after the second series of substorms, during which  $B_y$  is positive. The greatest decreases are seen in the last images of the fourth orbit, after a short period of relative auroral quiescence and following ~12 hours of strongly positive  $B_y$ .

The analysis of 127 images of the high latitude Southern Hemisphere from December 1982–January 1983 further demonstrates that IMF  $B_y$  may have an influence on the appearance of dayglow decreases on the dayside. The interrelationship of AE and  $B_y$  makes a firm conclusion difficult. This correlation may actually be inescapable as large values of IMF magnitude ( $B_t$ ) are often associated with more intense periods of magnetic activity. Additional imaging observations during periods of  $B_y \ll -5$  nT (when IMF magnitude is again large) might provide information to establish that the correlation between these parameters observed here is expected, reducing to zero the

slope of the fit shown in Figure 4-10. Furthermore, from the observations of sections 4.2 and 4.3, one would expect the greatest effect of Joule heating on dayside composition strongly negative values of  $B_y$ , which are not observed during the study period.

It has previously been established that the sign of  $B_y$  has a strong influence on the patterns of ion convection and neutral circulation in the thermosphere. It is consistent with the known  $B_y$  effect that the anti-sunward circulation associated with positive  $B_y$  aids the transport of heated sections of the thermosphere from the northern polar cap and auroral oval to the mid-latitude, post-midnight sector, where, through co-rotation, the disturbed sections are soon visible in the sunlit hemisphere. This is deemed a reasonable explanation for the observations made here: the occurrence of larger areas of strong composition disturbances in the morning sector for equal or lesser levels of activity are correlated with strong and consistently positive  $B_y$ .

It would be helpful to determine if compositional disturbances are observed more often in the evening sector at middle latitudes for  $B_y$  negative storms. Earth's rotation plays a large part in the appearance of Joule-heating related compositional disturbances in the morning sector, but images such as that shown in Figure 4-4a suggest that the appearance of strong disturbances in the afternoon sector of the Northern Hemisphere may be favored during periods of  $B_y < 0$ . The imaging geometry during mid-1982, with DE-1 apogee at low latitudes in the afternoon sector, offers an excellent opportunity for such an investigation.

## Chapter 5

### Variations in Thermospheric Composition within the Polar Caps

#### 5.1 Introduction

The polar cap is the region bounded at low latitudes by the auroral oval. Studies of thermospheric dynamics often concentrate on this region because of the strong electromagnetic coupling between the magnetosphere and ionosphere, and its collision-dominated coupling to the neutral thermosphere. This coupling has been addressed in several studies [Hays *et al.*, 1984; Killeen *et al.*, 1988, and others noted earlier in this thesis]. The goal of this chapter is to establish the response of the thermosphere within the polar cap to impulsive auroral activity. Another goal is to identify the effect of IMF on the development of polar cap composition disturbances, as done in Chapter 4 at mid-latitudes. In this work, observations of the Southern Hemisphere polar cap are presented.

Decreases in FUV dayglow brightness at high geomagnetic latitudes were first observed with OGO 4 by Meier *et al.* [1970], and it was noted that these decreases appeared during periods of magnetic activity [Meier, 1971]. This polar orbiting satellite measured OI and N<sub>2</sub> Lyman-Birge-Hopfield (LBH) emissions at the nadir and H L $\alpha$  emissions at the nadir and zenith. Measurements of dayglow emissions in the polar regions frequently revealed decreases in the nadir-direction H L $\alpha$  and OI emissions, while no such variations were observed in the nadir-direction N<sub>2</sub> LBH or zenith-direction H L $\alpha$  emissions. The absence of decreases in the N<sub>2</sub> LBH emissions may be attributable to contamination by spacecraft glow and should be interpreted accordingly [private communication, Meier, 1998]. These decreases in brightness correspond to reductions in HI and OI column densities below the satellite in response to auroral Joule heating. Another interesting effect that Meier [1970] observed was the absence of decreases in the southern polar cap during a week-long period where the northern polar cap exhibited consistent brightness decreases. This observation will be discussed again in the last section of this thesis.

Global-scale measurements of FUV dayglow brightness at OI, H  $\text{L}\alpha$ , and N<sub>2</sub> LBH were obtained with the polar-orbiting DE-1 from September, 1981, through 1989, many years after OGO-4. Dayglow decreases within the northern polar cap were noted by Nicholas *et al.* [1997] in a survey of DE-1 images from the first several months of imaging. Apsidal motion later brought the apogee of the highly elliptical orbit over the South Pole in early 1983, affording excellent viewing of the southern polar cap in January while the region is entirely sunlit. With a DE-1 orbit period of approximately 7 hours, the dayglow signature of the region was sampled repeatedly.

The bulk motion of thermospheric neutrals is also affected during enhancements in geomagnetic activity, not only in the auroral oval but throughout the polar cap. Neutral winds increase in velocity, driven by increased high-latitude plasma convection. This enhancement of convection is caused by strengthened local electric fields imposed by more rapid magnetospheric convection. Under different wind field configurations, dayglow decreases may develop in a different manner. The relation of the IMF to the polar neutral wind field should allow a correlation of the spatial development of dayglow decreases with IMF.

## 5.2 Dynamics Explorer 1 Observations

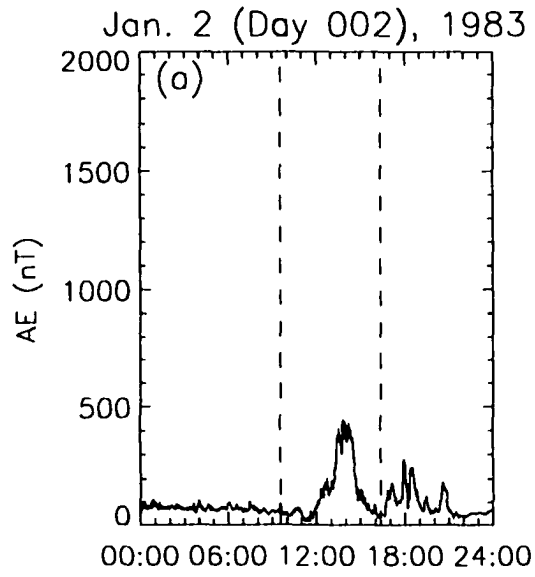
The quiet-time dayglow reference model developed in Chapter 3 is used here to provide reference photometer count rates for individual pixels as a function of solar and spacecraft zenith angles, S and D, respectively, and azimuth angle A. Model values are also adjusted according to variations in the daily 10.7-cm solar radio flux (F) although, as noted in Chapter 4, these corrections are insufficient to account for the low count rates which occur during the period of very low values of F later in January, 1983. Corrections for phase angle are not made here, as the change in phase angle across the polar cap is small. In any case the mechanism for variations in P (diurnal heating by solar EUV) measured at middle latitudes may have only have a minor effect within the polar cap. Percent differences from the quiet-time model are calculated for the disk-region of the

images used in this study in the same manner described in Chapters 3 and 4. By January, 1983, the FUV instrument's optics had been seriously affected by incident radiation, reducing its sensitivity by a factor of 0.52 since launch. This sensitivity correction is applied after azimuth and corrections for F are included in the model count rates.

Images obtained during two successive orbit passes with intervening auroral activity can reveal the effects of geomagnetic activity on the polar cap. As an example, four image pairs, taken during separate periods of varying geomagnetic activity, are shown in percent difference (PD) representations in Figure 5-1. Figure 5-1a shows the 1-minute AE indices for January 2, 1983, with the image times of 0932 and 1609 UT indicated with vertical dashed lines. The PD representation of images obtained during the 12-minute periods beginning at the listed times are shown in Figures 5-1b and 5-1c. These images are smoothed using a 5x5 boxcar averaging technique, as are all other images presented in Figures 5-1 and 5-2. Similar to images shown in Chapter 3, the solar terminator is to the lower right, but for these images of the southern polar region the morning sector is to the lower left. In each image presented here, contours of geographic latitudes  $-40^\circ$  and  $-70^\circ$  are shown using dashed lines, and PD values are indicated with the same color table used in Chapters 3 and 4, with values less than  $-20\%$  outlined with a solid white contour. Note the offset of the auroral oval from the geographic south pole.

In the time between the images of Figures 5-1b and 5-1c, the AE index is seen to increase from  $\sim 100$  nT to a peak value of  $\sim 450$  nT at 1400 UT, then drop again to 100 nT. During the  $\sim 6.5$  hours between images, the auroral oval and southern magnetic pole advance clockwise from the evening sector to the near-midnight sector. No significant dayglow decreases are present in Figure 5-1b at polar cap latitudes, though the auroral oval is clearly visible. The  $\pm 10\%$  percent difference values throughout this image are indicative of the low magnetic activity during the previous nine hours. In Figure 5-1c, auroral emissions have clearly increased and areas of decreases of  $-20\%$  from corrected model dayglow values is observed within the oval. No decreases of this significance are observed outside the auroral oval, except at the terminator.

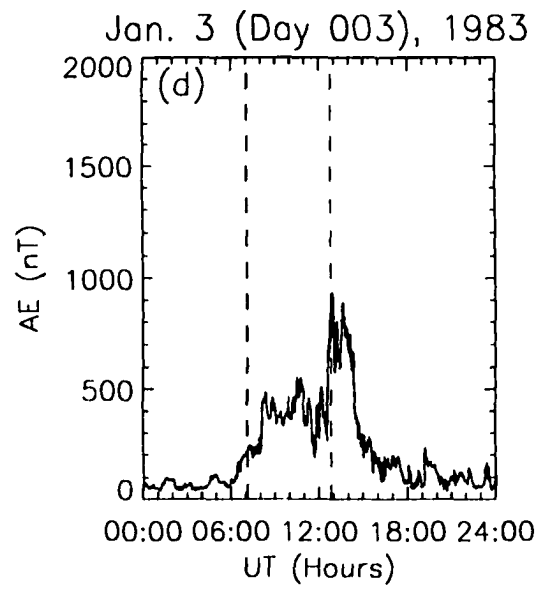
Figure 5-1. Percent Difference (PD) representations of images from successive orbits on days 2 (1b and 1c) and 3 (1e and 1f), 1983. AE indices for days 2 and 3 are shown in Figures 1a and 1d, respectively, where the imaging times are indicated with vertical dashed lines. The color scale represents PD values from -60 to +60%, as first presented in Figure 3-15.



(Day 002), 0932:35 UT



(Day 002), 1609:19 UT



(Day 003), 0707:21 UT



(Day 003), 1238:29 UT

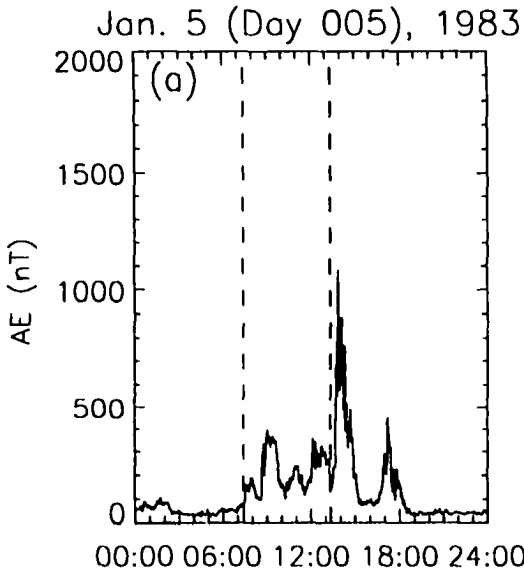


The AE indices for a similar image pair obtained on day 3, 1983, are shown in Figure 5-1d, with vertical dashed lines again indicating the imaging times of 0707 and 1238 UT. The PD representations of these image are shown in Figures 5-1e and 5-1f. The AE index rises from  $\sim 100$  nT to  $\sim 200$  nT in the hour prior to the first image time. Visible within the polar cap in Figure 5-1e are small areas where PD values are less than  $-20\%$ . In the  $\sim 5.5$  hours between the images, the AE index rises to  $\sim 450$  nT, then increases rapidly to  $>900$  nT just as the second image is obtained. It is evident in the second image that the auroral oval has expanded. Also, decreases to  $< -20\%$  in dayglow brightness are observed throughout the polar cap. Note that the second image is taken from a lower altitude, such that it is necessary to map the image to fixed coordinates to truly discern the variation in size of the oval, as is done in later sections.

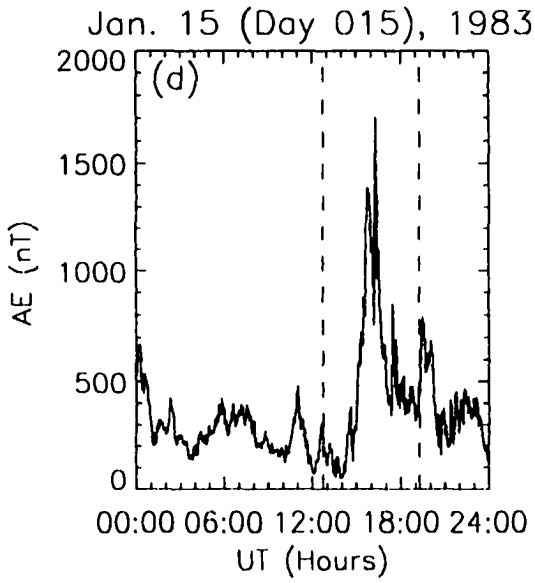
Using the format of Figure 5-1, the AE indices and a third pair of images obtained on day 5, 1983 are shown in Figures 5-2a, 5-2b, and 5-2c, respectively. The AE indices demonstrate magnetic activity similar in history to that observed on days 2 and 3: low activity ( $AE < 100$  nT) preceding the first image (taken at 0724 UT) and a period of moderate, variable activity ( $100 \text{ nT} < AE < 400$  nT) before the second image (taken at 1308 UT). The auroral oval (near the top of the image) is not entirely visible in the first image, as a portion of it lies in the limb region that is not subject to examination by the dayglow model. The disk-region polar cap exhibits insignificant decreases in brightness less than  $-20\%$  of the quiet-time values. After the increase in magnetic activity, localized brightness decreases of  $< -20\%$  are evident throughout the polar cap, as shown in Figure 5-2c. This reflects a very moderate effect of magnetic activity on polar cap composition.

The AE indices for day 15, 1983, are shown in Figure 5-2d, with PD representation of the images obtained at 1244 and 1904 UT in Figures 5-2e and 5-2f, respectively. The image times are indicated with two vertical dashed lines on the AE plot. Significant auroral activity during the several hours prior to the first imaging time is evident. Between imaging times, a significant increase in auroral activity is evidenced in the AE indices, with values briefly  $>1000$  nT around 1600 UT. The auroral oval is evident in

Figure 5-2. PD representations of images from successive orbits on days 5 (2b and 2c) and 15 (2e and 2f), 1983. AE indices for days 5 and 15 are shown in Figures 2a and 2d, respectively, where the imaging times are indicated with vertical dashed lines. Color scale is the same as for Figure 5-1.



(Day 005)



(Day 015)



, 0724:53 UT



(Day 005), 1308:57 UT



, 1244:24 UT



(Day 015), 1904:57 UT



Figure 5-2e, as are some >20% decreases in the polar cap and in the early morning sector at subauroral latitudes. After the large excursion of the AE indices, the oval has expanded and increased in brightness relative to the local dayglow emissions, as evidenced in Figure 5-2f. Dayglow decreases < -20% are evident throughout the polar cap, reaching a maximum deviation from reference brightness of -52%.

Any auroral emissions occurring within the polar cap would mask decreases in dayglow brightness therein. Such emissions are known to occur mostly during periods of Bz northward, and are often observed as a transpolar arc or other discrete structure. A case can be made that the apparent increases in size and magnitude of the thermospheric disturbances within the polar cap on the selected days are due to the diminution of previously present polar cap auroral emissions with southward turning IMF. It is improbable, however, that large scale decreases in dayglow brightness within the polar cap can be entirely masked by auroral emissions within the oval. We interpret the observed variations as decreases in dayglow emissions due to auroral heating of the thermosphere, while acknowledging that a decrease in auroral emissions within the polar cap could add to the apparent decrease in dayglow brightness. However, a hypothetical 1 kR auroral emission at 130.4 nm at 90° SZA would be seen as an ~30% increase over normal dayglow brightness. This is not observed within the polar cap at any time in this study, including very quiet times when no decreases in dayglow brightness within the polar cap are expected.

### 5.3 Variations in Polar Cap Dayglow Brightness

#### 5.3.1 Temporal Variability

To obtain a measure of the rates at which O densities in the polar cap decrease, and subsequently recover, the average PD value of the polar cap before and after the magnetic events of Figures 5-1 and 5-2 are determined. Images obtained using the 123-nm filter (including those shown above) are also available for three consecutive orbits on days 3, 5, and 15-16, 1983. Images obtained from two orbits on day 2, 1983.

shown in Figures 5-1b and 5-1c are followed by an orbit during which the 123-nm filter was not used. The imaging periods using the 123-nm filter and supporting information are summarized in Table 5-1. Six hours average IMF values are calculated from the available data [NSSDC, 1986] for the times prior to each imaging period to characterize solar wind conditions. Average  $\langle PD \rangle$  values within the polar cap for each orbit were determined from the images by first manually determining the aurora-polar cap boundary and digitally removing the surrounding auroral emissions (and subauroral dayglow). PD values were calculated for the remaining pixels of each image for a given orbit and then averaged over all images to obtain an average  $\langle PD \rangle$  value for the polar cap. These average  $\langle PD \rangle$  values for each orbit on days 2, 3, 5, and 15 are shown in the right column from top to bottom of Figure 5-3, as well as the AE indices for the 24 hour period during which the images were obtained, shown in the left column. The time at which the first image in an orbit series was obtained is marked with a vertical dashed line.

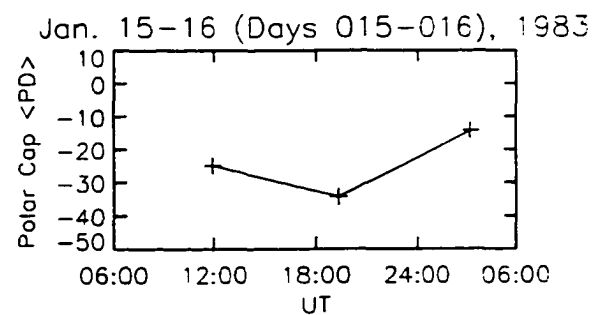
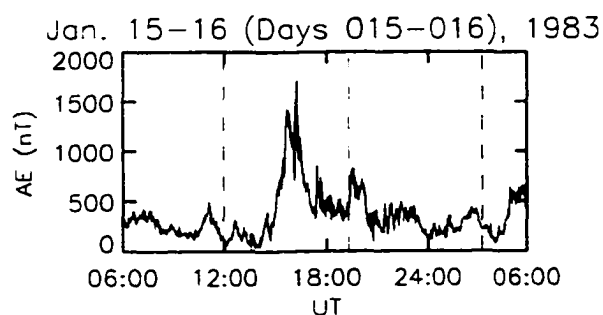
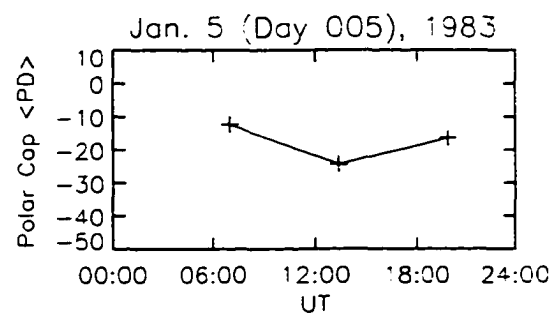
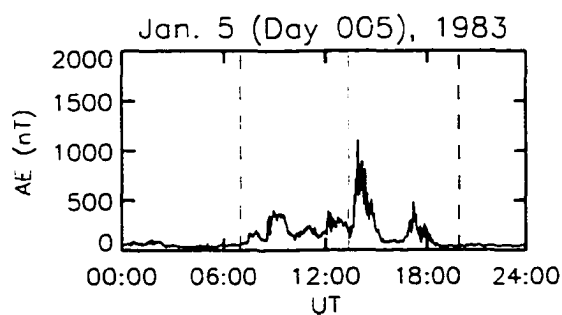
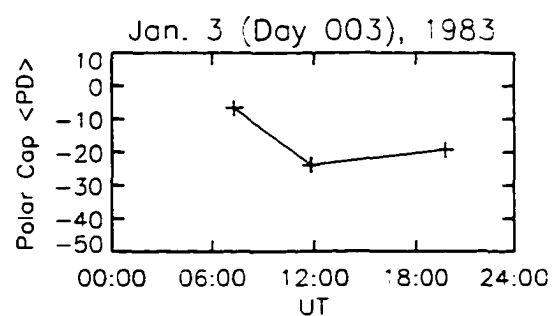
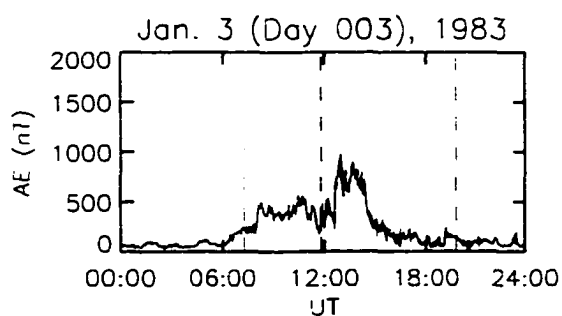
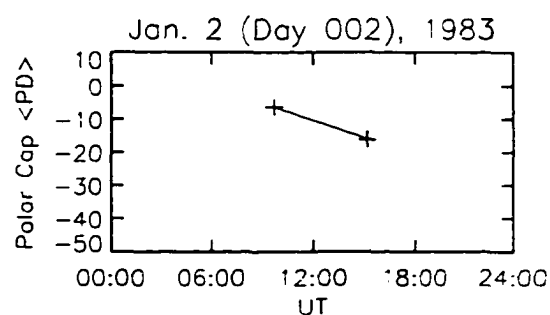
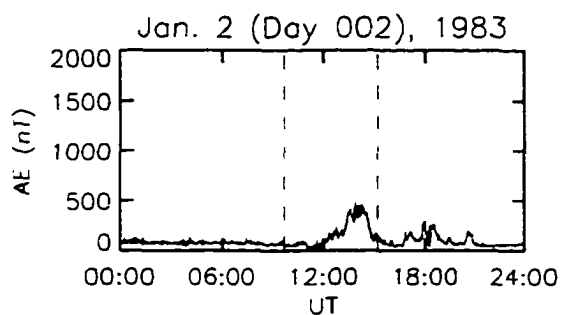
In each of these cases, the first two orbits provide images which effectively bracket an impulsive increase in geomagnetic activity, and the effect of the activity is a reduction in polar cap dayglow brightness, corresponding to a decrease in the oxygen column density. In the three cases where a third orbit provides further images, the recovery of polar cap FUV brightness to values more representative of pre-enhancement levels is evident. The appearance of a composition disturbance and subsequent recovery occurs in an approximately 12 hour period. This timescale for disturbances to appear within the polar cap (less than seven hours) is similar to that reported in modeling efforts and direct compositional measurements [Fuller-Rowell *et al.*, 1994, 1996; Prölss, 1980, 1981, 1982]. The  $\langle PD \rangle$  values observed in the third orbit on days 3 and 5 indicate an ~20–50% recovery of O densities to pre-enhancement levels in the seven hour orbit period. This also is described by Fuller-Rowell *et al.* [1994, 1996] (see also Figure 1-11 of this thesis), with a roughly 50% recovery of mass mixing ratios at high latitudes within six hours of the end of activity, though this example is for a very large storm. The day 016  $\langle PD \rangle$  value is greater than the pre-storm observed level. This may be due to the polar

**Table 5-1: Images Used in Polar Cap Study and IMF y- and z-components during 6 Hours Previous to Imaging**

Day of 1983	Orbit number	Imaging Times	# of Images	B <sub>y</sub> , nT	B <sub>z</sub> , nT
002	Orbit 1	0932–1033 UT	6	-3.4 <sup>2</sup>	1.4 <sup>2</sup>
	Orbit 2	1456–1734 UT	14	2.3	0.4
003	Orbit 1	0707–0731 UT	3	6.5	1.9
	Orbit 2	1137–1250 UT	7	2.1	-2.8
	Orbit 3	1937–2002 UT	3	0.2 <sup>3</sup>	0.4 <sup>3</sup>
005	Orbit 1	0648–0737 UT	5	5.0	3.0
	Orbit 2	1308–1357 UT	5	5.7	-2.8
	Orbit 3	1944–2044 UT	6	NA	NA
015	Orbit 1	1143–1256 UT	7	12.7 <sup>2</sup>	5.0 <sup>2</sup>
	Orbit 2	1904–1953 UT	5	8.5 <sup>2</sup>	1.4 <sup>2</sup>
016	Orbit 3	0306–0354 UT	5	7.2 <sup>4</sup>	1.8 <sup>4</sup>

If IMF coverage is incomplete, superscript indicates number of hourly IMF data values available in six-hour period.

Figure 5-3. Average polar cap percent difference values at orbit times indicated in AE plots. A plot of AE indices (left column) during a 24-hour period for which there are successive orbits and images with the 123-nm filter. A corresponding plot of average polar cap <PD> values (right column) indicates the levels of FUV brightness decreases. A dashed vertical line in an AE plot indicate the time, for a given orbit, of the first image used in the calculation of <PD>.



cap being partially in the limb region during this observation, with the low number of pixels available for the calculation being slightly affected by limb brightening.

### 5.3.2 Spatial Variations

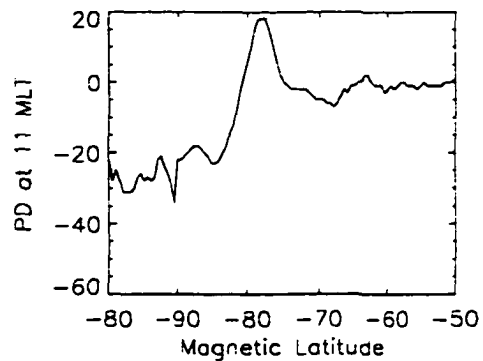
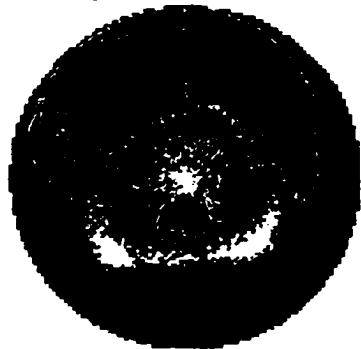
The images of Figure 5-3 showing the most significant dayglow decreases are now examined in greater detail. Average percent differences are again calculated using all images from each orbit produce an overall <PD> image for the orbit, at first including all pixels in the analysis. These are shown in Figure 5-4a through 5-4d, where the <PD> image is mapped to an orthographic projection of geomagnetic local time and latitude, where the center is the southern magnetic pole and the top is magnetic noon. The right-hand portion of each mapping is the pre-noon sector.

A plot of <PD> values along the 1100 MLT meridian (continuing beyond the magnetic pole to 80°N on the 2300 MLT meridian) is provided to the right of each image. Note that auroral emissions are not removed and are evident at about -75° to -80° magnetic latitude. <PD> values from Days 2 (Figure 5-4a) and 3 (Figure 5-4b), 1983, show the clear difference between the magnitude of dayglow brightness within the polar cap and outside the oval at sub-auroral latitudes. They demonstrate that thermospheric densities may be disturbed throughout the polar cap within 2-3 hours of the onset of moderate magnetic activity, while densities just equatorward of the dayside portion of the oval remain relatively unperturbed. Data from Days 5 (Figure 5-4c) and 15 (Figure 5-4d), 1983, show a more continuous variation of <PD> values along the meridian from sub-auroral latitudes into the polar cap (aside from the intervening auroral emissions). For day 15, this is clearly a result of the moderate magnetic activity over many hours prior to the imaging sequence. Heated portions of the thermosphere have corotated with Earth to appear on the dayside, at subauroral latitudes [Craven *et al.* 1994; Meier *et al.* 1995].

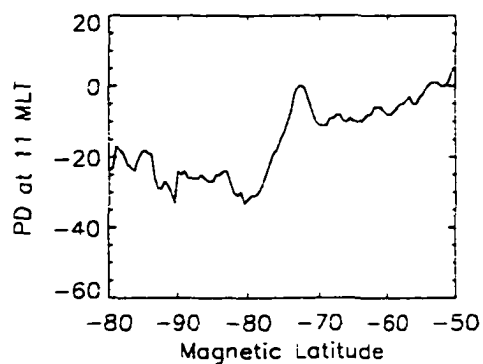
Note that in these meridional plots, the most significant decreases in dayglow brightness sunward of the magnetic pole are just poleward of the oval. This observation

Figure 5-4.  $\langle PD \rangle$  values calculated from images in the second orbit of each sequence. PD values are shown for days 2, 3, 5, and 15 in satellite projections of geomagnetic local time and latitude and in plots of  $\langle PD \rangle$  values along the 1100 MLT meridian in Figures 5a-5d. The center of the mapped images is  $-90^\circ\text{S}$  and the top of each map is 1200 MLT. Image times correspond to the first in the series of images taken during the orbit.

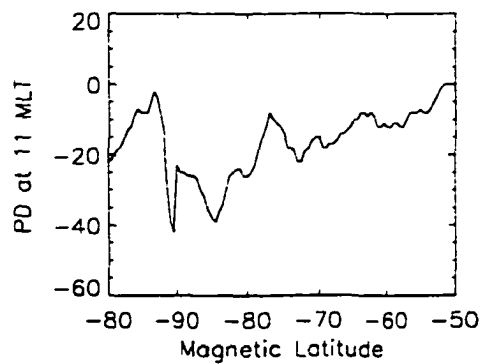
Jan. 2 (Day 002), 1983, 15:08 UT



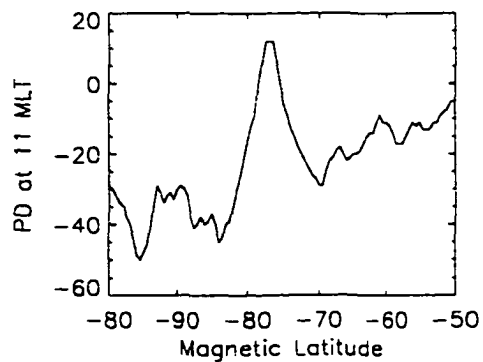
Jan. 2 (Day 003), 1983, 11:49 UT



Jan. 3 (Day 005), 1983, 13:21 UT



Jan. 5 (Day 015), 1983, 19:17 UT



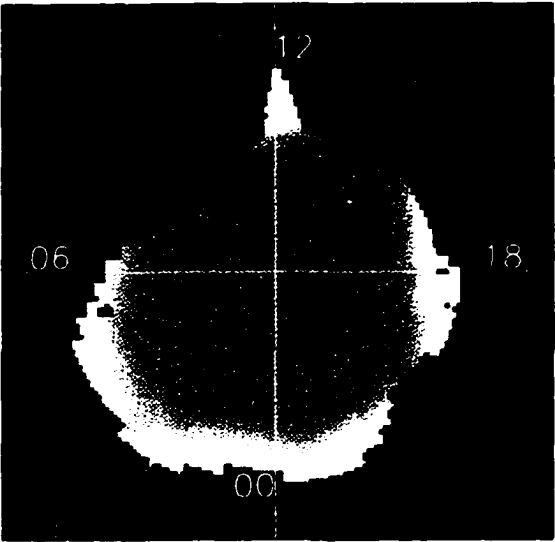
is consistent with the interpretation that dayside thermospheric parcels undergo significant heating while advecting through the auroral oval. The late morning sector of the auroral oval is a region of efficient Joule heating [Fuller-Rowell *et al.*, 1994], and heating of neutrals in this region is demonstrated in simulations by Idenden *et al.* [1997]. If these decreases are due to this heating, then it can be stated that there is a FUV signature of neutral atmosphere's heating within one hour of being so affected. This is the approximate transit time of an atmospheric parcel into the polar cap from subauroral latitudes. Hernandez *et al.* [1991] clearly show that the neutral winds at the 'throat' region are not always directed into the polar cap. However, IMF  $B_y$  is positive for all cases presented in this chapter, for which the neutral wind field (in the southern hemisphere) favors transport of neutrals through the late morning oval into the polar cap.

The distribution of dayglow decreases within the polar cap is more closely examined in Figure 5-5a through 5-5d, where the color bar now represents a range of percent decreases of  $-60$  to  $-0\%$  to better visualize percent difference values. The surrounding region of auroral emissions has been digitally removed from each <PD> image, now mapped to a Lambert equal-areas projection of geomagnetic local time and latitude, where the noon-midnight meridian is vertical and the morning sector is to the left. This projection allows for smoothing with a boxcar technique after the <PD> pixels are mapped to geomagnetic coordinates. A  $2^\circ \times 2^\circ$  boxcar averaging technique is used to bring out variations in dayglow brightness over distances  $>\sim 300$  km. The average distribution of compositional variations within the polar cap are thus shown in each image.

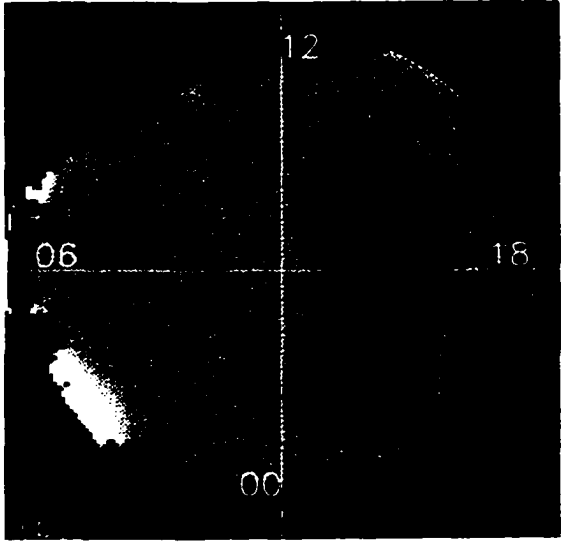
The mapped <PD> values from day 2 (Figure 5-5a) indicate a deep decrease in brightness to  $-33\%$  in the noon sector. Surrounding the polar cap is an area of increased brightness, where auroral emissions may not have been entirely excluded: the greatest <PD> values are  $+4\%$ . It is important to note that IMF  $B_z$  was northward for at least the first hour of imaging with data unavailable after 1600 UT. This may affect PD values

Figure 5-5. Average  $\langle PD \rangle$  values within the polar cap for the second orbit of each sequence. Four plots of  $\langle PD \rangle$  values within the auroral oval are shown for days 2, 3, 5, and 15 in Figures 5-5(a–d), respectively. Auroral contributions were digitally removed from each image used to calculate  $\langle PD \rangle$  values.

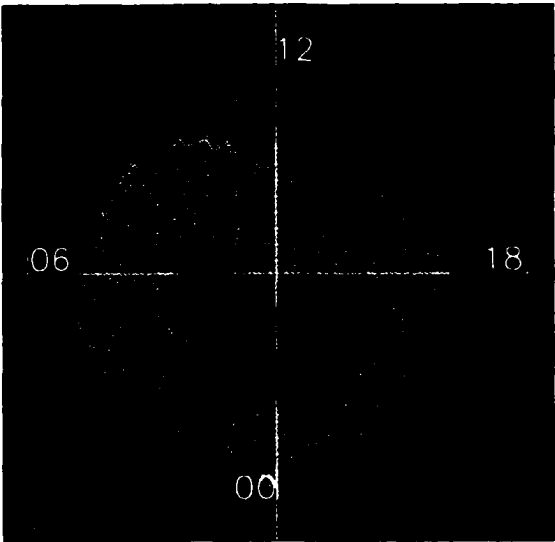
(Day 002)15:08 UT



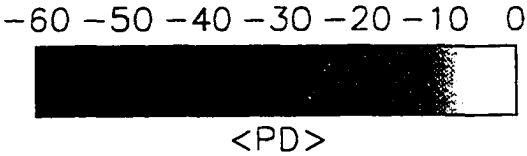
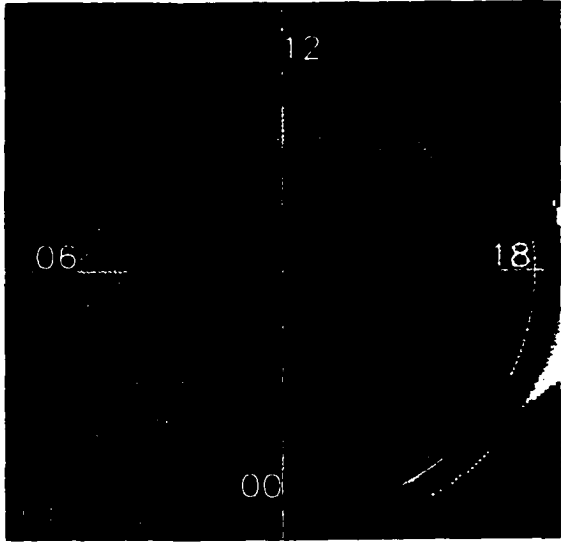
(Day 003)11:49 UT



(Day 005)13:21 UT



(Day 015)19:17 UT



within the polar cap.  $\langle PD \rangle$  values from day 3 (Figure 5-5b) show a very different pattern, with the most significant decreases ( $< -40\%$ ) in the evening sector. In this case,  $B_z$  is strongly negative throughout this period of imaging.  $\langle PD \rangle$  values from day 5 (Figure 5-5c) indicate a different distribution of dayglow variations, with decreases to  $-45\%$  in the midnight sector. No values of IMF  $B_z$  are available after 1300 UT. The plot of  $\langle PD \rangle$  values for day 15 (Figure 5-5d) shows strong decreases in the noon and evening sectors where the maximum decrease in brightness is  $-52\%$ , the most significant decrease observed in this series. Once again, no IMF  $B_z$  data are available for this period of imaging.

It is expected that IMF orientation will influence the dayglow signature of Joule heating of the thermosphere [Immel *et al.* 1997, and Chapter 4 of this thesis]. In each case, the average value of IMF  $B_y$  prior to the imaging period in the second orbit is positive (orbit following increased auroral activity), as shown in Table 5-1. This indicates that, with adequate entrainment of neutrals by ion drag forces, a dawn neutral circulation cell of greater size than the dusk cell will be present along with the associated increased noon-to-midnight velocities shifted to the dusk sector.

If the overall neutral circulation patterns at high latitudes are similar, it is not evident in the dayglow brightness decreases observed here. In particular, for the second orbit of days 2, 3, and 5 which provides images following an increase in activity from quiet times, there are three very different dayglow signatures within the polar cap. However, that there is a pattern in each mapped  $\langle PD \rangle$  image is interesting in itself, demonstrating the detection of spatial variations in thermospheric densities within the polar cap at scale sizes of  $\sim 300$  km.

That the patterns within the polar cap are different may be indicative of differences in the timing of substorm onset compared to imaging times. Furthermore, regions of Joule heating may be differently distributed about the oval in each case. Even with similar IMF values, it is not unexpected that dayglow signatures within the polar cap appear different. The five-to-seven images used to calculate the average PD values

within the polar cap are, unfortunately, insufficient to track the development and subsequent motion of dayglow decreases within the polar cap with an acceptable degree of statistical certainty. Determining the origin of dayglow decreases, tracking their apparent path, and confirming their motion due to advection by the imposed, IMF dependent, windfield requires an imager with greater temporal resolution with longer times near apogee.

#### 5.4 Summary

The DE-1 FUV images obtained during January 1983 provide excellent views of decreases in dayglow brightness directly related to compositional variations in the thermosphere generated by Joule heating in the auroral oval. This chapter concentrates on dayglow decreases within the polar cap, bounded at low latitudes by the auroral oval, and an attempt has been made to exclude auroral emissions from the analysis.

Heating during enhancements in auroral activity causes gas expansion and upwelling of lower thermospheric constituents to higher altitudes. The time scale on which this occurs is on the order of hours, as can be ascertained from DE-1 images shown in Figures 5-1 and 5-2 (summarized in Figure 5-3). Closer inspection of dayglow brightness within the auroral oval reveals deep decreases in brightness in close proximity to regions of strong Joule heating in the sunlit late-morning sector and strong gradients in PD values across the auroral oval in this area (Figure 5-4). At the same time, the IMF By values indicate the likelihood that neutral winds are directed through the heating zone and into the area of greatest brightness decrease. This indicates that DE 1 is observing perturbations of thermospheric O densities in less than an hour of a heating event, as soon as the heated gas enters the polar cap.

These observations of variations in the FUV dayglow on time scales of less than one hour provide the best temporal resolution of compositional variations obtained by an orbiting FUV imager. Nadir pointing FUV instruments aboard low-altitude polar-orbiting spacecraft recorded variations in dayglow values with temporal resolution of

one orbit period (typically ~90 minutes), but could not make multiple observations at fixed geomagnetic positions/local times.

Spatial structure within the polar cap is evident in the mapped  $\langle PD \rangle$  images presented in Figure 5-5. Whether the location of decreases in the evening and midnight sectors is due to the imposed neutral circulation or rather to Joule heating patterns is not discernible here. Imaging data were not selected which represented IMF orientations other than  $B_y > 0$ , which is due partly to the fact that the four best cases of isolated storms during this imaging period (day 350, 1982 to day 41, 1983) happened to occur during periods of positive  $B_y$ . The previous chapter addresses IMF orientation and its effect on the appearance of dayglow decreases at subauroral latitudes in the Southern Hemisphere. Many cases where  $B_y < 0$  are used in the analysis. However, in a majority of those images the polar cap falls mainly in the limb region and cannot be included in the analysis of the polar cap. In any case, imaging data with greater temporal resolution and longer imaging periods may better be able to simultaneously identify the effects of Joule (and energetic particle) heating and the advection of disturbed gas by the wind field.

## Chapter 6

### Comparison of Images, Magnetic Indices and Ground-Based Measurements

#### 6.1 Introduction

Response of the DE-1 auroral imager to the FUV dayglow has been characterized as functions of solar flux and Sun-Earth-Satellite geometry [Chapter 3]. Determinations of the effects of impulsive magnetic activity [Craven *et al.*, 1994; Nicholas *et al.*, 1996] and the influence of IMF orientation [Immel *et al.*, 1997; Chapter 5] have been made using this or related analysis techniques. A larger number of images is now surveyed with the goal of testing the utility of the model and searching for more examples of the varied effects of magnetic activity on the thermosphere. Ground-based observations of ionospheric variations are also included in this study, with the goal of establishing a relation between changes in the F2 peak electron densities at specific locations and PD values in FUV measurements.

During this 60-day period, there are several large geomagnetic storms, two of which resulted in Dst values less than -100 nT. The Dst index is an indicator of the magnitude of Earth's ring current, the equatorial drift currents which have greatest current densities four-to-six Re from Earth's surface and which increase with enhancement of convection velocities and plasma densities in the magnetosphere. As opposed to the high-latitude AE index, Dst is a measure of changes in the magnetic field at equatorial stations, and is reported in 1-hour increments. Significant excursions to negative values indicate enhanced ring currents and global geomagnetic disturbances, where the greatest ring current densities circle Earth at low latitudes and radial distances of 4–6 Re. The values of the Dst index for days 266–320, 1981, are shown in Figure 6–1 and will be referred to in this analysis. The DE-1 imaging times which are included in this analysis are indicated on the Dst plots as vertical dashed lines.

The primary source of electrons in the ionosphere is thermospheric O, via solar EUV ionization. Thermospheric storms can lower the column density of thermospheric O at middle latitudes on the dayside, as well as increase N<sub>2</sub> densities, consequently reducing

the source term for ionospheric electron production and increasing the loss term. See Chapter 1 for a detailed description of these processes. Areas where decreases in OI FUV brightness are observed in images have been shown to correlate with points in the ionosphere where the density at the F2 peak ( $N_mF2$ ) is lower than that during quiet times [Prölss and Craven, 1998]. Ionospheric perturbations are determined using ionosonde data taken from fixed ground-based stations. This chapter will expand upon that preliminary work, using the improved reference dayglow model and a significantly larger set of ground stations.

An ionosonde transmits an upward propagating EM signal and receives the time delayed echo as it sweeps through a range of frequencies (1–20 MHz is common). The frequency and time-delay information provide an ionization altitude-profile and peak ionization densities at the F1 and F2 heights. These altitudes are highly variable but easily identified. The F1 peak is the lower ionization maximum, generally occurring above 120 km, but below 180 km. This is a daytime phenomenon, as solar-ionized species at these altitudes can rapidly recombine with the ambient electrons. Without the solar EUV input, electron densities rapidly decrease. The F2 peak is a consistent ionospheric feature at all local times, as recombination rates at this altitude are much lower. Even so, the peak density can vary by a factor of three-to-four between day and night. Rishbeth and Garriott [1969] give an excellent review of ionospheric physics and observations.

A search of North American, European and Far Eastern stations for those which provide  $f_oF2$  (peak frequency of the ordinary EM mode returned from the F2 region) during the late months of 1981 yielded the select list presented in Table 6-1. These stations will be used to provide ionospheric data for comparison with FUV images. Plots of ionosonde data from four North American stations are presented in Figures 6-2a, 6-2b, and 6-2c, for September, October, and November of 1981, respectively. Data from four European stations are likewise presented in Figures 6-3a, 6-3b, and 6-3c, for the respective months. Finally, data from six Russian (Far Eastern) stations are shown in Figures 6-4a, 6-4b, and 6-4c, again for the months of September, October, and

**Table 6-1: Ionosonde Stations in Figures 6-2–6-4**

Station	Latitude	Longitude
<i>North America</i>		
Boulder	40.0° N	105.4° W
Churchill	58.7° N	94.2° W
Ottawa	45.3° N	75.6° W
Wallops	37.7° N	75.5° W
<i>Europe</i>		
Poitiers	46.7° N	0.2° E
Kiruna	67.9° N	20.1° E
Moscow	55.8° N	37.6° E
Archangel	64.4° N	40.5° E
<i>Far East</i>		
Tomsk	56.5° N	84.9° E
Irkutsk	52.5° N	104.0° E
Yakutsk	62.0° N	129.5° E
Khabarovsk	47.5° N	135.0° E
Magadan	60.0° N	151.0° E

November of 1981. Each  $f_oF2$  trace is color coded, corresponding to a particular station listed at the left of each figure. For reference to day numbers, the dates September 1–30 correspond to days 244–273, October 1–31 corresponds to days 274–304, and November 1–30 corresponds to days 305–334.

The parameter  $f_oF2$  is proportional to  $(N_mF2)^{1/2}$ , and at this time the variations in either parameter will suit the purpose of monitoring day-to-day ionospheric variations. Frequency information is shown in the summary plots of ionosonde data and provides just as valid an indicator of ionospheric disturbance as the calculated value of  $N_mF2$ . For comparison to PD values later in this chapter, the maximum electron densities are calculated in order to determine percent deviations of measured densities from monthly mean densities.

## 6.2 Data Selection and Processing

This work uses dayglow images selected from the first 60 days of the DE-1 imaging mission. This period is marked by several intense geomagnetic storms, as well as days of very low activity, and several periods of continuous substorms. The images, obtained with the 123-nm filter, are taken in 72 orbits from satellite positions which maximize spatial resolution and coverage of the sunlit Earth in the instrument's field-of-view. Three consecutive images were systematically selected and processed from each orbit using a pre-apogee satellite altitude of  $\sim 3.0 R_e$  as a primary criterion. During many orbits, filter #2 was not used at all, or was used at other times in the orbit. Images from these times are not included as they contribute little to this analysis. This results in gaps in coverage of up to two days in length which are evident in Figure 6-1 and the AE indices to follow.

PD representations of the three consecutive images from each orbit were mapped to geographic coordinates and averaged to produce  $\langle PD \rangle$  values with reduced statistical variation, a method similar to that used for the polar cap images of Chapter 4. The  $\langle PD \rangle$  values for each resulting image are shown in an orthographic projection of geographic coordinates (centered at  $50^\circ$  geographic latitude and local noon) in Figures 6-5(a–h).

with nine images shown in each figure. The AE indices for the appropriate period of time, including the day prior to that of the first image (Figure 6-5a only), are shown above the mapped images. Times at which the three image sequence began are marked by vertical dashed lines in the AE plots. A summary of the imaging days presented in each of these figures is given in Table 6-2. All available images are presented here, with images showing brightness variations at geographic locations in two- or four-day time intervals selected for further discussion. Additional discussion is limited to images which offer additional insight to earlier work or sections of this thesis. This chapter presents a large body of data which can be referenced at a later time.

The daily variation in  $f_oF2$  for each ionosonde station is due to the variation in electron density with solar zenith angle. Stations at lower latitudes usually report greater peak  $f_oF2$  values; with the time of the peak (or peaks) in Universal Time depending primarily on the longitude of the station. For the purposes of this study, the important parameters are the deviation from the daily trend of electron densities at any given station, and the relative difference in  $f_oF2$  values between stations. The baseline daily trend is inferred from values obtained during periods of low magnetic activity. Median hourly values would provide this but are not shown, avoiding the added complication of plotting median hourly values for four-to-five stations in addition to the observed values. Ionosonde stations are indicated in the mapped <PD> images by the *first two letters* of the corresponding station, not their proper international geophysical designation. This is for ease of reading. The letters are centered just above the station location. Average brightness <PD> values for ionosonde stations are obtained from an  $\sim 2^\circ \times 2^\circ$  area about the location of the station, which results in uncertainties of  $\sim 3\text{--}4\%$  in <PD>, depending on the actual photometer response.

### 6.3 Discussion of Images in Survey

#### 6.3.1 Days 267 and 269, 1981

These two days provide an excellent opportunity for comparisons of thermospheric conditions over the Far East and North America, with repeated imaging over each sector.

**Table 6-2: List of Days for Figure 6-5**

Figure 6-5	Range of Days	Range of Dates (1981)
a	266–272	September 23–September 30
b	272–280	September 30–October 7
c	280–290	October 7–October 17
d	290–296	October 17–October 23
e	297–304	October 24–October 31
f	305–311	November 1–November 7
g	312–317	November 8–November 13
h	318–325	November 14–November 21

With the  $\sim 6.85$  hour orbital period, the satellite is in nearly the same location above Earth every 48 hours. The difference in local time at these locations on the Earth is only eight minutes. Thus, images obtained 48 hours apart offer an excellent opportunity to compare  $\langle PD \rangle$  values to data from fixed ionosonde stations. Figure 6-5a contains two pairs of images obtained exactly two days apart (between days 267 and 269) where the same ionosonde stations are in the field of view of the imager. The first pair was taken at  $\sim 0400$  UT and shows the dayglow signatures over the Far East on days 267 and 269. The second pair, at  $\sim 1700$  UT on the two days, shows the dayglow signature over North America. These provide an example of the correspondence between ionosonde and dayglow signatures.

Images taken beginning at 0405 UT, day 267 (24 September), over the Russian Far East (top center panel of Fig. 6-5a) show small areas of decreased brightness at high subauroral latitudes extending from Archangel to Magadan. Weak decreases in brightness are observed over Tomsk, Irkutsk and Khabarovsk, with  $\langle PD \rangle$  values of  $-8\%$ ,  $-7\%$ , and  $-10\%$ , respectively. The higher latitude stations Yakutsk and Magadan each show  $\langle PD \rangle$  values of  $-14\%$ . This follows a period of low auroral activity, as evidenced in the AE plots. Two days later, at 0347 UT on day 269 (26 September), the general level of auroral activity has increased and decreases in brightness are now evident over a larger part of Siberia (right center panel of Fig 6-5a). The stations at Yakutsk and Magadan are clearly within a large area of  $< -20\%$  decreases in dayglow brightness, with  $\langle PD \rangle$  values of  $-22\%$  and  $-27\%$ , respectively, where Tomsk, Irkutsk, and Khabarovsk are well outside of this region.  $\langle PD \rangle$  values at these stations have actually increased to  $-3\%$ ,  $-5\%$ , and  $-9\%$ , respectively.

The ionosonde data for these five stations are shown in Figure 6-4a. Days 267 and 269 correspond to September 24 and 26, 1981, respectively. The ionosonde stations report similar maxima in  $f_oF2$  values at early UTs on day 267. The maximum is reached first at Khabarovsk and proceeds to stations farther west. This trend is evident in the several days preceding day 267 during the period of low magnetic activity. The following two days depart from this trend, with Yakutsk and Magadan reporting  $\sim 35\%$

decreases in peak  $f_oF2$  on day 269 relative to day 267 values. Tomsk and Khabarovsk, on the other hand continue to report  $f_oF2$  values similar to those reported two days earlier. This compares well with the observed dayglow decreases over the northernmost stations.

Another pair of image sets obtained on the same two days, but each beginning at 1724 UT, reveals a similar positive comparison between decreases in  $\langle PD \rangle$  and  $f_oF2$  values in the North American sector. Decreases in FUV brightness in the high latitude morning sector are evident in the mapped  $\langle PD \rangle$  image of day 267 (also presented in Chapter 4 and Immel *et al.* [1997]). The region of 20% decreases does not extend to any of the three ionosonde stations noted in the figure. The onset of intense auroral activity beginning at ~0800 UT on day 269 results in a large area of decreased FUV brightness over North America. Ottawa and Boulder are within the area of 20% dayglow brightness decrease, but not Wallops. Churchill is well within the area of decreased brightness and is located very close to the auroral oval.

Ionosonde data from these stations indicate  $f_oF2$  values on day 267 which reflect no strong deviation of ionospheric densities from the normal daily trend at any station, though peak values are lower at higher latitude stations. A disturbance is evident on day 269, with Boulder and Ottawa stations showing the lowest values of  $f_oF2$ . The two-day percent decrease in peak  $f_oF2$  values is ~10–15% at all stations, but the time histories show greater overall perturbation at Boulder and Ottawa than at Wallops. There are intermittent observations from Churchill which indicate decreases in  $f_oF2$  values on the order of 40–50%, as well as a transient increase which may be due to auroral precipitation.

Percent differences in observed electron densities from monthly mean values,  $PD(N_m)$ , are calculated using the same method as Prölss [1980], as discussed in Chapter 1, at each Far-Eastern and North American ionosonde station discussed here. The  $\langle PD \rangle$  and  $PD(N_m)$  values are compared at each station and are shown in Figure 6-6 for values on day 267 (asterisks) and day 269 (filled circles). The trend toward more negative  $PD(N_m)$  values with decreased brightness is evident. The datum from Churchill on day 269 is excluded, due to the possible contamination of PD values by auroral emissions.

These examples provide some indication of a positive correlation between decreases in FUV dayglow brightness and ionospheric electron density. One should also note the absence of any clear trend in the data for  $PD(N_m) > \sim 20\%$ , which are all from day 267. The apparent covariation of these two parameters is only evident where  $N_m$  values are near or below monthly mean values. This suggests that FUV measurements can provide an indication of variations in ionospheric electron densities only during negative ionospheric storms, similar to  $R(O/N_2)$ .

### 6.3.2 Quiet Period of Day 291, 1981

Several images were excluded from the original quiet-time set [Chapter 3] as they demonstrated decreases to  $< -20\%$  in brightness at high latitudes, even though the quiet-time criteria of low magnetic activity was met. This is the case for images obtained on day 291 (October 18), which were examined in Chapter 3. The available ionosonde data is reviewed in order to determine if an ionospheric disturbance accompanied the dayglow decreases. Dayglow decreases observed in three images taken beginning at 1649 UT, shown in the upper-right panel of Figure 6-5d, demonstrates an area of decreased dayglow brightness in the noon sector. Decreases of  $< -20\%$  extend to the latitude of Ottawa. This is an interesting dayglow signature, given the very low level of activity preceding the time of the image.

The day-291 ionosonde data for Ottawa, Churchill and Wallops (no Boulder data are available) are shown in Figure 6-2b and for Far Eastern stations in Figure 6-4b. For days during which magnetic activity is very low, Wallops and Ottawa often have very similar ionosonde traces. This is the case on day 291 (October 18), where the hourly  $f_oF_2$  values for the two stations are nearly identical for the third consecutive day. These data indicate that electron densities are relatively unaffected by geomagnetic activity on these three days (289, 290, and 291). The similarity between these two stations may be seen in the ionosonde data for any quiet day selected for the analysis in Chapter 3 (e.g., October 31, Figure 6-2b (day 304) and November 13, Figure 6-2c (day 317)) except for day 266.

which was also excluded from the determination of the quiet-time response due to the presence of strong dayglow decreases at high latitudes.

Churchill, the northernmost station, demonstrates no significant deviation from the daily trend in  $f_oF2$  values. This is significant in that Churchill is very close to the auroral oval and tends to show variations in  $f_oF2$  values after the weakest of magnetic events. Furthermore, it is well within the area of apparent 20% decreases in dayglow brightness.

The explanation of the apparent decrease in dayglow brightness given in Chapter 3 is based on the fact that values of  $F_{10.7}$  for this day are the highest observed in the period in which the 156 quiet-time images were obtained. The decrease in brightness with increasing azimuth angle of observed pixels is attributed to inordinately high effective emission altitudes due to the effect of strong solar EUV flux on the thermosphere, not to magnetic activity. Hence, it is a geometric effect for which the model cannot correct in the absence of accurate EUV flux measurements. The ionosonde data confirm that there is no upper atmospheric disturbance present at this time.

### 6.3.3 Storm Period of Days 293 – 296, 1981

The DE-1 images obtained during the geomagnetic storms of days 293 and 295 (October 20 and 22, 1981) are marked by strong dayglow decreases over large areas of Earth. Images from day 295 were investigated by Craven et al. [1994]. Ionosonde data from Europe (day 293) and North America (day 295) show extremely strong decreases in  $f_oF2$  values during this storm period.

Three PD images from day 295 taken at times beginning at 1644 UT are averaged and shown in the lower-center panel of Figure 6-5d. Dayglow decreases are observed throughout the now large polar cap and at mid-latitudes, with  $< -20\%$  decreases in brightness extending as far south as Mexico at  $\sim 1000$  LT. The decreases do not extend so far south at the noon meridian, where the  $-20\%$  level is  $3-4^\circ$  north of Wallops. The stations at Ottawa and Boulder are well within the area of 20% decreases, showing  $\langle PD \rangle$  values of  $-32$  and  $-28\%$ , respectively. Wallops shows a surprisingly small

deviation from quiet-time values of  $-3\%$ . Churchill is in an area of auroral emissions and just within the polar cap with a  $\langle PD \rangle$  value of  $-19\%$ .

North American ionosonde  $f_oF2$  values for day 295 (October 22) are shown in Figure 6-2b. Boulder and Ottawa show the most significant decreases in  $f_oF2$  for the day, with a  $\sim 70\%$  decrease at Boulder (from the previous day) and a transient increase at Ottawa around the time of imaging. The source of the transient increase at Ottawa is not known. Whether this is a traveling ionospheric disturbance (TID) or result of interference in the measurement by auroral precipitation cannot be determined. Wallops shows a decrease in  $f_oF2$  values of  $\sim 40\%$  from the previous day and Churchill provides very intermittent data which are not useful for this analysis.

The correspondence between the magnitude of brightness decreases over ionosonde stations and the  $f_oF2$  decreases is striking. The percent decreases observed at Boulder and Ottawa are much greater than those observed at Wallops, while the ionosonde data suggest that electron densities over Wallops are highly affected by the storm. Wallops is close to the limb region in the 1644 UT image, and it is possible that limb brightening is now greater at the edge of the disk region than in quiet times. This would occur if  $N_2$  scale heights were affected at mid-latitudes, increasing the brightness of LBH emissions as  $N_2$  densities increase in the F region. The model of Chapter 3 includes a linear  $\sim 10\%$  correction to  $\langle r \rangle$  values to account for increased photometer response with spacecraft zenith angle. It appears to be insufficient in this case.

As is clear from the North American ionosonde data and DE-1 images, these storm effects (reduction of OI brightness, decreases in  $f_oF2$ , possible increases in  $N_2$  emissions) represent a greater deviation from quiet times than those of day 269 (Section 6.3.1). Although the storms appear similar in magnitude (by the AE index), the disturbance on day 295 is much more intense. The one-hour Dst indices of Figure 6-1 show that the day 295 event is a classic geomagnetic storm, as is the event on day 293, while the event of day 269 may be more aptly described as a series of intense substorms accompanied by a gradual increase in magnetospheric convection and ring current intensity.

Examining other ionospheric data for this period, no significant changes in the daily  $f_oF2$  trend are observed at Poitiers (Figure 6-3b) or Khabarovsk (Figure 6-4b) after either the day 293 event or that of day 295. It is interesting to note that on day 270, Poitiers reported an ~30% decrease in  $f_oF2$  values (see Figure 6-3b), one of the few significant decreases observed at that station in this entire study period. Furthermore, similar decreases in  $f_oF2$  values are seen at Khabarovsk, the only station farther south in magnetic latitude than Poitiers. Unfortunately, no 123-nm imaging data from day 270 are available to confirm a disturbance in the FUV dayglow. Also interesting is that  $f_oF2$  values are not nearly so perturbed at Tomsk or Moscow on this day, two stations located practically on the great-circle route between Poitiers and Khabarovsk, and at higher magnetic latitudes. This suggests the presence of decreases in O and electron densities well away from the high latitude Joule heating region.

#### 6.3.4 Days 307 and 311, 1981

Although the images presented here are separated by 96 hours, they show another fine comparison between dayglow decreases and ionospheric perturbations. There are actually two image pairs, one taken at early UTs when Yakutsk and Magadan are on opposite sides of the noon meridian and another taken at very late UTs (of the same day) when the Bering Strait is at the noon meridian and four of the five Far Eastern stations have entered the dayside hemisphere. The level of activity on day 307 (November 3) is low, but does not meet the quiet-time condition used in Chapter 3. In the four days that follow, the level of activity increases slowly, with the highest level of activity on day 311 (November 7).

Images from these times are shown in Figure 6-5f, with the two images from day 307 in the second row and the two from day 311 in the bottom row. Decreases in brightness to  $< -20\%$  are not evident in either image of day 307, though decreases of  $\sim 10\%$  are visible at the higher latitude ionosonde stations at 0248 UT (e.g.,  $\langle PD \rangle = -13\%$  at Yakutsk), but not later at 2324 UT ( $\langle PD \rangle = -2\%$  at Yakutsk)

Increases in brightness on the order of ~10% are observed to the south and east of Irkutsk ( $\langle PD \rangle = 3\%$ ) at 0245 UT on day 311. Other stations are located farther from this region of brightness with Magadan and Yakutsk showing  $\langle PD \rangle$  values of  $-3\%$  and  $-1\%$ , respectively. Near the end of the day, and after an extended period of moderate magnetic activity, an area of 20% decreases in brightness is seen at sub-auroral latitudes centered over the Bering Sea. This is a highly localized decrease, with PD values of  $-14\%$  and  $-9\%$  at Magadan and Yakutsk respectively.

Ionosonde data show only slight disturbances in  $f_oF2$  values on day 307, with Yakutsk not reporting, but Magadan indicating a transient ~15% decrease at ~0500 UT. Ionospheric conditions are remarkably consistent for the next three days, with no strong deviations from the smoothly varying trend indicative of periods of low magnetic activity. The only change in the trends during this period is that Tomsk reports the highest maximum  $f_oF2$  values of all the stations on days 307–310, but the lowest values on day 311. The trend at the other stations is interrupted at ~0000 UT, when  $f_oF2$  values peak at Khabarovsk, while beginning to decrease at Magadan. Meanwhile, Yakutsk appears unaffected, closely following the trend of the previous days.

During periods of magnetic activity, decreases in  $f_oF2$  show correspondence with dayglow decreases. It can be inferred that no decrease in dayglow brightness occurred over Yakutsk from this imaging time through the next day, while dayglow decreases over Magadan remain strong or increase on day 312 (November 8), as evidenced in the ionosonde data for that day. This disturbance cell is similar to that described by Schoendorf et al. [1996], as it is well out of the polar cap and isolated from other disturbance zones. Furthermore, it adjoins areas of increased brightness and electron densities (from  $f_oF2$  at Tomsk and Yakutsk). The inferred decrease in O density in this area is matched by areas where increases in brightness and  $f_oF2$  suggest increases in O. This is in contrast to observations on days 267 and 269 where deviations of  $f_oF2$  above monthly mean values are shown not to correspond well with increases in brightness. Localized increases in FUV brightness have been observed previously by Nicholas [1993] and Nicholas *et al.* [1997], but in a limited number of cases.

This correspondence of highly localized decreases in dayglow brightness with highly localized variations in electron density demonstrate that small areas of decreased brightness in the FUV images reflect real variations in electron densities that are observable from ground stations. The observation of increases in electron density which are matched by increases in FUV brightness indicate that cases exist where increases in ionospheric electron densities may be related to increased O densities, in contrast to results from other days of this study.

#### 6.3.5 Days 312–325, 1981

This set of images clearly demonstrates a trend in the <PD> values observed in the images of this survey; that is, the decreasing effect of magnetic disturbances at middle latitudes as observations are made nearer to the winter solstice. This then supports the results of thermospheric modeling by Fuller-Rowell *et al.* [1996] and of studies by satellite gas-analyzers [Prölss, 1980] which show that magnetic activity has a much weaker effect on sub-auroral thermospheric composition in the winter than at equinox or in the summer. Without the enhancement of conductivity by solar EUV radiation, Joule heating is not as great in the winter hemisphere. Furthermore, the polar cap is farther into the nightside, where anti-sunward neutral winds across the terminator are less apt to transport composition disturbances out of the polar cap to mid-latitudes. Fuller-Rowell *et al.* [1996] clearly demonstrate the expected difference in thermospheric perturbations between solstice and equinox conditions. Figure 1-11 of this thesis (from Fuller-Rowell *et al.*, [1994]) show the effects of a storm in the summer hemisphere, which extend much farther equatorward than a similarly intense storm simulated for the winter hemisphere.

The <PD> images shown in Figure 6-5g and 6-5h were obtained mostly during periods of moderate-to-intense magnetic activity and varying orientation of IMF  $B_y$  (from ISEE 3, not shown). The AE index exceeds 1000 nT at least once on each of the days 312, 315, 316, 318, 321, and 322. The  $D_{st}$  index indicates significant increases in

Earth's ring current on days 315–316, 318 and 321. By any account, this period is marked by significant magnetic events.

There are no large areas (*e.g.*, days 269 or 293) of decreases to  $< -20\%$  in FUV dayglow brightness observed in the morning sector at any time in the series of images. Small areas of decreased dayglow brightness of this level are visible near the noon sector on day 312 (Figure 6-5g, top-center panel), within the polar cap on day 315 (Figure 6-5g, center panel), in the morning-to-noon sector of day 316 (Figure 6-5g, bottom left panel), and within the polar cap on day 323 (Figure 6-5h, bottom center panel). The appearance of these decreases is in good temporal agreement with the increased magnetic activity. Mid-latitude decreases on the order of 10% can be observed in several other images. These decreases, at 1259 UT on day 312, 2309 UT on day 321, and 1000 and 1622 UT on day 323, also are observed after significant activity.

#### 6.4 Summary

The survey of images presented here tests the ability of the reference model to produce photometer responses for comparison with images obtained during periods of greatly varying solar flux ( $F_{10.7}$ ) and magnetic activity (AE and  $D_{st}$ ). Aside from increased limb brightening during periods of strong magnetic disturbances (*e.g.*, Day 295), the quiet-time dayglow model developed in Chapter 3 provides a good reference for measuring the level of compositional perturbation in the thermosphere. Overall, most  $\langle PD \rangle$  values observed are negative, with few large areas of increased brightness observed. This is normal, as magnetic activity has the effect of (1) reducing O column densities and (2) increasing  $N_2$  scale heights. Both of these will result in a reduction of the OI 130.4-nm emission, which dominates the DE-1 FUV response when using the 123-nm filter.

Increases in  $N_m$  over monthly mean values can be on the order of 50%, where such increases in OI FUV brightness are never observed (aside from the auroral zone). The comparison of  $\langle PD \rangle$  values to  $PD(N_m)$  from images over the Far East and North America on days 267 and 269 demonstrate that variations in dayglow brightness better

reflect variations in  $N_mF2$  during periods where both show decreases below mean values. The relation between  $\langle PD \rangle$  and  $PD(N_m)$  where values of  $PD(N_m)$  are below +20% show a roughly linear relationship, with a variance lower than the set of points as a whole. All points are at negative values of  $PD$ , where  $PD(N_m)$  can be largely positive. This corresponds well with the conclusions of Prölss and von Zahn (1974), that perturbations in  $O/N_2$  ratios are not responsible for positive ionospheric storms. It is logical that only negative ionospheric storms have a FUV signature.

This work provides several more qualitative comparisons between dayglow brightness decreases and localized measurements of decreases in ionospheric electron density. Gradients in the  $\langle PD \rangle$  values in images correspond to variations in the relative level of  $f_oF2$  values. Images from day 295 and day 311 show qualitative agreement between dayglow brightness decreases and the associated ionospheric disturbances observed in ground-based observations. This set of images was taken during a period of only moderate activity, but demonstrates a degree of structure in the upper atmosphere which is not often seen in images obtained during larger magnetic events.

The ionosonde data confirm that dayglow decreases observed on day 291 are not due to the varying levels of geomagnetic activity of previous days, as little disturbance is observed in ionospheric electron densities for several days up to and including the time of imaging. Rather, the decreases are attributed to the inability of the reference model to correct for the high effective emission altitude that follows extreme, though briefly maintained, levels of solar radiation flux at Earth.

Studies of the dayglow variations on days 307–311 and 312–325 provide possible confirmation of modeling work by Schoendorf *et al.* [1996] and Fuller-Rowell *et al.* [1996]. Further study should include model runs using AE as a basis for the auroral energy inputs measured on these days, in the attempt to reproduce the observed variations in thermospheric composition and electron densities (for days 312–325). IMF data are available on these days to aid in providing the requisite magnetospheric inputs.

A useful addition to this study would be an investigation of the correspondence of dayglow decreases with changes in the F1 electron densities, via the  $f_oF1$  measurements.

This parameter provides a measure of electron densities at altitudes where photoelectron excitation of OI emissions is also great, but where  $N_2$  densities are also much higher than at the F2 peak. This could provide information useful in further investigation of anomalous decreases in OI dayglow brightness, such as those observed on day 291. Unfortunately, many ionosonde stations contributing to the ionospheric database did not measure or record this value on these study days. Only the values of  $f_oF2$  have been used in this chapter.

Figure 6-1. Dst index for the period under investigation. The hourly values of the Dst magnetic index are shown for 55 consecutive days of 1981. Vertical dashed lines indicate times at which DE-1 images used in this study were obtained. Significant geomagnetic storms are indicated by sudden decreases in Dst values on days 287, 293 and 295 (October 14, 20 and 22, respectively).

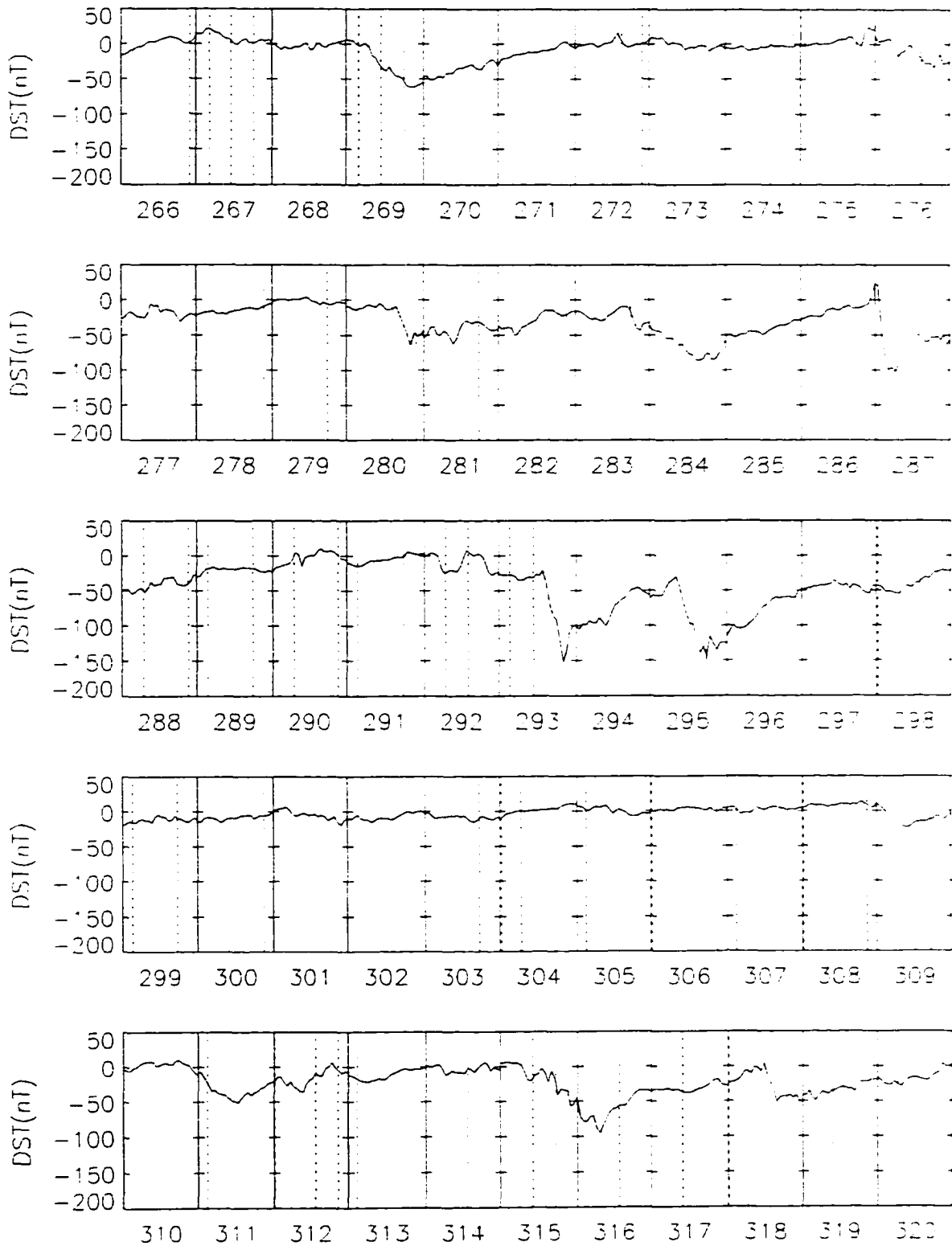


Figure 6-2. Ionosonde  $f_oF2$  values for selected stations in North America. (a) Hourly values of  $f_oF2$  for Boulder, Churchill, Ottawa and Wallops for September, 1981. Following pages: (b) same for November, (c) same for December.

Figure 6-2a.

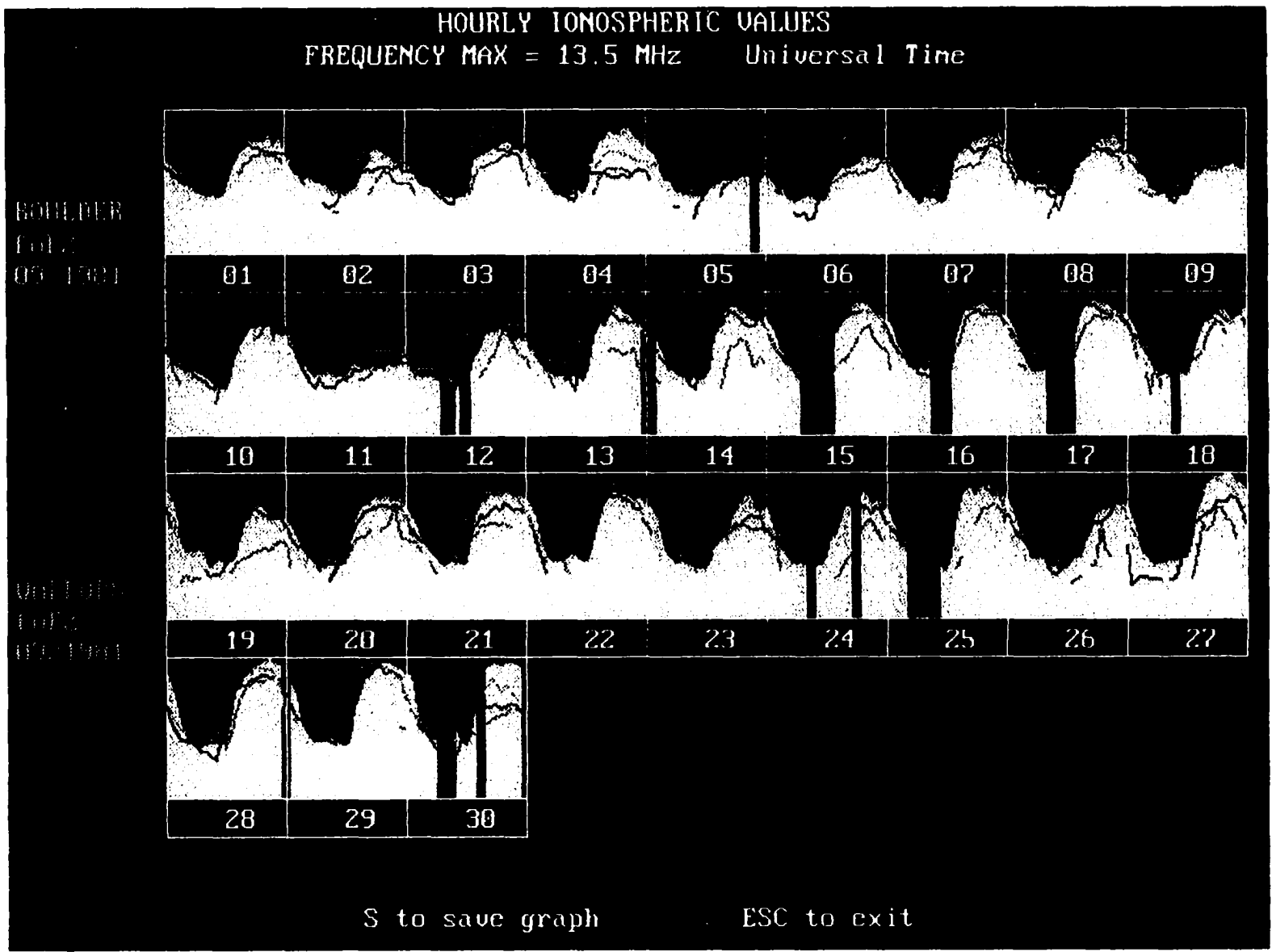
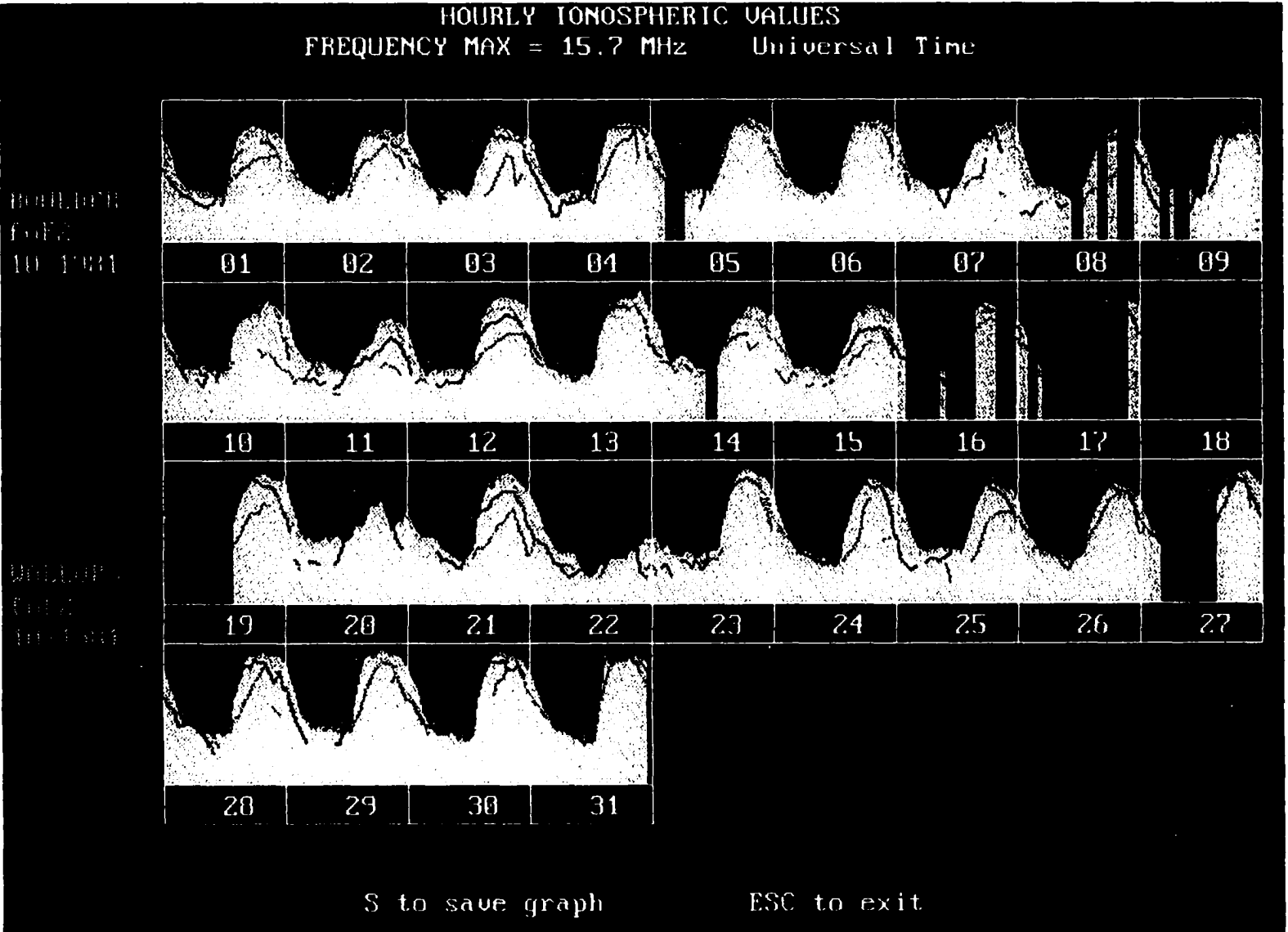


Figure 6-2b. See Figure 6-2a for description.



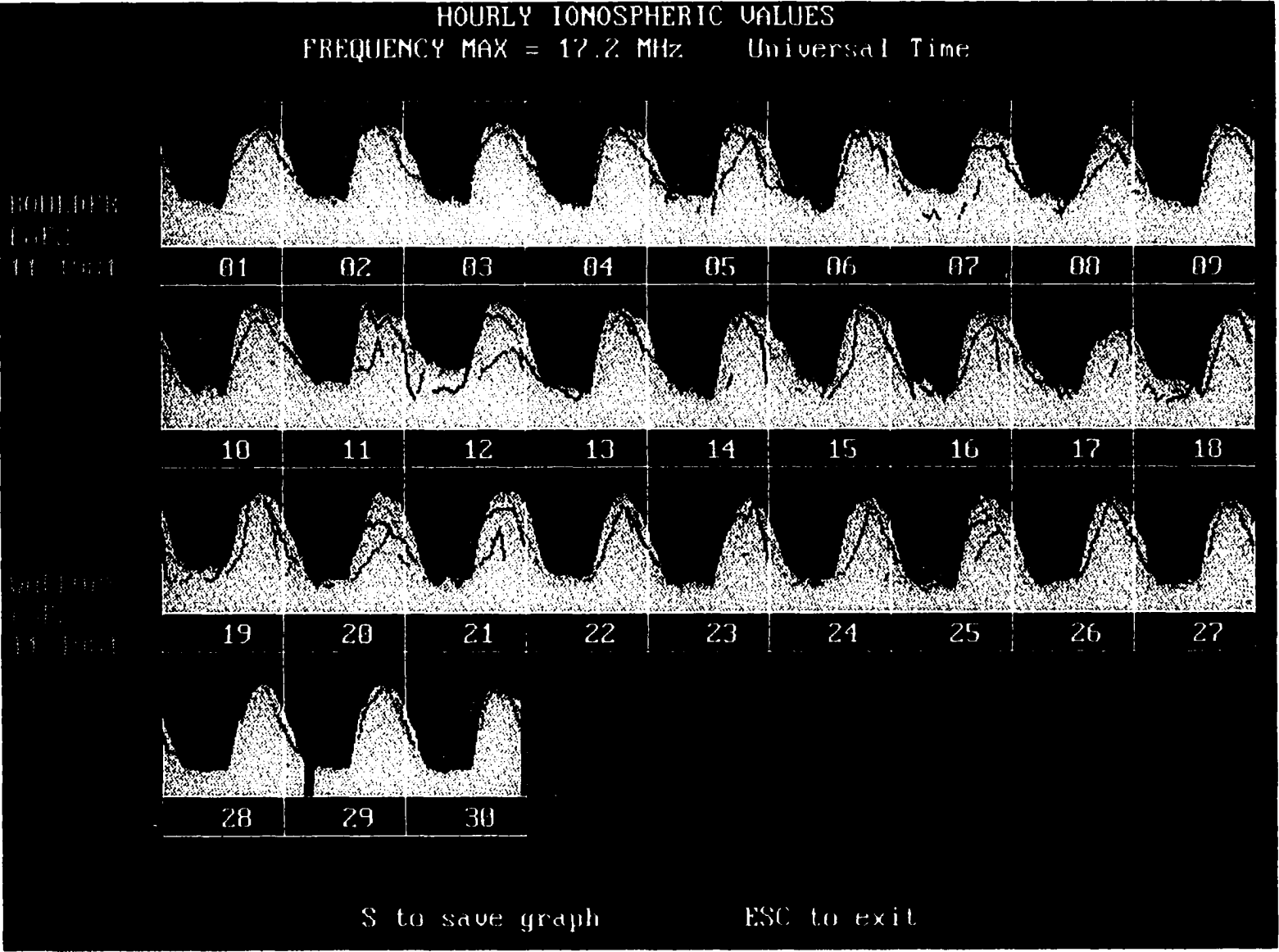


Figure 6-2c. See Figure 6-2a for description.

Figure 6-3. Ionosonde  $f_oF2$  values for selected stations in Europe. (a) Hourly values of  $f_oF2$  for Kiruna, Archangel, Moscow and Poitiers for September, 1981. Following pages: (b) same for November, (c) same for December.

Figure 6-3a.

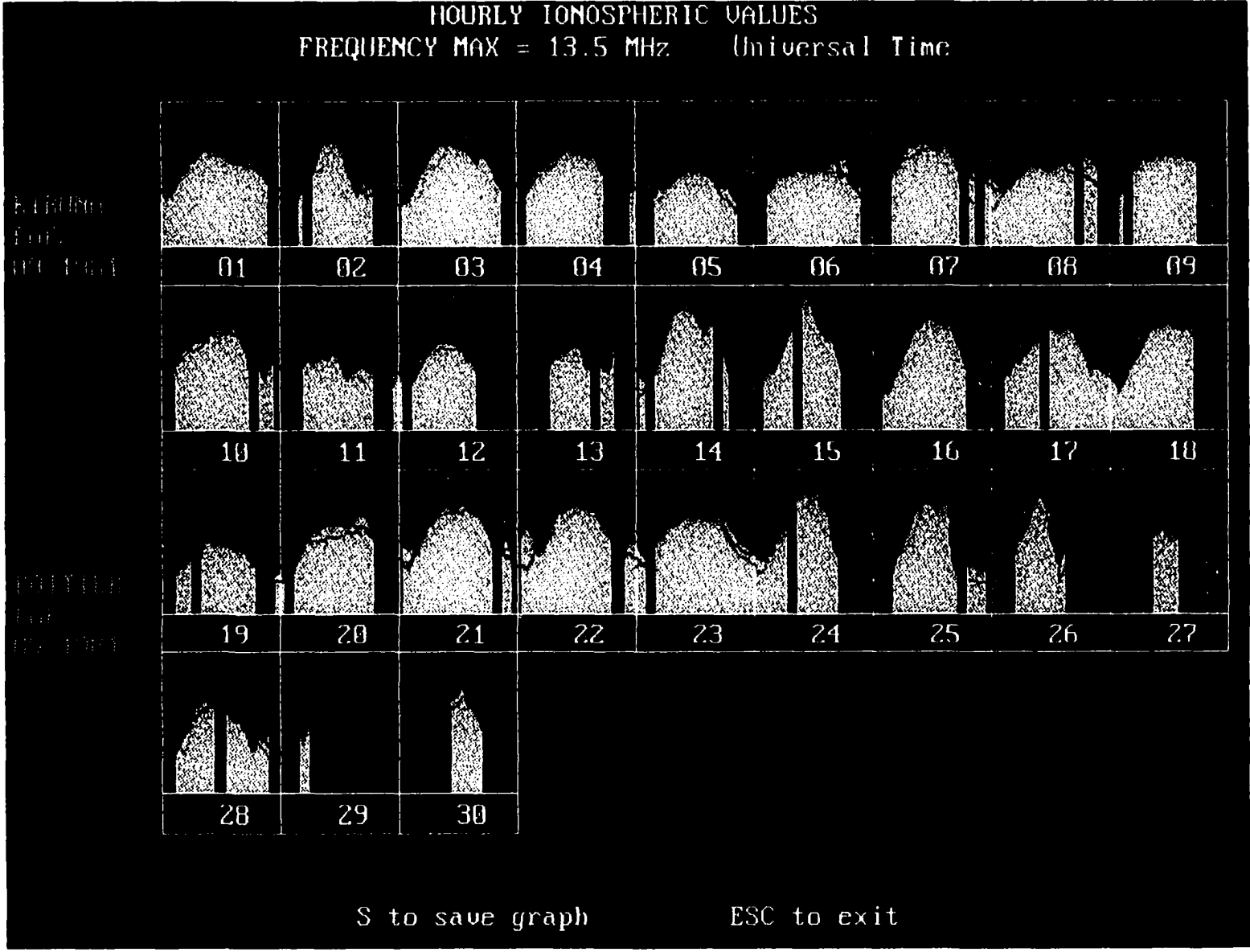


Figure 6-3b. See Figure 6-3a for description.

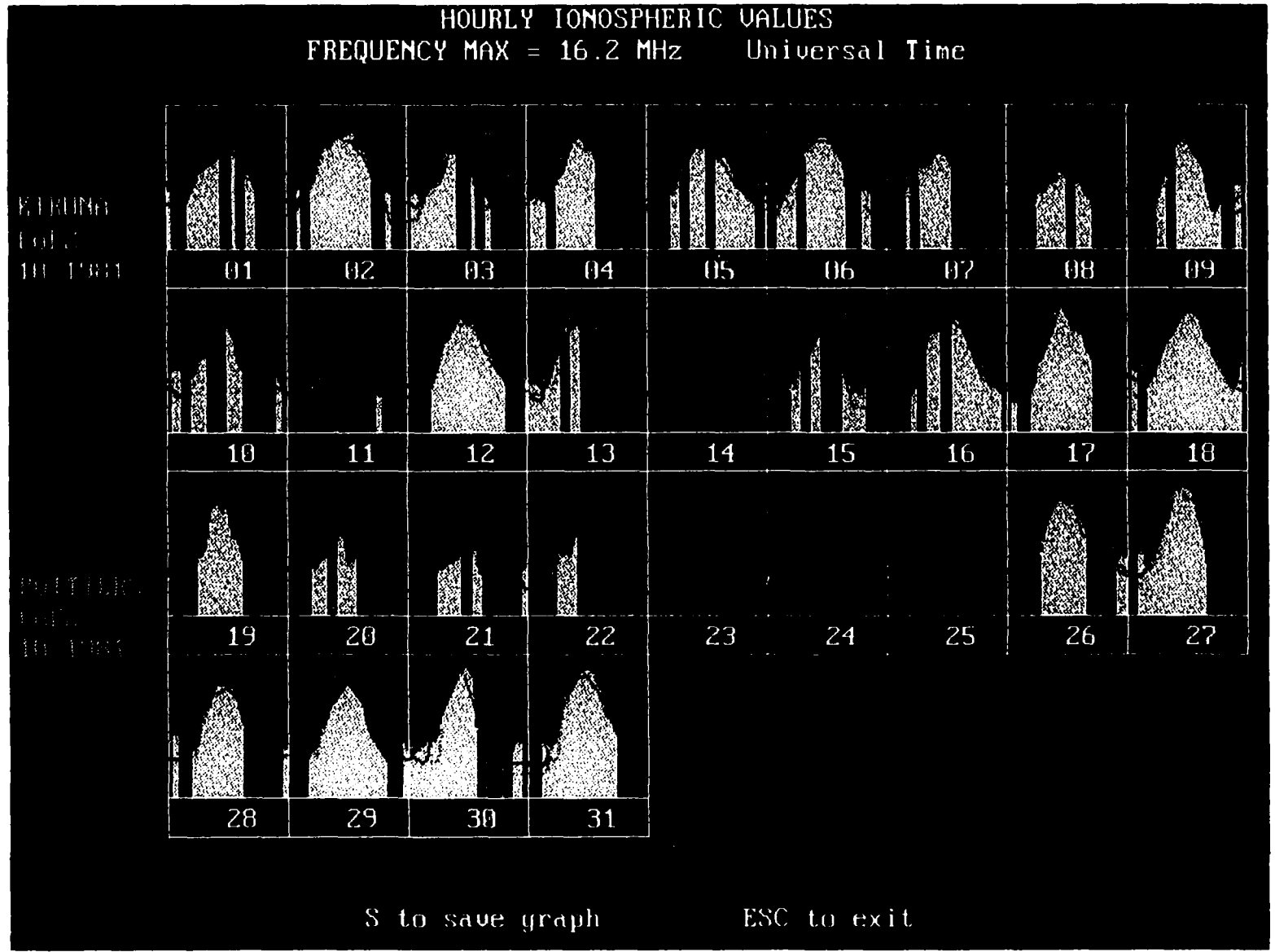


Figure 6-3c. See Figure 6-3a for description.

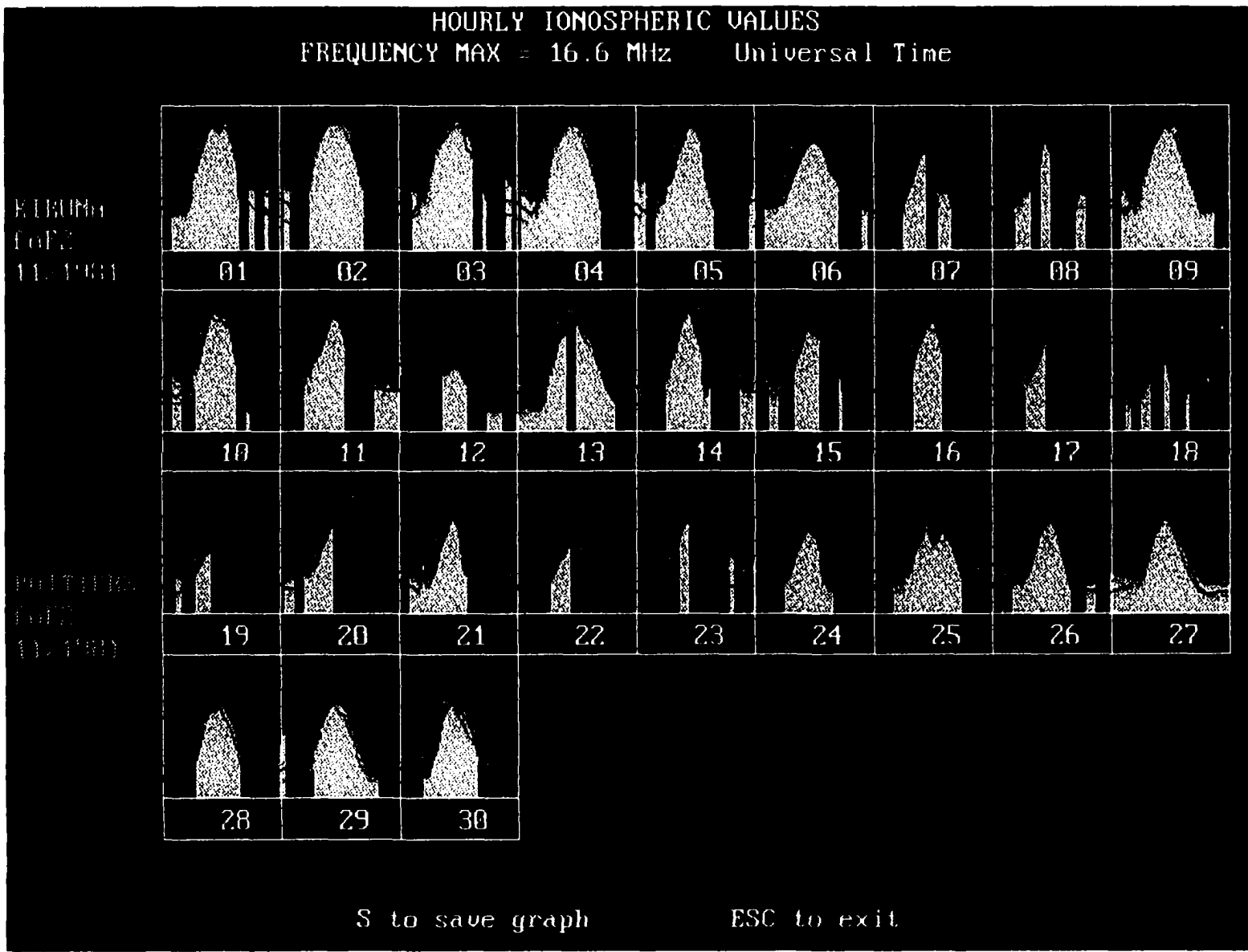


Figure 6-4. Ionosonde  $f_oF2$  values for selected stations in the Far East. (a) Hourly values of  $f_oF2$  for Tomsk, Irkutsk, Yakutsk, Magadan and Khabarovsk for September, 1981. Following pages: (b) same for November, (c) same for December.

Figure 6-4a.

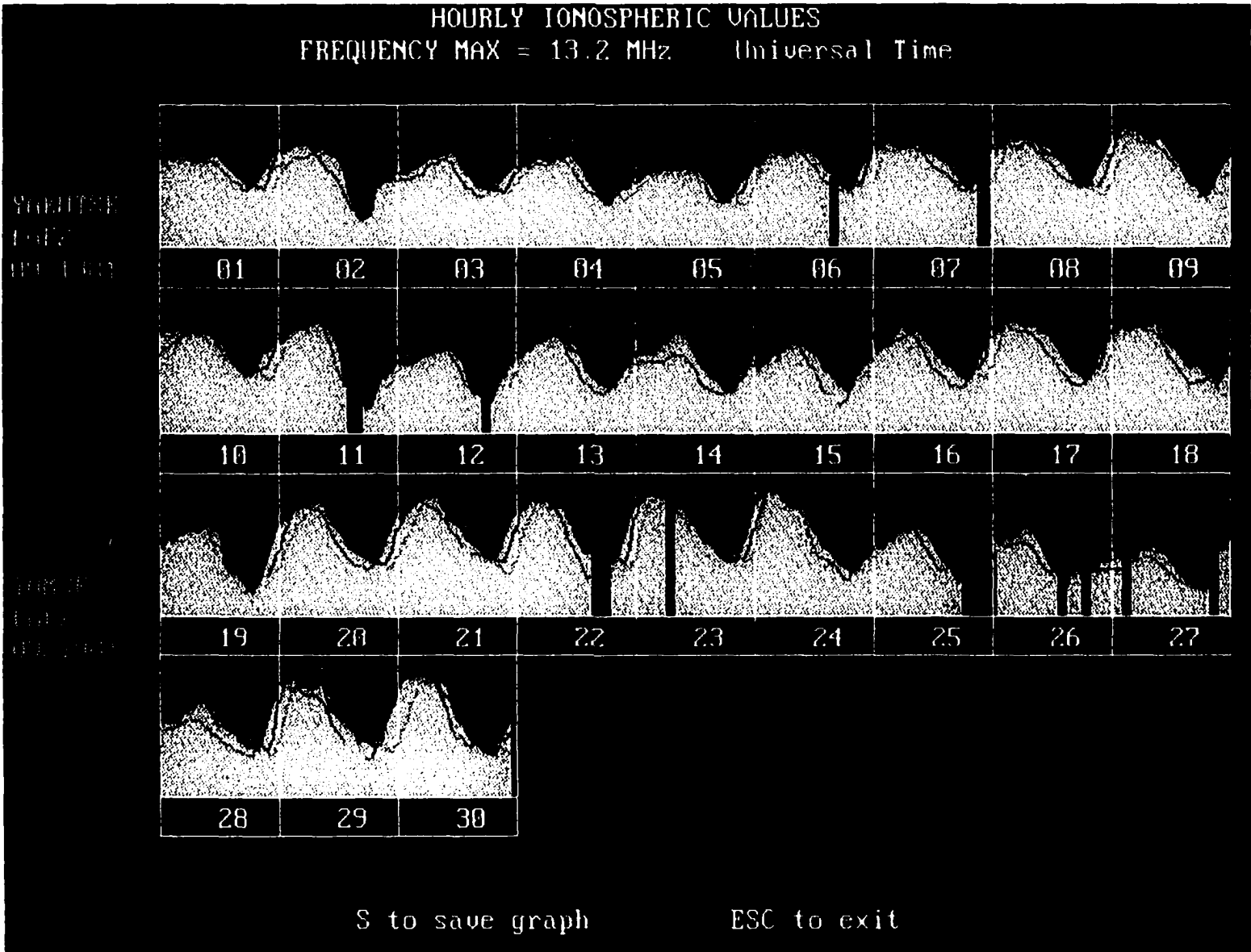


Figure 6-4b. See Figure 6-4a for description.

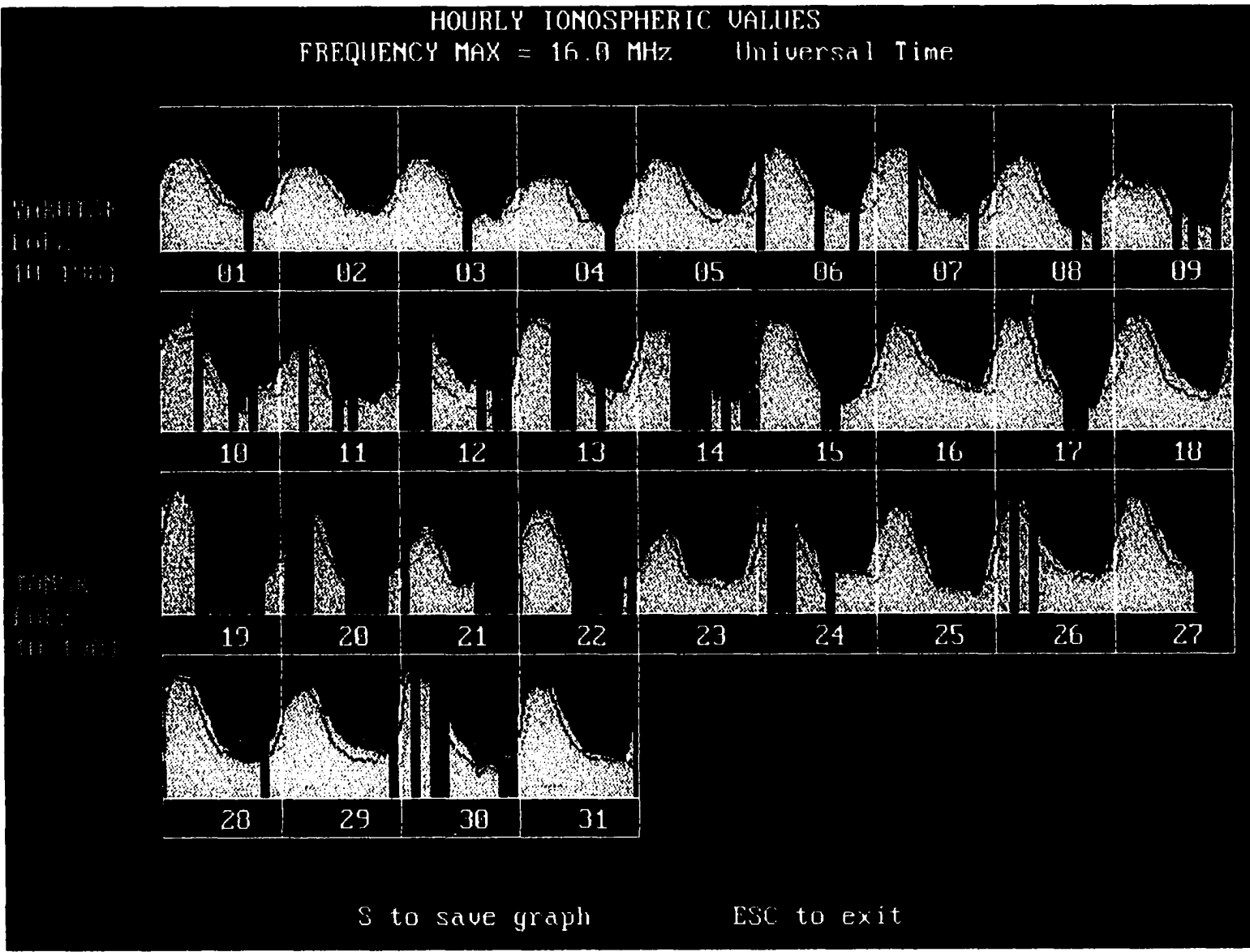
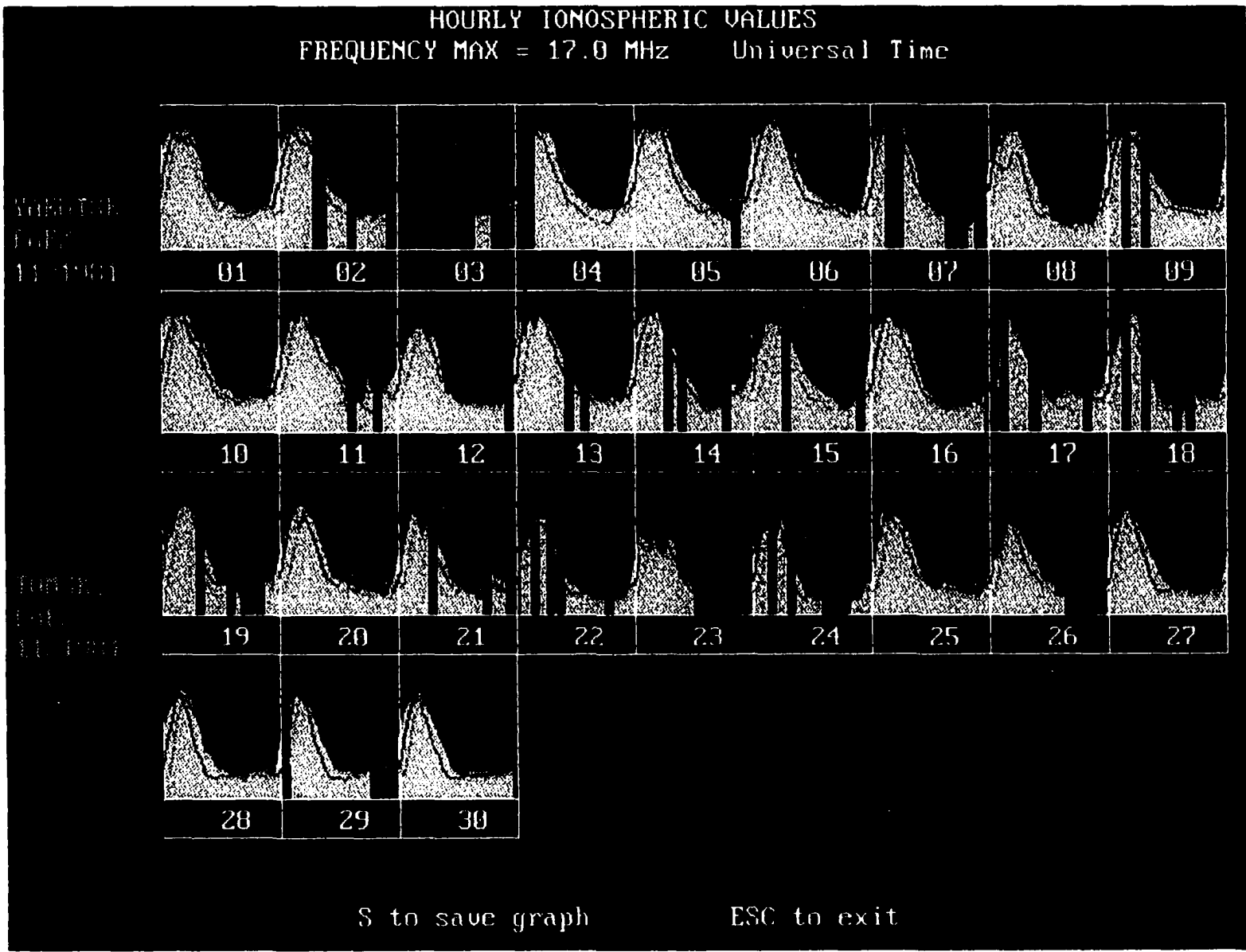
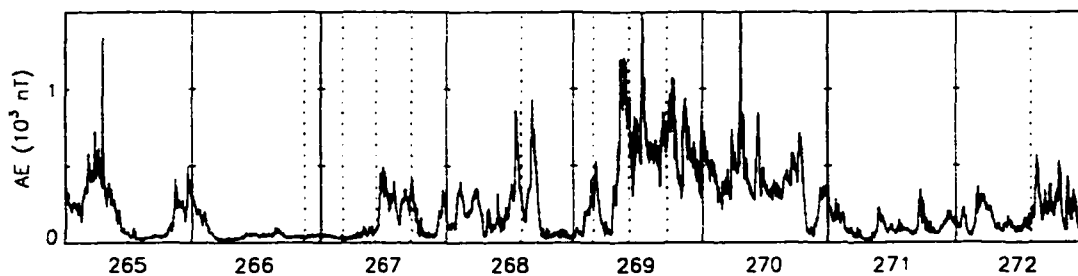


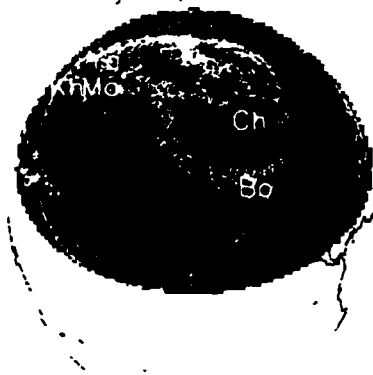
Figure 6-4c. See Figure 6-4a for description.



Figures 6-5(a-h). Mapped <PD> images and AE indices for study period. Nine <PD> images are shown mapped to an orthographic projection in geographic coordinates. The center of each mapping is at 50°N and 1200 Local Solar Time. Images from all days are presented in the same format as 6-5a.



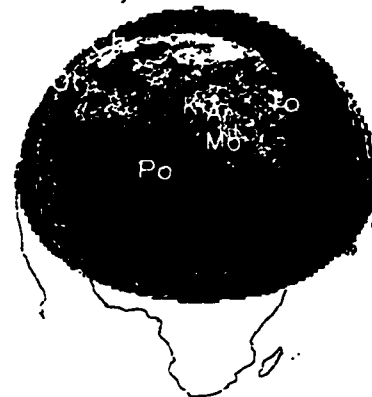
Day 266, 20:59 UT



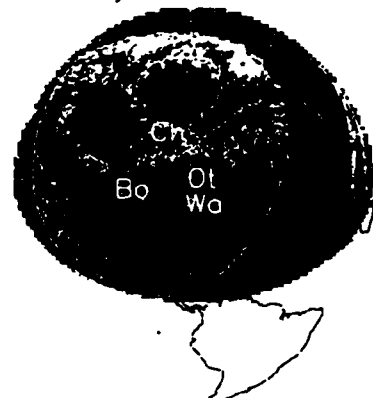
Day 267, 04:05 UT



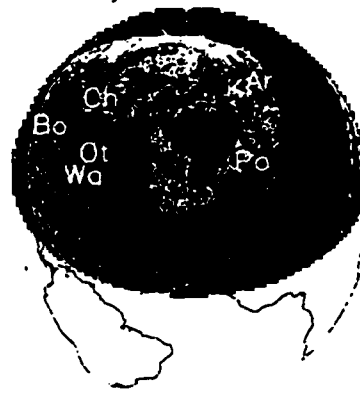
Day 267, 10:32 UT



Day 267, 17:24 UT



Day 268, 14:01 UT



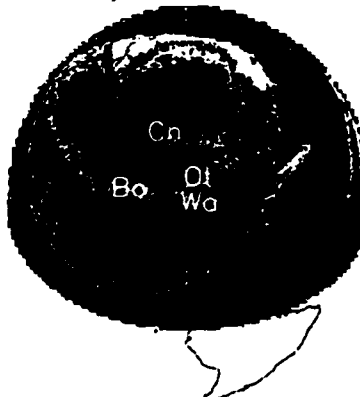
Day 269, 03:47 UT



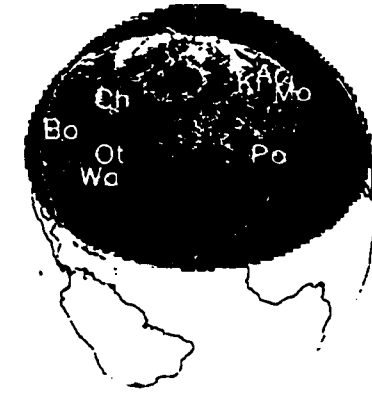
Day 269, 10:32 UT



Day 269, 17:24 UT



Day 272, 14:19 UT



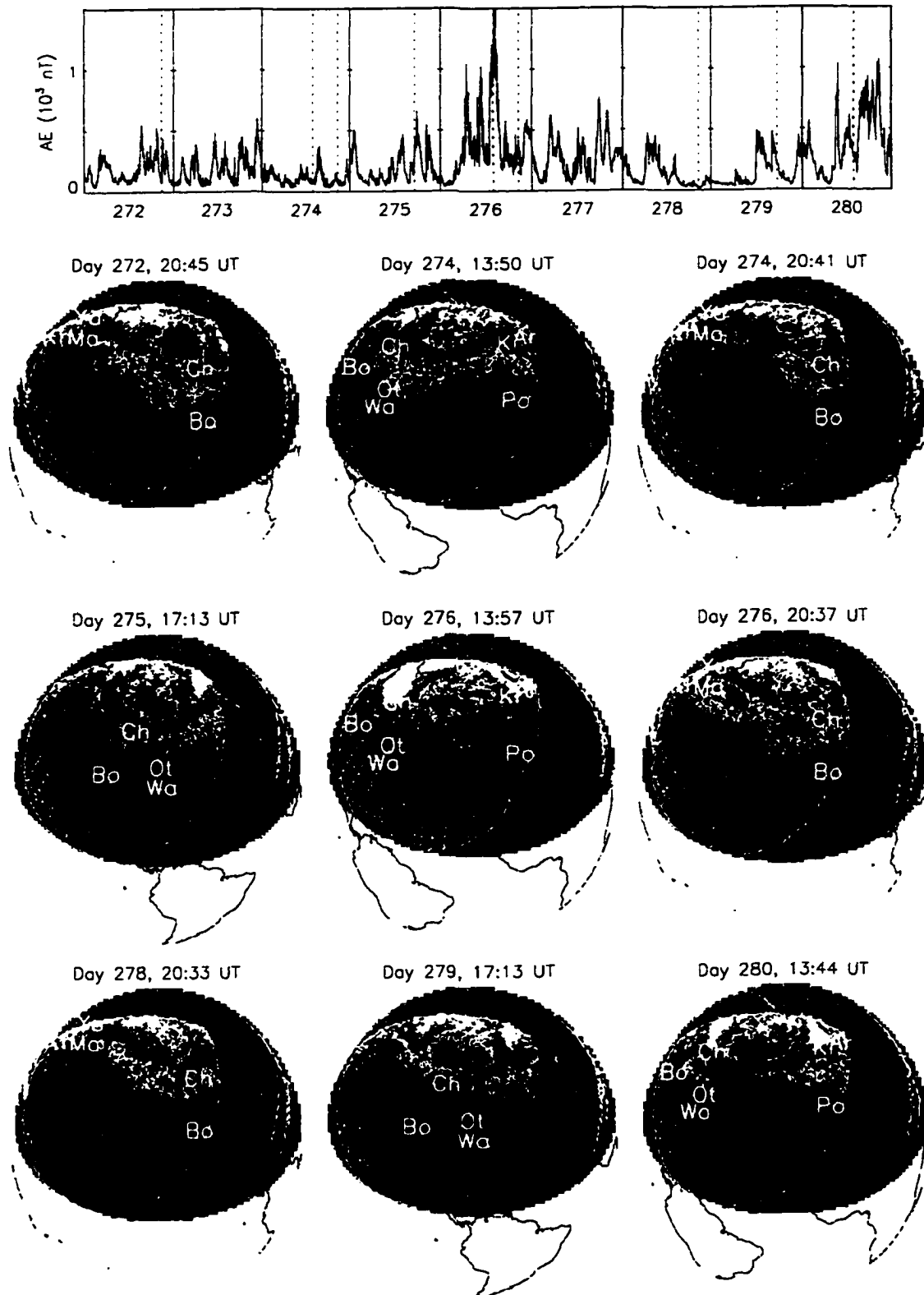


Figure 6-5b: See Figure 6-5a for description

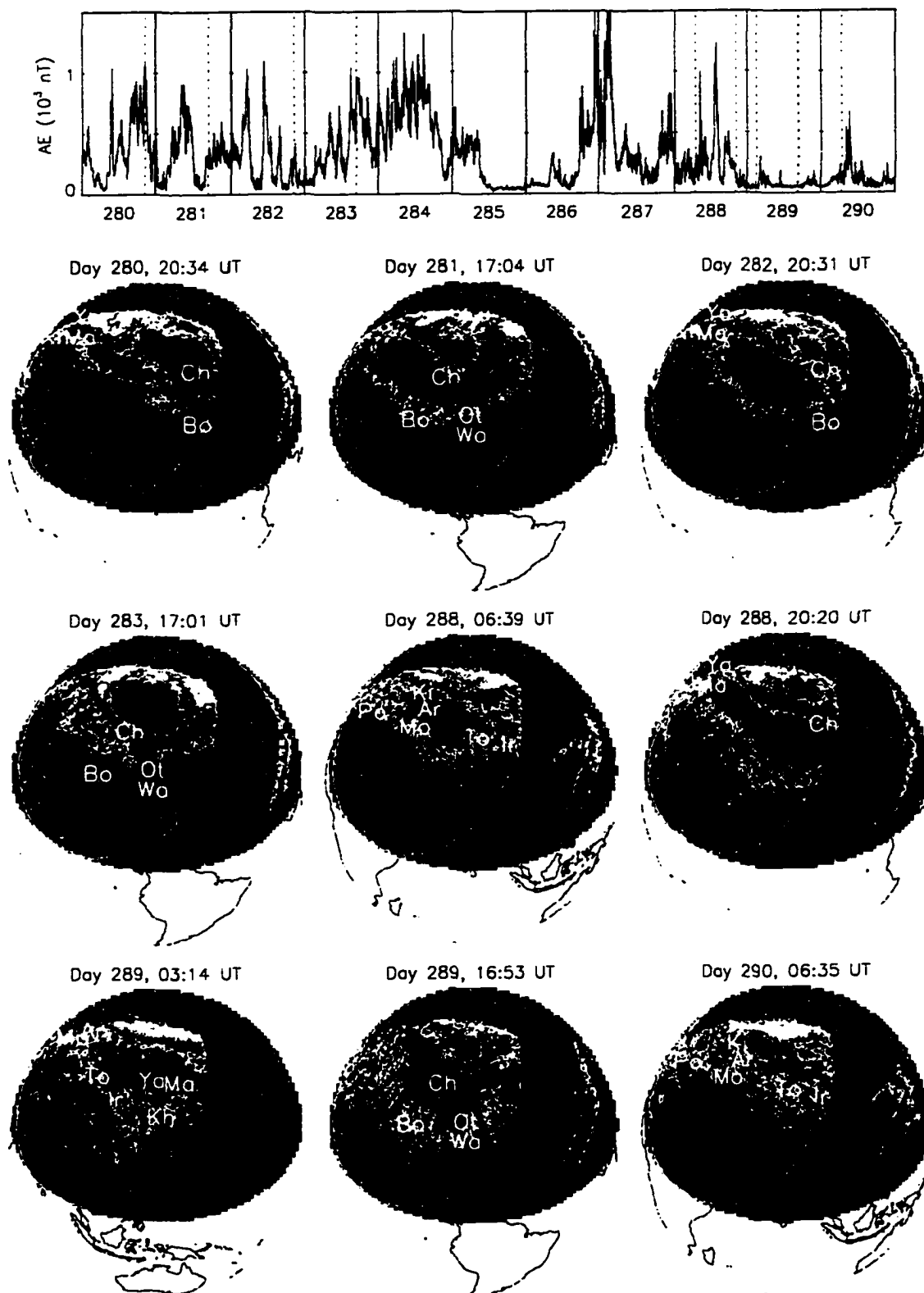


Figure 6-5c: See Figure 6-5a for description

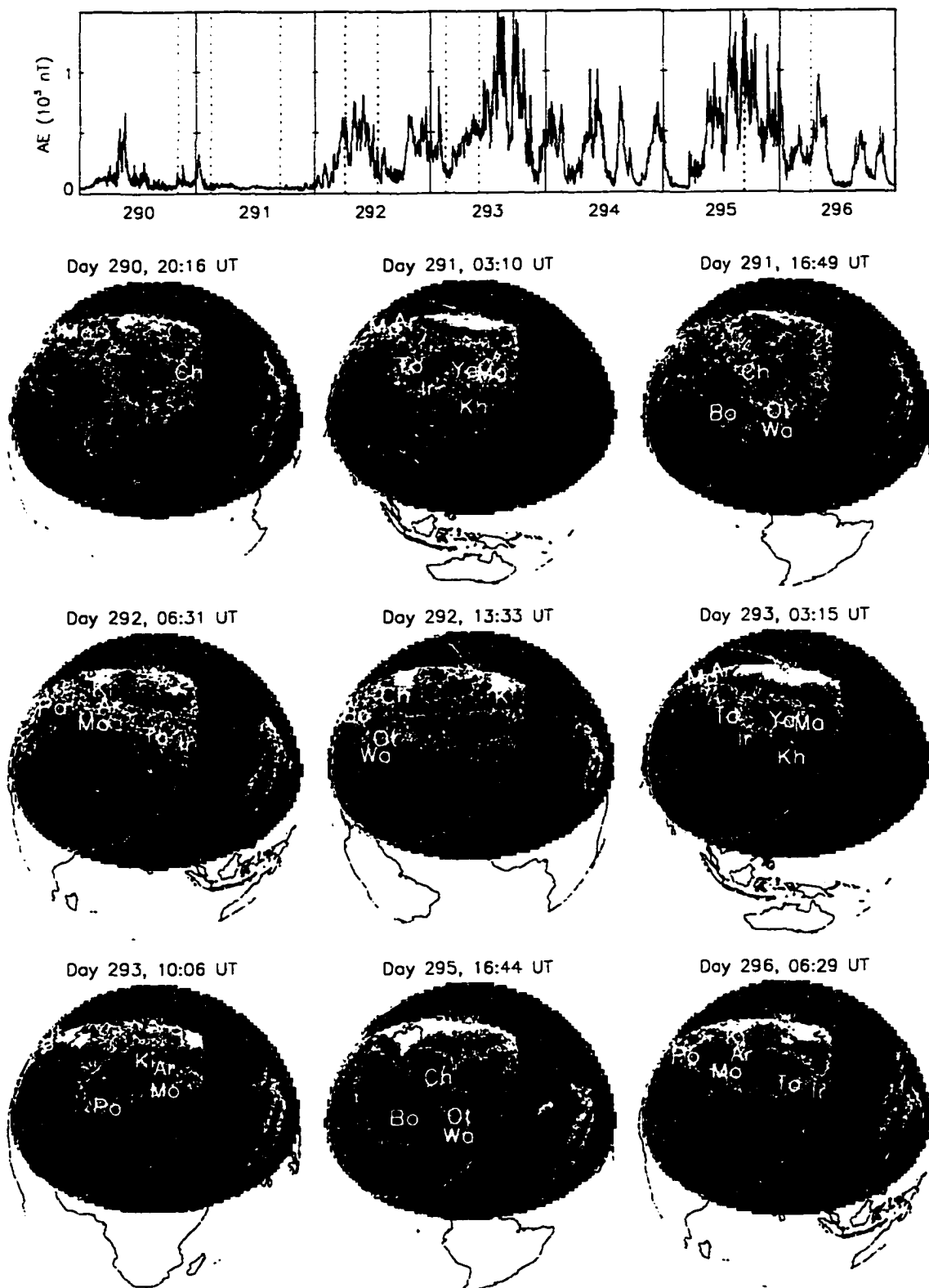


Figure 6-5d: See Figure 6-5a for description

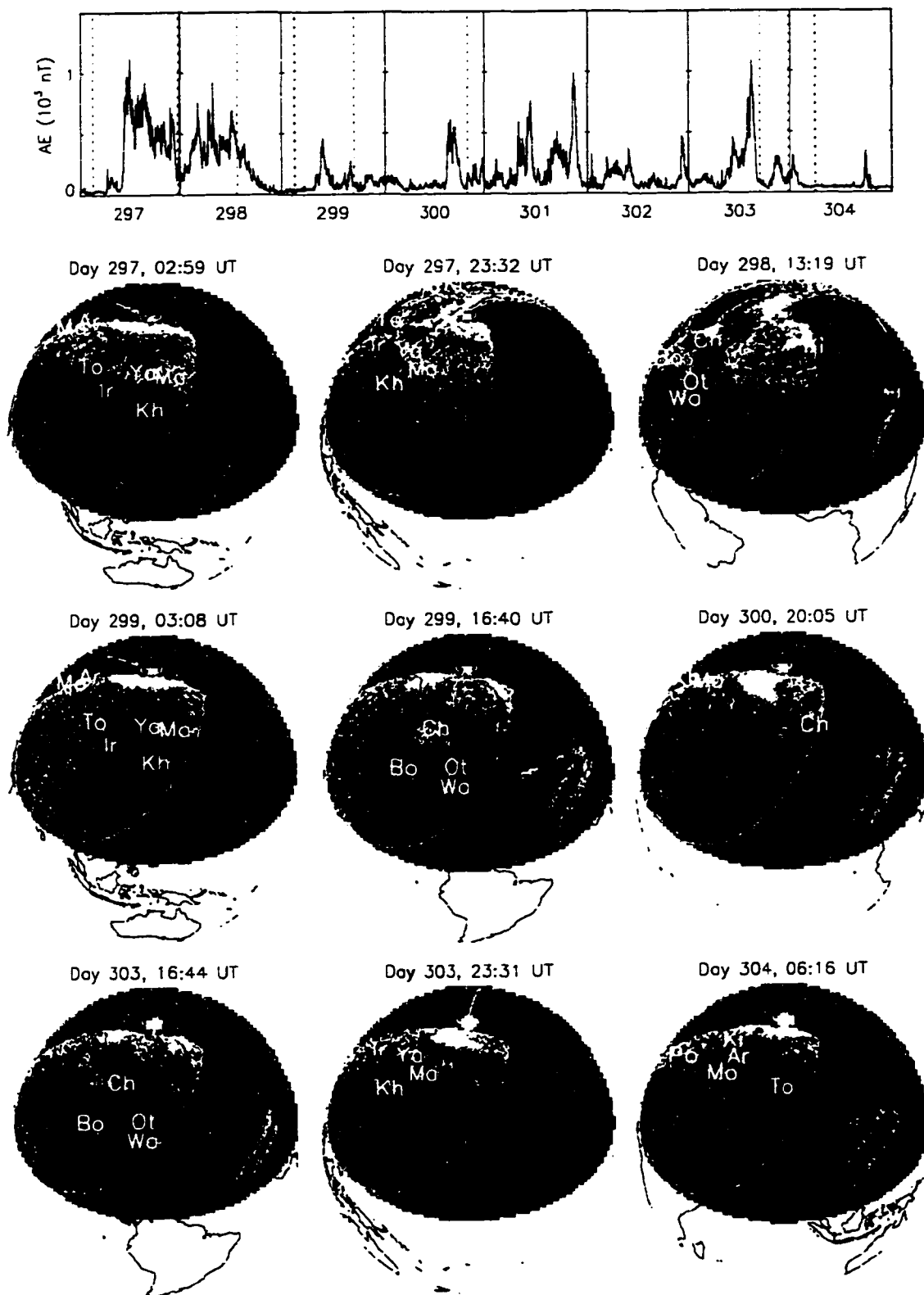


Figure 6-5e: See Figure 6-5a for description

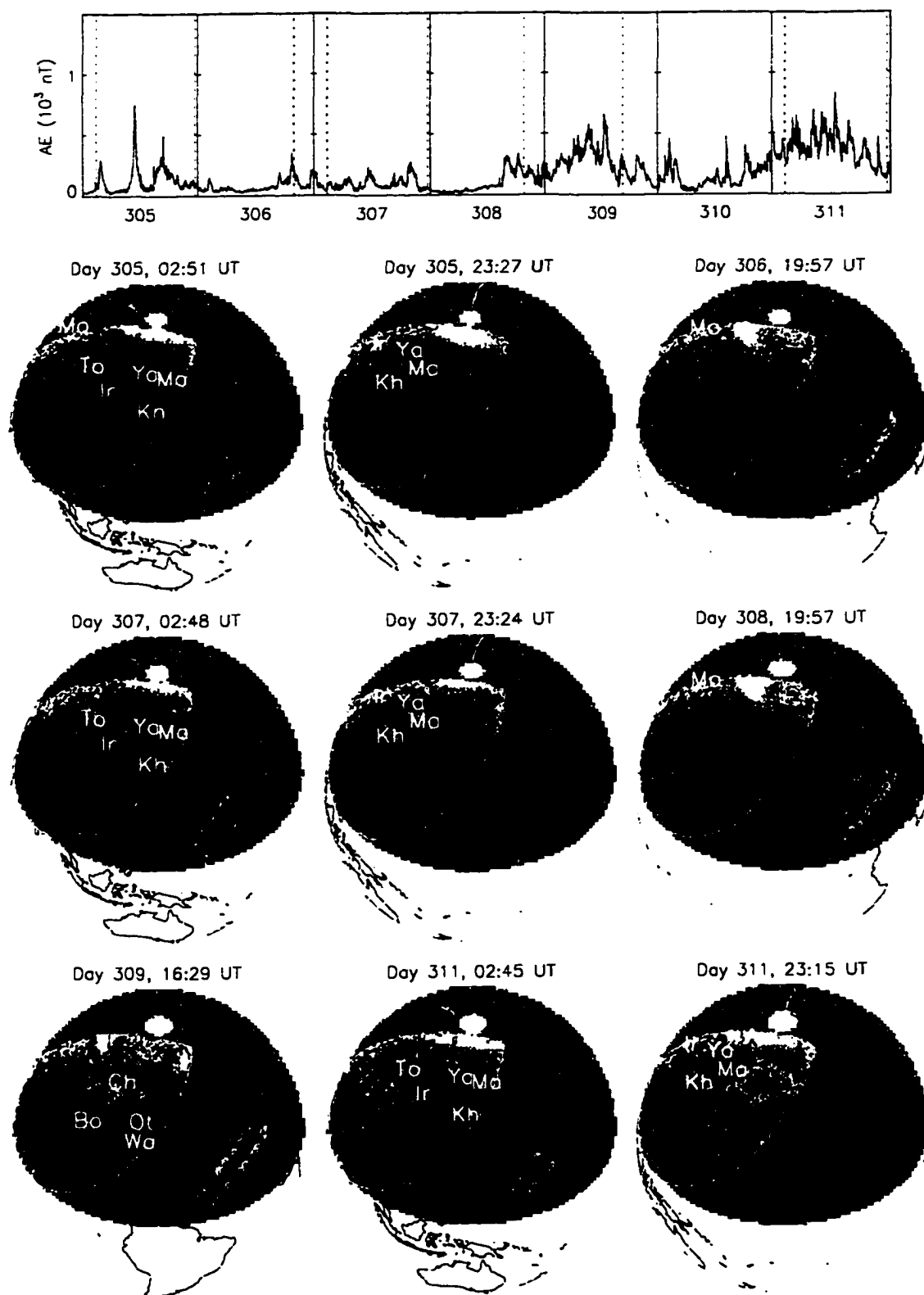


Figure 6-5f: See Figure 6-5a for description

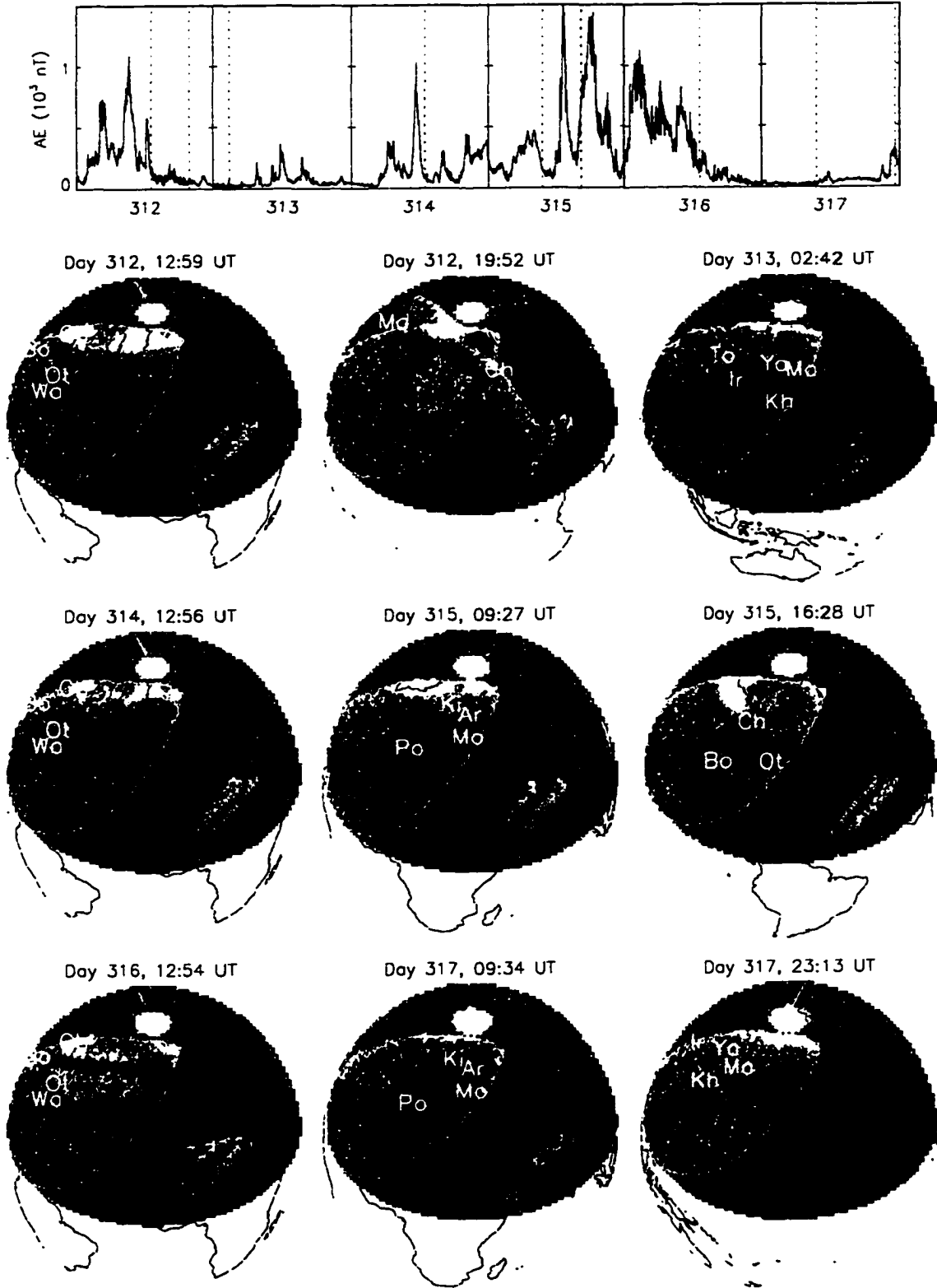


Figure 6-5g: See Figure 6-5a for description

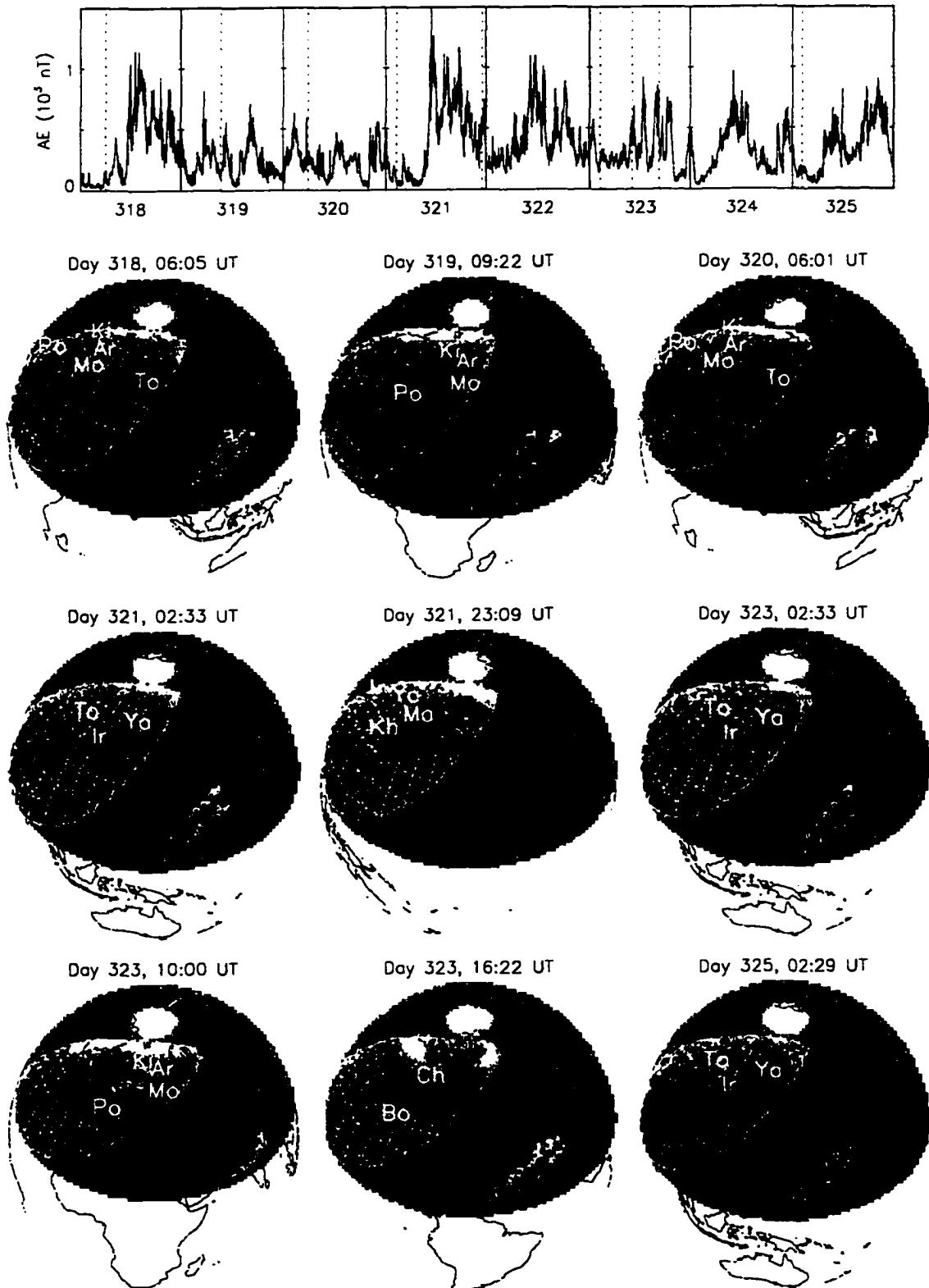


Figure 6-5h: See Figure 6-5a for description

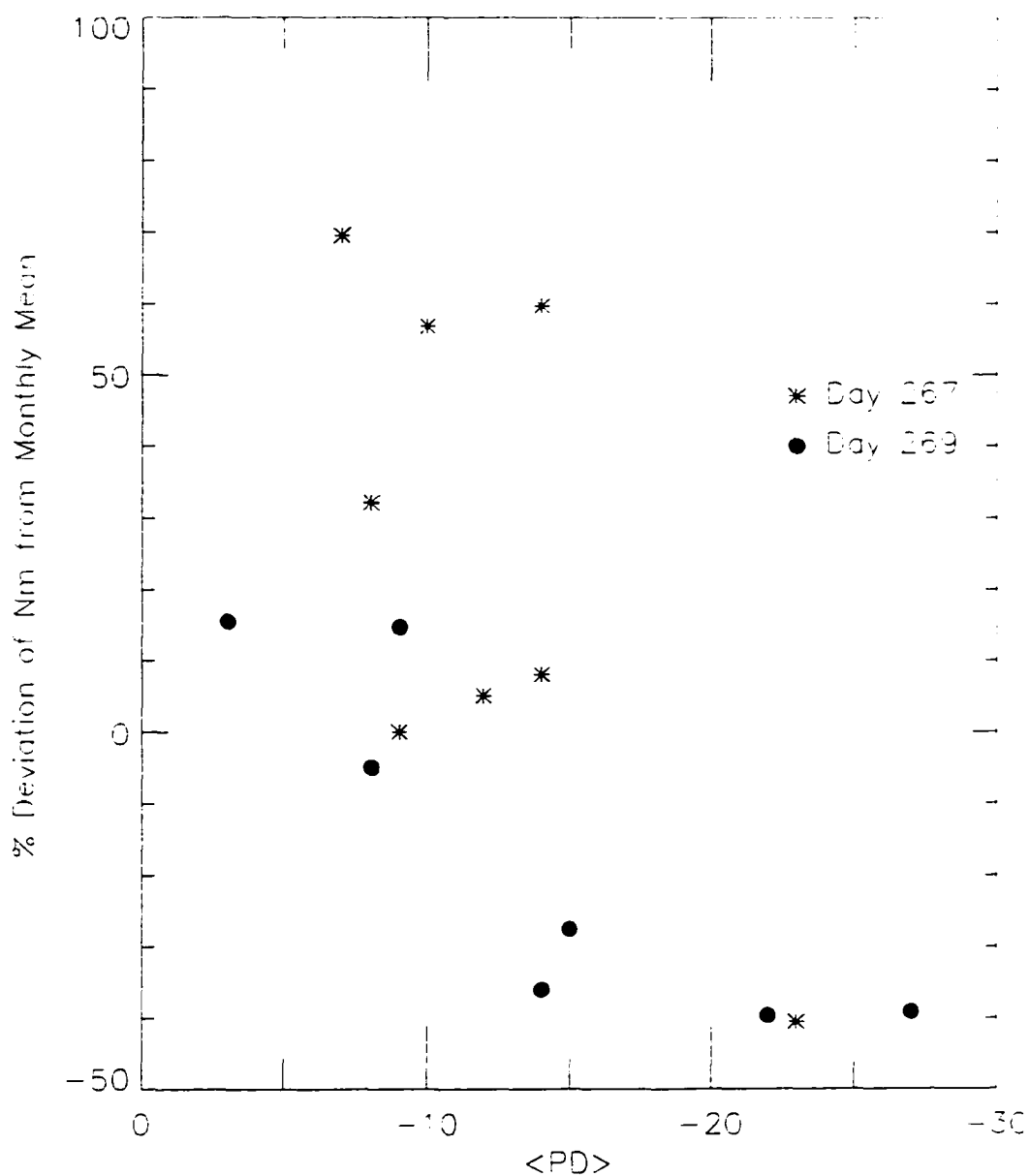


Figure 6-6. Comparison of  $\langle PD \rangle$  and  $PD(N_m)$  values for days 267 and 269. Percent differences in electron densities from monthly mean values over Far Eastern and North American stations are combined and compared to  $PD$  values at those stations on day 267 (asterisks) and day 269 (filled circles).

## Chapter 7

### Synthesis

#### 7.1 Review of Significant Results

This thesis presents a comprehensive set of observations made with the FUV imager onboard the DE 1 satellite that are directly related to large-scale compositional variations in Earth's thermosphere. Quantitative analyses of these perturbations is made possible in Chapter 3 by the development of a refined model for the imager's response under quiet geomagnetic conditions in the late 1981–early 1982 era. It is tested through application to images from the original quiet time set [Nicholas *et al.*, 1997] and to over 400 images from September 1981–February 1983. The test for quiet time images of day 291 (Figure 3-15) shows variations in percent difference (PD) values with satellite position but this is attributed to an extremely high effective emission altitude for the period in response to unusually large values of the solar FUV flux (as inferred from 10.7-cm radio measurements). Hence, care must be taken to estimate the solar FUV flux.

Corrections for reduced instrument sensitivity with time in orbit are necessary to make comparable observations of dayglow brightness at times later in the mission. The absolute correction factor of 0.52 is used to reduce mean pixel response values,  $\langle r \rangle$ , for application to images from early 1983. PD values calculated for quiet time images of this period (*e.g.* day 002, 1983, shown in Figure 5-1) result in  $-20\% < PD < 20\%$  for most image pixels, excluding the auroral oval. However, analysis of southern hemisphere images revealed that the relationship between the 10.7-cm solar radio flux,  $F$ , and  $\langle r \rangle$  during periods of very low solar activity departs from the linear trend determined from the original 1981 quiet-time images. Corrections for  $F$  determined from images obtained from the 1981 era images did not provide large enough corrections (reduction) to the model to match the extremely low values of  $F$  in mid-January, 1983, as can be seen in Figure 4-6. The variation of dayglow brightness with large variations in solar radio flux, or more importantly, the absolute values for FUV and EUV fluxes, would constitute a useful study for improving the method of analysis described in this thesis. Furthermore,

the replacement of the 10.7-cm solar radio flux with another parameter based on more direct solar EUV and FUV brightness would allow better modeling of day-to-day variations.

The effects of geomagnetic disturbances with similar geomagnetic index histories are investigated in Chapter 4, revealing the influence of IMF orientation on thermospheric composition, with the primary influencing factor being the sign and magnitude of the geocentric-solar-magnetospheric (GSM)  $y$ -component of the IMF. A pair of images demonstrates very different FUV signatures of composition variations at mid-latitudes, where the only input that is clearly different on the two days is the orientation, particularly in the  $y$  sense, and magnitude of the IMF (Section 4.2). A series of four images provides a time history of observations in a period of significant activity to demonstrate again that IMF  $B_y$  is most probably the external agent that causes a significant effect on dayside composition during storms (Section 4.3). In both sets of observations, the development of significant decreases in FUV brightness at sub-auroral and middle latitudes occurs under positive IMF  $B_y$  conditions and not during periods of negative  $B_y$ . A systematic search for a similar effect in 127 images of the Southern Hemisphere shows that the difference between PD values in the late and early morning sectors ( $\Delta PD$ ) decreases as IMF  $B_y$  tends toward negative values. This implies that Joule heating events have a greater effect on composition at later local times when the high-latitude dusk neutral circulation cell is enhanced in size and velocity. However, a rough correlation between  $\Delta PD$  and AE exists, as well as a slightly less significant correlation between AE and  $B_y$ . Hence, the variation in  $\Delta PD$  in the Southern Hemisphere cannot be attributed solely to IMF orientation.

Temporal variations in FUV brightness are best examined in the spatially confined polar cap regions, where one may expect changes in FUV brightness after even moderate magnetic activity. The clear development of such brightness variations within the polar cap during a single orbit is observed on days 002 and 003, 1983, during a period in which the sub-auroral dayglow remains unaffected. This interesting effect is inferred

from the distribution of PD values along a high latitude meridian which crosses the auroral oval at 11:00 MLT (Section 5.3). Ground-based studies by Hernandez *et al.* [1991] describe high latitude neutral winds in this sector which have a large poleward meridional component for the observed IMF orientation. Although these cited data were obtained in the winter, as opposed to the images shown in this thesis, the neutral winds are similarly influenced by ionospheric convection throughout the year. Knowing that thermospheric neutral winds are likely directed through a region of significant Joule heating and into an area where strong decreases in brightness are observed, a rapid change in thermospheric composition is inferred for the neutral gas passing through the auroral oval. Given the limited time at apogee and temporal resolution of the instrument, this effect could only be inferred from the strong gradient in brightness. Had the imager operated from high altitudes for the duration of each storm period, it would have been able to monitor the development of composition variations within the polar cap. A continued search of DE-1 images may yet produce images demonstrating the change of polar-cap brightness values from quiet-time to perturbed levels during a single orbit. One would expect to first view the effect of Joule heating near the dayside oval.

Select examples of substorm effects on thermospheric composition, from a survey of 72 orbits, are presented in Chapter 6. These are chosen to take advantage of the fact that DE 1 makes FUV observations from nearly identical vantage points over Earth on two-day intervals. This simplifies the incorporation of ground-based observations such as ionosonde data. As shown in Chapter 1, the ratio of observed to monthly F2 peak electron densities ( $N_mF2$ ) measured by ionosondes can closely follow variations in thermospheric  $O/N_2$  ratio during negative ionospheric storms. Comparisons of FUV percent difference (PD) values to percent differences of  $N_mF2$  from monthly mean values ( $PD(N_m)=100 \cdot R(N_m)$ , the parameter reported by Prölss) at ionosonde stations in the disk region of images in (Section 6.3.1) suggest a relationship between these parameters in images where decreases in brightness are observed. Additional comparisons of FUV PD to  $PD(N_m)$  for the images shown in this survey will further define the relation between these parameters and possibly show a relation of FUV PD

with  $PD(O/N_2)$  through the known relationship of  $R(N_m)$  to  $R(O/N_2)$  (Figure 1-3). In future studies, it will be of interest to identify cases where increases in F2 peak electron densities are complimented by FUV brightness increases (Section 6.3.4) and compare them to cases where such a correspondence is clearly not evident (Section 6.3.1)

The survey also provides a clear indication that mid-latitude FUV brightness variations are less prominent during winter than at equinox, in the Northern Hemisphere. This observation reflects the fact that composition variations generated by magnetic activity generally remain at high latitudes when solar insolation is low in the regions of Joule heating. The effect has been measured by mass spectrometers orbiting Earth at thermospheric altitudes [Prölss, 1980], is indicated in sophisticated time-dependent models of the upper atmosphere [Fuller-Rowell *et al.* [1994, 1996], and is now clearly evident in FUV images.

## 7.2 Future Work with DE 1 FUV Images

Future work with DE-1 images could elucidate the large-scale spatial structure of the thermosphere and its association with magnetic activity and IMF orientation, and on thermospheric compositional variations, particularly at high latitudes. Earlier high-latitude measurements by low-altitude nadir-oriented FUV instruments revealed surprising differences between the northern and southern polar caps near equinox. In the work by Meier [1970], there is a period of approximately one week (first week of April, 1968) in which OI and HI dayglow decreases are observed at the nadir over the northern polar cap, but not the southern polar cap. According to Meier, decreases in the OI FUV brightness within the northern polar cap were present "up to about April 7 [1968]", after which the brightness values reflected a less disturbed neutral composition. An examination of one-hour-averaged IMF from that period [NSSDC, 1977] shows that IMF  $B_y$  was negative for nearly the entire period of March 24–April 5, whereupon IMF  $B_y$  switched abruptly to positive values at ~0000 UT on April 6. One interpretation is that the appearance of dayglow decreases at northern middle latitudes is not favored during  $B_y$  negative, thus the associated composition variations are not forced out of the

polar cap. In the southern polar cap, By negative would favor the transport of disturbed parcels out of the polar cap and to middle latitudes, thus brightness decreases are not present in the southern polar cap, while being apparent in the north.

As opposed to this type of low altitude, nadir-directed measurement, DE 1 cannot, during a single orbit, make measurements of the FUV dayglow brightness within both polar caps with comparable spatial and temporal resolution. It can, however, repeatedly monitor the dayglow brightness within the polar cap in a particular hemisphere. The availability of IMF data during late 1982 is very good, with higher temporal coverage than January, 1983, for instance. This period may offer additional useful images of the polar cap for study. Images from this period have not been used due to an operational difficulty with the satellite nadir sensor, resulting in the loss of sampling over a small portion of the disk region. Utilizing the averaging techniques developed in Sections 4 and 5 of this thesis, the effect of this data loss can be minimized, allowing mapping of complete <PD> images to geomagnetic coordinates for further investigation of the polar cap.

### 7.3 Present and Future Missions

Global FUV imagers can continue to be useful tools for investigating the thermosphere, with current operational instruments providing greater spatial and/or temporal resolution than DE 1. Several current missions, POLAR VIS, POLAR UVI, GUVI and IMAGE are discussed here, briefly describing their capabilities and limitations.

POLAR, launched in 1996, carried two FUV imagers into a highly elliptical, nearly polar orbit with apogee over the Northern Hemisphere at an altitude of 8.0  $R_E$ . The UltraViolet Imaging system (UVI) [Torr *et al.*, 1995] and Visible Imaging System (VIS) [Frank *et al.*, 1995] both have FUV sampling capabilities. The VIS system's earth camera can obtain global FUV images of Earth and has approximately twice the spatial resolution of DE 1, providing full images at the rate of one per minute. The single filter has a sensitivity profile similar to filter #2 of the DE-1 FUV imager used throughout this

work. Recent studies of FUV dayglow variations with POLAR's earth camera reveal weaker variation in instrument response with magnetic activity than were observed with DE 1 [e.g., Craven *et al.*, 1996; Immel *et al.*, 1997]. It now appears that this may be partially attributed to a greater sensitivity of this instrument to MUV and NUV emissions on the part of the VIS earth camera than the DE-1 imager. The signature of clouds is clearly evident in earth camera images as structured increases in FUV brightness at mid latitudes, in good spatial correspondence to the appearance of bright clouds in GOES visible images. It is not known whether this is due to the modification of the O<sub>3</sub> concentration above large storm fronts or actual increases in terrestrial NUV emissions from cloud tops. Although infra-red (IR) emissions are a signature of high clouds, the suggestion that these apparent increases in UV emissions are actually due insufficient rejection of IR is improbable, as there is no apparent variation in brightness between continental and ocean surfaces, a clear feature in infrared images of Earth. Furthermore, the cloud-related emissions are considerably reduced as the satellite zenith angle increases. This is consistent with an increasingly long column of (FUV absorptive) O<sub>2</sub> and O<sub>3</sub> between the emission region and the imager. Infrared emissions would presumably not suffer such strong attenuation.

UVI shares the POLAR despun pointing platform with VIS. It operates with a selection of filters of much narrower wavelength passband than those used with either the DE-1 FUV imager or the POLAR VIS earth camera. These filters largely isolate the OI 130.4-nm and 135.6-nm emission lines and different portions of the N<sub>2</sub> LBH emission bands through the use of a sophisticated multilayering technique in their construction. Wavelengths outside the narrow passband are strongly attenuated. This instrument suffers from a reduction of spatial resolution along one axis of its CCD detector, because of a residual spacecraft-induced wobble arising from incorrect balancing by the spacecraft manufacturer. UVI does not have the capability (as VIS does) to repeatedly shutter its optics during the fastest motion of the field-of-view in the 10-second period wobble, and as a consequence a specific point in the object field is smeared across an approximately 1x15 pixel area in the image field. Furthermore, the

instrument's field-of-view does not allow for global imaging, with Earth's disk subtending a larger angle than the field of view of the instrument at all times during an orbit. Scheduled observations of dayglow brightness at sub-auroral latitudes are minimal. Images from this instrument are more suitable for FUV dayglow studies (like those described in this thesis) than those obtained by the VIS earth camera, though the spacecraft wobble provides added uncertainty to measurements, as each pixel in the image field gains FUV brightness information from a range of solar zenith angles. Furthermore, the establishment of quiet-time FUV brightness values would have to be established using the relatively small number of image pixels located away from the auroral oval. Without up-to-date AE indices, which cannot currently be provided in real time, one could not confidently construct a quiet-time model from observations within the polar cap, as the results presented in Chapter 5 of this thesis suggest.

The Global UltraViolet Imager (GUVI) on the TIMED satellite will operate at lower altitudes than either DE 1 or POLAR, and will spectroscopically isolate dayglow emissions. The TIMED mission launch is currently scheduled for May, 2000. Since the brightness measurements are spectroscopically isolated, unique determinations of line and band emission intensities can be made, which are not possible when broadband filters are used (*e.g.*, DE 1 and POLAR). Furthermore, the brightness of N<sub>2</sub> and O emissions can be monitored simultaneously, which will yield information on the relative scale heights of O and N<sub>2</sub> and the ratio of their concentrations (mixing ratio). GUVI will offer disk and limb information in each obtained image, as the 16 pixel wide window is swept up to  $\pm 140^\circ$  perpendicular to the orbit plane of TIMED with a pointing accuracy of  $0.1^\circ$ .

IMAGE is to be placed in a highly elliptical near-polar orbit similar to those of POLAR and DE 1, though with a lower apogee altitude of only  $\sim 4.2 R_e$ , more like that of DE 1. It will carry 4 instruments for magnetospheric and auroral imaging and is scheduled for launch in 1999. The FUV instrument is designed for auroral imaging, with possible application to remote sensing of thermospheric composition. The low apogee

altitude, however, limits observations of the polar regions to intermittent periods of much shorter time scale than the 12–15 hour development and subsequent recovery time of impulsive polar thermospheric disturbances [Section 5.3.1]. One might surmise that the low apogee is in support of the Energetic Neutral Atom imager, which will be measuring neutral He with low detection sensitivity. Furthermore, since IMAGE is a limited budget mission, it is too expensive to use larger launch vehicles capable of placing the satellite in very high apogee orbits. However, one understands that its primary mission is in support of the magnetospheric physics community.

To date, the DE-1 FUV imaging mission is unsurpassed by any other imager in returning useful information on Earth's FUV emissions. Data from DE-1 and -2 have been combined to study the physics of the thermosphere [Killeen *et al.*, 1988]. This thesis establishes the excellence of DE 1 itself as a platform for the study of the thermosphere and ionosphere and the response of these atmospheric regions to geomagnetic activity. The nearly 10 years of images it returned will continue to be part of auroral and thermospheric studies, serving as a testament to the utility of the imager. Let this thesis, and the new results presented herein, do the same.

### Bibliography

- Akasofu, S. I. Energy coupling between the solar wind and the magnetosphere, *Space Sci. Rev.*, 28, 121–190, 1981.
- Baumjohann, W., Hemispherical Joule heating and the AE indices, *J. Geophys. Res.*, 89, 383–388, 1984
- Buonsanto, M. J., M. Codrescu, B. A. Emery, C. G., Fesen, T. J. Fuller-Rowell, D. J. Melendez-Alvira and D. R. Sipler, Comparison of models and measurements at Millstone Hill during the January 24–26, 1993, minor storm interval. *J. Geophys. Res.*, 102, 7267–7277, 1997.
- Barth, C. A., *Ultraviolet Spectroscopy of Planets*, Jet Propulsion Laboratory Technical Report 32-822, Pasadena CA, 1965.
- Barth, C. A., W. K. Tobiska, G. J. Rottman and O. R. White, Comparison of 10.7-cm radio flux with SME solar Lyman alpha flux, *Geophys. Res. Lett.*, 17, 571–574, 1990.
- Bauer, P., P. Waldteufel and D. Alcayde, Diurnal variations in the atomic oxygen density and temperature determined from incoherent scatter measurements in the ionospheric F region. *J. Geophys. Res.*, 75, 4825–4832, 1970.
- Bowyer, S., R. Kimble, F. Paresce, M. Lampton and G. Penegor, Continuous-readout extreme-ultraviolet airglow spectrometer. *Appl. Optics*, 20, 477–486, 1981.
- Burns, A. G., and T. L. Killeen, The equatorial neutral thermospheric response to geomagnetic storms, *Geophys. Res. Lett.*, 19, 977–980, 1992.
- Burns, A. G., and T. L. Killeen, Changes of neutral composition in the thermosphere. *AAS/AIAA, Astrodynamics*, 76, 2295–2312, 1992 (b).
- Burns, A. G., T. L. Killeen, G. R. Carignan, and R. G. Roble, Large enhancements in the O/N<sub>2</sub> ratio in the evening sector of the winter hemisphere during geomagnetic storms. *J. Geophys. Res.*, 100, 14661–14671, 1995.
- Burns, A. G., T. L. Killeen, G. Crowley, B. A. Emery and R. G. Roble, On the mechanisms responsible for high-latitude thermospheric composition variations

- during the recovery phase of a geomagnetic storm. *J. Geophys. Res.*, 94, 16.961–16.968.
- Burns, A. G., T. L. Killeen, W. Deng, G. R. Carignan and R. G. Roble. Geomagnetic storm effects in the low- to middle-latitude upper thermosphere. *J. Geophys. Res.*, 100, 14673–14691, 1995.
- Burns, A. G., T. L. Killeen, and R. G. Roble, Thermospheric heating away from the auroral oval during geomagnetic storms, *Can. J. Phys.*, 70, 544–552, 1991.
- Burns, A. G., T. L. Killeen, and R. G. Roble. Thermospheric composition changes seen during a geomagnetic storm, *Adv. Space Res.*, 12, 253–256, 1992.
- Burroughs, W. J., Weather Cycles- Real or Imaginary, Cambridge University Press, 1992.
- Chamberlain, J. W., and D. M. Hunten, *Theory of Planetary Atmospheres*, Academic Press, 1987.
- Conway, R. R., R. R. Meier and R. E. Huffman. Satellite observations of the OI 1304, 1356, and 1641 Å dayglow and the abundance of atomic oxygen in the thermosphere. *Planet. Space Sci.*, 36, 963–973, 1988.
- Craven, J. D., and L. A. Frank. An apparent signature of modifications to the upper atmosphere during auroral substorms. *EOS Trans. AGU*, 65, 1021, 1984.
- Craven, J. D., T. J. Immel, L. A. Frank, T. L. Killeen and A. G. Burns. Simultaneous remote and local observations of variations in thermospheric composition with the DE-1 and -2 spacecraft, *EOS Trans. AGU*, 76, F446, 1995.
- Craven, J. D., T. J. Immel, L. A. Frank, J. B. Sigwarth, C.-I. Meng, G. K. Parks, T. L. Killeen, W. E. Sharp and R. P. Lepping, FUV observations of the active aurora and correlated perturbations to thermospheric composition as seen with the Visible Imaging System on the POLAR spacecraft, *EOS Trans.* 77, F620, 1996.
- Craven, J. D., A. C. Nicholas, L. A. Frank, D. J. Strickland and T. J. Immel. Variations in FUV dayglow with intense auroral activity, *Geophys. Res. Lett.*, 21, 2793–2796, 1994.

- Crowley, G., B. A. Emery, R. G. Roble, H. C. Carlson Jr. and D. J. Knipp. Thermospheric dynamics during September 18–19, 1984 1. Model Simulations. *J. Geophys. Res.*, *94*, 16925–16944, 1989.
- Dickinson, R. E., E. C. Ridley and R. G. Roble. A three-dimensional general circulation model of the thermosphere, *J. Geophys. Res.*, *86*, 1499–1512, 1981.
- Dickinson, R. E., E. C. Ridley and R. G. Roble. Thermospheric general circulation with coupled dynamics and composition. *J. Atmos. Sci.*, *41*, 205–219, 1984.
- Doyle, M. A., and W. J. Burke. S3-3 measurements of the polar cap potential. *J. Geophys. Res.*, *88*, 9125–9133, 1983.
- Evans, D. S., Global Statistical Patterns of Auroral Phenomena, in *Proceedings of the Symposium on Quantitative Modeling of Magnetospheric-Ionospheric Coupling Processes*, 325, Kyoto, 1987.
- Fastie, W. G., H. M. Crosswhite and D. F. Heath. *J. Geophys. Res.*, *69*, 4129–4140, 1964.
- Frank, L. A., and J. D. Craven. Imaging results from Dynamics Explorer 1. *Rev. Geophys.*, *26*, 249–283, 1988.
- Frank, L. A., J. D. Craven, K. L. Ackerson, M. R. English, R. H. Eather and R. L. Carvillano. Global auroral instrumentation for the Dynamics Explorer mission. *Space Sci. Instrum.*, *5*, 368–393, 1981.
- Frank, L. A., J. B. Sigwarth, J. D. Craven, J. P. Cravens, J. S. Dolan, M. R. Dvorsky, P. K. Hardebeck, J. D. Harvey and D. Muller. The Visible Imaging System (VIS) for the Polar Spacecraft. *Space Sci. Rev.*, *71*, 297–328, 1995.
- Fuller-Rowell, T. J., M. V. Codrescu, R. J. Moffett and S. Quegan. Response of the thermosphere and ionosphere to geomagnetic storms. *J. Geophys. Res.*, *99*, 3893–3914, 1994.
- Fuller-Rowell, T. J., M. V. Codrescu, H. Rishbeth, R. J. Moffett and S. Quegan. On the seasonal response of the thermosphere and ionosphere to geomagnetic storms. *J. Geophys. Res.*, *101*, 2343–2353, 1996.

- Gentieu, E. P., P. D. Feldman and R. R. Meier. Spectroscopy of the extreme ultraviolet dayglow at 6.5 Å resolution: Atomic and ionic emissions between 530 and 1240 Å. *Geophys. Res. Lett.*, 6, 325–328, 1979.
- Gladstone, G. R., Simulations of DE 1 UV airglow images. *J. Geophys. Res.*, 99, 11441–11448, 1994.
- Hays, P. B., T. L. Killeen, N. W. Spencer, L. E. Wharton, R. G. Roble, B. A. Emery, T. J. Fuller-Rowell, D. Rees, L. A. Frank and J. D. Craven. Observations of the dynamics of the polar thermosphere. *J. Geophys. Res.*, 89, 5597–5612, 1984.
- Hedin, A. E., A revised thermospheric model based on mass spectrometer and incoherent scatter data: MSIS-83. *J. Geophys. Res.*, 88, 10170–10188, 1983.
- Hedin, A. E., Correlations between thermospheric density and temperature, solar EUV flux, and 10.7-cm flux variations. *J. Geophys. Res.*, 89, 9828–9834, 1984.
- Hedin, A. E., MSIS-86 Thermospheric Model. *J. Geophys. Res.*, 92, 4649–4662, 1987.
- Heelis, R. A., The effects of interplanetary magnetic field orientation on dayside high-latitude ionospheric convection. *J. Geophys. Res.*, 89, 2881–2890, 1984.
- Heppner, J. P., Polar-cap electric field distributions related to the interplanetary field direction. *J. Geophys. Res.*, 77, 4877, 1972.
- Heppner, J. P., and N. C. Maynard, Empirical high-latitude electric field models. *J. Geophys. Res.*, 92, 4467–4489, 1987.
- Hernandez, G., F. G. McCormac and R. W. Smith, Austral thermospheric wind circulation and interplanetary magnetic field orientation. *J. Geophys. Res.*, 96, 5777–5783, 1991.
- Ho, C. M., A. J. Mannucci, U. L. Lindqwister, X. Pi and B. T. Tsurutani. Global ionosphere perturbations monitored by the worldwide GPS network. *Geophys. Res. Lett.*, 22, 3219–3222, 1996.
- Hoffman, R. A., G. D. Hogan and R. C. Maehl, Dynamics Explorer spacecraft and ground operations systems. *Space Sci. Instrum.*, 5, 349–367, 1981.

- Huang, K., *Statistical Mechanics, Second Edition*, Wiley and Sons, 1987.
- Huffman, R. E., F. J. Leblanc, J. C. Larabee and D. E. Paulsen. Satellite vacuum ultraviolet airglow and auroral observations. *J. Geophys. Res.*, 85, 2201–2215, 1980.
- Idenden, D. W., R. J. Moffett and S. Quegan. Ionospheric and thermospheric effects due to a rapid polar cap expansion (abstract), *EOS Trans. AGU*, 78, F515, 1997.
- Immel, T. J., J. D. Craven and L. A. Frank, Influence of IMF By on large-scale decrease in O column density at middle latitudes, *J. Atmos. and Solar-Terr. Phys.*, 59, 725–737, 1997.
- Immel, T. J., J. D. Craven, L. A. Frank and J. B. Sigwarth. Variations in Earth's FUV dayglow within the polar caps, *EOS Trans.*, 78, F520, 1997.
- Killeen, T. L., J. D. Craven, L. A. Frank, J.-J. Ponthieu, N. W. Spencer, R. A. Heelis, L. H. Brace, R. G. Roble, P. B. Hays and G. R. Carignan. On the relationship between dynamics of the polar thermosphere and morphology of the aurora: Global-scale observations from Dynamics Explorers 1 and 2, *J. Geophys. Res.*, 93, 2675–2692, 1988.
- Killeen, T. L., P. B. Hays, N. W. Spencer and L. E. Wharton. Neutral winds in the polar thermosphere as measured from Dynamics Explorer, *Geophys. Res. Lett.*, 9, 957–960, 1982.
- Killeen, T. L., Y.-I. Won, R. J. Niciejewski and A. G. Burns. Upper thermosphere winds and temperatures in the geomagnetic polar cap: Solar cycle, geomagnetic activity, and interplanetary magnetic field dependencies, *J. Geophys. Res.*, 100, 21327–21342, 1995.
- Keating, G. M., J. D. Craven, L. A. Frank, D. F. Young and P. K. Bhartia. Initial results from the DE-1 ozone imaging instrumentation, *Geophys. Res. Lett.*, 12, 593–596, 1985.
- Lean, J., Solar ultraviolet irradiance variations: A review, *J. Geophys. Res.*, 92, 839–868, 1987.

- Lummerzheim, D., M. Brittnacher, D. Evans, G. A. Germany, G. K. Parks, M. H. Rees and J. F. Spann, High time resolution study of the hemispheric power carried by energetic electrons into the ionosphere during May 19/20, 1996 auroral activity, *Geophys. Res. Lett.*, 24, 987–990, 1997.
- Mayr, H. G., and H. Volland, Magnetic storm characteristics of the thermosphere, *J. Geophys. Res.*, 78, 2251–2264, 1973.
- McCormac, F. G., T. L. Killeen, E. Gombosi, P. B. Hays and N. W. Spencer, Configuration of the high-latitude thermosphere neutral circulation for IMF  $B_y$  negative and positive, *Geophys. Res. Lett.*, 12, 155–158, 1985.
- McCormac, F. G., T. L. Killeen and J. P. Thayer, The influence of IMF  $B_y$  on the high-latitude thermospheric circulation during northward IMF, *J. Geophys. Res.*, 96, 115–128, 1991.
- Meier, R. R., Depressions in the far-ultraviolet airglow over the poles, *J. Geophys. Res.*, 75, 6218–6232, 1970.
- Meier, R. R., Ultraviolet spectroscopy and remote sensing of the upper atmosphere, *Space Sci. Rev.*, 58, 1–185, 1991.
- Meier, R. R., and D. E. Anderson Jr., Determination of atmospheric composition and temperature from the UV airglow, *Planet. Space Sci.*, 31, 967–976, 1983.
- Meier, R. R., R. Cox, D. J. Strickland, J. D. Craven and L. A. Frank, Interpretation of Dynamics Explorer far UV images of the quiet time thermosphere, *J. Geophys. Res.*, 100, 5777–5794, 1995.
- Meier, R. R., and J.-S. Lee, An analysis of the OI 1304 A dayglow using a Monte Carlo resonant scattering model with partial frequency redistribution, *Planet. Space Sci.*, 30, 439–450, 1982.
- Meier, R. R., and D. K. Prinz, Observations of the OI 1304-A airglow from Ogo 4, *J. Geophys. Res.*, 76, 4608–4620, 1971.
- National Academy of Sciences, *Studies in Geophysics: Solar Variability, Weather, and Climate*, National Academy Press, Washington D. C., 1982.

- National Space Science Data Center, World Data Center A for Rockets and Satellites: Interplanetary Medium Data Book - September 1977, 1977.
- National Space Science Data Center, World Data Center A for Rockets and Satellites: Interplanetary Medium Data Book - Supplement 3A, 1977–1985, 1986.
- Nicholas, A. C. Spatial and temporal variations of the FUV dayglow with geomagnetic activity, Master Thesis, University of Alaska, 1993.
- Nicholas, A. C., J. D. Craven and L. A. Frank, A survey of large-scale variations in thermospheric oxygen column density with magnetic activity as inferred from observations of the FUV dayglow, *J. Geophys. Res.*, *102*, 4493–4510, 1997.
- Parish, H. F., G. R. Gladstone and S. Chakrabarti, Interpretation of satellite airglow observations during the March 22, 1979, magnetic storm, using the coupled ionosphere-thermosphere model developed at University College London, *J. Geophys. Res.*, *99*, 6155–6166, 1994.
- Prölss, G. W., Magnetic Storm Associated Perturbations of the Upper Atmosphere: Recent Results Obtained by Satellite-Borne Gas Analyzers, *Rev. of Geophys. and Space Phys.*, *18*, 183–202, 1980.
- Prölss, G. W., Latitudinal structure and extension of the polar atmospheric disturbance, *J. Geophys. Res.*, *86*, 2385–2396, 1981.
- Prölss, G. W., Perturbation of the low-latitude upper atmosphere during magnetic substorm activity, *J. Geophys. Res.*, *87*, 5260–5266, 1982.
- Prölss, G. W., On explaining the local time variation of ionospheric storm effects, *Ann. Geophys.*, *11*, 1–9, 1993.
- Prölss, G. W., and J. D. Craven, Perturbations of the FUV dayglow and ionospheric storm effects, *Adv. Space. Res.*, in press, 1998.
- Prölss, G. W., and K. H. Fricke, Neutral composition changes during a period of increasing magnetic activity, *Planet. Space. Sci.*, *24*, 61–67, 1976.
- Prölss, G. W., K. H. Fricke and U. von Zahn, Observations during a magnetic storm in late October, 1973, *Space Res.*, *15*, 216–220, 1975.

- Prölss G. W., and M. Roemer, Thermospheric storms. *Adv. Space Res.*, 7, 10223–10235, 1987.
- Prölss, G. W., M. Roemer and J. W. Slowey, Disipation of solar wind energy in the earth's upper atmosphere: The geomagnetic activity effect, CIRA 1986. *Adv. Space Res.*, 8, 215–261, 1988.
- Prölss, G. W., and U. von Zahn, Esro 4 gas analyzer results. 2. Direct measurements of changes in neutral composition during an ionospheric storm. *J. Geophys. Res.*, 79, 2535–2539, 1974.
- Rairden, R. L., Geocoronal imaging with Dynamics Explorer. Ph.D. Thesis, University of Iowa, 1985.
- Rairden, R. L., L. A. Frank and J. D. Craven, Geocoronal imaging with Dynamics Explorer: A first look. *Geophys. Res. Lett.*, 10, 533–536, 1983.
- Ratcliffe, J. A., Physics of the Upper Atmosphere, Academic Press, 1960.
- Rees, M. H., Physics and Chemistry of the Upper Atmosphere, Cambridge Atmospheric and Space Sciences Series, 1989.
- Rees, M. H., D. Lummerzheim, R. G. Roble, J. D. Winningham, J. D. Craven and L. A. Frank, Auroral energy deposition rate, characteristic electron energy, and ionospheric parameters derived from Dynamics Explorer 1 images. *J. Geophys. Res.*, 93, 12841–12860, 1988.
- Reiff, P. H., R.W. Spiro and T. W. Hill, Dependence of polar cap potential drop on interplanetary parameters, *J. Geophys. Res.*, 86, 7639–7648, 1981.
- Rich, F. J., and M. Hairston, Large-scale convection patterns observed by DMSP. *J. Geophys. Res.*, 99, 3827–3844, 1994.
- Richmond, A. D., and Y. Kamide, Mapping electrodynamic features of the high-latitude ionosphere from localized observations: technique, *J. Geophys. Res.*, 93, 5741–5759, 1988.
- Richmond, A. D., Y. Kamide, B.-H. Ahn, S. -I. Akasofu, D. Alcaydé, M. Blanc, O. de la Beaujardière, D. S. Evans, J. C. Foster, E. Friis-Christensen, T. J. Fuller-Rowell, J. M.

- Holt, D. Knipp, H. W. Kroehl, R. P. Lepping, R. J. Pellinen, C. Senior and A. N. Zaitzev, Mapping electrodynamic features of the high-latitude ionosphere from localized observations: combined incoherent-scatter radar and magnetometer measurements for January 18–19, 1984. *J. Geophys. Res.*, 93, 5760–5776. 1988.
- Rishbeth, H., and O. K. Garriott, *Introduction to Ionospheric Physics*. Academic Press, 1969.
- Roble, R. G., T. L. Killeen, N. W. Spencer, R. A. Heelis, P. H. Reiff and J. D. Winningham, Thermospheric dynamics during November 21–22, 1981: Dynamics Explorer measurements and thermospheric general circulation model predictions. *J. Geophys. Res.*, 93, 209–225, 1988.
- Rottman, G. J., P. D. Feldman and H. W. Moos, Far ultraviolet spectra and altitude profiles of the dawn airglow. *J. Geophys. Res.*, 78, 258–265. 1973.
- Ruohoniemi, J. M., and R. A. Greenwald, Observation of IMF and seasonal effects in high-latitude convection, *Geophys. Res. Lett.*, 22, 1121–1124. 1995.
- Schoendorf, J., G. Crowley, R. G. Roble and F. A. Marcos, Neutral density cells in the high latitude thermosphere–1. Solar maximum cell morphology and data analysis. *J. Atmos. Solar Terr. Phys.*, 58, 1751–1768, 1996.
- Schoendorf, J., G. Crowley, R. G. Roble and F. A. Marcos, Neutral density cells in the high latitude thermosphere–2. Mechanisms. *J. Atmos. Solar Terr. Phys.*, 58, 1769–1768. 1996.
- Smith, R. W., D. Rees and R. D. Stewart, Southern Hemisphere Thermospheric Dynamics: A Review, *Rev. of Geophys.*, 26, 591–622. 1988.
- Spiro, R. W., P. H. Reef and L. J. Maher Jr., Precipitating electron energy flux and auroral zone conductances -an empirical model, *J. Geophys. Res.* 87, 8215–8227. 1982.
- Strauss, J. M., and L. A. Christopher, Dynamical effects in the global distribution of thermospheric atomic oxygen, *J. Geophys. Res.*, 84, 1241–1252. 1979.

- Strickland, D. J., T. Majeed, A. B. Christensen and J. H. Hecht. Remote sensing of atomic oxygen in auroral rocket experiments using topside zenith viewing O/N<sub>2</sub> brightness ratios, *J. Geophys. Res.*, *102*, 2475–2482. 1997
- Strickland, D. J., and G. E. Thomas, Global atomic oxygen density derived from OGO-6 1304 Å airglow measurements, *Planet. Space Sci.*, *24*, 313–326, 1976.
- Thayer, J. P., T. L. Killeen, F. G. McCormac, C. R. Tschan, J.-J. Ponthieu and N. W. Spencer, Thermospheric neutral wind signatures dependent on the east-west component of the interplanetary magnetic field for Northern and Southern Hemispheres as measured from Dynamics Explorer-2, *Ann Geophys.*, *5A*, 363–368. 1987.
- Torr, M. R., D. G. Torr, M. Zukic, R. B. Johnson, J. Ajello, P. Banks, K. Clark, K. Cole, C. Keffer, G. Parks, B. Tsurutani, and J. Spann, A Far Ultraviolet Imager for the International Solar Terrestrial Physics Mission, *Space Sci. Rev.*, *71*, 329–383. 1995.
- Trinks, H., K. H. Fricke, U. Laux, G. W. Prölss and U. von Zahn, *J. Geophys. Res.*, *80*, 4571–4575, 1975.
- Webb, W. L., Structure of the Stratosphere and Mesosphere, Academic Press, 1966.
- Weimer, D. R., Models of high-latitude electric potentials derived with a least error fit of spherical harmonic coefficients, *J. Geophys. Res.*, *100*, 19595–19607. 1995.

### Appendix A Coefficients of Reference Model

Coefficients reported for the F and P dependences of  $\langle r \rangle$  are for functions fitted to the slopes  $m_F$  and  $m_P$  at all S. Once fit, the slopes can be expressed as

$$m_F = ((1 - \tanh(S/a - b))/c)^d \text{ and}$$

$$m_P = a \exp(-1 * ((s-b)/4c)^2)$$

for the ranges of S described in the respective sections in this report. For the F dependence, values for a, b, c, and d are 28.92, 3.629, 2.799, 6.582 respectively. For the P dependence, values for a, b, and c are -0.0876, 62.45 and 9.183, respectively.

No functional form was used for the dependence of  $\langle r \rangle$  on A. In this case, the slopes, m, of the individual fits are reported in Table A-1 for  $S > 81^\circ$  and  $D > 20^\circ$ , where all values are reported to four significant digits.

**Table A-1 : Slopes of Azimuth Dependence of  $\langle r \rangle$** 

D↓ \ S→	81°-84°	84°-87°	87°-90°	90°-93°	93°-96°	96°-99°	99°-102°	102°-105°
20°-25°	0.0026 ± 0.0029	0.0050 ± 0.0019	0.0023 ± 0.0026	0.0058 ± 0.0021	0.0064 ± 0.0013	0.0033 ± 0.0010	0.0018 ± 0.0010	0.0003 ± 0.0016
25°-30°	0.0035 ± 0.0192	-0.0049 ± 0.0086	0.0038 ± 0.0034	0.0064 ± 0.0030	0.0059 ± 0.0012	0.0059 ± 0.0021	0.0023 ± 0.0005	0.0008 ± 0.0004
30°-35°	-0.0058 ± 0.0124	-0.0024 ± 0.0104	0.0130 ± 0.0028	0.0170 ± 0.0041	0.0165 ± 0.0037	0.0070 ± 0.0012	0.0014 ± 0.0014	0.0012 ± 0.0003
35°-40°	-0.0017 ± 0.0160	0.0146 ± 0.0084	0.0288 ± 0.0052	0.0257 ± 0.0032	0.0144 ± 0.0029	0.0075 ± 0.0014	0.0020 ± 0.0005	0.00076 ± 0.0007
40°-45°	0.0144 ± 0.0104	0.0298 ± 0.0117	0.0270 ± 0.0033	0.020 ± 0.0054	0.017 ± 0.0021	0.0099 ± 0.0010	0.0032 ± 0.0019	0.0011 ± 0.0003
45°-50°	0.0328 ± 0.0169	0.0254 ± 0.0051	0.0284 ± 0.0073	0.0234 ± 0.0032	0.0238 ± 0.0024	0.0130 ± 0.0010	0.0049 ± 0.0018	0.001 ± 0.0010
50°-55°	0.0248 ± 0.0058	0.0324 ± 0.0028	0.0428 ± 0.0080	0.0361 ± 0.0022	0.0258 ± 0.0024	0.0189 ± 0.0026	0.0059 ± 0.0013	0.0025 ± 0.0015
55°-60°	0.0357 ± 0.0065	0.0430 ± 0.0092	0.0470 ± 0.0117	0.0457 ± 0.0042	0.0373 ± 0.0029	0.0268 ± 0.0041	0.0104 ± 0.0021	0.0004 ± 0.0012
60°-66°	0.0444 ± 0.0273	0.0672 ± 0.0011	0.0785 ± 0.0147	0.0734 ± 0.0169	0.0900 ± 0.0186	0.0430 ± 0.0136	0.0226 ± 0.0045	0.0012 ± 0.0005

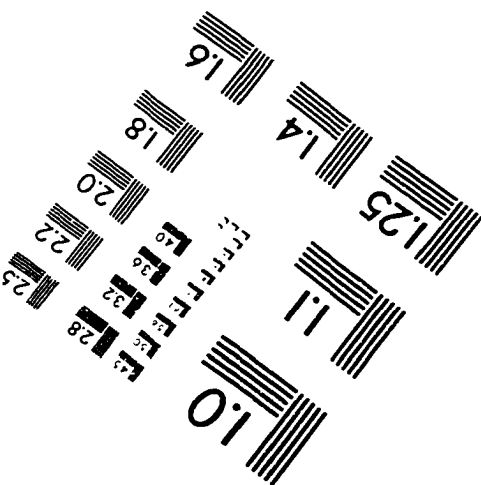
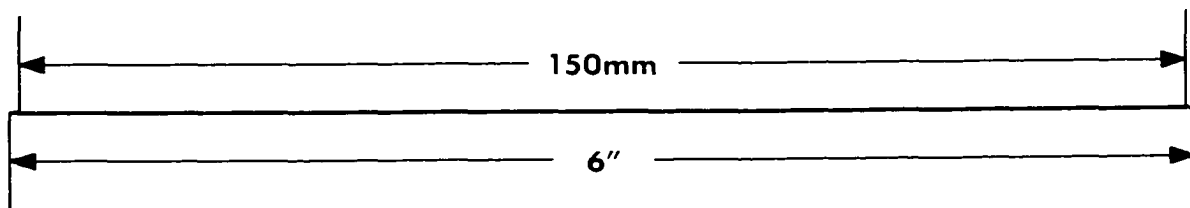
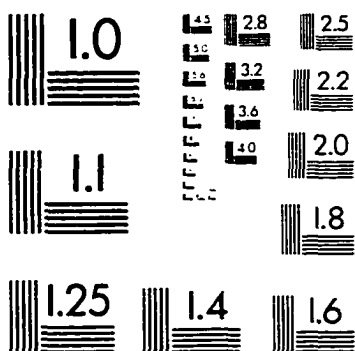
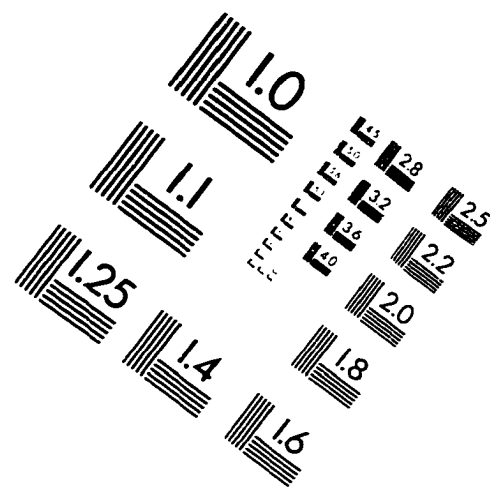
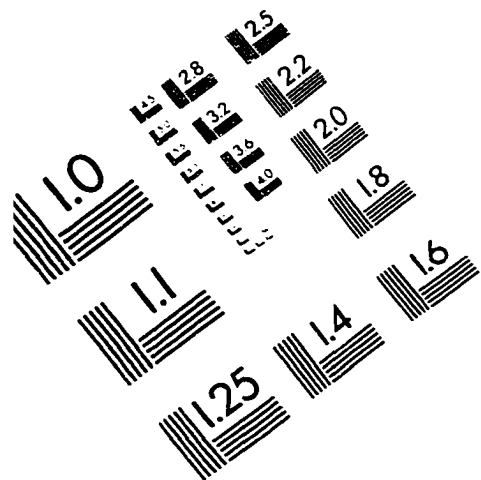
### Appendix B- Statistical Correlation

If a linear relationship exists between two variables,  $x$  and  $y$ , the degree of correlation,  $C$ , can be measured. With  $N$  measurements of  $x$  and  $y$ , the correlation coefficient is determined by

$$C = \frac{\sum_{i=1}^N (x_i - \bar{x})(y_i - \bar{y})}{\left[ \sum_{i=1}^N (x_i - \bar{x})^2 \sum_{i=1}^N (y_i - \bar{y})^2 \right]^{1/2}}$$

The coefficient is always between 1 and -1, where zero indicates no correlation and 1 (-1) indicates perfect (anti-)correlation. The coefficient indicates a likelihood that the variables are not uncorrelated. The percent probability that two uncorrelated ten-element vectors will yield  $|C| > 0.5$  (0.8), for example, is only 14% (0.5%). Larger sample sizes reduce these percent values. Matrix correlation is not performed on matrices in Chapter 3 as the data presented (binned in  $S$  and  $P$ ) will not fill an  $m$  by  $n$  matrix. Vectors of data points are compared for all  $P$  in fixed ranges of  $S$  and the average correlation is reported.

# IMAGE EVALUATION TEST TARGET (QA-3)



APPLIED IMAGE, Inc  
1653 East Main Street  
Rochester, NY 14609 USA  
Phone: 716/482-0300  
Fax: 716/288-5989

© 1993, Applied image, Inc.. All Rights Reserved

